Tracking, b-Tagging and Measurement of the b-Jet Production Cross Section with the ATLAS Detector

Dissertation

zur Erlangung des Grades

"Doktor der Naturwissenschaften"

am Fachbereich Physik, Mathematik und Informatik
der Johannes Gutenberg-Universität in Mainz
im Rahmen des Wolfgang-Gentner Doktoranden Programmes am CERN.

JOHANNES GUTENBERG
UNIVERSITÄT MAINZ

Johanna Elisabeth Fleckner
geb. in Gießen

Mainz, den 10. Juni 2010

Dekan: *)

1. Berichtserstatter: *)

2. Berichtserstatter: *)

mündliche Prüfung: 05. Oktober 2011

Dissertation an der Universität Mainz (D77)

*) wurden aus Datenschutzgründen aus der elektronischen Version gelöscht

Abstract

The Standard Model of elementary particle physics was developed to describe the fundamental particles which constitute matter and the interactions between them. The Large Hadron Collider (LHC) at CERN in Geneva was built to solve some of the remaining open questions in the Standard Model and to explore physics beyond it, by colliding two proton beams at world-record centre-of-mass energies. The ATLAS experiment is designed to reconstruct particles and their decay products originating from these collisions. The precise reconstruction of particle trajectories plays an important role in the identification of particle jets which originate from bottom quarks (b-tagging). This thesis describes the step-wise commissioning of the ATLAS track reconstruction and b-tagging software and one of the first measurements of the b-jet production cross section in pp collisions at $\sqrt{s} = 7$ TeV with the ATLAS detector. The performance of the track reconstruction software was studied in great detail, first using data from cosmic ray showers and then collisions at $\sqrt{s} = 900$ GeV and 7 TeV. The good understanding of the track reconstruction software allowed a very early deployment of the b-tagging algorithms. First studies of these algorithms and the measurement of the b-tagging efficiency in the data are presented. They agree well with predictions from Monte Carlo simulations. The b-jet production cross section was measured with the 2010 dataset recorded by the ATLAS detector, employing muons in jets to estimate the fraction of b-jets. The measurement is in good agreement with the Standard Model predictions.

Abstract

Das Standard Modell der Elementarteilchenphysik beschreibt die Elementarteilchen, aus denen die Materie besteht, und die Wechselwirkungen zwischen ihnen. Um die meisten der offenen Fragen des Standard Modells zu klären sowie Theorien darüber hinaus zu testen, wurde der Large Hadron Collider (LHC) am CERN in Genf entwickelt. Der LHC kollidiert zwei Protonenstrahlen mit der welthöchsten Schwerpunktsenergie. ATLAS, eines der Experimente am LHC, ist darauf ausgerichtet, Teilchen aus diesen Kollisionen und deren Eigenschaften zu messen. Die präzise Rekonstruktion von Teilchentrajektorien spielt eine große Rolle bei der Identifikation von Teilchenjets, die von bottom-Quarks stammen (b-Tagging). Themen dieser Arbeit sind die stufenweise Inbetriebnahme der Spurrekonstruktions- und b-Taggingsoftware sowie eine der ersten Messungen des b-Jet-Wirkungsquerschnitts mit dem ATLAS Detektor bei einer Schwerpunktsenergie von 7 TeV. Die Eigenschaften der Spurrekonstruktionssoftware wurden zunächst mit Hilfe der kosmischen Hintergrundstrahlung und dann in Kollisionen bei einer Schwerpunktsenergie von 900 GeV und 7 TeV detailliert studiert und mit entsprechenden Monte Carlo Simulationen verglichen. Das gute Verständnis der Spurrekonstruktionssoftware gewährleistete eine sehr frühe Inbetriebnahme der b-Taggingalgorithmen. Erste Studien dieser Algorithmen und die Messung der b-Taggingeffizienz in Daten werden präsentiert und stimmen gut mit Vorhersagen aus Monte Carlo Simulationen überein. Der b-Jet-Wirkungsquerschnitt wurde mit Hilfe von Myonen in Jets gemessen und ist in guter Übereinstimmung mit den Vorhersagen des Standard Modells.

Contents

Chapter 1

Introduction

The ambition to understand the world we live in is a constant factor in the history of mankind. Many different approaches have been pursued to answer the question "was die Welt im Innersten zusammenhält" [1][1], to quote Johann Wolfgang von Goethe, one of the most famous German writers. Scientists have worked on understanding the world ever since the ancient Greeks. Many experiments were carried out in the course of the 19^{th} and 20^{th} century to study and understand the composition of matter. These experiments have led, for example, to the discovery of: the electron, the atomic structure of the elements consisting of a nucleus and surrounding electrons, protons and neutrons building the nucleus and the fact that protons and neutrons themselves are a composition of yet even smaller particles, the quarks. To describe the underlying structure of matter on the basis of observed phenomena, a common theoretical framework, the Standard Model of elementary particle physics, was developed. Refined techniques and more powerful experiments, like the Large Hadron Collider (LHC), are required to solve the remaining open questions. The LHC collides two proton beams at world-record centre-of-mass energies. The ATLAS experiment is designed to reconstruct particles and their decay products originating from these collisions. The precise reconstruction of particle trajectories plays an important role in the identification of particle jets which originate from bottom quarks (b-tagging). This thesis presents many aspects of commissioning the ATLAS track reconstruction and b-tagging software and one of the first measurements of the b-jet production cross section with the ATLAS detector at a centre-of-mass energy of 7 TeV.

Chapter 2 introduces the basic aspects of the Standard Model of elementary particle physics, which describes the fundamental particles in nature and the interactions between them. The concepts used to calculate the theoretical predictions for hadron colliders are discussed, focusing on the production mechanisms in pp collisions of one of the elementary particles, the bottom quark (b-quark). Matter consisting of b-quarks (b-hadrons) will be of special interest for this thesis. Properties and decay channels of b-hadrons and past b production measurements at hadron colliders will be discussed in detail.

[1] "whatever holds the world together in its innermost"

The LHC at the CERN laboratory in Geneva, Switzerland, is the world's newest and most sophisticated tool for particle physics research. The LHC and one of its experiments, ATLAS, are introduced in Chapter 3. The LHC produces short-lived, heavy particles which only existed in nature nano-seconds after the big bang. The ATLAS experiment is designed to efficiently and precisely reconstruct particles or their decay products originating from these collisions. Chapter 4 describes the techniques employed by the ATLAS experiment to reconstruct the particles and their properties like mass, trajectory, charge and energy.

The reconstruction of the trajectories of charged particles in the detector is a crucial element in the understanding of the underlying topologies of the events. Chapter 5 discusses the commissioning of the track reconstruction software and its performance. First tests of the software using the real detector response from cosmic ray showers were carried out. These events typically only contain one trajectory per event and are therefore ideal for the commissioning of the track reconstruction software. More stringent tests due to the higher track multiplicities were carried out using proton-proton collisions at a centre-of-mass energy of 900 GeV and 7 TeV. Chapter 6 compares the expected track reconstruction performance in a high-luminosity environment of the present ATLAS detector layout and an upgraded layout, which includes an additional pixel layer close to the beam pipe.

The precision track reconstruction plays an important role in the identification of particle jets which originate from bottom quarks (b-tagging). b-tagging is a crucial part of the LHC physics program, since precision measurements in the top quark sector as well as in searches for the Higgs boson and new phenomena use this technique to suppress background processes containing predominantly light-flavour jets. Chapter 7 presents first studies of the b-tagging algorithms in proton-proton collisions at $\sqrt{s} = 7$ TeV and the measurement of the b-tagging efficiency in the data.

The measurement of the b-quark jet production rate with the ATLAS detector at a centre-of-mass energy of 7 TeV is presented in Chapter 8. This measurement relies on the 2010 dataset recorded by ATLAS and uses muons from b-quark decays to estimate the fraction of b-quark jets. The measurement is compared to Standard Model predictions, thereby testing the underlying strong interaction dynamics and probing the validity of Standard Model predictions in the newly opened energy frontier at the Large Hadron Collider.

Chapter 2

Physics at the Large Hadron Collider

The Large Hadron Collider at CERN in Geneva is the world's newest and most sophisticated tool for particle physics research. This chapter gives a short introduction into the underlying physics models which describe the dynamics of hadron collisions. One of the main results of this thesis is the measurement of the bottom-quark jet production cross section. Bottom-quark jets (b-jets) are particle jets which originate from a bottom-quark, one of the fundamental particles in the Standard Model of elementary particle physics. This chapter discusses the theoretical principles needed to interpret the measurement.

A very brief description of the Standard Model of elementary particle physics is given in the first section. This model describes the fundamental particles in nature and the interactions between them. The principles of the Standard Model are the basis for the theory of Quantum Chromodynamics (QCD). Quantum Chromodynamics provides the framework to make precise calculations of processes predicted by the Standard Model. The fundamentals of QCD and the formalism to calculate the predictions are introduced in the second section. The implementation of these principles in Monte Carlo event generators are discussed next. Monte Carlo event generators combine the precise QCD predictions with phenomenological models to generate realistic event topologies which can be compared to experimental data. The last section in this chapter details the different production mechanisms for bottom-quarks, their properties and decay channels and gives an overview of bottom production measurements at hadron colliders.

2.1 The Standard Model of Elementary Particles

The Standard Model [2] describes the elementary particles in nature and their interactions. Three kinds of elementary particles exist: leptons, quarks and mediators. There are six leptons, which can be divided into three families or generations. Six different flavours of quarks exist, which can be grouped into three generations as well. Unlike the leptons, each quark comes in three colours, the "charge" of the strong interaction; the leptons are colourless.

Both leptons and quarks are spin-$\frac{1}{2}$-particles and therefore obey the Fermi-Dirac statistics [3] and are referred to as fermions. An antifermion exists for each fermion, which has identical mass and spin but which has reversed charge and other quantum numbers. The fundamental fermion classifications are listed in Table 2.1. Natural units ($\hbar = c = 1$) are assumed throughout this thesis.

Particle	Flavour generation			Charge $Q/\lvert e\rvert$	weak Isospin T_3
(*mass* [GeV])	1st	2nd	3rd		
leptons	$\boldsymbol{e}$	$\boldsymbol{\mu}$	$\boldsymbol{\tau}$	-1	$-1/2$
	$(0.51 \cdot 10^{-3})$	(0.11)	(1.8)		
	$\boldsymbol{\nu_e}$	$\boldsymbol{\nu_\mu}$	$\boldsymbol{\nu_\tau}$	0	$+1/2$
		$(< 2 \cdot 10^{-9})$			
quarks	$\boldsymbol{up}$	$\boldsymbol{charm}$	$\boldsymbol{top}$	$+\frac{2}{3}$	$+1/2$
	$(\approx 2 \cdot 10^{-3})$	(1.3)	(171)		
	$\boldsymbol{down}$	$\boldsymbol{strange}$	$\boldsymbol{bottom}$	$-\frac{1}{3}$	$-1/2$
	$(\approx 5 \cdot 10^{-3})$	$(0.10 \cdot 10^{-3})$	(4.2)		

Table 2.1: The fundamental fermions, from Reference [4].

The Standard Model not only describes the elementary particles, but also the interactions via mediators between them. The different interactions [3] are mediated by the exchange of characteristic particles with integral spin, the bosons. Four fundamental forces are known:

- The strong interaction which is responsible for binding the quarks is mediated by massless particles, the gluons. Eight gluons are predicted by the Standard Model, which themselves carry colour, the "charge" of the strong interaction. Therefore gluons can interact with themselves, and neither gluons nor quarks exist as isolated particles.
- The electromagnetic interaction which is responsible for all phenomena in extra-nuclear physics like the bound states of electrons with nuclei is mediated by photon exchange. Its charge is the electromagnetic charge Q.
- The weak interaction which is typified by the slow process of nuclear β-decays is mediated by the $W^\pm$ and Z^0 bosons. The weak interaction is the only flavour-changing force. Its "charge" is the weak isospin T_3.
- The gravitational interaction between all types of particles which is predicted to be mediated by a spin-2 boson, the graviton. Gravitation is by far the weakest of all the fundamental interactions.

The four interactions and their mediator bosons are summarised in Table 2.2 [2].

Force	Strength	Theory	Mediator
Strong	10	Chromodynamics	Gluon
Electromagnetic	10^{-2}	Electrodynamics	Photon
Weak	10^{-13}	Flavourdynamics	$W^{\pm}$ and Z^0
Gravitational	10^{-42}	Geometrodynamics	Graviton

Table 2.2: The four fundamental interactions, from Reference [2].

Only colourless particles are observed in nature, an effect which is known as confinement. The colour force between two quarks rises with growing distance, which is attributed to the self-interaction of the gluons. Quarks therefore do not exist as isolated particles, but need to form either quark-antiquark pairs (mesons) or particles consisting of three quarks (baryons) respectively three antiquarks (antibaryons) which are colourless. Examples for mesons are the pion $\pi^+ = u\bar{d}$ or the kaon $K^+ = u\bar{s}$, and for baryons the proton $p = uud$ or the neutron $n = udd$.

The Higgs mechanism [2] in the Standard Model is understood as the primary method of mass generation for gauge bosons. The minimal model predicts a single physical neutral scalar particle - the Higgs boson. As of today, the Higgs particle is the only particle predicted by the Standard Model that has not yet been measured in a laboratory.

2.2 Quantum Chromodynamics

Quantum Chromodynamics (QCD) is the theory of the strong interactions [5]. It describes the interactions between quarks and gluons and is regarded as one of the cornerstones of the Standard Model of elementary particle physics. QCD has been used successfully to describe scattering processes at high-energy e^+e^-- and hadron-colliders [6]. The scattering processes can be divided into two categories, hard or soft, depending on the energy scale Q. Hard processes like high-p_{T} jet production can be predicted with good precision using QCD perturbation theory in the coupling constant $\alpha_S(Q^2)$. Soft processes on the other hand like the underlying event are dominated by non-perturbative QCD effects and are less well understood. The coupling $\alpha_S(Q^2)$ becomes large compared to the energy scale of the process, and the perturbation series breaks down. The strong interaction depends therefore on the energy scale of the process, and the coupling constant α_S is referred to as the "running coupling constant" of QCD.

This section will give a short introduction into the perturbative framework used to calculate predictions for hard-scattering processes, for example the ones that occur at the Large Hadron Collider (LHC). A much more complete review of this matter can be found in Reference [5]

or Reference [6]. Experimental measurements have shown that only mesons and baryons are observed in nature. The concept of quarks was needed to have a physical manifestation for the $SU_f(3)$ of flavour as observed in the spectra of mesons and baryons. One could therefore argue that the most fundamental principle of QCD is the fact that matter consists of quarks [5].

2.2.1 Lagrangian of QCD and Feynman Rules

A perturbative analysis of QCD requires the knowledge of the Feynman rules which describe the interactions of the quarks and gluons, in analogy to Quantum Electrodynamics. Starting from a Lagrangian density, the Feynman rules can be derived. The Lagrangian of QCD [5] can be written as

$$\mathcal{L}_{\mathrm{QCD}} = -\frac{1}{4} F^A_{\alpha\beta} F_A^{\alpha\beta} + \sum_{\text{flavours}} \bar{q}_a (i \not{D} - m)_{ab} q_b, \tag{2.1}$$

except for gauge-fixing terms. It describes the interaction of spin-$\frac{1}{2}$ quarks of mass m and massless spin-1 gluons. $\not{D}$ is a short notation for $\gamma_\mu D^\mu$. The metric is given by $g^{\alpha\beta} = \mathrm{diag}(1, -1, -1, -1)$, and the gamma matrices satisfy the anti-commutation relations $\{\gamma^\mu, \gamma^\nu\} = 2g^{\mu\nu}$.

$F^A_{\alpha\beta}$ is the field strength tensor derived from the gluon field $\mathcal{A}^A_\alpha$,

$$F^A_{\alpha\beta} = [\partial_\alpha \mathcal{A}^A_\beta - \partial_\beta \mathcal{A}^A_\alpha - g f^{ABC} \mathcal{A}^B_\alpha \mathcal{A}^C_\beta], \tag{2.2}$$

and the indices A, B and C run over the eight colour degrees of freedom of the gluon field. g is the coupling constant for the strength of the interactions between coloured quanta and f^{ABC} the structure constants of the $SU_c(3)$ colour group. The third term in Equation (2.2) is non-Abelian and gives rise to triplet and quartet gluon self-interactions and ultimately to the property of asymptotic freedom. It is this term which distinguishes QCD from QED.

The covariant derivatives D in Equation (2.1) act on triplet fields q_a and relate to the matrices t and T in the fundamental and adjoint representations of the $SU_c(3)$ respectively,

$$\begin{aligned} (D_\alpha)_{ab} &= \partial_\alpha \delta_{ab} + ig(t^C \mathcal{A}^C_\alpha)_{ab} \\ (D_\alpha)_{AB} &= \partial_\alpha \delta_{AB} + ig(T^C \mathcal{A}^C_\alpha)_{AB} \end{aligned} \tag{2.3}$$

The second term in the definitions of D in Equation (2.3) describes the interaction between quarks and gluons. A representation for the matrices t is provided by the eight Gell-Mann matrices, which are hermitean and traceless.

Equation (2.1) can be used to calculate Feynman rules as summarised in Figure 2.1.

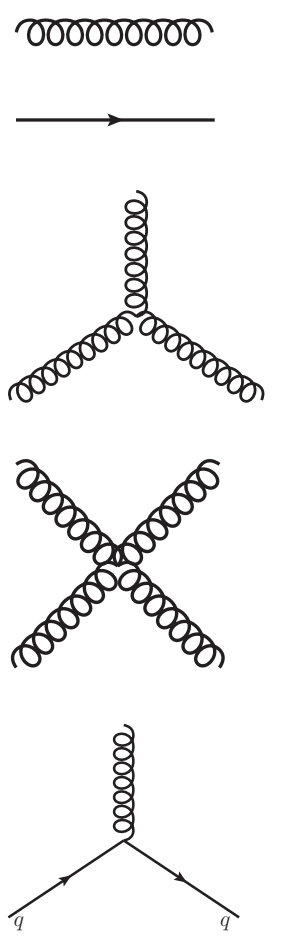

$\delta^{AB}[-g^{\alpha\beta} + (1-\lambda)\frac{p^\alpha p^\beta}{p^2+i\epsilon}]\frac{i}{p^2+i\epsilon}$

$\delta^{ab}\frac{i}{(\not{p}-m+i\epsilon)_{ji}}$

$-gf^{ABC}[(p-q)^\gamma g^{\alpha\beta}+(q-r)^\alpha g^{\beta\gamma}+(r-p)^\beta g^{\gamma\alpha}]$
(all momenta incoming, $p+q+r=0$)

$-ig^2 f^{XAC}f^{XBD}[g^{\alpha\beta}g^{\gamma\delta} - g^{\alpha\delta}g^{\beta\gamma}]$
$-ig^2 f^{XAD}f^{XBC}[g^{\alpha\beta}g^{\gamma\delta} - g^{\alpha\gamma}g^{\beta\delta}]$
$-ig^2 f^{XAB}f^{XCD}[g^{\alpha\gamma}g^{\beta\delta} - g^{\alpha\delta}g^{\beta\gamma}]$

$-ig(t^A)_{cb}(\gamma^\alpha)_{ji}$

Figure 2.1: QCD Feynman rules for gluons (curly lines) and fermions (solid lines), from Reference [5].

2.2.2 Hard-Scattering Formalism and the QCD Factorisation Theorem

The Lagrangian formalism and the Feynman rules for QCD introduced in the section before describe the interactions between quarks, leptons and gluons. Physics experiments at hadron colliders, however, require the knowledge of the interactions of quarks which are bound in hadrons. Parton-model ideas developed for deep-inelastic scattering have been extended to certain processes in hadron-hadron collisions [6], like the production of a massive lepton pair by quark-antiquark annihilation, the Drell-Yan process. The parton models were originally developed to describe the deep inelastic scattering of leptons and hadrons [5]. Structure functions parameterise the structure of the target as seen in the interaction, and measurements imply that the scattering occurs between leptons and point-like constituents of the hadrons, the quarks. It was postulated [6] that the hadronic cross section $\sigma(AB \to \mu^+\mu^- X)$ could be obtained by weighting the subprocess cross section $\hat{\sigma}$ for $q\bar{q} \to \mu^+\mu^-$ with the parton distribution functions (pdfs) $f_{q/A}(x)$ extracted from deep-inelastic scattering. These calculations showed very good agreement with the measured cross sections and confirmed the parton-model formalism. However, problems seemed to arise when perturbative corrections were calculated from real and virtual gluon emissions. These

calculations showed large logarithms from gluons emitted collinearly with the incoming quarks which seemed to spoil the convergence of the perturbative expansion. These logarithms, however, were the same as those that arise in deep-inelastic scattering structure function calculations, and could therefore be absorbed in the definition of the parton distributions. The factorisation theorems [6] show that this is a general feature of hard-scattering processes.

The hadronic cross section $\sigma(AB \to \mu^+\mu^- X)$ can therefore be expressed as

$$\sigma_{AB} = \int dx_a dx_b f_{a/A}(x_a, Q^2) f_{b/B}(x_b, Q^2) \hat{\sigma}(x_a, x_b, Q^2)_{ab \to X}, \tag{2.4}$$

where for the Drell-Yan process $X = l^+l^-$ and $ab = q\bar{q},\ \bar{q}q$. This calculation is valid in the asymptotic scaling limit (analogous to the Bjorken scaling limit in deep-inelastic scattering) $M_X = M^2_{l^+l^-},\ s \to \infty,\ \tau = M^2_{l^+l^-}/s$ fixed. The schematic structure of the hard scattering process is shown in Figure 2.2. The Q^2 appearing in the parton distribution functions is a large momentum scale that characterises the hard-scattering, e.g. $M^2_{l^+l^-}$, ${p_{\mathrm{T}}}^2$ etc.

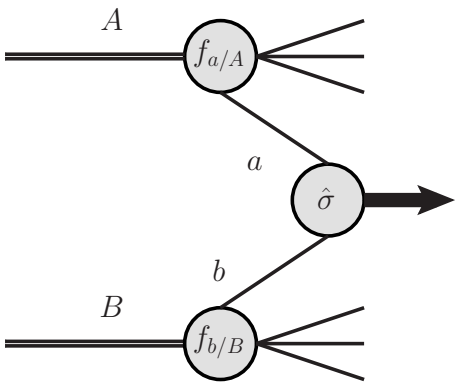

Figure 2.2: Schematic structure of a hard-scattering process, from Reference [6].

It turned out that the finite corrections left behind after the logarithms had been factored into the pdfs were not universal and needed to be calculated for each process separately. This gives rise to perturbative corrections $\mathcal{O}(\alpha_S^n)$ to the leading logarithm cross section in Equation (2.4)

$$\sigma_{AB} = \int dx_a dx_b f_{a/A}(x_a, \mu_F^2) f_{b/B}(x_b, \mu_F^2) \times [\hat{\sigma}_0 + \alpha_S(\mu_R^2)\hat{\sigma}_1 + ...]_{ab \to X}, \tag{2.5}$$

where μ_F denotes the factorisation scale, which can be interpreted as the scale that separates the long- and short-distance physics, and where μ_R is the renormalisation scale for the QCD running coupling. The physical cross section result calculated to all orders in perturbation theory is formally independent of the choices of μ_F and μ_R. The dependence of the coefficients like e.g. $\hat{\sigma}_1$ on these parameters is compensated exactly by the scale dependence of the parton distributions and the coupling constant. The compensation becomes more exact as more terms are included in the perturbation series. In case of a limited set of higher-order

corrections, it is necessary to make a specific choice for the calculation of the cross section prediction. A common choice for μ_F and μ_R are values of the order of the typical momentum scale of the hard-scattering process. This avoids unnaturally large logarithms reappearing in the perturbation series.

2.2.2.1 Partonic cross sections

The partonic cross sections $\hat{\sigma}_i$ in Equation (2.5) are obtained using the Feynman rules as introduced in Section 2.2.1 to calculate the squared matrix element of the hard interaction in question, and then integrating this over the appropriate phase-space. The calculations of the matrix elements can be done at different levels in the perturbative expansion. Three examples for the production of a quark pair are given in Figure 2.3. The lowest-order calculations are represented by tree-level Feynman diagrams which are characterised as the diagrams with the smallest number of vertices contributing to the hard process (left diagram). Higher-order calculations are usually characterised by adding additional gluons or quarks, which can be divided into two categories, virtual (loop) contributions (middle diagram) and the real radiation component (right diagram).

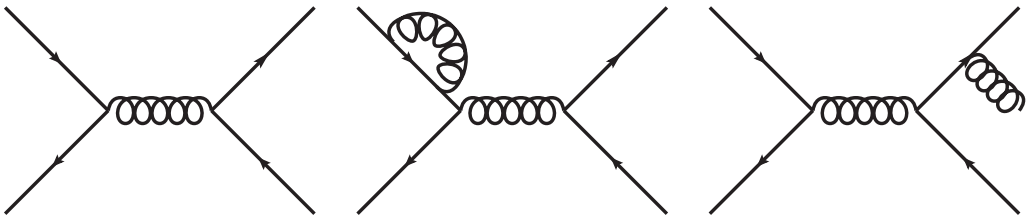

Figure 2.3: Tree-level Feynman diagram (left) and higher-order corrections to the same process: example for a virtual loop contribution (middle) and a real radiation component (right).

2.2.2.2 Parton distribution functions

The calculations of the production cross sections at hadron colliders rely on the knowledge of the distribution of the momentum fraction x of the partons (quarks and gluons) in the proton, see Equation (2.4) or Equation (2.5). The parton distribution functions (pdfs) used in the cross section calculations are solutions of the DGLAP equations [6]. The DGLAP equations have perturbative expansions and determine the Q^2 dependence of the pdfs. Their x dependence has been obtained from global fits to the data from deep-inelastic scattering, Drell-Yan and jet production at pre-LHC energy ranges. The perturbative theoretical predictions and the data in the pdf fits show a remarkable consistency over a wide range of x and Q^2. Figure 2.4 (top) shows the CTEQ6M parton distribution functions at two momentum scales $Q = 2$ and 100 GeV [7].

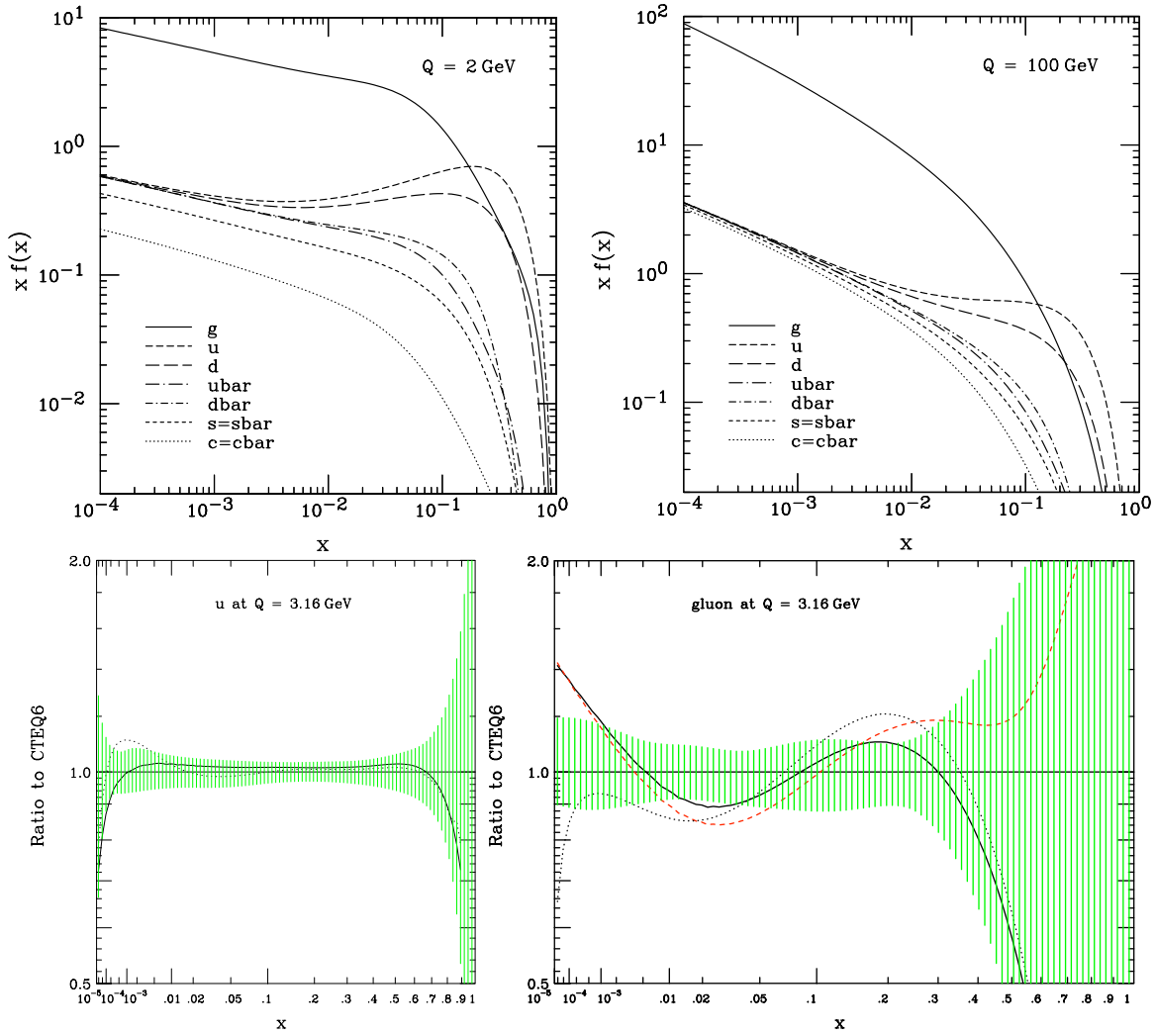

Figure 2.4: top: The CTEQ6M parton distribution functions at $Q = 2$ (left) and 100 GeV (right). bottom: Uncertainty bands at $Q^2 = 10$ GeV^2 for the u-quark distribution function (left - the solid line is CTEQ5M1 and the dotted line is MRST2001) and the gluon distribution function (right - the solid line is CTEQ5M1, the dashed CTEQ5HJ, and the dotted MRST2001). From Reference [7].

The quark distributions are very well measured, with systematic uncertainties of a few per cent. The gluon distributions, however, are less well known. Their uncertainties are roughly a factor of two larger. Figure 2.4 (bottom) shows the uncertainty bands at $Q^2 = 10$ GeV^2 for the CTEQ6M u-quark distribution function (left) and the CTEQ6M gluon distribution function (right) [7]. The uncertainty bands correspond to the envelopes of possible parton distributions that are consistent with the data. The CTEQ6M pdf distributions are in good agreement with the other pdf distributions shown, except at very small values of x.

2.2.3 Hadronisation

The process which converts the partons into the hadrons observed in the experiment is called hadronisation [5]. Hadronisation is a low momentum-transfer, long-distance regime in which

non-perturbative effects become important. It occurs at a time scale which is characterised by $1/\Lambda$, where Λ is the scale at which the coupling α_S becomes strong. The hadronisation occurs much later compared to the time scale $1/Q^2$ at which the strong interaction takes place. At present, only phenomenological models exist for the hadronisation process. They will be explained in more detail in Section 2.3.4.

2.3 Monte Carlo Event Generation

Monte Carlo event generators divide a hadron-hadron collision into several steps [8], which are simulated subsequently: the determination of the energy fraction of the partons and the calculation of the primary hard subprocess, the parton shower of the outgoing coloured participants in the hard subprocess and non-perturbative interactions that convert the partons into outgoing hadrons. The basic implementation of these steps in the event generation chain will be outlined in this section.

2.3.1 Primary Interaction Generation

The first step in the Monte Carlo event generation chain is the generation of the primary hard interaction. Most generators have the option to specify a specific hard production process, for example the production of a bottom-quark-antiquark pair, or a vector or a Higgs boson. The parton density functions are used to determine the fraction of the hadron energy that the incoming partons carry. Their interaction is calculated using the formalism introduced in Section 2.2.2.1. The allowed Feynman diagrams contributing to the process are generated with a probability according to their production cross section.

2.3.2 Parton Shower Models

Parton shower models are used to approximate higher-order contributions to a given matrix element calculation of the partonic cross section. They aim for an approximate result in which enhanced terms are taken into account to all orders instead of a precise prediction to some fixed order in perturbation theory [5]. Parton shower models give an approximate perturbative treatment of QCD dynamics at scales of momentum transfer-squared t greater than some infra-red cut-off value t_{cut}, which is usually of the order of 1 GeV^2. This is particularly useful because the perturbative treatment at $t > t_{cut}$ can be combined with a non-perturbative model of the hadronisation process at scales $t < t_{cut}$.

Several types of parton branching are considered in parton shower models: gluon splitting into two gluons $g \to gg$, gluon splitting into a quark-antiquark pair $g \to q\bar{q}$ and emission of a gluon by a quark (antiquark) $q \to qg$ ($\bar{q} \to \bar{q}g$). The corresponding diagrams are shown in

Figure 2.5. The branching can happen on incoming as well as outgoing lines in the Feynman graphs.

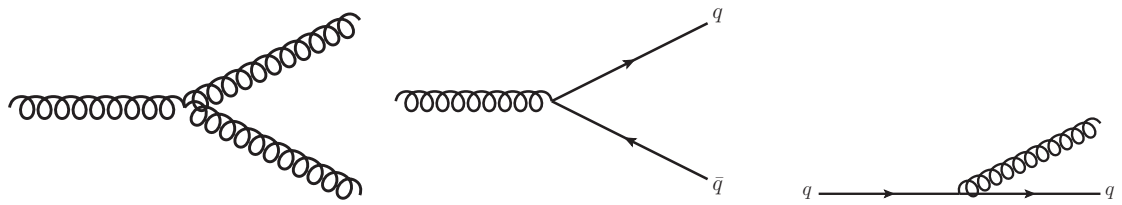

Figure 2.5: Parton branching processes considered in parton shower models: gluon splitting into two gluons $g \to gg$ (left), gluon splitting into a quark-antiquark pair $g \to q\bar{q}$ (middle) and emission of a gluon by a quark (antiquark) $q \to qg$ ($\bar{q} \to \bar{q}g$) (right), from Reference [5].

2.3.2.1 Evolution equations: the Sudakov form factor

The effect of multiple branching is the main ingredient of parton shower programs. A schematic of multiple branching is shown in Figure 2.6 (only gluon emission is considered in the schematic). A quark q with a virtual mass-squared t_0 and a momentum fraction x_0, moves to lower virtual masses and momentum fractions by successive small-angle emissions of gluons.

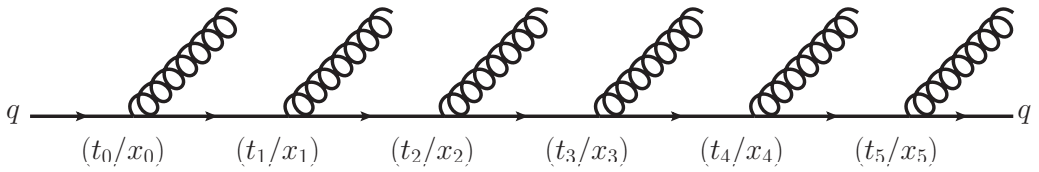

Figure 2.6: Multiple initial state branching, from Reference [5].

One can introduce a function $\Delta(t)$ which is the probability of evolving from t_0 to t without branching. $\Delta(t)$ is called the Sudakov form factor. Each parton species i (gluon or quark) has its own form factor $\Delta_i(t)$ describing its probability of evolving from t_0 to t without branching. The Monte Carlo branching algorithm has to solve the evolution of a state with the virtual mass scale and momentum fraction (t_1,x_1) to the next step (t_2, x_2), and to generate values for (t_2, x_2). The probability of evolving from t_1 to t_2 without branching is $\Delta(t_2)/\Delta(t_1)$. Therefore t_2 can be generated by solving

$$\frac{\Delta(t_2)}{\Delta(t_1)} = \mathcal{R}, \tag{2.6}$$

where $\mathcal{R}$ is a random number in the interval [0,1]. In case the value of t_2 is smaller than the cut-off value t_{cut}, no further branching occurs. Otherwise the value of the momentum fraction $z = x_2/x_1$ is calculated using a similar Monte Carlo technique with the appropriate

probability distribution. Each emitted parton in a parton shower can itself undergo further branching until it reaches t_{cut}. Consequently a parton cascade develops until no further branching is prohibited. A similar technique is used to generate initial state radiation.

2.3.3 Combining NLO Calculations and Parton Showers

Combining fixed-order matrix elements with parton showers is a very desirable but non-trivial task [8]. Tree-level matrix elements are inclusive, they give the probability of having at least n partons in a state calculated to the lowest order in α_S. The corresponding state generated by a parton shower on the other hand is exclusive, it gives the probability that there are exactly n partons. A second problem is double-counting some regions of phase space or undercounting others when combining the fixed-order matrix elements with parton showers.

There are several ways to solve these problems [8], one of them being the NLO matching procedure. This procedure corrects the first (hardest) parton shower emission with exact next-to-leading order (NLO) matrix elements. Prerequisite for this is a Monte Carlo parton shower program which implements a veto for branchings above a certain momentum (called p_{T}-veto) or which allows a p_{T}-ordered emission of the parton shower below the momentum defined by the NLO matrix element. The higher-order corrections to the first parton shower emission influence the shape of distributions related to the hardest emission as well as the total cross section of the sample. One of the programs implementing this approach is the Powheg generator, which uses an advanced matrix element reweighting procedure for the calculation of the theoretical cross section. More details about this generator will be given in Section 2.3.5.6.

2.3.4 Hadronisation Models

After the parton shower has terminated, the set of partons with virtualities (virtual masses-squared) need to be converted into the observed hadrons. Several models [5] exist which can describe this process. One general approach is the local parton-hadron duality, which states that the flow of momentum and quantum numbers at the hadron level follows the ones at the parton level. The two most common models will be introduced in the following.

2.3.4.1 The string model

Once the produced quark and antiquark move out in opposite directions, they loose energy to the colour field, which collapses into a string-like configuration between them (confinement). A schematic of the production of a multi-hadronic final state in e^+e^- annihilation using the string model is shown in Figure 2.7. The string which connects the outgoing partons

(grey blobs) corresponds to a linear quark confining potential with uniform energy per unit length. It breaks up into hadron-sized pieces by spontaneous production of $q\bar{q}$ pairs in its intense colour field. Gluons which remain after the parton shower produce kinks on the string, which leads to an angular distribution of the hadrons. Whenever a gluon splits into a quark-antiquark pair, a separate string segment is produced. One implementation of this model is the Lund string model used by the Pythia [9] generator.

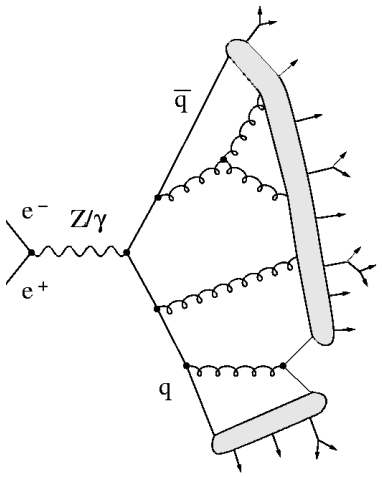

Figure 2.7: Schematic of the string hadronisation process, from Reference [5] and Reference [10].

2.3.4.2 The cluster model

In cluster hadronisation models colour-singlet clusters of partons form after the perturbative phase of the jet development and subsequently decay into the observed hadrons. Figure 2.8 shows a schematic of the cluster hadronisation process, using the same parton shower as in Figure 2.7. The colour-singlet clusters form through non-perturbative splitting of gluons into $q\bar{q}$ pairs, where neighbouring quarks and antiquarks can combine into the singlets. These singlets are then assumed to decay isotropically in their rest frame into a pair of hadrons. The branching ratios for these decays are determined by the density of the state. The cluster model is used by the Herwig generator [11].

2.3.5 Monte Carlo Event Generators

ATLAS supports a large number of Monte Carlo event generators. In the following, the generators for the Monte Carlo datasets used in this thesis will be introduced. Specific datasets are detailed in Appendix A.

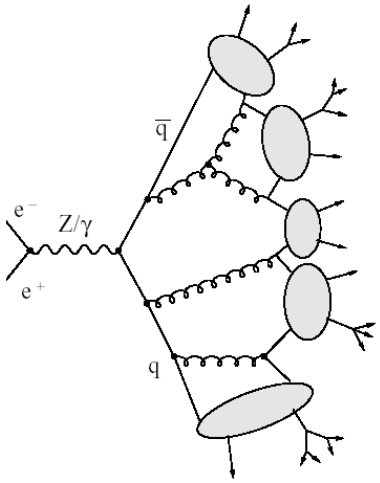

Figure 2.8: Schematic of the cluster hadronisation process, from Reference [5] and Reference [10].

2.3.5.1 Pythia

Pythia [9] is the most commonly used program in ATLAS to generate high-energy physics events. Pythia provides as accurate as possible a representation of event properties in a wide range of reactions. The program is based on a combination of analytic results and various QCD-based models. Tree-level matrix-element calculations are combined with a parton-shower description as an alternative to higher-order matrix elements. The Lund string model is used for the hadronisation process, within which the long-range confinement forces are allowed to distribute the energies and flavours of a parton configuration among a collection of primary hadrons.

2.3.5.2 Herwig

Herwig [11] is a general-purpose Monte Carlo event generator of hard lepton-lepton, lepton-hadron and hadron-hadron scattering and soft hadron-hadron collisions. It uses the cluster parton shower approach as outlined in the section before for the jet hadronisation.

2.3.5.3 Jimmy

The Jimmy [12] generator is a library of routines to generate multiple parton scattering events in hadron-hadron, photon-photon or photon-hadron events and should be linked with the Herwig Monte Carlo generator.

2.3.5.4 Evtgen

The Evtgen program [13] implements physics processes relevant for decays of b-mesons and other resonances. Its most important implementations are models of time-dependent CP asymmetries in neutral b-meson decays, semi-leptonic form-factor models and a full decay table for b-decays. Evtgen has been tuned using the results of the high precision b-physics measurements made at the b-factories.

2.3.5.5 MC@NLO

MC@NLO [14] is a method for matching the next-to-leading order (NLO) calculation of a given QCD process with a parton shower Monte Carlo program. MC@NLO generates the exclusive events, and the subsequent hadronisation is calculated by the parton shower Monte Carlo program. The total exclusive rates are accurate to NLO. Hard emissions are treated as in NLO computations and soft and collinear emissions by the Monte Carlo program. MC@NLO is most commonly combined with the Herwig generator or a combination of the Herwig and the Jimmy generators.

2.3.5.6 Powheg

The Powheg program [15] (Positive Weight Hardest Emission Generator) combines next-to-leading order calculations with a shower Monte Carlo program that is either p_{T}-ordered or allows a p_{T}-veto (see Section 2.3.3). Powheg generates the hardest radiation using the exact NLO calculation, and subsequent softer radiations and the hadronisation are generated by the shower Monte Carlo program, for example Pythia. The resulting distributions of infrared-finite observables are correct to NLO accuracy.

2.4 Bottom-Quarks

2.4.1 Production Mechanisms of b-Quarks

The production cross section of b-quarks has been calculated perturbatively in QCD [16]. The comparison between theory and experiment can test the underlying strong interaction dynamics and is thus of great interest both for experimentalists and theorists. The first terms in the perturbation series which contribute are from quark-antiquark annihilation and gluon-gluon fusion and are of $\mathcal{O}(\alpha_S^2)$:

$$\begin{aligned} q\bar{q} &\rightarrow b\bar{b}, \\ gg &\rightarrow b\bar{b}. \end{aligned} \tag{2.7}$$

The Feynman diagrams contributing to these processes are shown in Figure 2.9.

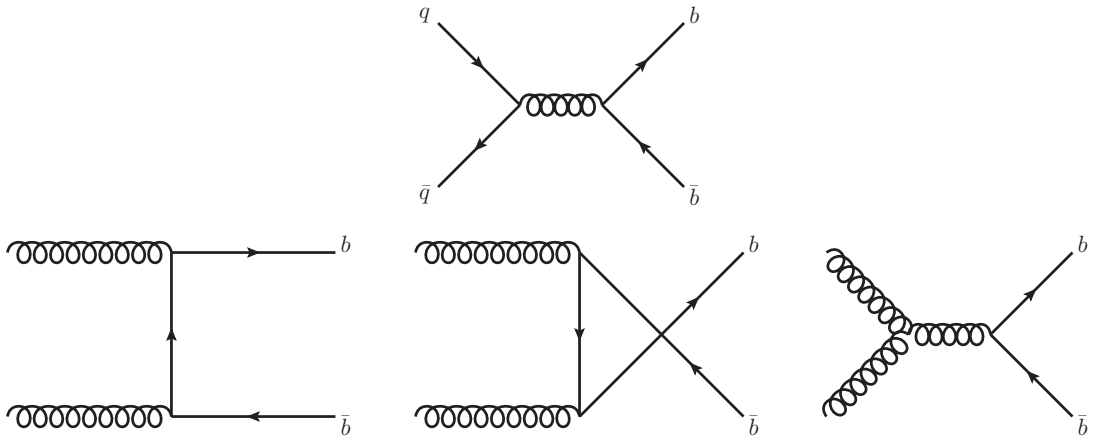

Figure 2.9: Lowest-order Feynman diagrams $\mathcal{O}(\alpha_S^2)$ for the production of b-quarks: quark-antiquark annihilation $q\bar{q} \to b\bar{b}$ (top) and gluon-gluon fusion $gg \to b\bar{b}$ (bottom), from Reference [16].

Corrections to the lowest-order production mechanisms of b-quarks are non negligible and have to be taken into account. The fragmentation process

$$gg \to gb\bar{b} \tag{2.8}$$

as shown in Figure 2.10 (left), although of order α_S^3, has contributions comparable to the lowest order $\mathcal{O}(\alpha_S^2)$ cross section. This is due to the fact that the lowest order cross section for the process $gg \to q\bar{q}$ is about 100 times smaller than the cross section for $gg \to gg$. A gluon jet fragments into a b-quark pair with a probability of $\alpha_S(m_b^2)/2\pi$. Since the cross section for gluon production is large, the gluon fragmentation process into two b-quarks will still be competitive to the mechanisms given in Equation (2.7). The following subprocesses contribute to the inclusive cross section:

$$\begin{aligned}
q\bar{q} &\to b\bar{b}, & \alpha_S^2, \alpha_S^3,\\
gg &\to b\bar{b}, & \alpha_S^2, \alpha_S^3,\\
q\bar{q} &\to b\bar{b}g, & \alpha_S^3,\\
gg &\to b\bar{b}g, & \alpha_S^3,\\
gq &\to b\bar{b}q, & \alpha_S^3,\\
g\bar{q} &\to b\bar{b}\bar{q}, & \alpha_S^3.
\end{aligned} \tag{2.9}$$

For the calculation of the full $\mathcal{O}(\alpha_S^3)$ cross section it is necessary to include both real and virtual gluon emission diagrams. Figure 2.10 shows examples for the b-quark production at

order $\mathcal{O}(\alpha_S^3)$ through gluon splitting (left and middle diagrams) and flavour excitation (right diagram).

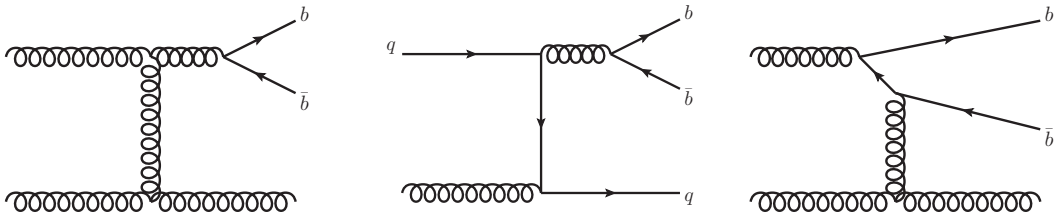

Figure 2.10: Examples of higher-order Feynman diagrams $\mathcal{O}(\alpha_S^3)$ for the production of b-quarks: gluon splitting $gg \to gb\bar{b}$ (left), $gq \to qb\bar{b}$ (middle) and flavour excitation $gg \to gb\bar{b}$ (right).

An alternative to the calculation of the production cross section of b-quarks at next-to-leading order is the calculation of the production rate of particle jets originating from b-quarks [17] at the same order in the perturbative expansion. This second approach calculates the properties of a jet originating from one or more b-quarks, regardless of the fraction of jet momentum that the b-quark carries. Collinear logarithms which appear in the calculation of the b-quark transverse momentum p_{T} distribution are not present in the calculation of the p_{T} distribution of b-quark jets, since the the p_{T} of the jet does not depend on gluons which have been emitted collinearly by the b-quark. A second advantage is that the experimental measurement of the jet-p_{T} distribution is less sensitive to the knowledge of the b-quark fragmentation function than the measurement of the b-quark p_{T} distribution. Experimental systematic errors are therefore greatly reduced.

2.4.2 Fragmentation of b-Quarks

The energy transfer of the b-quark momentum onto the b-hadron during the hadronisation process is parameterised by a fragmentation function [4], which gives the probability that the b-quark fragments into the b-hadron carrying a fraction x_b of the b-quark's momentum. The shape of this function is extracted from global fits to the data. b-hadrons retain a large fraction of the momentum of the b-quark, and their fragmentation function is therefore much harder than that for a light hadron. Experimental results of the b-fragmentation function [4] from e^+e^- collisions at $\sqrt{s} = 91$ GeV are presented in Figure 2.11.

2.4.3 Decay Modes and Properties of b-Hadrons

The bottom-quark belongs to the third generation of quarks, together with the top quark. Its existence was proposed in 1973 by Kobayashi and Maskawa [4], and measured for the first time in 1977. The bound states of bottom-antiquarks with a second u, d, s or c quark are referred to as the $B_u(B^+)$, $B_d(B^0)$, B_s^0 and B_c^+ mesons. Possible bound $b\bar{b}$ states are

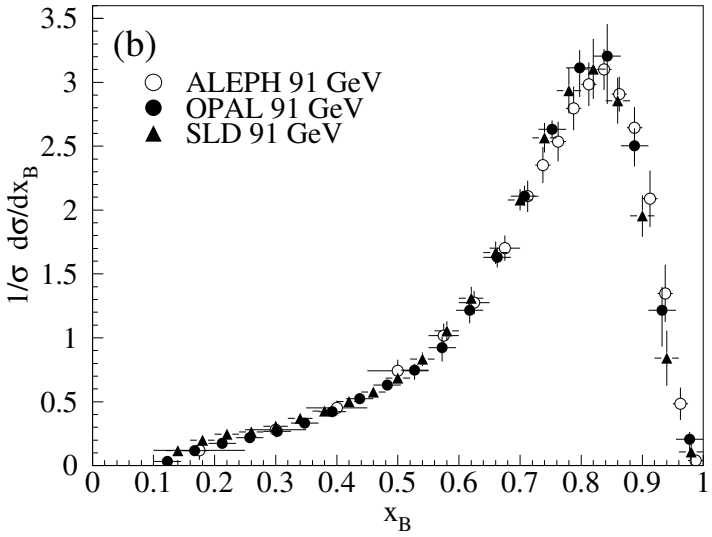

Figure 2.11: Measured e^+e^- fragmentation function of b-quarks into b-hadrons at $\sqrt{s} = 91$ GeV, from Reference [4].

the Υ series and the χ_b. Baryons containing a bottom-quark are labelled in the same way as non-b-baryons, but with a b-subscript. Examples are $\Lambda_b^0 = udb$, $\Xi_b = dsb$, $\Sigma_b^+ = uub$ and $\Sigma_b^- = ddb$.

The decay of b-hadrons occurs via weak generation-changing processes, which are well described by the decay of the b-quarks in the spectator model. The dominant decay mode is $b \to cW^{*-}$, where the W^{*-} itself decays either into a pair of leptons $l\bar{\nu}_l$ ("semi-leptonic decay mode"), or into a pair of quarks which then hadronises ("hadronic decay mode"). The semi-leptonic decay mode with a muon in the final state will be of special importance for this thesis. The branching fractions for the three dominant semi-leptonic decay modes into a muon $\bar{b} \to \mu^+\nu_\mu X$, $\bar{b} \to \bar{c} \to \mu^-\bar{\nu}_\mu X$ and $\bar{b} \to c \to \mu^+\nu_\mu X$ are listed in Table 2.3. Their Feynman-diagrams are presented in Figure 2.12. The direct decay mode $\bar{b} \to \mu^+\nu_\mu X$ will be referred to as $\bar{b} \to \mu^+ X$ in this thesis, the cascade decays $\bar{b} \to \bar{c} \to \mu^-\bar{\nu}_\mu X$ and $\bar{b} \to c \to \mu^+\nu_\mu X$ as $\bar{b} \to \bar{c}/c \to \mu^{-/+} X$ and all semi-leptonic modes with a muon in the final state as $\bar{b} \to \mu X$.

$BR(\bar{b} \to \mu^+\nu_\mu X)$	$(11.0\ ^{+0.3}_{-0.3})\%$
$BR(\bar{b} \to \bar{c} \to \mu^-\bar{\nu}_\mu X)$	$(8.0\ \pm 0.2)\%$
$BR(\bar{b} \to c \to \mu^+\nu_\mu X)$	$(1.6\ ^{+0.4}_{-0.5})\%$
$BR(\bar{b} \to \mu X)$	$(20.6\ ^{+0.5}_{-0.6})\%$

Table 2.3: Branching ratios for semi-leptonic b-quark decays, from Reference [4].

The lifetime of the different b-hadrons are of the same order of magnitude, and only small differences exist between the particles: $\tau(B^+) \geq \tau(B^0) \approx \tau(B_s^0) > \tau(\Lambda_b^0) \gg \tau(B_c^0)$. The averaged lifetime of a b-baryon mixture is (1.345 ± 0.032) ps, and of a b-hadron mix-

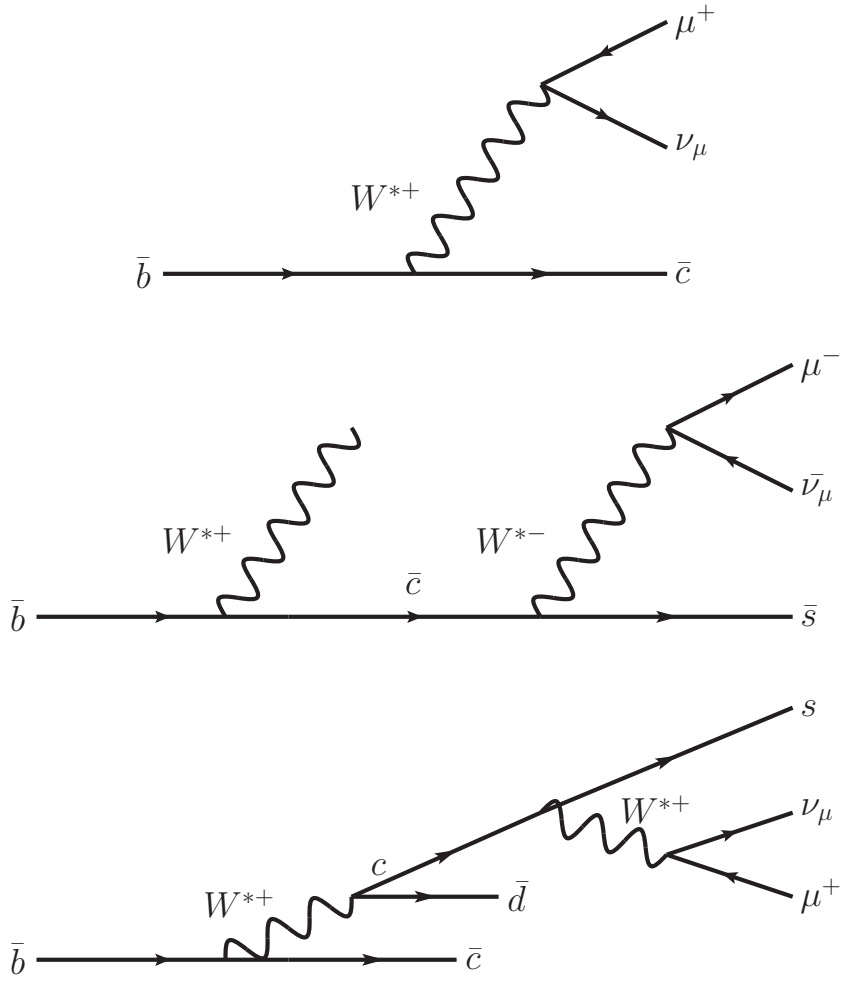

Figure 2.12: Feynman diagrams of dominant semi-leptonic b-decays: $\bar{b} \to \mu^+ \nu_\mu X$ (top), $\bar{b} \to \bar{c} \to \mu^- \bar{\nu}_\mu X$ (middle) and $\bar{b} \to c \to \mu^+ \nu_\mu X$ (bottom).

ture (1.568 ± 0.009) ps [4]. This implies typical decay lengths of the order of a millimetre. The displaced vertices from the b-hadron decays are the base of many algorithms for the identification of particle jets which originate from b-quarks.

2.4.4 Bottom Production Measurements in Hadronic Collisions

The history of bottom production measurements in hadronic collisions, especially in $p\bar{p}$ collisions at the Tevatron collider, was marked by large discrepancies between the data and the theoretical predictions. The first bottom production measurements in hadronic collisions [18] were carried out by the UA1 experiment at the S$\bar{p}p$S collider at a centre-of-mass energy of 630 GeV. The data showed good agreement with NLO QCD calculations. The first results from the Tevatron collider using $p\bar{p}$ collisions at a centre-of-mass energy of 1.8 TeV were reported by the CDF experiment in 1992, see Figure 2.13 [19]. These results showed large discrepancies between the data and the QCD NLO predictions. Increased statistics and

the use of vertexing detectors allowed the CDF experiment to improve their measurement of fully reconstructed exclusive decays of $B^0 \to \psi K^*$ and $B^\pm \to \psi K^\pm$ in 1995. The measured production cross section was still significantly higher than the theoretical prediction.

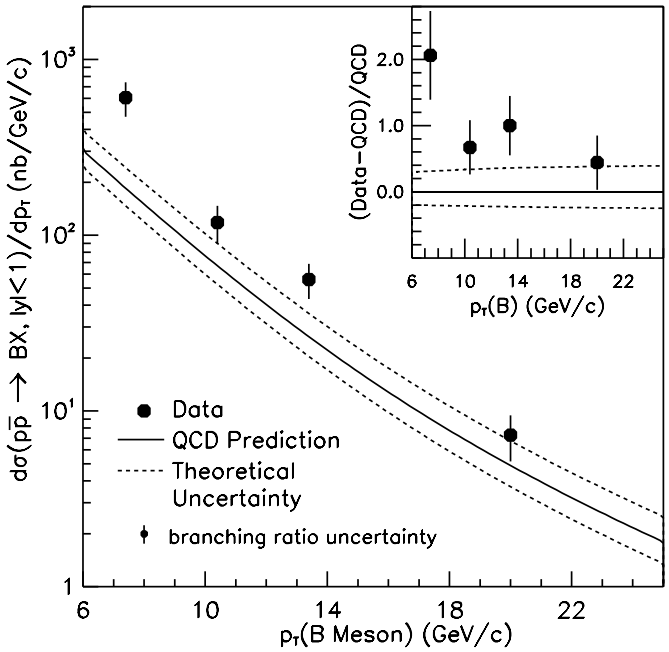

Figure 2.13: First measurement of the b-hadron production cross section at $\sqrt{s} = 1.8$ TeV by the CDF experiment in 1995, from Reference [19].

The Tevatron experiment DØ reported the first b cross section measurements in 1994 and 1996, which were in good agreement with QCD predictions. In 2000, a new analysis was presented that was in very good agreement with the CDF results but showed a significantly

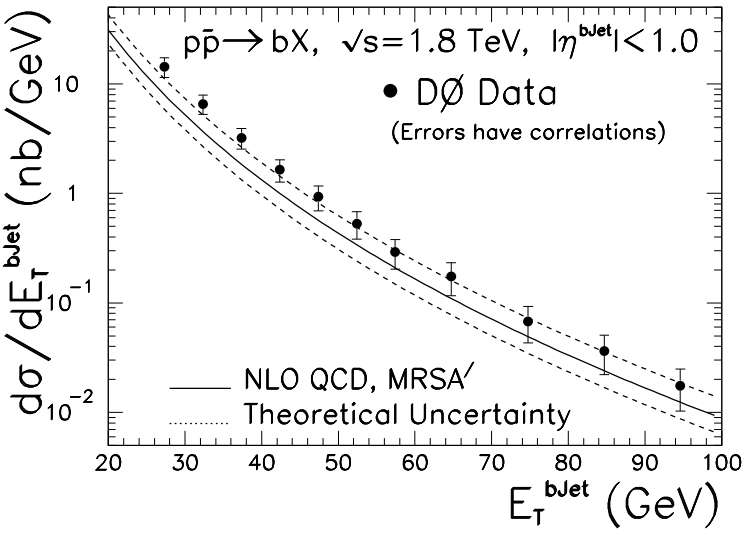

Figure 2.14: b-jet production cross section measured at $\sqrt{s} = 1.8$ TeV by the DØ experiment, from Reference [20].

higher cross section than predicted from QCD NLO calculations. All measurements to this point depended greatly on the non-perturbative part of the QCD calculation, in particular the fragmentation function. Therefore a measurement of the rate of b-quark jets was carried out by the DØ experiment, which is presented in Figure 2.14 [20]. Measuring the b-jet cross section has the advantage that the theoretical calculation is only marginally affected by the details of the b-quark to b-hadron fragmentation. In addition, this measurement is not affected by higher-order large-p_{T} logarithms. The measured b-quark jet cross section by DØ showed a much improved agreement between the data and the theory.

A new technique on the theoretical side which resummed the large logarithms with next-to-leading logarithmic accuracy (NLL) and matched them to the fixed-order NLO calculation (called Fixed-Order with Next-to-Leading-Log resummation: FONLL) made it possible to extract the non-perturbative fragmentation function from LEP and SLC data with much improved accuracy. Figure 2.15 shows the comparison of the b-hadron spectrum measured by the CDF experiment in 2007 with the predictions by the FONLL method [21]. A much better agreement can be observed between the data and the theory. The "saga" of large discrepancies between the measurements and the theoretical predictions of bottom production in $p\bar{p}$ collisions was finally solved [18].

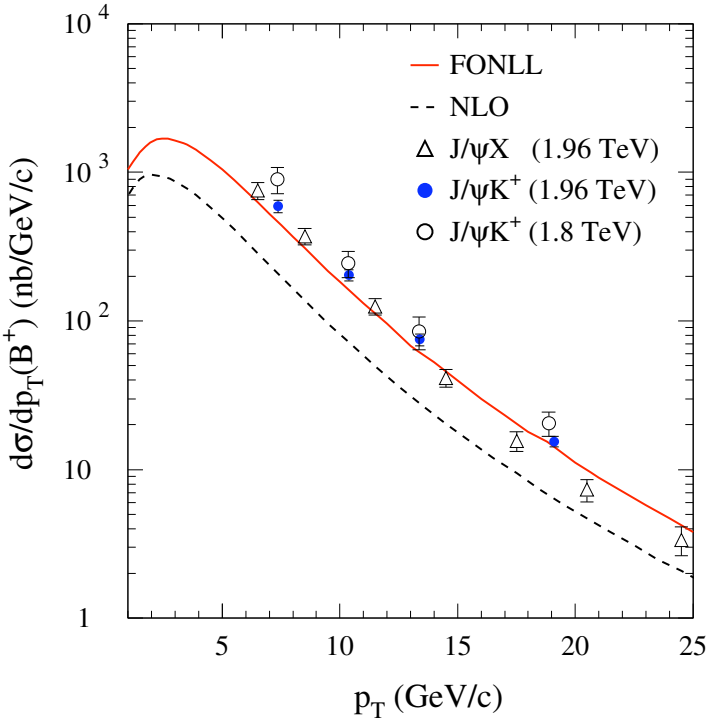

Figure 2.15: b-hadron production cross section measured at $\sqrt{s} = 1.8$ and 1.96 TeV by the CDF experiment in 2007, compared to predictions by the FONLL method. From Reference [21].

The first measurements of b-hadron production at the LHC at $\sqrt{s} = 7$ TeV have been reported by the LHCb collaboration for the forward rapidity region [22, 23] and by the CMS collaboration in the central region [24, 25]. The measurement of the b-hadron cross section by

the CMS experiment [24] is presented in Figure 2.16. A good agreement between the data and the NLO QCD calculations can be observed.

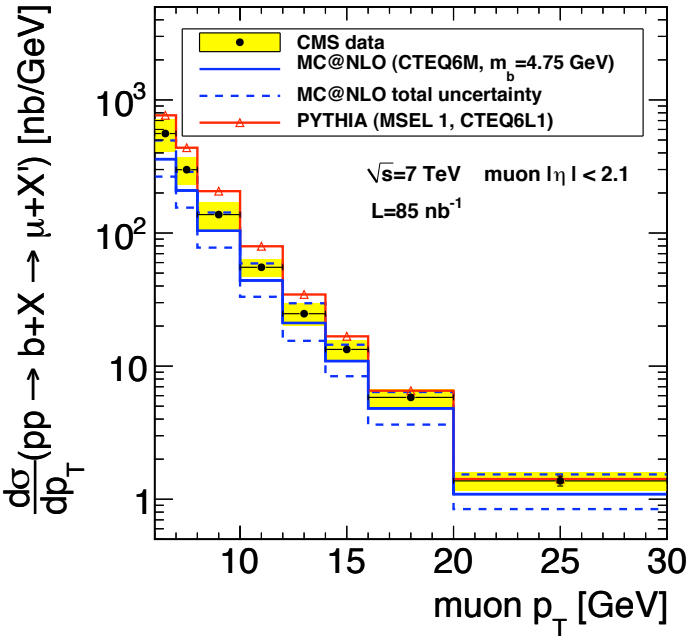

Figure 2.16: Measurement of the b-hadron cross section at $\sqrt{s} = 7$ TeV by the CMS experiment, from Reference [24].

Both the ATLAS [26] and the CMS [27] experiment have carried out preliminary measurements of the b-jet production cross section at $\sqrt{s} = 7$ TeV. The ATLAS measurement [26] is shown in Figure 2.17, which agrees well with the NLO QCD predictions.

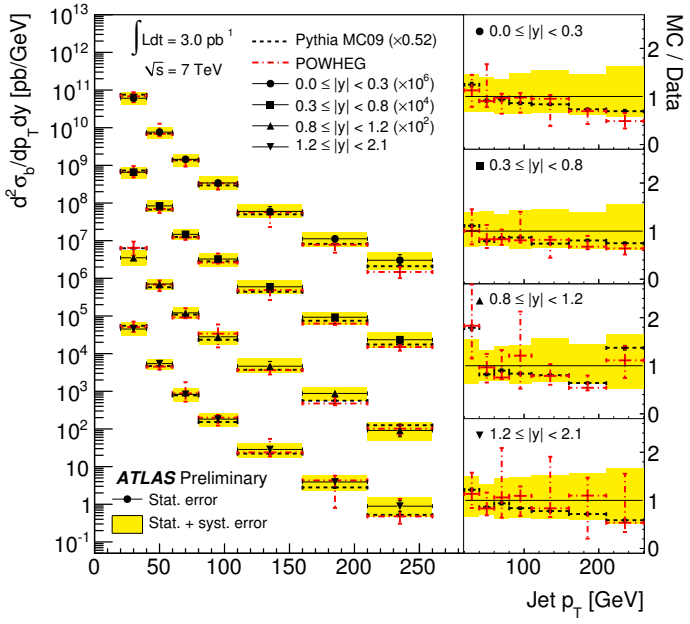

Figure 2.17: Preliminary measurement of the b-jet cross section at $\sqrt{s} = 7$ TeV by the ATLAS experiment, from Reference [26].

Chapter 3

The ATLAS Experiment

This chapter introduces the Large Hadron Collider (LHC) and one of its main experiments, ATLAS. The LHC collides two proton beams at the world's highest centre-of-mass energy. ATLAS is a general-purpose experiment, designed to study both known and yet unknown phenomena at the TeV scale. The ATLAS detector subsystems and the offline data processing are discussed in the second section of this chapter.

3.1 The Large Hadron Collider

3.1.1 Accelerator and Experiments

The Large Hadron Collider (LHC) [28] at CERN near Geneva is designed to collide proton beams with a centre-of-mass energy of 14 TeV and a luminosity of 10^{34} cm^{-2}s^{-1}. The LHC is a two-ring superconducting hadron accelerator and collider installed in a 26.7 km tunnel between 45 m and 170 m below the surface. It consists of two rings with counter-rotating beams. The tunnel accommodating the LHC was originally designed and used by the electron-positron machine LEP and allowed for eight crossing points of the beams. It was decided to equip only four of the eight possible interaction points with particle experiments. The four experiments are ALICE, ATLAS, CMS and LHCb. A cartoon showing the layout of the LHC underground areas [29] is presented in Figure 3.1.

ALICE [30], A Large Ion Collider Experiment, is a dedicated heavy-ion experiment which focuses on the physics of strongly interacting matter and the quark-gluon plasma at extreme values of energy density and temperature in nucleus-nucleus collisions.

The two general-purpose detectors ATLAS [31], A Toroidal LHC ApparatuS, and CMS [32], Compact Muon Solenoid, are designed to study proton-proton (and lead-lead) collisions at a centre-of-mass energy of 14 TeV (5.5 TeV per nucleon pair). The experiments are designed for high precision tests of QCD, electro-weak interactions and flavour physics and

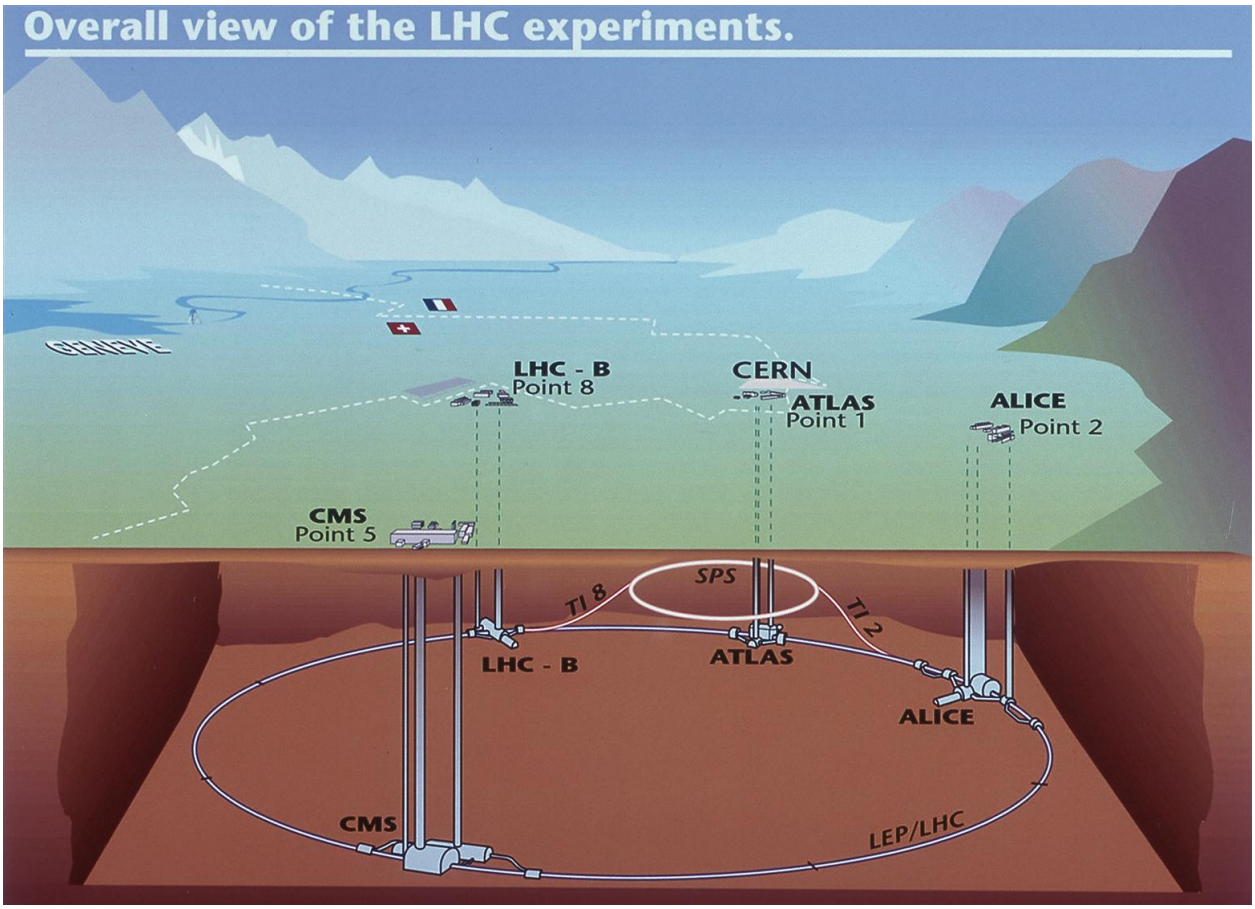

Figure 3.1: A cartoon showing the layout of the LHC underground areas, from Reference [29].

for the discovery of predicted or new phenomena like the Standard Model Higgs boson, Super Symmetry or Extra Dimensions.

The fourth experiment, LHCb [33], the Large Hadron Collider beauty experiment, is dedicated to precision measurements of CP violation and rare decays of b-hadrons as well as the search for indirect evidence of new physics in these processes.

ATLAS and CMS are high-luminosity experiments, both aiming at a peak luminosity of 10^{34} cm^{-2}s^{-1}, whereas LHCb aims at lower peak luminosities of 10^{32} cm^{-2}s^{-1}. ALICE is designed for a peak luminosity of 10^{27} cm^{-2}s^{-1} for nominal lead-ion operation. To reach a luminosity of 10^{34} cm^{-2}s^{-1}, a very high beam intensity is required together with a large number of bunches (2 808 for each proton beam) and a small bunch spacing (25 ns). The bunches are collided with a small crossing angle to reduce the number of additional or displaced proton-proton interactions.

3.1.2 LHC Commissioning towards First Collisions

The commissioning of the LHC towards first proton-proton collisions in November 2009 was done step-wise. One of the most important milestones was the successful injection of beams

into the LHC in August and September 2008 [34, 35], leading to the first circulating beams on September 10$^{\text{th}}$, 2008. On September 19$^{\text{th}}$, 2008, an electrical fault occurred, producing an electrical arc and resulting in mechanical and electrical damage, release of helium from the magnet cold mass and contamination of the insulation and beam vacuum enclosures [36]. This presented a major fall-back for the LHC commissioning and resulted in several months of repairs and improvements of the machine and its monitoring system.

The LHC was fully operational again by summer 2009, and the next injection tests were carried out in October and November [34]. First circulating beams were established on November 19$^{\text{th}}$, and only four days later, on November 23$^{\text{rd}}$, first collisions at the injection energy of 450 GeV per beam took place. The next milestone in the LHC commissioning was the declaration of stable beams to the experiments on December 6$^{\text{th}}$, which allowed the experiments to switch on their silicon tracking detectors close to the beam pipe. Before then, these detectors were kept at lower voltage due to safety reasons. The next phase of the LHC commissioning concentrated on acceleration aspects in order to increase the beam energy to 3.5 TeV per beam. First collisions at this energy were recorded on March 30$^{\text{th}}$, 2010. Due to safety concerns, it was decided to operate the LHC at this energy in the years 2010 and 2011. Only in later years after a longer shut-down involving substantial work on the LHC hardware and monitoring systems will the design beam energy of 7 TeV per beam be reached.

3.2 The ATLAS Detector

The ATLAS detector [31] has been installed in an underground cavern at CERN. Fifteen years of design, development and construction preceded the installation of the detector, which was finalised in 2008. A schematic of the ATLAS detector [29] is presented in Figure 3.2. The ATLAS detector is forward-backward symmetric along the beam direction with respect to the interaction point. The detector components and their expected performance are described in this section.

3.2.1 Required Performance

A set of processes covering many of the new phenomena which one can hope to observe at the TeV scale were used as benchmarks to define the required performance of the ATLAS detector. High precision tests of QCD, electro-weak interactions and flavour physics will be possible due to the higher luminosity and the increased cross sections at the LHC. The search for the Higgs boson as predicted by the Standard Model was used to establish the performance of important sub-systems of ATLAS. Due to the small cross sections for many of these processes, the extremely high LHC luminosity and resulting interaction rate are needed. This presents a serious experimental difficulty because it means that every candidate event

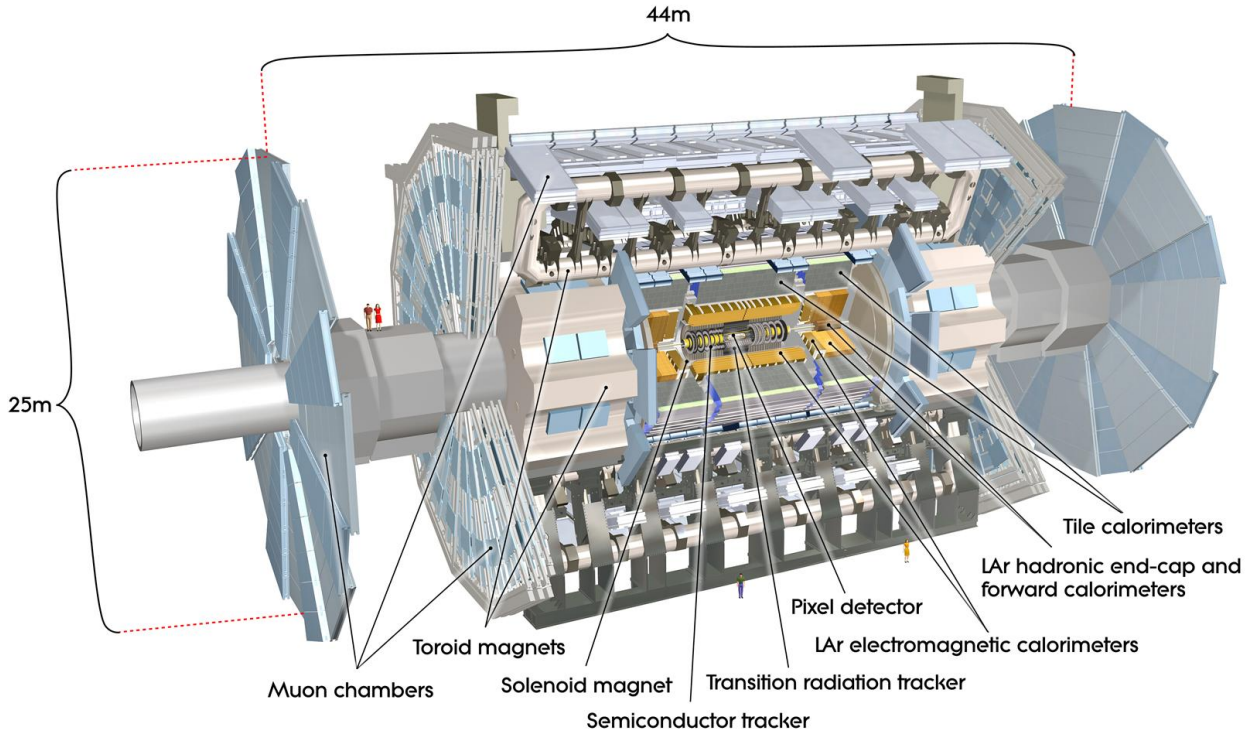

Figure 3.2: A schematic of the ATLAS Detector, from Reference [29].

for new physics will be accompanied by ~ 23 inelastic proton-proton collisions on average per bunch crossing. The following performance requirements for the ATLAS detector [31] have been identified:

- Fast, radiation hard electronics and sensor elements. Additionally, high detector granularity is needed to handle the particle fluxes.
- Large acceptance in pseudorapidity with almost full azimuthal angle coverage.
- Fast and reliable triggers for electrons, muons, jets and τ leptons, photons and missing transverse energy.
- Very good electromagnetic calorimetry for electron and photon identification and reconstruction, complemented by full-coverage hadronic calorimetry for accurate jet and missing transverse energy measurements.
- Good muon identification and momentum resolution over a wide range of momenta and the ability to determine unambiguously the charge of high p_{T} muons.
- Adequate momentum resolution and good reconstruction efficiency in the inner tracker for charged particles. Vertex detectors close to the interaction region are required for the reconstruction of secondary vertices for the identification of b-jets and τ-leptons.

- Highly efficient triggers for low transverse-momentum objects with sufficient background rejection.

Coordinate system definition

The origin of the coordinate system used in ATLAS is defined by the nominal interaction point. The direction of the beam defines the z-axis and transverse to it lies the $x-y$ plane, also referred to as transverse plane. The positive x-axis points from the interaction point towards the centre of the of the LHC ring and the positive y-axis points upwards. The azimuthal angle ϕ is measured around the beam axis, and the polar angle θ is the angle from the beam axis. The pseudorapidity is defined as

$$\eta = -\ln\tan(\frac{\theta}{2}). \tag{3.1}$$

In case of massive objects such as jets, the rapidity

$$y = 1/2\ln[(E+p_z)/(E-p_z)] \tag{3.2}$$

is used instead, where E denotes the energy and p_z is the component of the momentum along the beam direction. Many calculations use quantities defined in the transverse plane, since the vector sum of all quantities in this plane must be zero. The transverse momentum p_{T}, transverse energy E_{T} and missing transverse energy $\not{E}_{\mathrm{T}}$ are defined in this plane. The distance ΔR in pseudorapidity-azimuthal space is defined as

$$\Delta R = \sqrt{\Delta\phi^2 + \Delta\eta^2}. \tag{3.3}$$

3.2.2 The Inner Detectors

The inner detectors are contained in a 2 T solenoidal field. They consist of a combination of high-resolution semiconductor pixel and strip detectors in the inner part of the tracking volume and straw-tube tracking detectors with the capability to generate and detect transition radiation in the outer part. The layout of the ATLAS inner detector system [29] is shown in Figure 3.3.

The pixel and semi-conductor (SCT) detectors cover the region $|\eta| < 2.5$. Their basic functionality is discussed in Section 3.2.2.1. In the barrel region, the detector modules are located on concentric cylinders around the beam axis, while in the two endcap regions they are located on disks perpendicular to the beam direction. The innermost pixel layer closest to the interaction point is also referred to as the b-layer or layer-0. The pixel layers are segmented uniformly in $R-\phi$ and z. Three pixel layers are crossed by a track in the barrel region. All pixel sensors are identical and have a minimum pixel size in $R-\phi\times z$ of 50×400 $\mu\mathrm{m}^2$. The

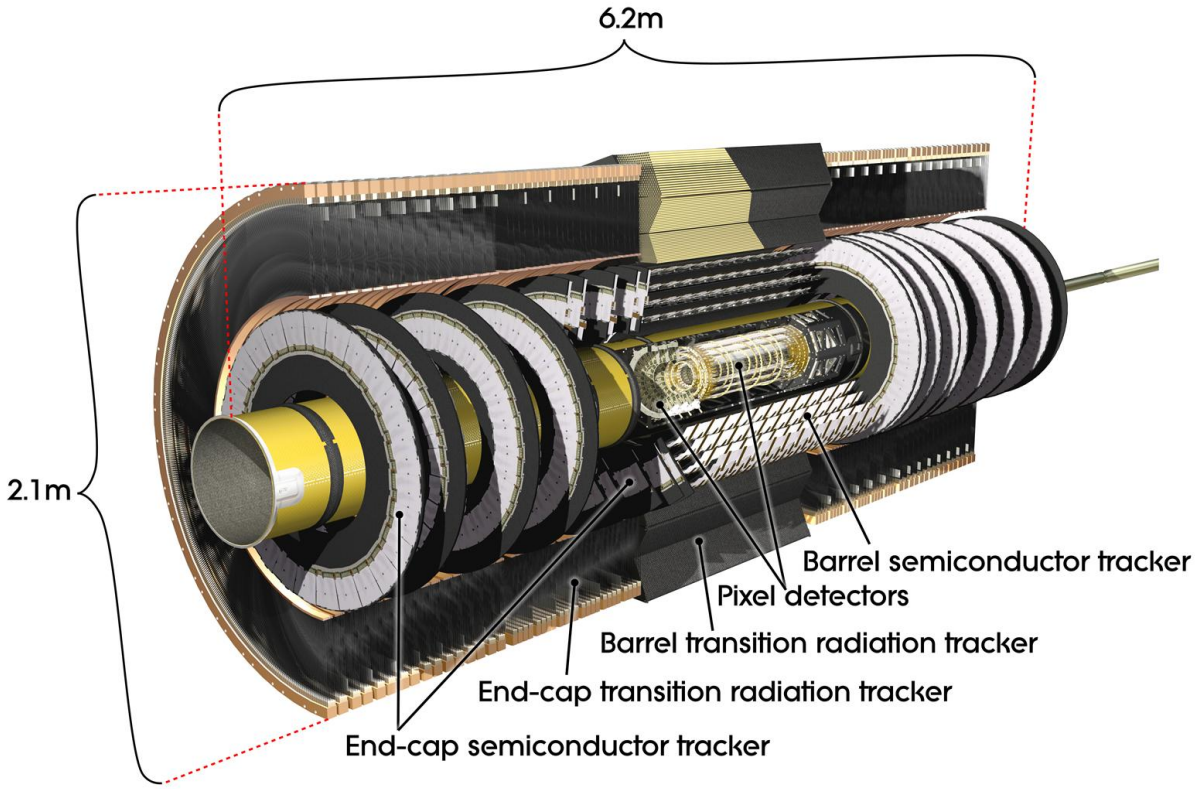

Figure 3.3: A schematic of the ATLAS inner tracking system, from Reference [29].

modules have an intrinsic accuracy of 10 μm in $R-\phi$ and 115 μm in z (R in case of the endcaps). The pixel detector consists of approximately 80.4 million readout channels.

The semi-conductor tracker uses small-angle (40 mrad) stereo-strips to measure both coordinates. One set of strips in each layer is parallel to the the beam axis and measures $R-\phi$. Each track crosses on average eight strip layers or four space points in the SCT barrel region. The stereo-strips consist of two 6.4 cm long daisy-chained sensors with a strip pitch of 80 μm. In the endcap regions, the SCT consists of a set of strips running radially and a set of stereo-strips at an angle of 40 mrad. The mean pitch of these strips is approximately 80 μm as well. The intrinsic accuracy of a pair of double-sided modules is 17 μm in $R-\phi$ and 580 μm in z (R in case of the endcaps). The total number of readout channels in the SCT is approximately 6.3 million.

The transition-radiation tracker (TRT) provides a large number of hits (typically 36 per track) within $|\eta| < 2.0$. Its basic functionality is discussed in Section 3.2.2.2. The TRT consists of 4 mm diameter straw tubes and provides $R-\phi$ information only with an accuracy of 130 μm per straw. The straws are parallel to the beam direction in the barrel region and arranged radially in wheels in the endcaps. The TRT consists of approximately 351 000 readout channels.

The combination of precision semi-conductor trackers at small radii with the TRT at larger radius results in robust pattern recognition and high precision in both $R-\phi$ and z coordinates. The large number of straw hits at outer radii improve significantly the momentum measurement. The lower precision per point in the TRT compared to the silicon detectors is compensated by the large number of measurements and the longer lever arm. The semi-conductor detectors allow impact parameter measurements and vertexing for heavy-flavour tagging. For this, the high granularity of the pixel detector and the radial position of its innermost layer at about 5 cm are crucial.

3.2.2.1 Functionality of semiconductor detectors

Semiconductor detectors like the pixel or the SCT detector are based on the operating principle of a semiconductor diode [37]. Their mode of operation can be understood using the band model of solids. The discrete energy levels of individual electrons in the atomic crystal structure of a semiconductor merge to form continuous energy bands. The highest fully filled band is referred to as the valence band, and the lowest partially filled or empty band as the conductor band. The energy difference between the two bands is called the energy gap, which is in the range of 1 eV for semiconductors. Semiconductors are materials whose conduction band is basically empty, like materials from group IV of the period table. Electrons which have been excited from the valence band to the conduction band carry the electric charge in these materials and can move in an electric field; they leave behind a positive charge in the valence band, so-called "holes". The electronic properties of intrinsic semiconductors can be altered by incorporating impurities into the crystal lattice ("doping"). The introduction of an atom from group V leaves one of the electrons in the lattice only weakly bound. That electron populates a state near the bottom of the conduction band. Materials doped in this way are referred to as n-type, since they have a high concentration of free electrons. The introduction of an atom from group III on the other hand will leave one silicon bond incomplete, which will attract an electron from a neighbouring silicon atom and thus create a hole. Materials with this property have a high concentration of free holes and are referred to as p-type.

At the interface of two semiconductors with p- and n-type, the pn-junction, electrons will diffuse from the n-type to the p-type and create an area with a low concentration of free carriers (depletion zone). The depletion zone can be increased by applying an external positive voltage to the n-region, called bias voltage. This is the basis for semiconductor particle detectors. Charged particles or photons crossing the depletion zone create electron-hole pairs, which are separated by the electric field. Their charge is collected on the electrodes, inducing a current pulse. This current pulse is compared to a predefined threshold to form the digital detector signal, which is propagated to the detector readout.

3.2.2.2 Functionality of the TRT

The TRT detector consists of cylindrical drift tubes (straws) which at the same time serve for charged-particle tracking and electron/pion separation [37]. The drift tubes are filled with a gas mixture which has good counting characteristics and high X-ray absorption. The straw tube walls serve as cathode, and a wire in the centre of the straw as an anode. The layers of straws are interleaved with polypropylene foils or fibres working as a radiator. Particles traversing the straw ionise the gas mixture and induce a signal on the wire. The straws which show an energy deposition above a certain threshold are propagated to the detector readout. A drift-time measurement is used to determine the coordinate of the trajectory with a spacial resolution of 130 μm. The TRT exploits in addition the fact that electrons deposit more energy in the gas mixture than pions. The number of straws along the particle trajectory which have an energy deposition above a second, higher threshold is used to separate electrons from pions.

3.2.3 The Calorimeters

The calorimeters in ATLAS cover a range $|\eta| \leq 4.9$ and use different technologies to meet the requirements for measuring the physics processes of interest. Figure 3.4 shows a schematic of the ATLAS calorimeter system [29].

Liquid-argon (LAr) electromagnetic sampling calorimeters with high granularity and excellent performance in terms of energy and position resolution cover the range $|\eta| < 3.2$. In the region devoted to precision physics ($|\eta| < 2.5$), the EM calorimeter is segmented in three sections in depth, with a typical fractional energy resolution of $\frac{\sigma(E)}{E} = \frac{10\%}{\sqrt{E/\mathrm{GeV}}} \oplus 0.2\%$. The fine granularity is suited for precision measurements of electrons and photons.

The hadronic calorimeters in the barrel with $|\eta| < 1.7$ use a scintillating-tile technology and are separated into a large barrel and two smaller extended barrel cylinders. They are segmented in three layers in depth and have a typical energy resolution for pions of $\frac{\sigma(E)}{E} = \frac{56\%}{\sqrt{E/\mathrm{GeV}}} \oplus 5\%$. In the endcaps ($|\eta| > 1.5$) and the forward region ($|\eta| \leq 4.9$) LAr technology is also used for the hadronic calorimeters, with a segmentation in four layers per endcap and a fractional energy resolution for pions of $\frac{\sigma(E)}{E} = \frac{83\%}{\sqrt{E/\mathrm{GeV}}}$. The hadronic calorimeters with their coarser granularity satisfy the physics requirements for jet reconstruction and $\not{E}_{\mathrm{T}}$ measurements.

Calorimeters must provide good containment for electromagnetic and hadronic showers as well as limit particles other than muons to reach the muon system ("punch-through"). Therefore, the calorimeter depth is an important design consideration. The electromagnetic calorimeter has a thickness of more than 22 radiation lengths X_0 in the barrel and more than 24 X_0 in the endcaps. The total thickness of the electromagnetic and hadronic calorimeters together is 9.7 interaction lengths λ in the barrel and 10 λ in the endcaps. This is adequate

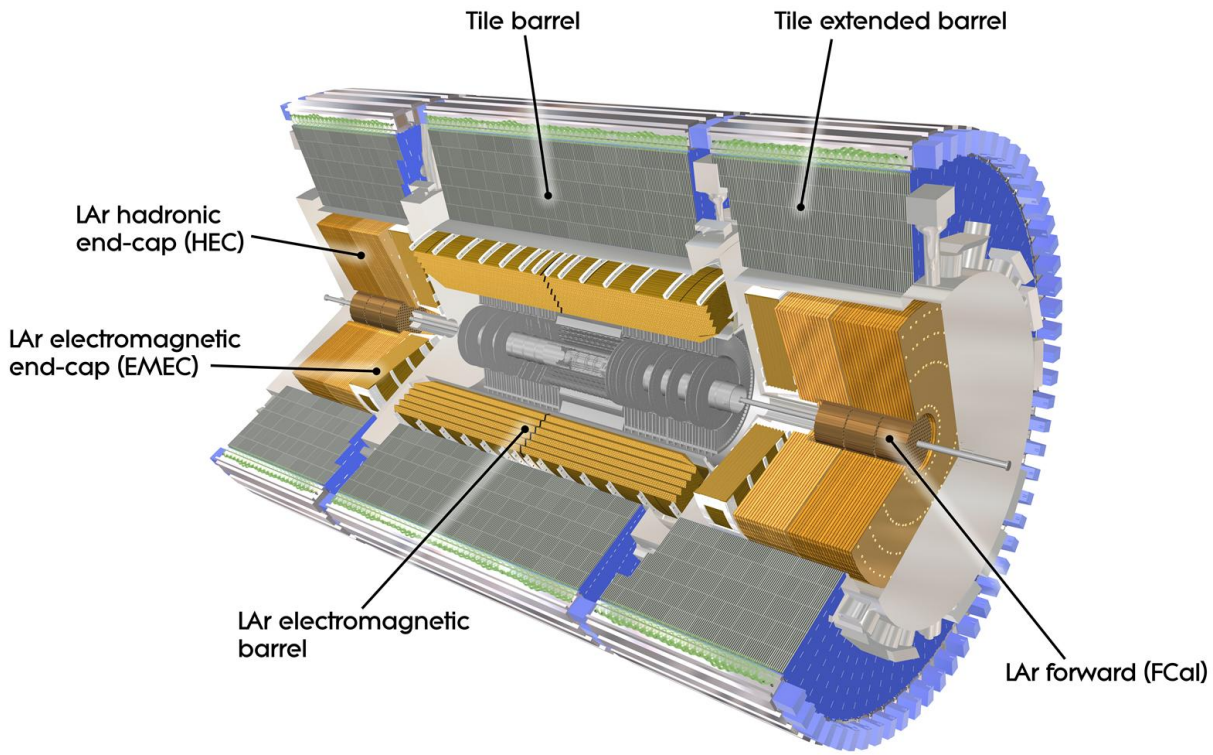

Figure 3.4: A schematic of the ATLAS calorimeter system, from Reference [29].

to provide good resolution for high-energy jets and sufficient to reduce punch-through well below the irreducible level of prompt or decay muons.

3.2.4 The Muon System

The muon system encloses the calorimeters and consists of an air-core toroid system, fast trigger chambers and high precision tracking chambers. Its layout [29] is presented in Figure 3.5. Tracks are measured in three cylindrical layers around the beam pipe in the barrel region and in three planes perpendicular to the beam direction in the endcaps. The dimensions of the muon spectrometer define the overall size of the ATLAS detector. The muon system is designed to reconstruct the transverse momenta of 1 TeV tracks with a resolution of 10%, which translates into a sagitta measurement with a resolution of less than 50 μm.

The toroid system generates strong bending power in a large volume within a light and open structure. The excellent momentum resolution is obtained with three layers of high precision tracking chambers. These measurements are provided in the bending plane by Monitored Drift Tubes (MDT's) over most of the η-range. At large pseudorapidities, Cathode Strip Chambers (CSC's) with higher granularity are used in the innermost plane. The MDT's

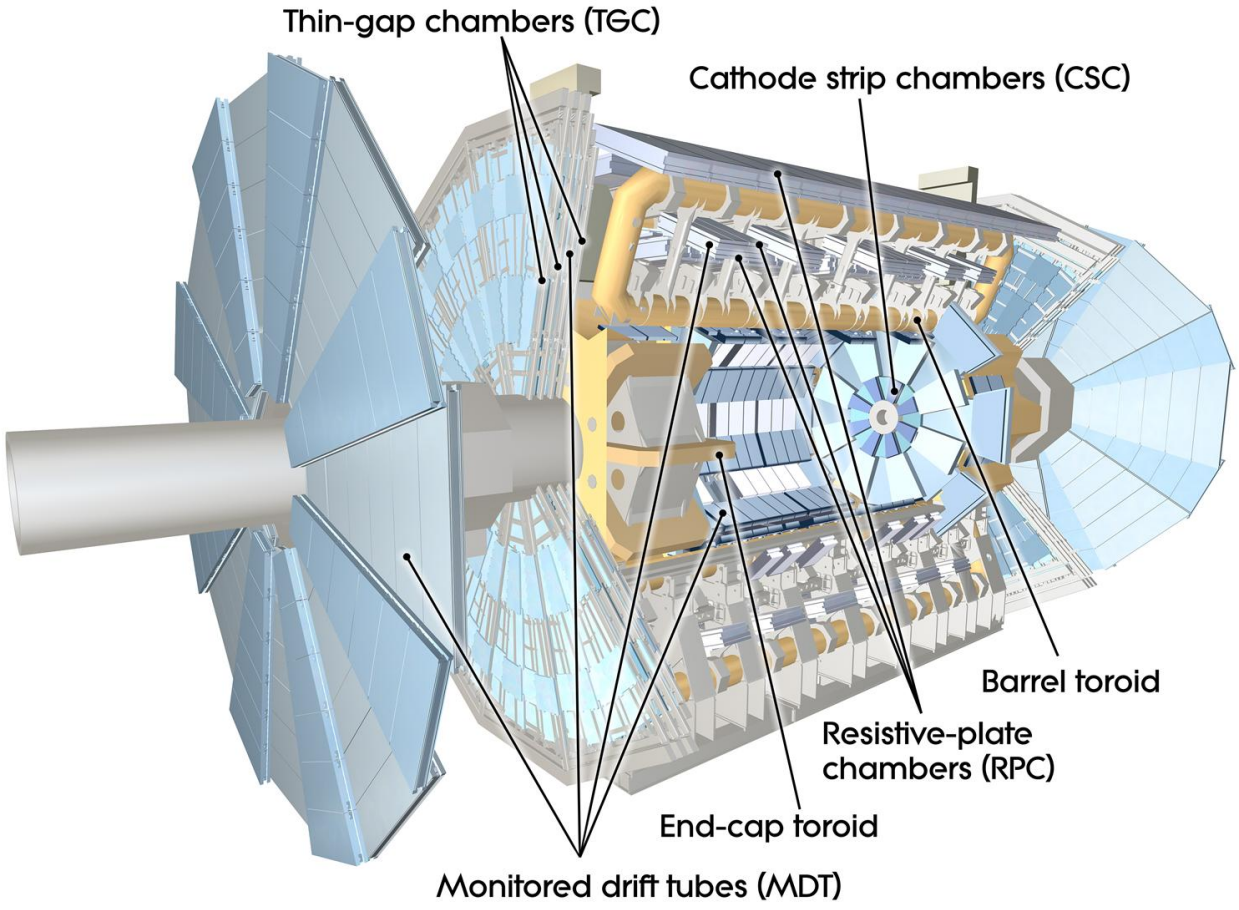

Figure 3.5: A schematic of the ATLAS muon system, from Reference [29].

show a chamber resolution of 35 μm in z, and the CSC's of 10 μm in R and 5 mm in ϕ. The combination of precision mechanical-assembly techniques and optical alignment systems ensures that the stringent alignment requirements of the muon chamber layers are met.

Resistive Plate Chambers (RPC's) in the barrel and Thin Gap Chambers (TGC's) in the endcaps constitute the muon trigger system with high timing resolution of the order of $1.5 - 4$ ns. They serve a threefold purpose: provide bunch-crossing identification, provide well-defined p_{T} thresholds and measure the muon coordinate in the direction orthogonal to the precision-tracking chambers. The RPC's have a chamber resolution of 10 mm in both z and ϕ directions, and the TGC's of $2 - 6$ mm in R and $3 - 7$ mm in ϕ.

3.2.5 Trigger and Data Acquisition

The interaction rate at the LHC at design luminosity will be approximately 1 GHz. The data recording on the other hand is limited to about $200 - 500$ Hz due to technology and computing resource limitations. A dedicated trigger system in three stages ensures a rejection factor of $5 \cdot 10^6$ against inelastic processes while maintaining maximum efficiency for interesting

physics processes. Figure 3.6 gives an overview of of the ATLAS trigger system [38]. The numbers stated in Figure 3.6 date from the time of the trigger technical design report in 1998; the Level 2 trigger is operated now up to a rate of 2 kHz, and the Event Filter up to 200 Hz.

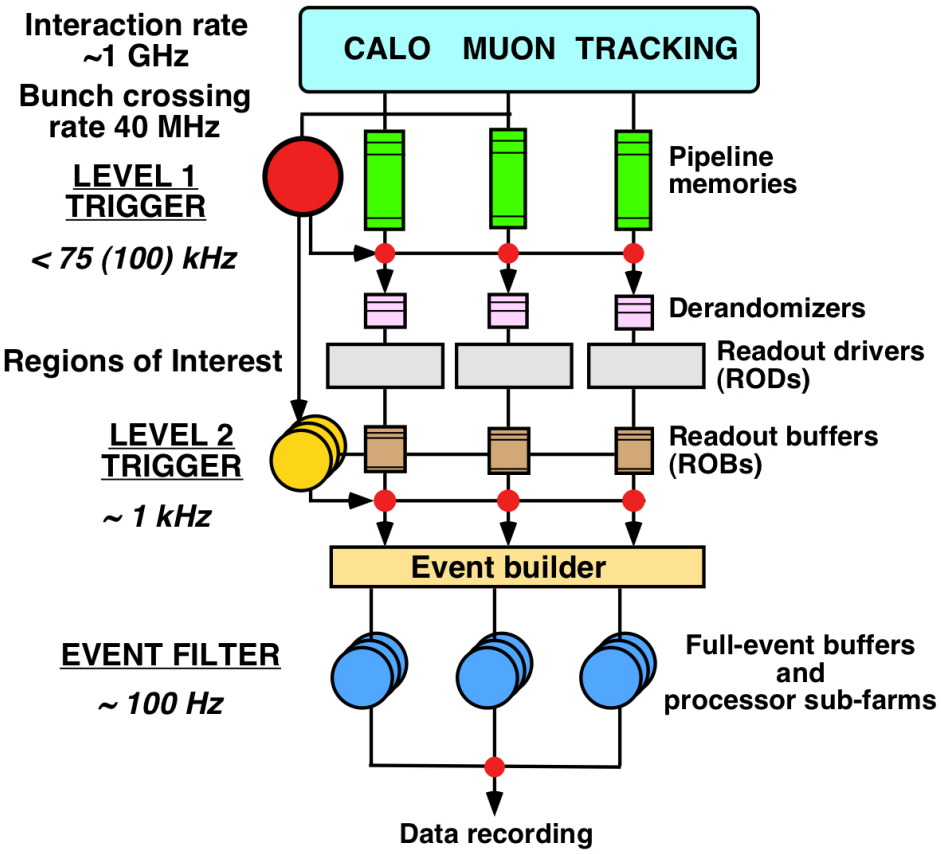

Figure 3.6: A schematic of the ATLAS trigger system, from Reference [38].

Each of the three levels of the trigger system, the Level-1 (L1) trigger, the Level-2 (L2) trigger and the Event Filter (EF), refines the decision made at the previous stage and, where necessary, applies additional selection criteria. The L1 trigger is implemented using custom-made electronics, whereas the L2 trigger and the EF are almost entirely based on commercially available computers and networking hardware. The data acquisition system receives and buffers the event data from the detector-specific readout electronics.

The L1 trigger bases its decision on information only from a subset of the detectors and with reduced granularity. It searches for high transverse-momentum muons, electrons, photons, jets, τ-leptons decaying into hadrons and large missing and total transverse energy. The decision is made in less than 2.5 μs and reduces the event rate to less than 75 kHz. Events selected by the L1 trigger are transferred to the next stages of the detector-specific electronics and subsequently to the data acquisition system.

The L2 trigger selection is seeded by so-called Regions-of-Interest (RoI's), which are defined by the L1 trigger and give geographical coordinates in η and ϕ of those regions within the

detector where the L1 trigger has identified interesting topologies. The Level-2 selection uses the full granularity and precision of the available detector data within the RoI's (≈2% of the total event data). This trigger stage reduces the event rate to approximately 3.5 kHz with an average event processing time of about 40 ms.

The Event Filter constitutes the final stage of the event selection and reduces the event rate to roughly 200 Hz. Its selection is implemented using mostly offline analysis procedures within an average event processing time of approximately 4 seconds.

3.2.5.1 Triggers used for the event selection

The following triggers are used to select events in the different analyses presented in this thesis.

Trigger for cosmic ray events

At L1, the TRT Fast-OR trigger [39] selects cosmic ray events based on a fast digital OR of a group of approximately 200 TRT straws. At L2, dedicated track triggers [40] are employed, which trigger on events with inner detector tracks. The TRT Fast-OR trigger was deployed during the commissioning phase with cosmic ray events in 2009.

Minimum bias trigger

Dedicated minimum bias trigger scintillators (MBTS) [41] are used to trigger on minimum bias events at L1. The MBTS detector consists of two scintillator disks on each side of the ATLAS detector, directly in front of the end-cap calorimeters. The trigger bases its decision on the number of MBTS hits, which are defined as a signal above discriminator threshold.

Jet triggers

At L1, the jet triggers [42] are based on a sliding-window algorithm selecting high-energy depositions in a square of 0.4×0.4, 0.6×0.6 or 0.8×0.8 in $\Delta\eta \times \Delta\phi$. The algorithm does not use the full calorimeter granularity, but coarser "trigger towers". At L2, the jet triggers use a simplified cone clustering algorithm and calorimeter clusters at full granularity, but only within the RoI around the jet identified at L1. At the event filter level, the offline jet reconstruction algorithms are used, but without the final jet calibration and only using clusters inside the RoI as well. Different jet triggers exist using different energy thresholds at the three trigger levels. The L2 and EF implementation of the triggers were not used to reject events in most of 2010, they were configured in "pass-through" mode instead.

This thesis relies on the L1_J5 trigger in several studies, which uses a window size of 0.4×0.4 in $\Delta\eta \times \Delta\phi$ and a threshold of ≈ 5 GeV at the electromagnetic scale to select the events at L1.

Jet-muon triggers

Jet-muon triggers [43] enhance the heavy-flavour content in the selected data sample and have been developed for measuring the b-tagging efficiency of lifetime-based b-tagging algorithms. They apply an angular matching between the L2 muon and the L2 jet direction

$$\Delta R = \sqrt{\Delta\phi^2 + \Delta\eta^2} < 0.4 \tag{3.4}$$

at the second trigger level. At the event filter, the jet-muon triggers were operating in pass-through mode for most of 2010.

The studies in this thesis use the EF_mu4_j5_matched trigger. It requires the L1_J5 trigger at L1, and a muon with with $p_{\mathrm{T}} > 4$ GeV at L2, which fulfils the matching criteria in Equation (3.4). The trigger was not prescaled until late 2010. Thereafter, it was prescaled by factors up to about 160.

3.3 Offline Data Processing and Analysis

The ATLAS computing model [44] incorporates the Grid paradigm and a high level of decentralisation and sharing of computing resources. This means that off-site facilities are vital for the operation of ATLAS. A complex set of tools and distributed services for the automatic distribution and processing of large amounts of data were developed.

3.3.1 Data Streaming, Calibration and Processing Cycles

To divide the data into logical datasets, ATLAS uses an event streaming technique [45] based on the trigger decision. Each event is assigned to a certain stream, and the entire offline data processing and distribution thereafter is stream-driven. The streaming in ATLAS follows an inclusive model: a copy of the event appears in each stream it is assigned to. An overlap of the order of 10% at nominal luminosity is expected. The physics data is further subdivided in files containing short time intervals of constant data taking conditions like the status of the detector or the configured trigger menu, and of approximately constant instantaneous luminosity. These time intervals are referred to as "luminosity blocks".

The reconstruction of the data involves three main stages [46]: the first-pass reconstruction of only a subset of the data (prompt reconstruction), the computation of calibration constants

from this subset of the data and first assessment of its quality, and the second-pass reconstruction of the entire dataset using these calibration constants (bulk reconstruction). All three steps are carried out at the computing facility Tier-0 at CERN and provide the reconstructed data within $3-4$ days of acquisition. The current computing model [44] assumes that the new data will be reprocessed $2-3$ months after acquisition using the same software version but improved calibration and alignment constants. A second reprocessing of the complete dataset, including the data from previous years, is envisaged at the end of data taking each year, using up-to-date algorithms and calibrations.

3.3.2 Data Formats

The data processing is done in several steps, beginning with raw or simulated data and progressing through reconstruction into more streamlined event representations suitable for analysis [44].

RAW Data: RAW data are events stored for reconstruction after the Event Filter step of the trigger system. Events are in "byte-stream" format as delivered by the detector systems and need to be transformed into object-oriented representations during the reconstruction.

Event Summary Data (ESD): ESD refers to event data written as the output of the reconstruction process. It is an object-oriented representation of the RAW data with additional reconstructed physics objects and is intended to make access to the RAW data unnecessary for most analyses.

Analysis Object Data (AOD): AOD is a reduced representation derived from ESD and is suitable for analysis. It contains all physics objects and other elements of analysis interest, and has a much reduced disk size compared to ESD.

Derived Physics Data (DPD): DPD is an n-tuple-style representation of event data for end-user analysis. It consists of only a subset of the data stored in AOD or ESD, and its content is customised by each analysis group.

3.3.3 Identification of Good Runs for Physics Analyses

The assessment of the quality of the recorded data is the base for the identification of good runs for physics analyses. The data quality (DQ) assessment takes into account each subdetector individually and its performance during the data taking, but also the performance of the object reconstruction of particle trajectories, jets, electrons or muons. The results of the data quality assessments, the data quality flags, are used to compile a list of good runs and luminosity blocks, referred to as good runs list (GRL) [47]. The GRL is created by applying DQ flag selection criteria, and possibly other criteria like the beam energy, to a list

of physics runs. The GRL is created before the physics analysis, and contains run numbers and, for each run, luminosity block ranges. The GRL is subsequently used during the physics analysis to select these good runs and luminosity blocks.

3.3.4 The Athena Software Framework

The ATLAS reconstruction software is embedded in the software framework Athena [44, 48], which is an enhanced version of the C++ based software framework Gaudi that was developed by the LHCb [33] collaboration. The Athena framework supports a modular software design with a common interface structure. Major design principles for Athena comprise abstract interfaces allowing different implementations with similar functionality, the extensive use of dynamic libraries, a clear separation between data and algorithms, a recognition that different types of data have different lifetimes within the software and a clear separation between persistent and transient data.

3.3.5 Event Generation and Detector Simulation

For the analysis of the detector response for a wide range of physics processes and scenarios, a detailed simulation has been implemented [49] that processes events from the event generation through the detailed detector response to a format which is identical to that of the real detector. The simulation process is done in three steps. The first step consists of the generation of event topologies, including immediate decays of the particles involved, which is in general independent of the detector geometry. A number of different Monte Carlo generators can be used for this; a short introduction to the ones relevant for this thesis is given in Section 2.3.5. The second step consists of the simulation of the detector and the physics interactions of the generated particles in the detector material. Each generated particle is propagated through the full ATLAS detector by the Geant4 [50] toolkit. The energies deposited in the sensitive detector material are recorded as "hits", typically containing the total energy deposition, position and time. They are passed to the third step in the simulation chain, the digitisation. During the digitisation, the energies deposited in the sensitive regions of the detector geometry are converted to detector signals like voltages or times. At this stage, detector noise is added to the event.

During both event generation and detector simulation, the information of the history of interactions and decays is kept, including incoming and outgoing particles from the generator. This information is called "truth". During the simulation job, the generated particles and the association of energy deposits in the detector to these particles are stored. This information can be used to quantify the success of the reconstruction software and to calculate its efficiency.

Chapter 4

Object Reconstruction in ATLAS

Reliable algorithms are crucial for the object reconstruction in ATLAS. The deployment of the algorithms and their commissioning follows a step-wise model: robust implementations first, and only after a phase of thorough commissioning the deployment of more sophisticated algorithms. This is highly supported by one of the major design principles of Athena, the use of abstract interfaces. This chapter introduce the algorithms which were used during the 2010 data taking period to reconstruct tracks in the inner detectors and the muon system, the primary event vertex and particle jets in the calorimeters and to identify jets originating from b-quarks.

4.1 The Tracking Event Data Model

ATLAS has developed a common event data model (EDM) for the reconstruction of tracks at the same time in the innermost tracking subdetectors and in the muon detectors in offline as well as online reconstruction [51]. The tracking EDM follows the clear distinction between event data classes and algorithmic classes as laid out by the Athena framework. At the level of the tracking EDM, this implies that the track class does not contain code to perform track fits for example, but that a fitting tool uses tracking EDM objects as input and the track class as output. Common interfaces to objects representing detector data at different stages of the reconstruction help to structure the reconstruction process as a highly modular data flow, which is presented in Figure 4.1. In the first step, the detector information is prepared for the track reconstruction by applying measurement and geometric calibrations which depend on the part of the detector the data is coming from. All different types of input data are combined under one common base class. The actual track finding and subsequent processing of tracks is done using common services and tools. The base class structure and its equivalents at later stages during the track reconstruction allows the definition of a common container class, the track, which is the output of the high-level pattern recognition algorithms. The tracks are then passed through various processing stages until track particles are created, which are used in physics analyses.

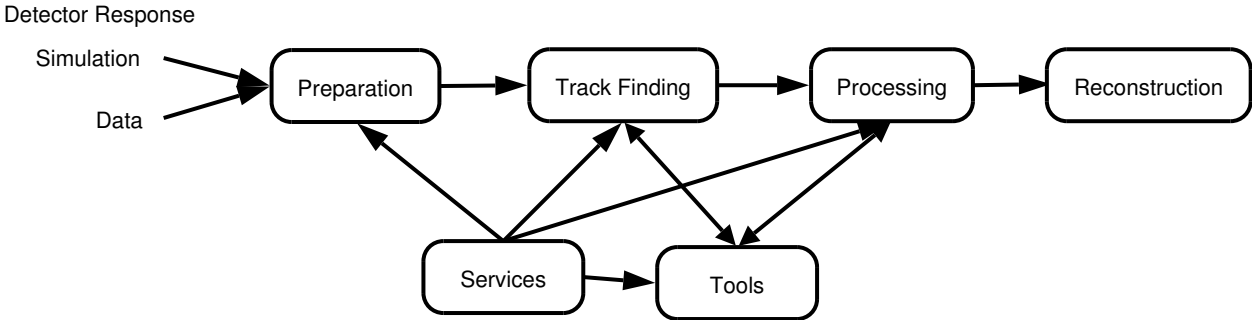

Figure 4.1: Simplified steps for the reconstruction of tracks. The detector information is prepared for the reconstruction using common classes. The track finding and subsequent processing of tracks use common services and tools due to common interfaces. From Reference [51].

4.2 Inner Detector Track Reconstruction with New Tracking

The ATLAS New Tracking (NEWT) [52, 53] reconstruction software consists of a sequence of algorithms. The single components are defined through interfaces and use - where possible - common tools and services to perform certain tasks. The tracking EDM as introduced in the section before acts hereby as the language between the different components. This allows single parts of the entire reconstruction process to be modified or exchanged without disrupting the untouched parts of the software chain. One example for this is the adaptation of NEWT for the reconstruction of trajectories from cosmic ray particles, which will be discussed in Section 5.1.1.

The main sequences of the NEWT software chain are the inside-out and the consecutive outside-in track reconstruction, which will be outlined in the following.

Preprocessing of silicon detector measurements

The creation of three-dimensional representations of the silicon detector measurements, which are called SpacePoint objects, takes place before the actual track reconstruction. In case of the pixel detector, a SpacePoint corresponds to the two-dimensional local measurement of the pixel chip and its constraint on the surface that represents the detector element. A single SCT cluster consists of a one-dimensional precision measurement only, which cannot be directly transformed into a three-dimensional point. Due to the SCT module geometry however, which comprises a sandwich module structure with a stereo-angle between two modules, the relation of the two modules together with a beam spot constraint can be used to construct the three-dimensional SpacePoint.

4.2.1 Inside-Out Track Reconstruction

The primary pattern recognition in the inner detectors follows an inside-out strategy for the track finding and is realised as a sequence of modules. Many of the modules can be divided into two pattern recognition steps, where the second step only works on the reduced output sample of the first. The inside-out sequence can be repeated several times with different parameters to extend the track reconstruction efficiency, e.g. for dedicated low-p_{T} tracking.

4.2.1.1 SpacePoint seeded track finding

The SpacePoint objects from both silicon subdetectors are used for seeding the track candidate search. This search can be divided into two different tasks, the track seed finding and the track candidate creation. The latter is based on the seeds found in the first step. The track seed finding can be done with or without a constraint on the longitudinal position z of the estimated track origin. Once the SpacePoint seeds are found, the track candidate creation is started with a road building process. The seeds provide enough directional information to build roads of detector elements. The association of hits from these detector elements uses a Kalman filter-smoothing formalism [54] to form a track candidate. Only about 10% of the seeds are successfully extended to track candidates, which is confirmed in the data [55].

4.2.1.2 Ambiguity solving

The SpacePoint seeded track finding results in a high number of ambiguous track candidates, which have to be resolved before extending them into the outer TRT. Many of these track candidates share hits, are incomplete or describe fake tracks, i.e. tracks where the majority of associated measurements do not originate from the same particle. Therefore the tracks have to be ranked according to their likelihood to describe the real trajectory of particles from the underlying physics event. For the classification of tracks, a track scoring strategy has been developed that involves morphological parameters of the track in addition to the fit quality: different characteristics of a track are hereby represented by a beneficial or penalising score, which form together an overall track score. In general, each hit associated with the track leads to a better score value to favour fully reconstructed tracks rather than small track segments. Hits which are associated to more than one track are attempted to be resolved. An iterative procedure of ranking, hit re-association and fitting determines the new hit content of the tracks which formerly shared hits: the tracks "compete" for the shared hit. Preference is given to well reconstructed tracks with a high track score. This procedure results in only a small fraction of shared hits on the tracks after the ambiguity solving process. Tracks that fall beyond a certain quality cut are not considered for further processing.

4.2.1.3 TRT extension

The track extension from the silicon detectors into the TRT consists of two steps. The first step steers the extension finding on a single track-by-track basis. The tracks which are resolved by the ambiguity processing are used as inputs to find compatible sets of TRT measurements, the candidate extensions. In a second step, every extended track is evaluated with respect to the pure silicon track. The comparison of the two tracks is based on a combined track fit and uses the track scoring mechanism to compare the track score of the original track with the one after the fit. The track with the higher score is kept for further processing. The fit in this step can modify the silicon hits by flagging them as "outlier" measurements, which are not used for the final track parameter estimate. In case the track score of the silicon track is higher than the one of the extended version, the silicon track is kept and the TRT hits are added onto the track as outlier measurements.

4.2.2 Outside-In Track Reconstruction

In the track reconstruction process, some of the track candidates may not have been found by the inside-out reconstruction sequence: ambiguous hits influence the track seeds in the silicon and could prevent the score of the silicon seeded tracks to survive the ambiguity processor; tracks coming from secondary decay vertices further inside the inner detector volume (e.g. K_S decays) or from photon conversions may not have any or only insufficient silicon hits to be reconstructed by the inside-out sequence. To recover these tracks, the outside-in track reconstruction sequence [52, 56] is realised as two different modules, starting with a dedicated segment finding algorithm in the TRT and a successive back tracking of the segments into the SCT detector.

4.2.2.1 TRT segment reconstruction

The TRT segment reconstruction consists of a typical two-step pattern recognition in the TRT detector. The first step uses a Hough transform technique [57] to find the initial group of straws for the segment candidates. A Hough transform is based on the fact that points associated with a line in the projection plane $R - \phi$ (respectively $z - \phi$ in the endcaps) are transformed into one single cell in the parameter space of the straight line. The track segment search is thus reduced to a local maximum finding in a two-dimensional histogram. The next step uses a Kalman filter-smoothing formalism [54] to build the track segments. A cut is placed on the minimal number of straw hits on the segments to select them for further processing.

4.2.2.2 Extension into the SCT detector

The directions indicated by the transverse parameters of the TRT segment tracks are used to search for SpacePoint pairs in the last three layers of the SCT detector. This procedure is also referred to as back tracking. Only SpacePoints are considered that have not been associated to another track in the event by the NEWT reconstruction sequence. The silicon extensions are reconstructed with track parameters from the TRT segment tracks and the collected silicon elements. The TRT extension processor is used for this, with a slightly modified scoring strategy to give some preference to TRT hits on the initial track segments.

4.3 Reconstruction of the Primary Event Vertex

The reconstruction of the primary event vertex is done in a very modular way and consists of two main tasks: the vertex finding and the vertex fitting [58, 59]. During the primary vertex finding step, vertex seeds are identified and tracks are associated to these seeds. After this, the vertex fit reconstructs the vertex position and its corresponding error matrix. During the 2010 data taking period, ATLAS used a very robust vertex finding and fitting approach:

A vertex seed is obtained by finding the global maximum in the distribution of z coordinates of all tracks which are compatible with originating from the interaction region. The z coordinates are expressed with respect to the point of closest approach to the beam spot centre. The beam spot centre is determined periodically during each physics run using an adapted version of the vertex reconstruction. For the vertex fit, a robust χ^2 fitting algorithm is used which takes the vertex seed position and the surrounding tracks as input. The fitter deals with outlying track measurements by iteratively down-weighting their contribution to the overall vertex χ^2. Tracks which are incompatible with this vertex are used to seed a new vertex. This iterative procedure is repeated until no unassociated tracks remain or no additional vertex seeds can be reconstructed.

By default, both the finding and the fitting procedure use the knowledge of the beam spot parameters. This has a very large impact on vertices reconstructed in events with low track multiplicities. Preliminary results of the primary vertex reconstruction in pp collisions at $\sqrt{s} = 7$ TeV have been documented in Reference [59].

4.4 Jet Reconstruction in the Calorimeters

4.4.1 Topological Cell Clusters

The calorimeters are the most important detectors for jet reconstruction in ATLAS and consist of ≈ 200 000 individual cells of various sizes and with lateral segmentations. For the jet finding, these individual cells are combined into larger signal objects with physically meaningful four-momenta, the topological cell clusters [58]. They are used as input signals by the jet clustering algorithms. Topological cell clusters are the attempt to reconstruct three-dimensional energy depositions without geometric constraints ("energy blobs"). The clustering uses seed cells with a signal significance $\Gamma = E_{cell}/\sigma_{noise,cell} > 4$. All directly neighbouring cells in three dimensions with $\Gamma > 2$ are collected into the cluster in a next step. Finally, a ring of guard cells with $\Gamma > 0$ is added. After this, the clusters are analysed for local signal maxima. In case local signal maxima are found, the clusters are split between those maxima by a splitting algorithm.

The clusters are formed using the basic electromagnetic scale cell signals and are directly used as input for the jet reconstruction. The calibration of the jets to the final energy scale is done on a jet-by-jet basis as described in Section 4.4.4.

4.4.2 The Anti-k_t Jet Clustering Algorithm

The default jet reconstruction algorithm in ATLAS is the anti-k_t jet clustering algorithm [60]. This algorithm is a simple, infrared and collinear safe, soft-resilient jet algorithm that reconstructs jets whose shape is not influenced by soft radiation. The anti-k_t algorithm introduces distances d_{ij} between pseudo-jets i and j and d_{iB} between pseudo-jet i and the beam B. The clustering algorithm identifies the smallest distance in a list containing all pseudo-jets. If the smallest entry is the distance d_{ij} between two pseudo-jets i and j, they are added together. If it is d_{iB} then i is called a jet and removed from the list of pseudo-jets. All distances are recalculated and the procedure repeated until no pseudo-jets are left. The distance measure for the anti-k_t jet algorithm is defined as follows:

$$\begin{aligned} d_{ij} &= \min(k_{ti}^{-2}, k_{tj}^{-2}) \frac{(\Delta R)_{ij}^2}{R^2} \\ d_{iB} &= k_{ti}^{-2}, \end{aligned} \tag{4.1}$$

where $(\Delta R)_{ij}^2 = (y_i - y_j)^2 + (\phi_i - \phi_j)^2$. k_{ti} denotes the transverse momentum, y_i the rapidity and ϕ_i the azimuth of pseudo-jet i. The variable R is a resolution parameter which sets the relative distance at which jets are resolved from each other as compared to the beam. In this thesis, only jets with values $R = 0.4$ are considered.

4.4.3 Truth Jets

Truth jets are jets formed by clustering stable truth particles ($\tau > 10$ ps) from the truth record in the Monte Carlo simulation using the anti-k_t algorithm. In the definition used in this thesis, stable particles include muons and neutrinos from hadron decays.

4.4.4 Jet Energy Scale Calibration

The basic signal scale for the ATLAS calorimeters is the electromagnetic scale [61]. The energy at this scale accounts correctly for the energy deposited in the calorimeters by electromagnetic showers. This energy scale has been established using test-beam measurements and muons from cosmic ray events. It has subsequently been corrected using the invariant mass of $Z \rightarrow ee$ events from proton-proton collisions.

The jet energy calibration corrects for detector effects like partial measurement of the energy deposited by hadrons, energy losses in inactive regions of the detector or energy deposits from particles not contained in the calorimeters. All of these effects influence the energy and the momentum of the jets as measured in the calorimeters, which need to be corrected. The correction factors are calculated using truth jets from Monte Carlo simulations as a reference.

At present, ATLAS uses a calibration scheme referred to as *EM+JES* that applies jet-by-jet corrections to the jets reconstructed at the electromagnetic scale. These corrections depend on the jet energy and pseudorapidity of the jet. The calibration restores the jet energy scale within 2% for the full kinematic range. The uncertainties of this calibration have been measured using both Monte Carlo and data-driven approaches [61]. In the central region ($|\eta| < 0.8$), the uncertainty is lower than 4.6% for all jets with $p_{\mathrm{T}}^{jet} > 20$ GeV, while for jet transverse momenta between 60 and 800 GeV the uncertainty is below 2.5%. In the very forward region (up to $|\eta| = 4.5$), the uncertainty amounts to a total of about 14%.

4.5 Track Reconstruction in the Muon System

ATLAS uses a combination of three strategies for the identification and reconstruction of particle trajectories in the muon system [58]. The first strategy reconstructs standalone tracks in the muon spectrometer and then extrapolates these to the beam line, resulting in very pure sample of muon trajectories. In the second approach, standalone muons are matched to inner detector tracks and the measurements from the two systems are combined, which improves the track parameter resolutions. In the third approach, inner detector tracks are extrapolated to the muon spectrometer and nearby hits are added to the tracks, enabling the reconstruction of low-momentum muons in the muon system. The current ATLAS reconstruction includes

two implementations for each strategy. The STACO [62] collection (named after the combined algorithm) is currently the default for physics analyses and will be described in the following.

4.5.1 Standalone Muon Reconstruction

The standalone algorithm Muonboy builds track segments in each of the three muon stations and then links the segments to form tracks. After this, the tracks are extrapolated to the beam line. For the extrapolation, the energy loss and the multiple scattering based on the material crossed in the inner detectors and the calorimeters are taken into account.

4.5.2 Combined Muon Reconstruction

The algorithm combining muon spectrometer tracks with inner detector tracks is called STACO. STACO uses the match chi-square χ^2_{match} as a measure of the quality of the match. χ^2_{match} is defined as the difference between the muon spectrometer (MS) and inner detector (ID) track vectors $\vec{T}$ weighted by their combined co-variance matrices $\vec{C}$:

$$\chi^2_{match} = (\vec{T}_{MS} - \vec{T}_{ID})^T (\vec{C}_{ID} + \vec{C}_{MS})^{-1} (\vec{T}_{MS} - \vec{T}_{ID}). \tag{4.2}$$

$\vec{T}$ denotes the vector of five track parameters, expressed at the point of closest approach to the beam line and $\vec{C}$ is its co-variance. The STACO algorithm uses the χ^2_{match} to decide which ID-MS track pairs are kept. The final trajectory is obtained by a combination of the inner detector and the muon spectrometer track vectors, weighted by their co-variance matrices:

$$\vec{T}_{combined} = (\vec{C}^{-1}_{ID} + \vec{C}^{-1}_{MS})(\vec{C}^{-1}_{ID}\vec{T}_{ID} + \vec{C}^{-1}_{MS}\vec{T}_{MS}). \tag{4.3}$$

4.5.3 Reconstruction of Tagged Muons

The spectrometer tagging algorithm MuTag propagates all inner detector tracks with sufficient momentum and which have not been used by the STACO combined algorithm out to the first station of the muon spectrometer. Here it searches for nearby segments. A chi-square defined by the difference between any nearby segments and the prediction from the inner detector track extrapolation is used for the tagging of the inner detector track. If a muon spectrometer segment is close enough to the predicted track position, the inner detector track is tagged as corresponding to a muon. Only the inner detector track information is used to form the tagged muon track.

4.6 Identification of Jets originating from b-Quarks

Jets which originate from b-quarks (b-jets) distinguish themselves from generic light-flavour jets in a number of different ways. The longer lifetime of b-hadrons compared to light-flavoured hadrons implies that the b-hadrons cover a distance of the order of a millimetre before they decay. b-jets can therefore be identified (*tagged*) by particle trajectories in the jets which are significantly displaced from the primary interaction point, or by the explicit reconstruction of the b-decay vertices inside the jets. Impact parameter tagging algorithms exploit the former, whereas secondary vertex tagging algorithms the latter. A third category of b-tagging algorithms identifies jets which originate from the semi-leptonic decays of b-quarks by the presence of muons or electrons inside the jets.

Two algorithms are of great importance for the identification of b-jets in the first data analyses, the jet probability tagging algorithm JetProb and the secondary vertex tagging algorithm SV0. The baseline b-tagging algorithm in ATLAS, the combination of the impact parameter tagging algorithm IP3D and the secondary vertex tagging algorithm SV1, will supersede these first data algorithms once it is fully calibrated. The functionality of all four algorithms [58] will be presented in the following.

4.6.1 Definition of b-Jets

Jets originating from b-quarks (so-called b-jets) are defined as jets (either truth or calorimeter jets) within $\Delta R = \sqrt{\Delta\phi^2 + \Delta\eta^2} < 0.3$ of a generated b-quark.

4.6.2 Jet Associations

In addition to the properties of the reconstructed jet, the b-tagging algorithms also use associated objects like tracks or muons for their decisions. Objects are associated to the jet if they fulfil

$$\Delta R = \sqrt{\Delta\eta^2 + \Delta\phi^2} < C. \tag{4.4}$$

For tracks a variable distance C depending on the transverse momentum of the jet is used. It is ~ 0.5 for small jet momenta and decreases for larger jet momenta. For the association of muons, a value $C = 0.4$ is typically used.

4.6.3 Likelihood Ratio Method

Both the impact parameter tagging algorithm IP3D and the secondary vertex tagging algorithm SV1 use a likelihood ratio method to calculate the discriminating variable between b- and light-jets. The measured value of the discriminating variable is compared to pre-defined smoothed and normalised distributions for both the b- and the light-jet hypothesis. The ratio of the two probabilities defines the track or vertex weight, which can be combined into a jet weight as the sum of the logarithms of the individual weights.

4.6.4 Impact Parameter Tagging Algorithms

The input of impact parameter tagging algorithms is the point of closest approach of the tracks associated to the jets to the primary event vertex. A sign can be assigned to the tracks which depends on their origin. The sign of the transverse impact parameter is defined using the jet direction $\vec{P}_j$ as measured in the calorimeters, the direction $\vec{P}_t$ and the position $\vec{X}_t$ of the track at the point of closes approach to the primary vertex and the position $\vec{X}_{PV}$ of the primary vertex itself:

$$\text{sign}(d_0) = (\vec{P}_j \times \vec{P}_t) \cdot (\vec{P}_t \times (\vec{X}_{PV} - \vec{X}_t)) \cdot \frac{1}{N}, \tag{4.5}$$

where $N = |(\vec{P}_j \times \vec{P}_t) \cdot (\vec{P}_t \times (\vec{X}_{PV} - \vec{X}_t))|$. Tracks originating from the primary vertex generate a random sign due to the experimental resolution while tracks from b- and c-decays tend to have a positive sign as the decay point lies along the jet axis. The distributions of the signed transverse impact parameter and its significance $S_{d0} = \text{sign}(d_0) \cdot \frac{|d_0|}{\sigma_{d0}}$ for the three different flavours light, charm and bottom are shown in Figure 4.2 [58]. The sign of the longitudinal impact parameter z_0 is defined by the sign of $(\eta_j - \eta_t) \cdot z_{0t}$, where t refers to the track at the point of closest approach to the primary vertex and j to the jet as measured in the calorimeters.

4.6.4.1 The jet probability tagging algorithm JetProb

One of the most robust tagging algorithms, the jet probability tagging algorithm JetProb [58], relies on the combination of the positive signed transverse impact parameter significances $S_{d0} > 0$ of all tracks in the jet. The the positive signed transverse impact parameter significance of each selected track i in a jet is compared to a resolution function $\mathcal{R}$ for prompt tracks, in order to measure the probability that the track i originates from the primary vertex:

$$\mathcal{P}_i = \int_{-\infty}^{-|d_0^i/\sigma_{d0}^i|} \mathcal{R}(x)dx\,. \tag{4.6}$$

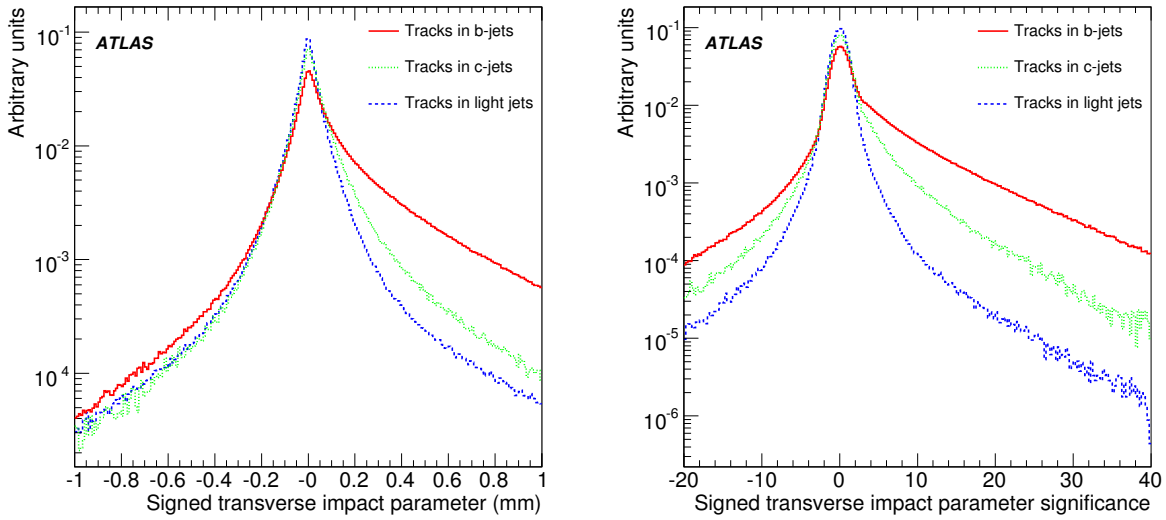

Figure 4.2: Signed transverse impact parameter d_0 distribution (left) and signed transverse impact parameter significance $S_{d0} = \text{sign}(d_0) \cdot \frac{|d_0|}{\sigma_{d0}}$ (right) for b-jets, c-jets and light-jets. From Reference [58].

The track resolution function $\mathcal{R}$ can be derived from data using the negative side of the signed transverse impact parameter distribution, assuming the contribution from heavy-flavour particles is negligible here.

The individual probabilities of all N tracks associated to the jet are combined to obtain a jet probability $\mathcal{P}_{jet}$ in the following way:

$$\mathcal{P}_{jet} = \mathcal{P}_0 \sum_{k=0}^{N-1} \frac{(-\ln(\mathcal{P}_0))^k}{k!}\,, \tag{4.7}$$

where

$$\mathcal{P}_0 = \prod_{i=1}^{N} \mathcal{P}_i\,. \tag{4.8}$$

The jet probability $\mathcal{P}_{jet}$ is therefore the product $\mathcal{P}_0$ of all the individual track probabilities, with a weighting factor depending on the track multiplicity. The physical interpretation of $\mathcal{P}_{jet}$ is the probability that the jet originates from the primary vertex (and therefore has no decay products from long-lived particles). Preliminary results of the JetProb tagging algorithm with 900 GeV and 7 TeV are documented in Reference [63] and Reference [64], a study showing the performance of the JetProb algorithm using p_{T}- and η-dependent track resolution functions is presented in Section 7.1.

4.6.4.2 The impact parameter tagging algorithm IP3D

The impact parameter tagging algorithm IP3D [58] uses two-dimensional histograms of the longitudinal versus the transverse impact parameters and thus takes advantage of their correlations.

4.6.5 Secondary Vertex Tagging Algorithms

Secondary vertex tagging algorithms [58] reconstruct the inclusive vertex formed by the decay products of the b-hadron. They might also include products of the eventual subsequent c-hadron decay. The reconstruction starts by forming two-track vertices which are significantly displaced (in three dimensions) from the primary vertex. Two-track vertices with a mass consistent with a K_s^0 meson, a Λ^0 baryon or a photon conversion are excluded. In addition, two-track vertices at a radius consistent with one of the three pixel detector layers or the beam pipe are removed, as these vertices likely originate from material interactions. All tracks from the remaining two-track vertices are combined and fitted to a single secondary vertex. Tracks with the largest χ^2 contribution to the common vertex are removed in an iterative process.

4.6.5.1 The secondary vertex tagging algorithm SV0

The secondary vertex tagging algorithm SV0 places a cut on the signed decay length significance $L/\sigma(L)$ of the reconstructed secondary vertex. An illustration of a SV0-tagged jet is shown in Figure 4.3 [65]. The sign of $L/\sigma(L)$ is given by the sign of the projection of the decay length vector on the jet axis. Secondary vertices from real b-decays tend to have a positive sign, whereas secondary vertices in light-jets have a random sign. Preliminary results of the SV0 algorithm with 900 GeV and 7 TeV are documented in Reference [66] and Reference [65]

4.6.5.2 The secondary vertex tagging algorithm SV1

The secondary vertex tagging algorithm SV1 [58] relies on a two-dimensional distribution of the invariant mass of all tracks associated to the vertex and the ratio of the sum of the energies of the tracks associated to the vertex to the sum of the energies of all tracks in the jet. It also considers a one-dimensional distribution of the number of two-track vertices.

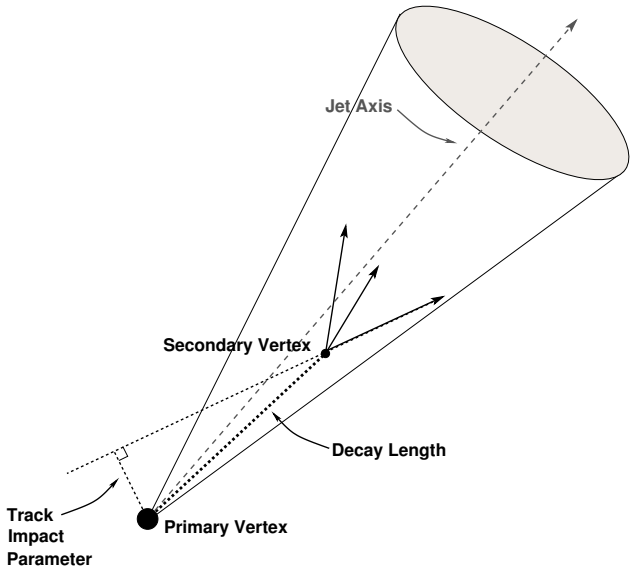

Figure 4.3: A secondary vertex with a positive decay length indicates the presence of a long-lived particle in the jet. The secondary vertex is reconstructed from tracks with a large impact parameter significance with respect to the primary vertex. From Reference [65].

4.6.6 Combination of Tagging Algorithms

The combination of the two likelihood-based tagging algorithms IP3D and SV1 is very easy: the weights of the individual tagging algorithms are simply summed up. The combination of IP3D and SV1 is the baseline tagging algorithm for many analyses in ATLAS and will be commissioned next after the early tagging algorithms JetProb and SV0.

4.6.7 Energy Scale Correction for Jets from Semi-Leptonic b-Decays

b-jets which originate from b-quarks decaying via the semi-leptonic mode $\bar{b} \rightarrow \mu X$ contain in addition to the muon also a neutrino from the decay. The neutrino carries away approximately 10% of the jet energy according to Monte Carlo estimates. An average correction for b-jets from semi-leptonic decays has been obtained from Monte Carlo simulations [67]. This correction is referred to as μJES, and denotes the fully corrected b-jet transverse momentum as p_{T}^{b-jet}. The correction is implemented as a parameterisation of p_{T}^{b-jet} as a function of the muon momentum p_{T}^{μ} and the jet momentum p_{T}^{jet}. The function $p_{\mathrm{T}}^{b-jet}\left(p_{\mathrm{T}}^{jet}, p_{\mathrm{T}}^{\mu}\right)$ is determined from Monte Carlo simulations within different bins of p_{T}^{jet} and is designed to be applied after the jet transverse momentum p_{T}^{jet} has been fully corrected to the jet energy scale. The validation of the semi-leptonic b-jet correction and the estimation of its uncertainty are presented in Section 8.3.3.

Chapter 5

Commissioning of the Inner Detector Track Reconstruction Software

The reconstruction of trajectories from charged particles in the detector is a crucial element in the reconstruction of the entire event topology. The commissioning of the track reconstruction software and its performance both in the data and the Monte Carlo simulations are presented in this chapter. First tests of the software using the data from cosmic ray showers are presented in the first section. These events typically only contain one trajectory per event and are therefore ideal for commissioning. More stringent tests are presented in the next two sections using the data from proton-proton collisions at a centre-of-mass energy of 900 GeV and 7 TeV, respectively.

5.1 Commissioning of New Tracking using Cosmic Ray Events

After the LHC incident in September 2008, the ATLAS experiment took two global runs in autumn 2008 and summer 2009, recording several hundred million events from cosmic ray showers. At the beginning of the data taking period in 2008, only the dedicated ATLAS Cosmics and Testbeam (CTB) Tracking [68] was capable of reconstructing cosmic ray trajectories efficiently in the inner detectors. In order to commission New Tracking (NEWT) with these trajectories, several adjustments were required to the reconstruction sequence with respect to the nominal collision setup. As part of the validation process, the performance of the adjusted NEWT sequence was compared to CTBTracking in Monte Carlo simulations of cosmic ray events. Detailed comparisons between the data from the 2009 run period and the Monte Carlo simulations completed the validation. The results of these studies are documented in an internal ATLAS report [69]. NEWT has now replaced CTBTracking as default for the reconstruction of cosmic ray data. But CTBTracking is still used to study the remaining inefficiencies in the New Tracking algorithm.

5.1.1 Adjustments for the Reconstruction of Cosmic Ray Tracks

This section details the modifications to the tracking software for the reconstruction of cosmic ray trajectories in the inner detectors. Both NEWT and CTBTracking use the same common code base such as event data model, track fitter and extrapolator. Adjustments of common tools are therefore used by both reconstruction algorithms.

5.1.1.1 New Tracking Inside-Out Reconstruction of Cosmic Ray Trajectories

The basic functionality of the ATLAS New Tracking inside-out reconstruction sequence has been described in Section 4.2.1. Figure 5.1 shows the sequence of modules and the most important algorithms and tools used in the adjusted New Tracking inside-out sequence for the reconstruction of cosmic ray trajectories. The overall structure is the same as for collisions. Where indicated by a grey box with white "c", a special implementation of an algorithm or a tool is used. A special parameter tuning is indicated by a box with a "t" next to the algorithm or the tool name.

SpacePoint seeded track finding

In the cosmic implementation of the `SiSpacePointSeedMaker`, no constraint is placed on the impact parameters, only on the transverse momentum p_{T} of the seeds. The track seeds can consist of SpacePoints from both the upper and the lower part of the detector. In the `SiTrackMakerTool` adapted for the reconstruction of cosmic ray trajectories, the Kalman filter-smoothing formalism [54] for adding clusters to the trajectory is used along and contrary to the track direction.

Ambiguity solving

The `InDetAmbiguitySolver` uses a special implementation of the track scoring tool for the ranking of trajectories from cosmic ray showers.

TRT extension

A special implementation of the `TRT_ExtensionTool` is used to extend the resolved tracks into the outer TRT. The `InDetExtensionProcessor` uses the implementation of the track scoring tool for cosmic ray trajectories to evaluate the extended tracks with respect to the pure silicon tracks.

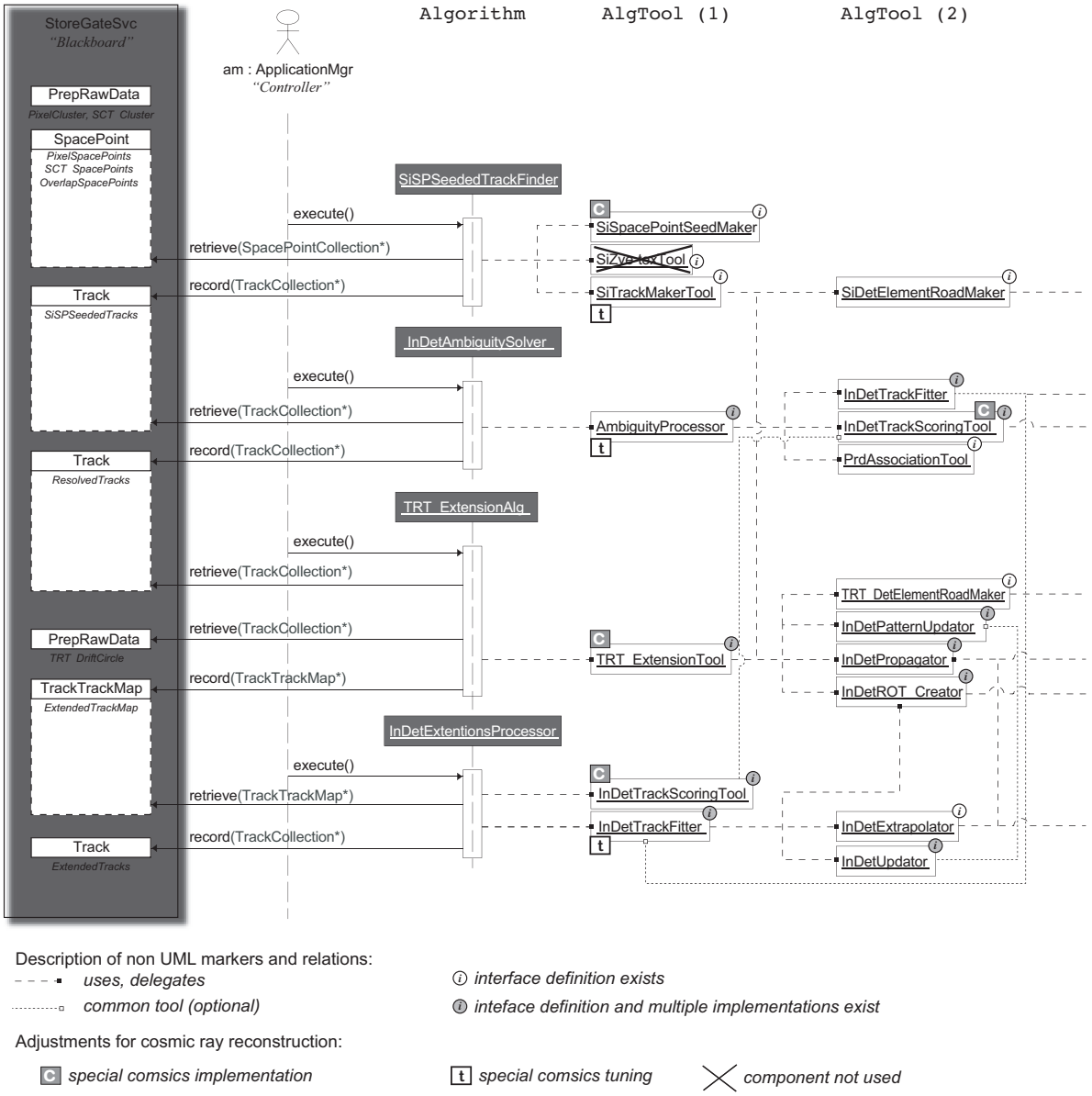

Figure 5.1: Main module sequence of the New Tracking track reconstruction chain for cosmic ray trajectories. Where indicated by a grey box with white "c", a special implementation of an algorithm or a tool is used. A special parameter tuning is indicated by a box with a "t" next to the algorithm or the tool name.

5.1.1.2 TRT-Only Reconstruction of Cosmic Ray Trajectories

The TRT-only reconstruction of cosmic ray trajectories [69] can be divided into two tasks: the reconstruction of trajectories in the barrel and the reconstruction of trajectories in the endcaps of the TRT detector. The track reconstruction in the TRT barrel uses the track finder of CTBTracking, whereas a dedicated TRT pattern recognition algorithm has been developed to reconstruct cosmic ray trajectories in the TRT endcaps.

5.1.1.3 Combining Inside-Out and TRT-Only Tracks

The last step of the cosmic ray track reconstruction consists of merging the tracks from the inside-out and the TRT-only track reconstruction sequences to get a complete set of tracks. The merging uses the cosmic implementation of the ambiguity solver. In case a track is reconstructed by both the inside-out and the TRT-only sequence, the ambiguity solver selects the track with the better precision.

5.1.1.4 Adjusted Tools for the Track Reconstruction

Many common tools and services are used by the two main reconstruction algorithms, some of which needed to be adapted or tuned for the reconstruction of cosmic ray trajectories.

Hole search tool

The hole search tool searches for active detector elements that were crossed by a track but did not contribute to it with a measurement. The missing detector measurement is called a "hole". The schematics in Figure 5.2 illustrate a track traversing three detector elements which all register its passage (left) and a track passing three detector elements, while only two of them register the passage; the middle detector element shows a "hole" on the trajectory (right). Taking the excellent hit efficiency of the silicon detectors into account, several missing measurements on a track are an indicator for a wrongly reconstructed or fake track. This tool is therefore very powerful in rejecting fake tracks in the course of the reconstruction.

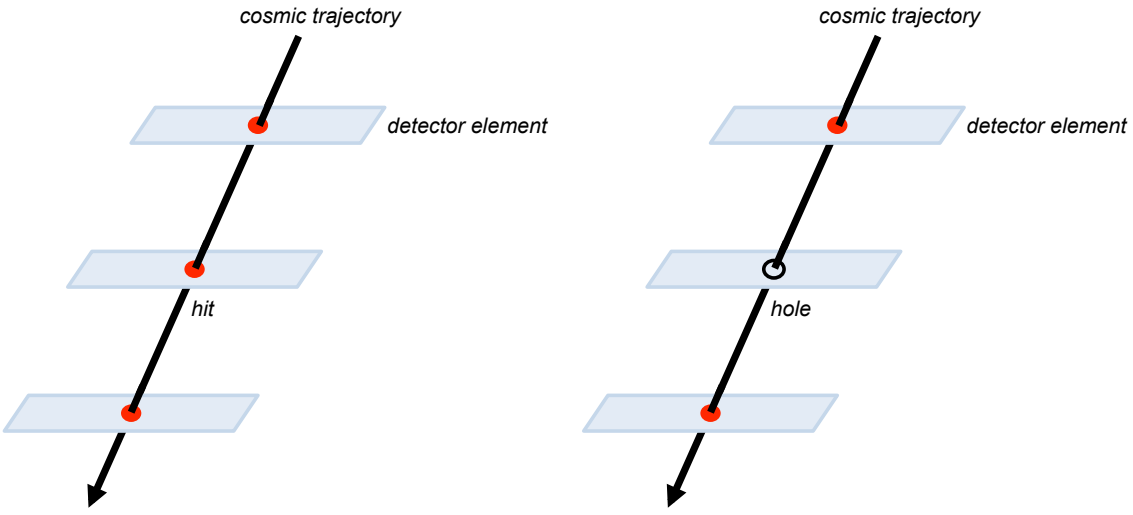

Figure 5.2: Schematic of a track passing three tracking layers.
left: All three detector elements register the passage of the track.
right: The middle detector element did not register a hit where the track traversed it, the missing measurement is called a "hole".

The already existing hole search tool was adjusted for the reconstruction of cosmic ray trajectories. The adjusted version starts the search for missing measurements at the boundary of the SCT detector (instead of the detector centre in case of collisions). It uses the ATLAS extrapolator [70] to extrapolate from one measurement to the next and gathers the information as to whether a detector element was crossed or not. Only detector elements which were functioning during the data taking are considered. Due to uncertainties in the extrapolation procedure, the area near the sensor edge or ambiguously mapped pixels are excluded from the hole search. Only after taking this information into account, a missing measurement is declared as a hole.

The functionality of the hole search tool can also be used to measure the intrinsic efficiency of the pixel and SCT detectors [71]. The intrinsic efficiency denotes the probability of a hit to be registered in an operational detector element when a charged particle traverses its sensitive part. The efficiency ϵ can be calculated by

$$\epsilon = \frac{N_{clusters}}{N_{clusters} + N_{holes}}, \tag{5.1}$$

where $N_{clusters}$ denotes the number of measurements on the tracks and N_{holes} the number of missing measurements (i.e. holes). Detector elements which were excluded from the data taking were excluded from the efficiency measurement as well. This amounts to $\sim 2\%$ of the SCT detector and $4-6\%$ of the pixel detector. The measured efficiency of each barrel layer in the pixel and SCT detectors is presented in Figure 5.3 [71] for cosmic ray data from the 2008 data taking period. The overall efficiency of the pixel barrel is $(99.974 \pm 0.004(\text{stat}) \pm 0.003(\text{syst}))\%$, and of the SCT barrel $(99.78 \pm 0.01(\text{stat}) \pm 0.01(\text{syst}))\%$.

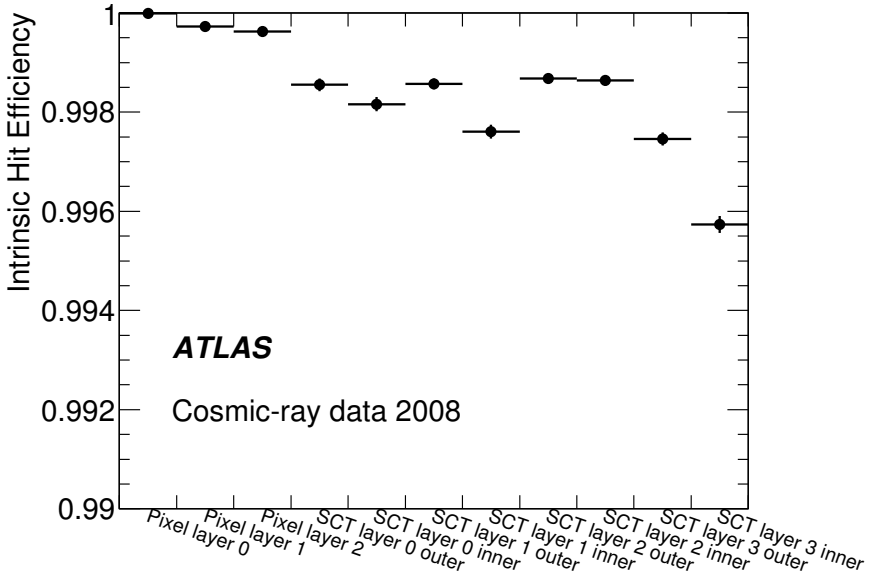

Figure 5.3: Measured efficiency of each barrel layer in the pixel and SCT detectors, from Reference [71].

Track scoring tool

For the reconstruction of cosmic ray tracks, a very simple scoring scheme was used to rank the tracks according to their likelihood to describe the real trajectory of the cosmic ray muon. For this classification, a special track scoring strategy has been developed. Different characteristics of a track are weighted in different ways to form an overall track score:

- Hits in the different subdetectors have different weights (pixel: 20, SCT: 10, TRT: 1).
- Penalties are given for tube hits in the TRT (i.e. a hit where the tracking does not use the drift time information) and an overall bad fit quality.

TRT extension tool

The resolved tracks as output of the ambiguity solving are used to find a compatible set of TRT measurements that are further processed as candidate extensions. In case of cosmic ray tracks [69], extensions into the TRT are not only searched for along the track direction, but also against it (since the cosmic ray particle traverses the TRT twice - once before entering the silicon detector and once after leaving it).

5.1.2 Validation of the Adjustments using Monte Carlo Simulations

The validation of the adjusted NEWT sequence relied on Monte Carlo simulations. The dedicated reconstruction algorithm for cosmic ray trajectories, CTBTracking, has been used as a benchmark to judge the performance of the adjusted NEWT sequence. An overview of the simulated datasets used in this study is given in Appendix A.1.

5.1.2.1 Track reconstruction efficiencies

The ability to reconstruct a trajectory within the acceptance of the tracking detectors is one of the most important qualities of a reconstruction algorithm. The reconstruction efficiency ϵ is defined as the fraction of all true trajectories within the acceptance which have been reconstructed by the algorithm:

$$\epsilon = \frac{\#(\text{reconstructable truth tracks matching a reconstructed track})}{\#(\text{reconstructable truth tracks})}. \tag{5.2}$$

A reconstructable truth track is defined as a truth track which

- is charged and stable,
- has a transverse momentum p_{T} above 1 GeV,

- generates at least four SpacePoints in two different layers in the pixel and SCT detectors together.

Figure 5.4 shows the track reconstruction efficiencies for both NEWT and CTBTracking versus the track parameters $|\eta|$, p_{T}, $|d_0|$ and $|z_0|$. To be less sensitive to statistical fluctuations, only bins with more than 500 entries are shown. The integrated efficiency of the NEWT sequence is above 99.7%, and is almost identical to CTBTracking. The adjustments to the New Tracking sequence have therefore rendered it compatible with a dedicated algorithm for the reconstruction of cosmic ray trajectories.

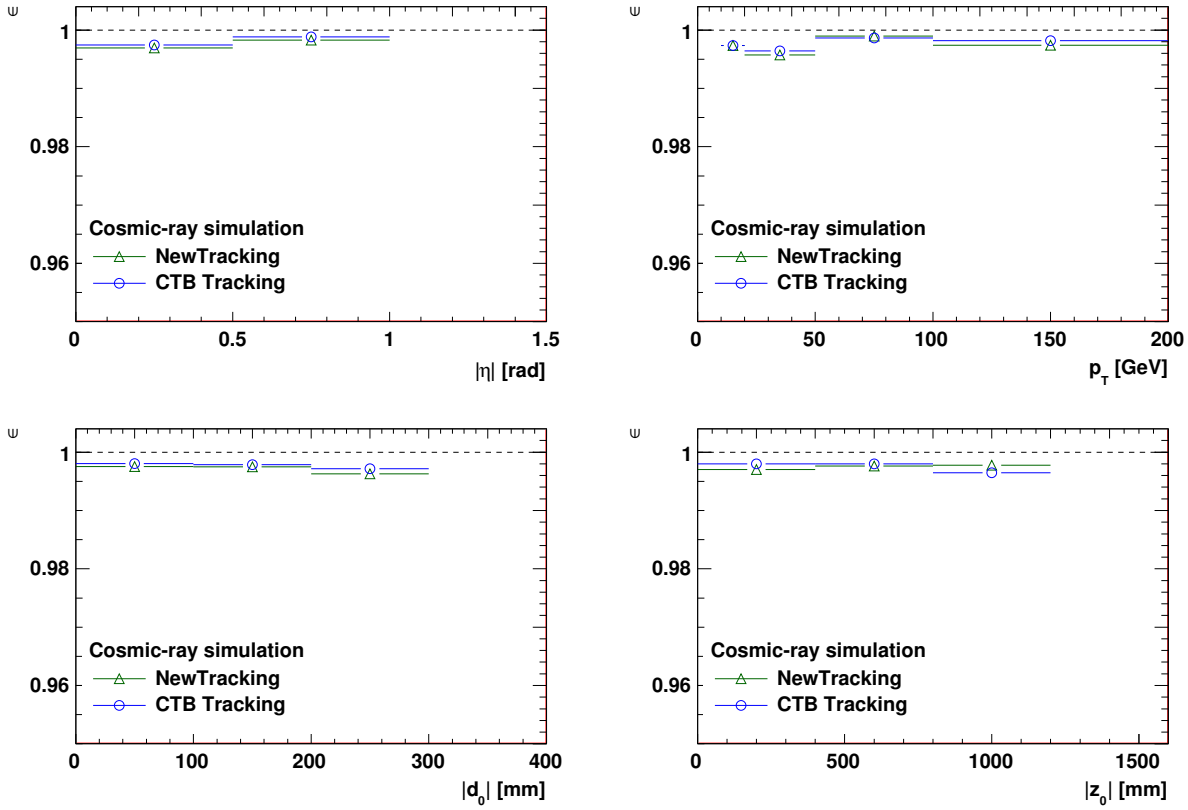

Figure 5.4: Track reconstruction efficiencies for the inside-out track reconstruction algorithms New Tracking and CTBTracking versus the track parameters $|\eta|$, p_{T}, $|d_0|$ and $|z_0|$.

The upper left plot in Figure 5.4 shows the tracking efficiency versus $|\eta|$. A small dependency on the sub-percent level is visible. Cosmic muons typically only span the $|\eta|$-region in ATLAS with $|\eta| < 1.5$ due to their special event topology (originating from the surface and crossing the detector from top to bottom). Due to the limited statistics of the simulated sample for this analysis, the bin for $|\eta| > 1.0$ is not shown. The plot on the upper right shows the track reconstruction efficiency versus p_{T}. This plot shows no clear trend, the efficiency fluctuates between 99.6% and 99.9% for the different bins. The tracking efficiency versus the transverse impact parameter $|d_0|$ (bottom left) shows a value around 99.7% between $0 < |d_0| < 300$ mm. Tracks with larger transverse impact parameter $|d_0|$ do not fulfil the cut on the generator level requiring at least four generated SpacePoints

in different layers of the silicon detectors. The efficiency of reconstructing a track versus the longitudinal impact parameter $|z_0|$ is around 99.8% for $|z_0| < 1200$ mm (bottom right plot). A combination of the fact that tracks from cosmic ray showers are typically limited to $|\eta| < 1.0$ in ATLAS and the requirement of generating at least four SpacePoints in different layers of the silicon detectors means that not many trajectories fulfil $|z_0| > 1200$ for the efficiency calculation in Equation (5.2). Overall, the efficiencies are uniform over the entire detector and no dependencies on the track parameters are observed.

The number of poorly matched or fake tracks is negligible for both New Tracking and CTBTracking.

5.1.2.2 Parameter resolutions

The resolution of a track parameter is defined as the width of its residual distribution

$$residual(\tau) = \tau_{true} - \tau_{reco}, \quad \tau \in \{d_0,\ z_0,\ \phi,\ \theta,\ q/p\}. \tag{5.3}$$

The resolutions are given as the width of a Gaussian function fitted to the residual distribution. In the following, the parameter resolutions of the five track parameters $d_0,\ z_0,\ \phi,\ \theta$ and q/p will be discussed for both NEWT and CTBTracking. Since both algorithms use the same fitter for the track parameter estimate, differences in the resolutions are due to differences in the track finding and the hit association.

b-layer hits	Si hits	TRT hits	$\lvert d_0 \rvert$ [mm]	p_{T} [GeV]
≥ 2	≥ 8	≥ 30	< 40	> 1

Table 5.1: Track selection cuts.

The reconstructed tracks have to fulfil the cuts described in Table 5.1. A tight cut of $|d_0| < 40$ mm is used to exclude tracks with larger impact parameters passing the pixel modules almost tangentially. This can lead to very broad clusters or cluster splitting, where the error description used in the track reconstruction is not accurate anymore. A direct comparison of the resolutions obtained in this study to the results presented in Section 5.1.4 from Reference [71] is not possible. The study presented in Section 5.1.4 measures the resolutions of collision-like tracks in the data by splitting the cosmic ray tracks into two, whereas this study measures the resolutions of the complete tracks in the Monte Carlo simulations. The resolutions of these two types of tracks are significantly different, since the complete tracks have more measurements to constrain the track fit and therefore have a better resolution.

Impact parameter resolutions

Figure 5.5 shows the resolutions of the transverse impact parameter d_0 (left) and the longitudinal impact parameter z_0 (right). NEWT and CTBTracking show almost identical results. The resolution of the transverse impact parameter d_0 varies between 13 μm for $p_{\mathrm{T}} < 5$ GeV and 6 μm for $50 < p_{\mathrm{T}} < 100$ GeV, whereas the resolution of the longitudinal impact parameter z_0 is constant around 50 μm over the full p_{T} range. The first analysis bin suffers from the limited statistics in the simulated Monte Carlo sample. The longitudinal impact parameter resolution is dominated by the intrinsic resolution of the pixel detector with 150 μm.

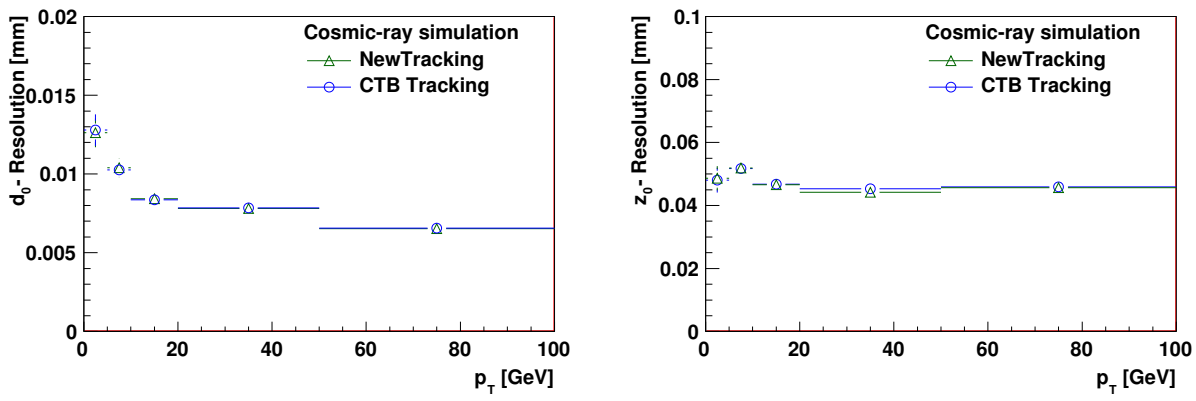

Figure 5.5: Impact parameter resolutions versus p_{T}: transverse (left) and longitudinal (right).

Angular parameter resolutions

The resolutions of the angular parameters ϕ and θ are shown in Figure 5.6 (left and right, respectively). The resolution of ϕ varies between 0.28 mrad for small and 0.03 mrad for large p_{T}, and the resolution of θ between 0.65 mrad and 0.3 mrad.

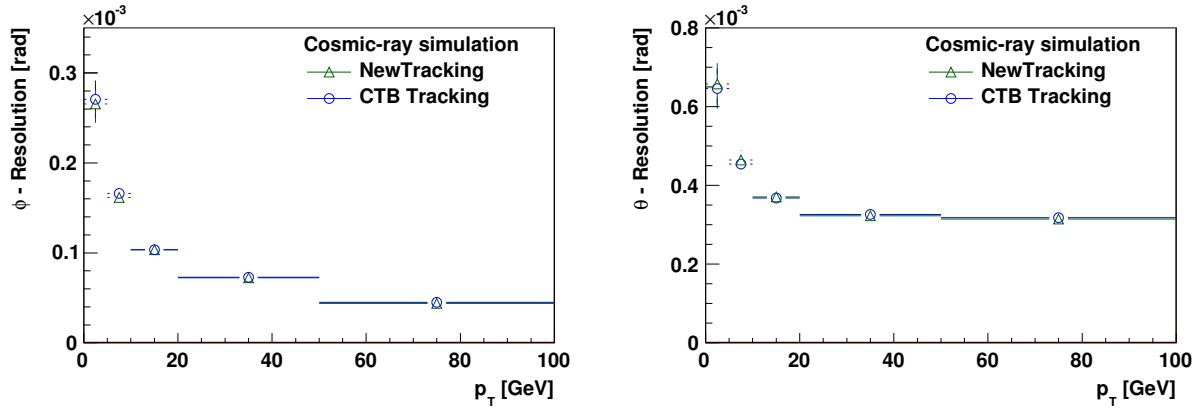

Figure 5.6: Angular parameter resolutions versus p_{T}: ϕ (left) and θ (right).

Momentum parameter resolution

The track reconstruction algorithms measure the inverse transverse momentum multiplied by the charge of the particle, q/p_{T}. The track parameter q/p is obtained by multiplying q/p_{T} by $\sin(\theta)$. Its resolution is presented in Figure 5.7 for both NEWT and CTBTracking, which ranges from $4 \cdot 10^{-3}$ GeV^{-1} for small p_{T} to $0.2 \cdot 10^{-3}$ GeV^{-1} for large p_{T} values.

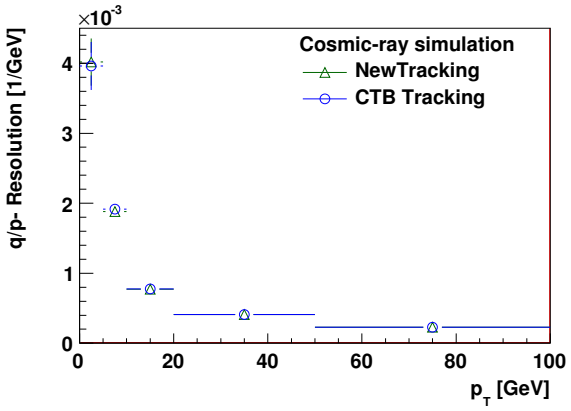

Figure 5.7: Momentum parameter resolution versus p_{T}.

Overall, New Tracking and CTBTracking show identical resolutions for cosmic ray trajectories.

5.1.2.3 Parameter error descriptions

A measure for the correct description of the intrinsic measurement errors and the accuracy of the applied material corrections in the track fit is the width of the pull distribution

$$pull(\tau) = \frac{\tau_{true} - \tau_{reco}}{\sigma_\tau}, \quad \tau \in \{d_0,\ z_0,\ \phi,\ \theta,\ q/p\}. \tag{5.4}$$

Ideally, the width of the pull distribution is one. For the track reconstruction in cosmic ray data, a conservative error of (pixel-cluster-width/$\sqrt{12}$) is assumed for the pixel measurements, which dominates the overall track parameter error. In the following, the pull widths of the five track reconstruction parameters $d_0,\ z_0,\ \phi,\ \theta$ and q/p are presented and discussed. The pull width is given as the width of a Gaussian function fitted to the pull distribution. The same track selection requirements are used as listed in Table 5.1.

Impact parameter pull widths

The pull widths for the impact parameters d_0 and z_0 are shown in Figure 5.8 (left respectively right). Both pull distributions show a width which is slightly smaller than one. The d_0 pull width ranges from 0.8 at small p_{T} to very close to unity at high p_{T}. The pull width for the

longitudinal impact parameter z_0 is quite constant around 0.9. This means that the track fits overestimate the errors for both parameters.

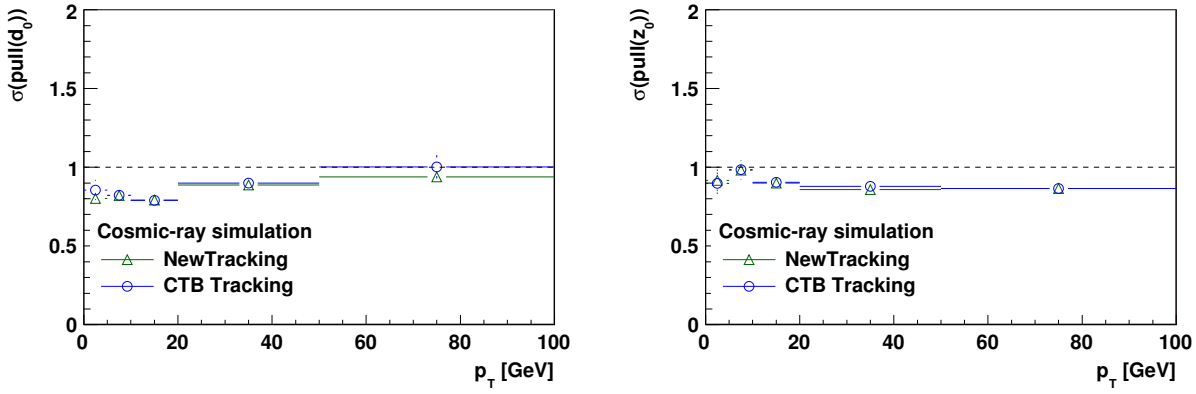

Figure 5.8: Pull distribution widths for the transverse impact parameter (left) and the longitudinal impact parameter (right) versus p_{T}.

Angular parameter pull widths

Figure 5.9 shows the pull widths for the angular parameters ϕ (left) and θ (right). The pull width for ϕ is very close to unity, whereas the pull width for θ shows a clear shift towards smaller values (around 0.8) for large values of p_{T}. As said before, this indicates that the errors evaluated in the track fits are overestimated.

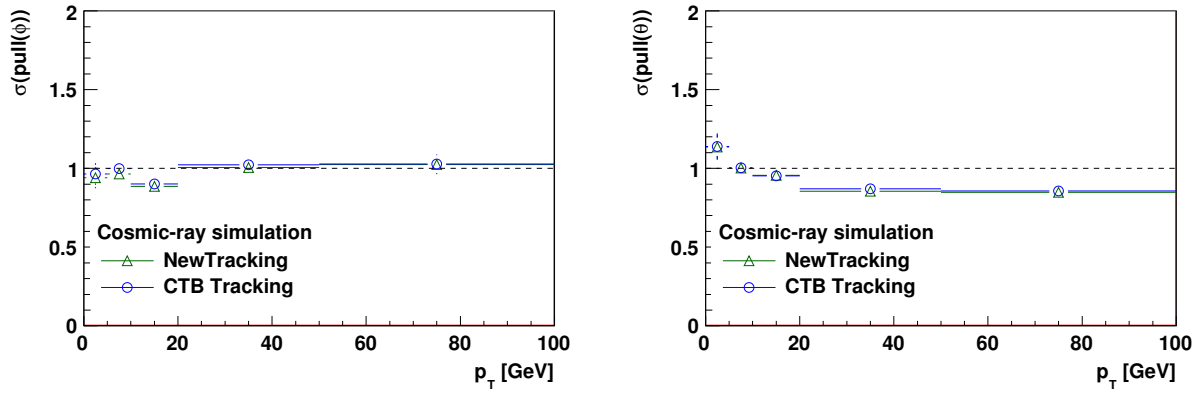

Figure 5.9: Width of the angular pull distributions versus p_{T}: ϕ (left) and θ (right).

Momentum parameter pull width

The width of the pull distribution for the inverse momentum q/p is shown in Figure 5.10. Unlike the pull distributions before, the pull width for q/p shows a bias towards large values: up to 1.4 for very small and very large transverse momenta and a minimum at 1.2 for

intermediate transverse momenta 10 GeV $< p_T <$ 20 GeV. This indicates that the errors for q/p are underestimated. This underestimation is due to the fact that during the track reconstruction, a very loose cut of 5σ is used in the TRT detector to distinguish between a precision hit on the track and a tube hit. A precision hit has a small error and larger contribution to the overall track error, whereas a tube hit obtains a larger error and therefore a smaller contribution to the track error. Having a large number of precision hits on the track (which is the case with a 5σ cut for tube hits) therefore underestimates the overall error of the momentum measurement.

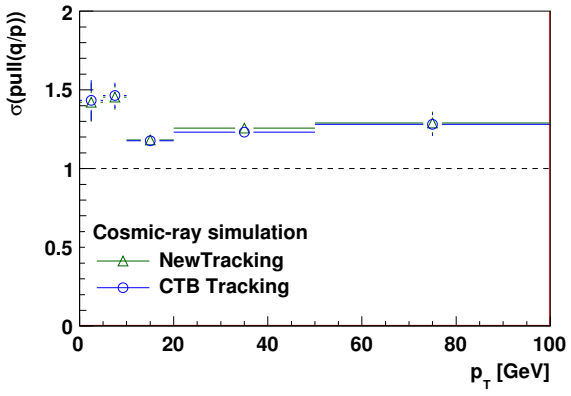

Figure 5.10: Width of the momentum pull distribution versus p_T.

5.1.3 Commissioning of New Tracking with Data from Cosmic Ray Showers

The validation study using Monte Carlo simulations in the section before showed that the adjusted NEWT sequence reconstructs efficiently and accurately trajectories from cosmic ray showers, and that it demonstrates identical performance compared to an algorithm which was specifically developed for this task. This is the prerequisite for the commissioning of New Tracking using the data from the global cosmic ray runs recorded in 2008 and 2009. Given the different sizes of the individual ATLAS subdetectors, the rate of cosmic ray events differs between about 700 Hz in the muon system and about 1 Hz in the pixel detector. A special trigger was deployed in this study, which selects cosmic ray events with a trajectory crossing the inner detectors (see Section 3.2.5.1). This section shows the track parameter and hit distributions of the NEWT sequence for the data from run 121330 in June 2009, compared to Monte Carlo simulations. More details on the reconstruction software setup can be found in Appendix A.1.

Slightly modified and looser cuts with respect to the studies presented in the section before were used to select the reconstructed tracks in both the data and the Monte Carlo simulations, as detailed in Table 5.2. The cut on $|d_0| < 40$ mm was replaced by the much looser requirement of the track to just traverse the pixel barrel detector. This is ensured by requiring at least 1 pixel hit and the longitudinal impact parameter $|z_0|$ to be smaller than

500 mm. The cut on the momentum was raised from 1 GeV to 5 GeV in order to be less sensitive to differences in the modelling of the trigger between the data and the Monte Carlo simulations.

Pixel hits	Si hits	TRT hits	$\lvert z_0 \rvert$ [mm]	p_{T} [GeV]
1	≥ 8	≥ 30	< 500	> 5

Table 5.2: Track selection cuts for the comparison of data and Monte Carlo simulations.

5.1.3.1 Track parameter distributions

The next two figures show the four track parameters p_{T}, η, d_0 and z_0 and the number of hits on the tracks. The data is represented by filled triangles and the Monte Carlo simulations by filled histograms. All distributions are normalised to unity area.

Figure 5.11 shows the distributions of the track parameters p_{T} (upper left), η (upper right), d_0 (lower left) and z_0 (lower right) for data and Monte Carlo simulations. Overall, a good agreement can be observed between the data and the simulation. The spectrum

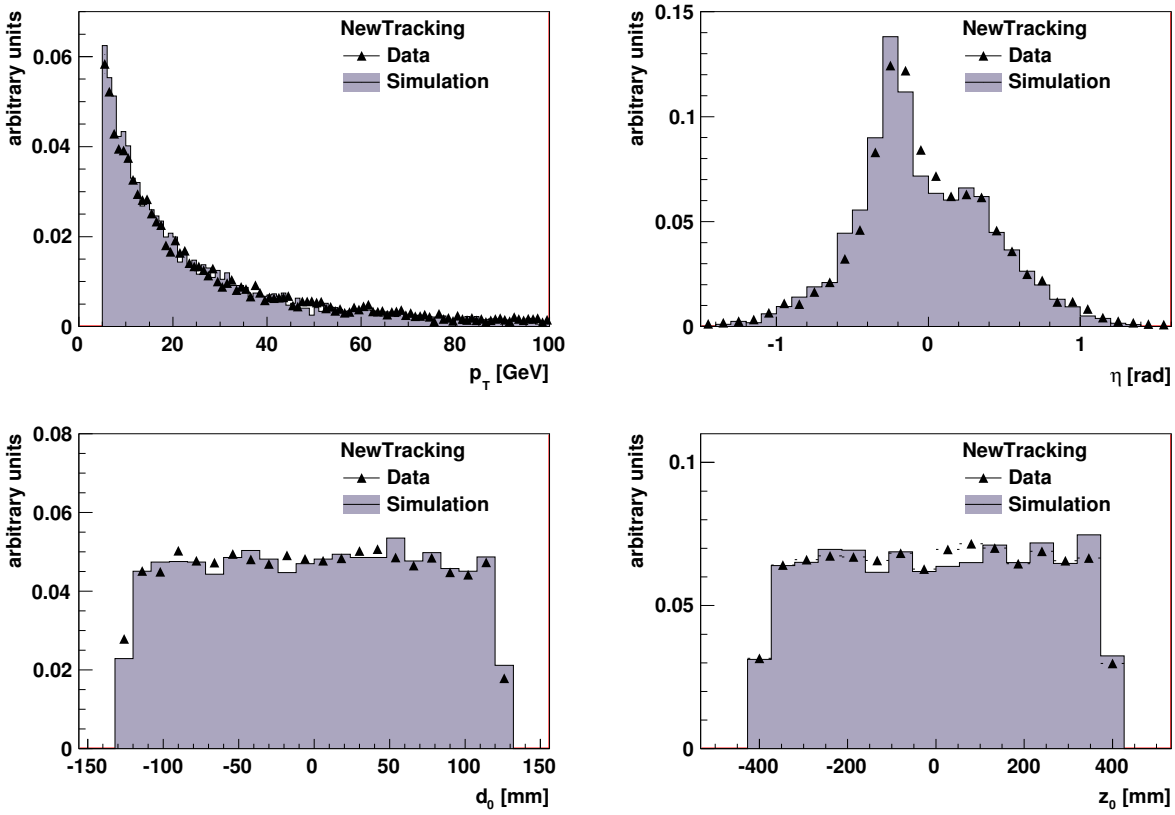

Figure 5.11: Track parameter distributions for data (triangles) and Monte Carlo simulation (filled histograms). All distributions are normalised to unity area.

of the transverse momentum p_{T} shows a steeply falling distribution towards large values for both data and Monte Carlo simulation. A cut of $p_{\mathrm{T}} > 5$ GeV was applied in the track selection to avoid trigger effects: the rate of cosmic muons which are triggered during data taking is reduced for lower momenta, an effect which is not taken into account in the Monte Carlo simulations. The agreement between the data and the simulation is very good. The η spectrum shows two peak structures at $\eta \approx -0.3$ and $\eta \approx +0.3$ and falling edges towards larger eta values. The two peaks are due to the construction shafts through which the ATLAS detector was lowered into the experiment cavern. The discrepancy around $\eta \approx 0$ is due to the fact that the two shafts housing the elevators which lead into the detector cavern are not simulated. The lower two plots in Figure 5.11 show the distributions of the impact parameters d_0 and z_0. The distribution of the transverse impact parameter d_0 shows a plateau between -120 mm $< d_0 < 120$ mm with very steeply falling edges. This behaviour is due to the fact that the radius of the last pixel barrel layer is 122.5 mm. In combination with the requirement to have at least one pixel hit on the track, this forms a natural limit for the transverse impact parameter. The longitudinal impact parameter z_0 shows a constant value over the length of the pixel barrel and falls very steeply towards its edge at 400.5 mm. The cut of $|z_0| < 500$ mm removes the tracks passing through the endcap disks.

Figure 5.12 presents the number of hits on the reconstructed tracks in the pixel (upper left), SCT (upper right) and TRT detectors (lower left). The number of missing hits on the tracks ("holes") is shown in the lower right. The number of pixel hits on the tracks shows a very good agreement between the data and the simulation. Small differences are visible in the distribution of SCT hits on the tracks. They are due to the fact that some of the modules which were disabled during data taking[1] were not disabled in the simulation. The bottom left plot shows the number of TRT hits on the tracks. The Monte Carlo simulation underestimates the number of TRT hits on the tracks significantly. This effect is caused by an inaccurate modelling of the drifttime distribution in the TRT simulation, and is improved in later Monte Carlo simulation samples. The number of holes on the tracks (i.e. active detector layers that were crossed by the track but did not contribute to it with a measurement) is calculated by the hole search tool (see Section 5.1.1.4). This number is an indicator for either imperfections in the pattern recognition, detector inefficiencies or detector misalignments. The distribution of holes on the tracks in Figure 5.12 shows that approximately 85% of the tracks in the data do not have any holes. In combination with the very high intrinsic hit detection efficiencies in the pixel and SCT detectors of $(99.974 \pm 0.004(\mathrm{stat}) \pm 0.003(\mathrm{syst}))\%$ and $(99.78 \pm 0.01(\mathrm{stat}) \pm 0.01(\mathrm{syst}))\%$ [71] respectively, this hints at remaining detector misalignments which are large enough to prevent the pattern recognition to attach a small number of hits to the tracks. The larger number of holes in the simulation compared to the data is due to the fact that in the simulation, a random hit inefficiency of 1% was assumed in both the pixel and the SCT detectors. It is now clear that this number is too large and does not reflect the measured hit efficiencies in both detectors.

[1] 2.3% of SCT modules (92 out of 4088) were disabled during the analysed run.

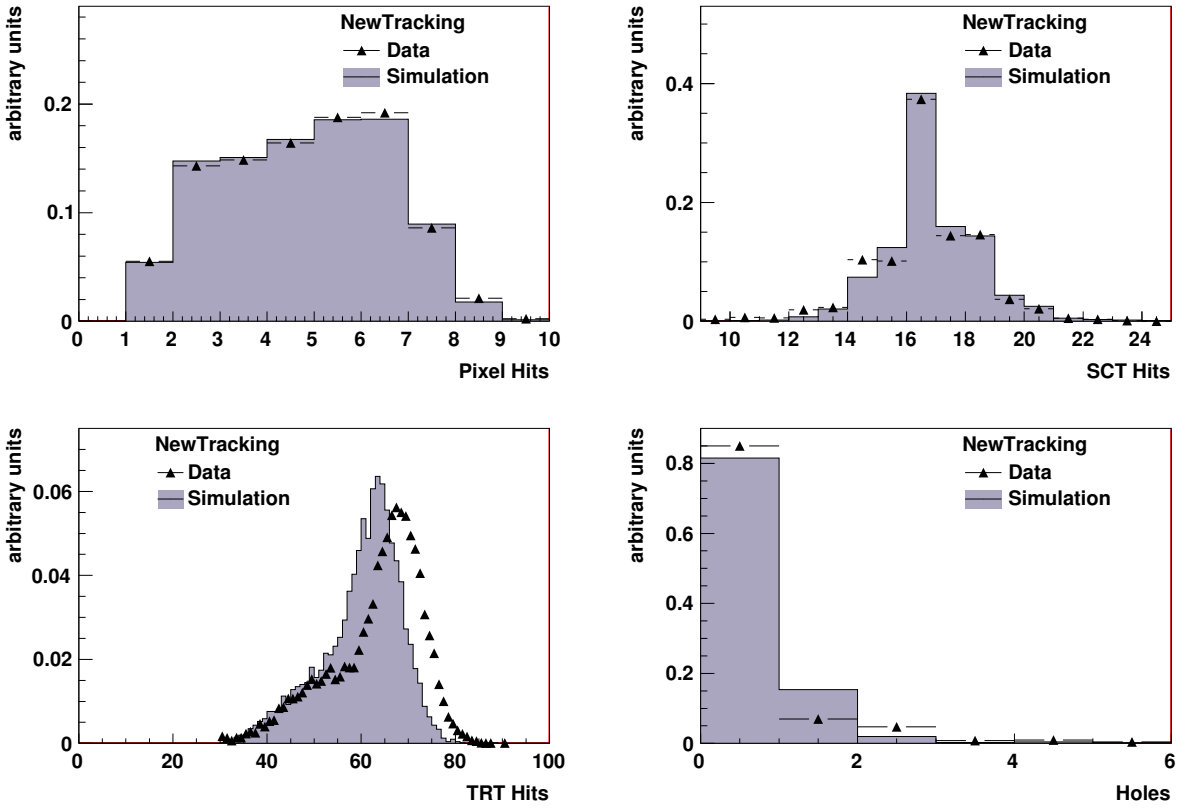

Figure 5.12: Number of hits and holes on the tracks for data (triangles) and Monte Carlo simulation (filled histograms). All distributions are normalised to unity area.

5.1.3.2 Successful track extension into the TRT

The inside-out track reconstruction can be divided into two major steps: first the pattern recognition in the silicon detectors and then the extension of the tracks into the TRT detector. Section 5.1.2.1 presented the efficiency of the first step; in this section, the efficiency to find an extension of the silicon track into the TRT is discussed. The results are presented in Figure 5.13. The plots show the efficiency to find an extension of the silicon-only track into the TRT (either on one side or on both sides) versus the transverse momentum p_{T} (left) and the pseudorapidity $|\eta|$ (right) of the track. In order to be less sensitive to statistical fluctuations, the minimal number of entries for both plots is 500.

The efficiency versus p_{T} is above 99.4% for both data and Monte Carlo simulation. A clear dependency is visible versus $|\eta|$. The drop in efficiency for $|\eta| > 0.5$ in data is due to remaining misalignment effects in the TRT endcaps. The agreement in the barrel between the data and the simulation is excellent.

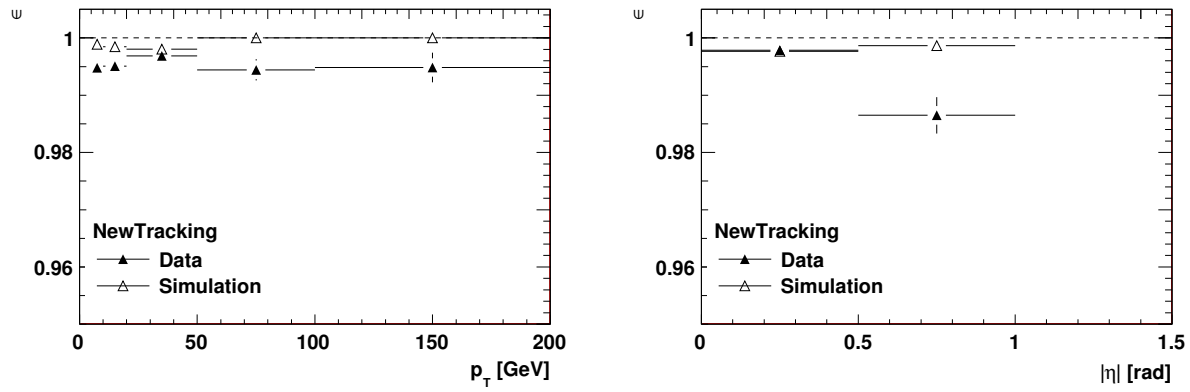

Figure 5.13: Successful track extension into the TRT detector for data and Monte Carlo simulation versus p_{T} (left) and $|\eta|$ (right).

5.1.3.3 Momentum measurement uncertainty

Figure 5.14 shows the track momentum p multiplied by the error of q/p as estimated by the track reconstruction algorithm, $p \cdot \sigma(q/p)$, in the data and the Monte Carlo simulation for both silicon-only tracks (circles) and tracks successfully extended into the TRT (triangles). The simulation is represented by open symbols, and the data by filled ones. It is clearly visible that the extended tracks have a much smaller momentum uncertainty than the silicon-only tracks. This is due to the longer track length in the TRT detector which allows to measure the momentum with higher precision. It is also clearly visible that the simulation shows a better momentum uncertainty (up to a factor of 2) compared to the data from June 2009. This is due to remaining misalignments in the inner detectors.

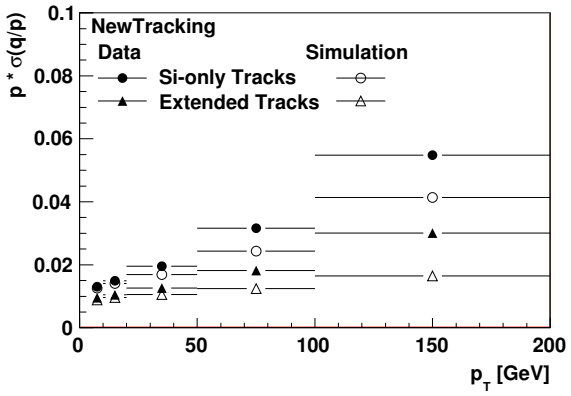

Figure 5.14: Momentum uncertainty $p \cdot \sigma(q/p)$ in data and Monte Carlo simulations.

5.1.4 Impact Parameter Resolution of collision-like Tracks

The impact parameter resolution of collision-like tracks from cosmic ray data was studied using the "split-tracks" method [71]. In the split-tracks method, cosmic ray tracks which traverse the detector from top to bottom are split into two halves; the two new tracks

are fitted individually, each track containing the hits from the upper or lower half of the detector only. To determine the track parameter resolution, pairs of split tracks are selected where both split tracks are required to have at least 2 pixel, 6 SCT and 25 TRT hits and a transverse momentum $p_{\mathrm{T}} > 1$ GeV. The transverse impact parameter $|d_0|$ has to be less than 40 mm to ensure that the tracks traverse the interaction region inside the ATLAS detector. To extract the track parameter resolution, the difference Δ between the track parameter of the upper and the lower split track is calculated. The resolution of the track parameter is given by the root mean square of the Δ distribution divided by $\sqrt{2}$. Figure 5.15 shows the transverse impact parameter resolution (left) and longitudinal impact parameter resolution (right) of collision-like tracks from cosmic ray events [71]. Full inner detector tracks (solid triangles) and silicon-only tracks (open triangles) from the data are compared to full inner detector tracks from the Monte Carlo simulation. A good agreement of the transverse impact parameter resolution between the data and the simulation can be observed for small transverse momenta, for larger transverse momenta $p_{\mathrm{T}} > 10$ GeV remaining misalignments in the detector worsen the impact parameter resolution in the data. The full inner detector tracks have a slightly better resolution compared to the silicon-only tracks. This is contributed to the fact that the TRT measurements on the full tracks improve the momentum resolution and thus the precision of the track extrapolation to the interaction region. The longitudinal impact parameter resolution shows a good agreement between the data and the simulation over the full p_{T}-range.

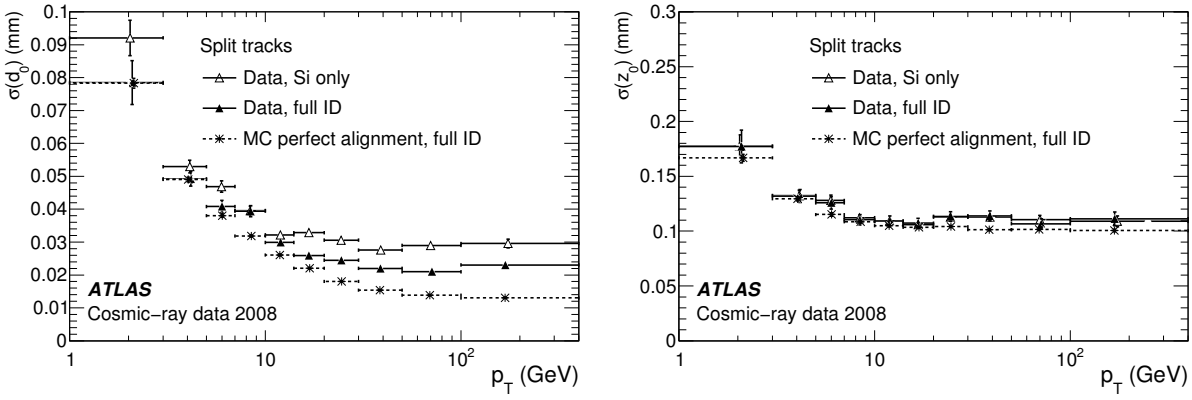

Figure 5.15: Transverse impact parameter resolution (left) and longitudinal impact parameter resolution (right) of collision-like tracks from cosmic ray events. Full inner detector tracks (solid triangles) and silicon-only tracks (open triangles) from the data are compared to full inner detector tracks from the Monte Carlo simulation. From Reference [71].

5.2 Validation of New Tracking at the Start-up of the LHC

5.2.1 Reconstruction Robustness in case of Detector Failures

This study presents the robustness of the track reconstruction software in the event of a catastrophic failure of large fractions of the SCT detector, which was carried out in 2008 in preparation for the first proton-proton collisions. These failures can arise due to problems with the read-out or detector cooling systems of the SCT detector and can cause whole sections of the detector, several or all layers, not to be operational during data taking. In the event of such a failure, the efficiency of the New Tracking inside-out track reconstruction sequence goes down to almost zero. Several changes were needed in the track reconstruction software to recover this inefficiency.

The main cause for the inefficiency in the event of a catastrophic SCT detector failure lies in one of the basic track reconstruction quality requirements, namely a cut which is placed on the minimal number of seven silicon measurements on the track. With only the pixel measurements available, this requirement cannot be met by the tracks. To overcome this problem, the software needed to be modified to adjust this cut dynamically, depending on the presence of inactive detector modules on the track. The knowledge about non-operational modules during the data taking is present in the offline reconstruction framework Athena through one of the Athena services, the conditions service, and was already used by the hole search tool. The hole search tool counts the number of active detector elements which were crossed by a track but which did not contribute to the track with a measurement. The tool also counts the number of inactive detector elements $N_{inactive}$ that were crossed by the track between the first and last silicon measurement. Although present, this knowledge was not used during the track reconstruction. Two main changes were introduced in the reconstruction software: to use the knowledge about $N_{inactive}$ consistently throughout the track reconstruction to adjust the requirement on the minimal number of measurements on the track, $N^{effective}_{min\ cluster} = N_{min\ cluster} - N_{inactive}$, and to adjust the hole search tool to search for inactive detector elements also after the last silicon measurement on the track.

Figure 5.16 shows the comparison of the track reconstruction before and after the software changes. Pythia Monte Carlo simulations of top-antitop events were used for the validation. The track reconstruction efficiencies for track seeds (upper left), resolved tracks after the ambiguity solving (upper right) and the rate of misreconstructed tracks (lower plot) are presented. In light green, the track reconstruction using the perfect detector is shown and in dotted red the modified track reconstruction software using a detector with a full SCT barrel failure. The results of the track reconstruction for this case before the software modifications is not shown since it shows a negligible efficiency in the barrel. In dark green and dashed, the modified track reconstruction is shown using a fully operational detector. The adjusted track reconstruction software recovers most of the inefficiencies in case of a catastrophic

SCT failure at the cost of a much higher rate of misreconstructed tracks. The loss of 10% efficiency with respect to the nominal case is caused by the reduced number of measurements which are available for the track reconstruction. In the case of a perfect detector, neither the reconstruction efficiency nor the rate of misidentified tracks are changed by the modifications.

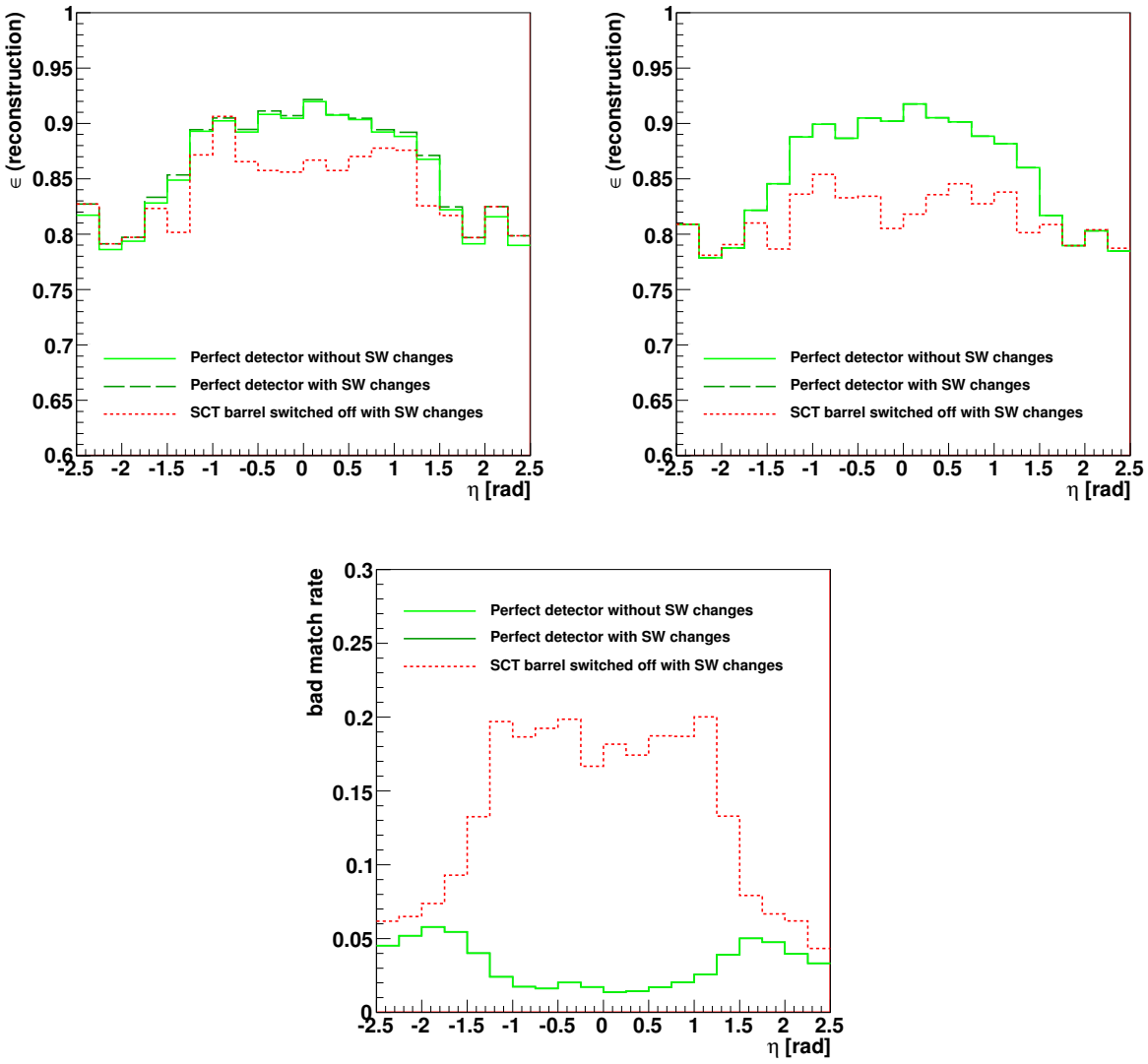

Figure 5.16: Track reconstruction efficiencies for track seeds (upper left) and resolved tracks after ambiguity solving (upper right) as well as the rate of misreconstructed tracks (lower plot). In light green, the track reconstruction using a perfect detector is shown and in dotted red, the modified track reconstruction using a detector where the full SCT barrel failed. The track reconstruction for this case before modifications is not shown; it would show a negligible efficiency in the barrel. In dark green and dashed, the modified track reconstruction is shown using a fully operational detector.

5.2.2 Track Reconstruction in First Collisions at $\sqrt{s} = 900$ GeV

On December 6$^{\text{th}}$, 2009, ATLAS recorded the first collisions at a centre-of-mass energy of 900 GeV with the "Stable Beams" flag being declared by the LHC for the first time. This meant that the silicon detectors could be used at their nominal operating point for the first time during collisions data taking. Figure 5.17 shows one of the very first collision events from this day where all inner detectors were fully operational [72].

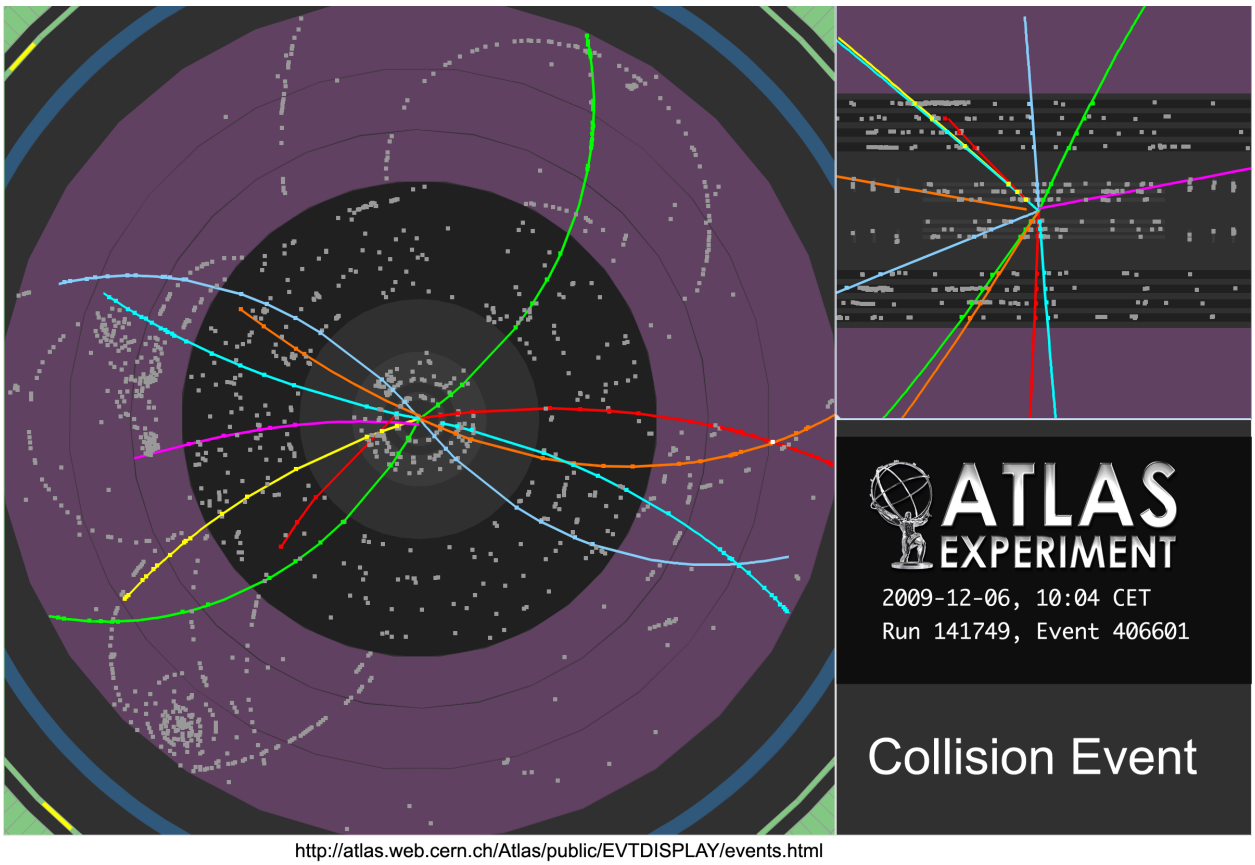

Figure 5.17: One of the first collision events recorded by ATLAS at $\sqrt{s} = 900$ GeV where all inner detectors were fully operational (6$^{\text{th}}$ December 2009), from Reference [72].

In the following, very first results from run 141811 taken on December 6$^{\text{th}}$, 2009, are presented. The run contained 457 953 events, but only a subset of these events were analysed. Figure 5.18 shows a scatter plot [73] in the $x - y$ plane of all hits on the tracks in the pixel (green), SCT (red) and TRT detectors (blue). The three respectively four barrel layers in the pixel and SCT detectors are clearly distinguishable as well as the many straw hits per track in the TRT detector.

The number of tracks per event and basic track parameter distributions such as the transverse momentum p_{T}, η and ϕ are presented in Figure 5.19. The data is compared to a sample of fully simulated Minimum Bias events (filled histograms) as described in Appendix A.2, which have been normalised to the data. Within statistical errors, the

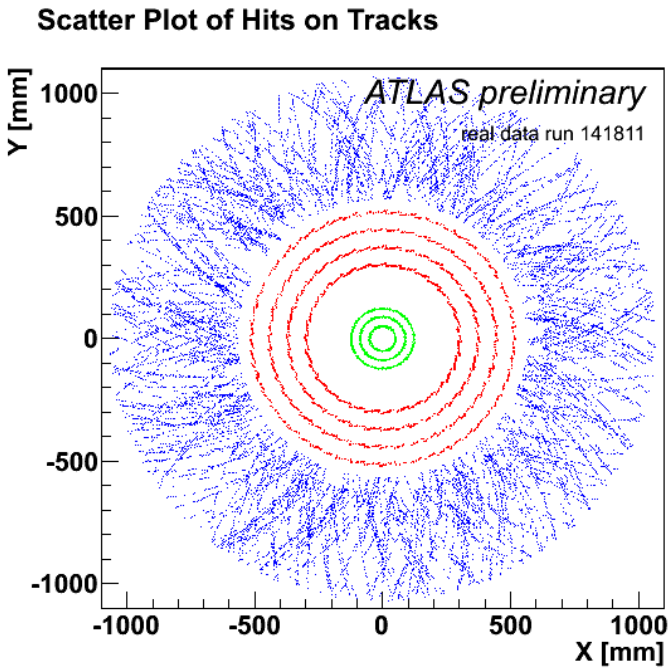

Figure 5.18: First collision tracks in the inner detectors at $\sqrt{s} = 900$ GeV.

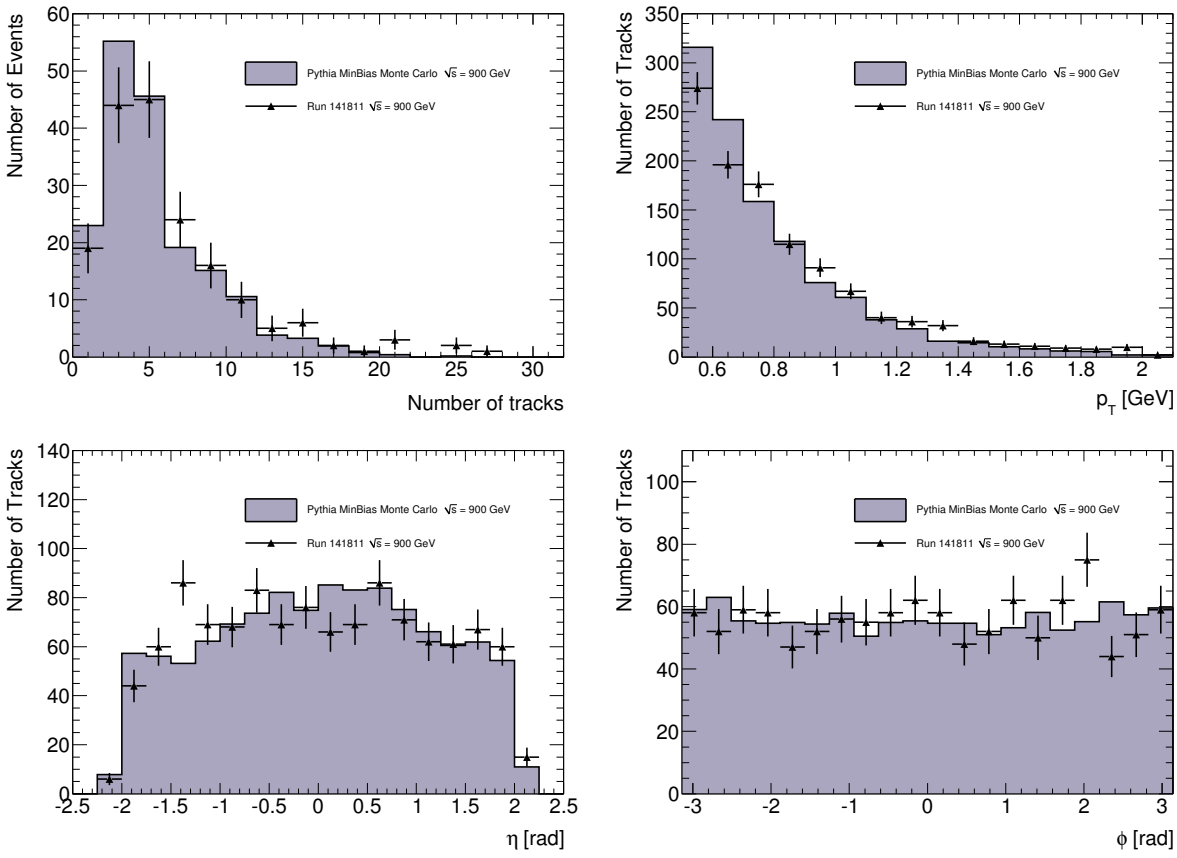

Figure 5.19: Number of tracks (upper left), transverse momentum p_{T} (upper right), η (lower left) and ϕ (lower right) distributions of tracks from run 141811.

agreement between the data and the Monte Carlo simulations is very good, which is a first indicator for a good track reconstruction performance.

Figure 5.20 shows the number of pixel, SCT and TRT hits on the tracks as well as the number of missing detector hits (holes). A very good agreement can be observed between the data and the simulation for the number of pixel and SCT hits on the tracks. In the TRT detector, the data shows a slight shift towards a larger number of hits on the tracks. The same effect has been observed in the comparison of the data and the Monte Carlo simulation from cosmic ray events in Figure 5.12. This is caused by an inaccurate modelling of the drifttime distribution in the TRT simulation, which was corrected in the following simulation version (see Figure 5.24). The simulation shows a slightly higher number of holes on the tracks in Figure 5.20 (lower right) than the data. This is due to the fact that the simulation assumes a random inefficiency in the silicon detectors which is slightly too high. This has been adjusted in later Monte Carlo simulations as well.

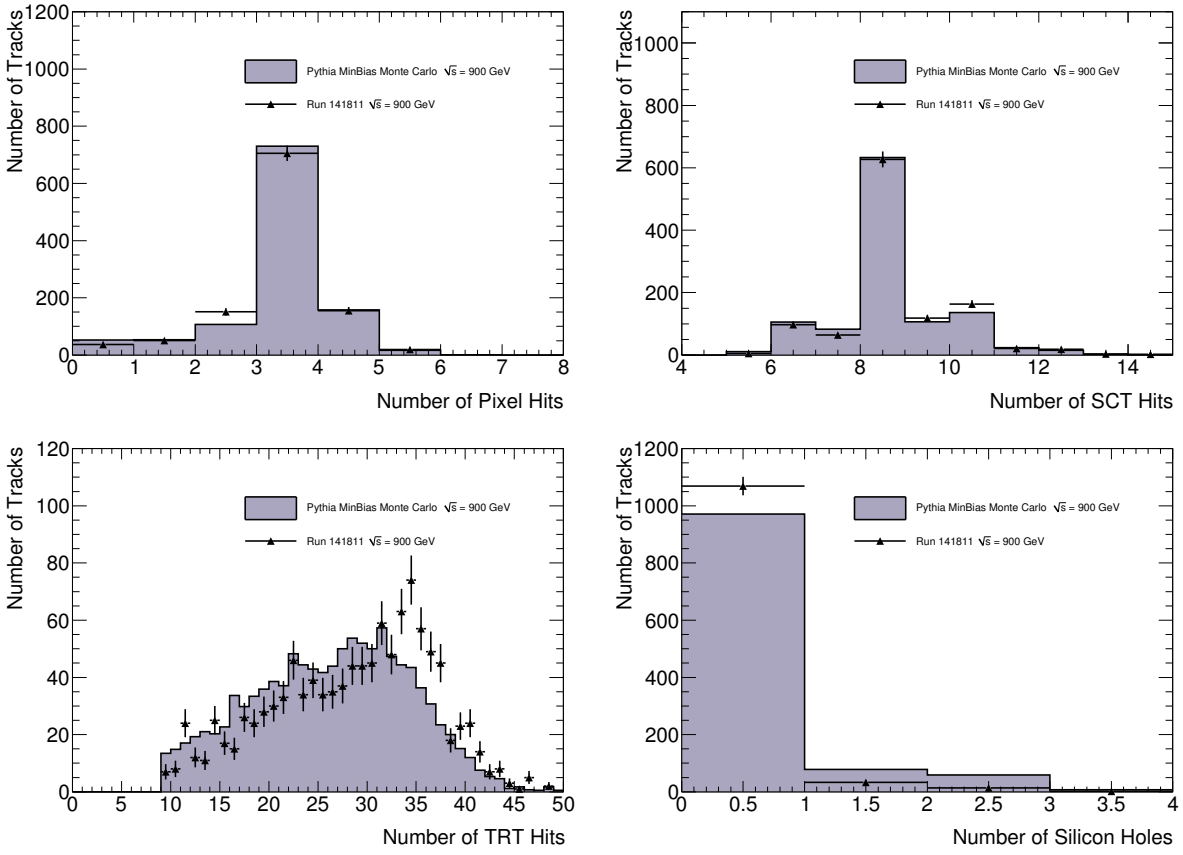

Figure 5.20: Number of pixel (upper left), SCT (upper right) and TRT (lower left) hits on the tracks as well as the number of missing detector hits on the tracks (lower right) from run 141811.

5.3 Commissioning of New Tracking at $\sqrt{s} = 7$ TeV

After a thorough phase of commissioning the LHC at a centre-of-mass energy of 900 GeV, the first collisions at $\sqrt{s} = 7$ TeV were produced on March 30$^{\text{th}}$, 2010. Figure 5.21 shows one of the first collision events in ATLAS at this energy where the entire inner detector was fully operational. In the following months, the track reconstruction was studied in great detail at this highest centre-of-mass energy. This section presents a study focusing on the track parameters which are of special interest for the identification of jets originating from b-quarks (b-tagging). Impact-parameter- and vertexing-based b-tagging algorithms rely on precisely measured trajectories to distinguish between the particles coming from the primary event vertex and others coming from a displaced b-hadron decay vertex. A good resolution of the primary vertex reconstruction and the transverse impact parameter as well as a good agreement between the data and the Monte Carlo simulation are crucial. The results of this study are documented as a conference note [74] and were in parts presented at the 35$^{\text{th}}$ International Conference of High Energy Physics [75].

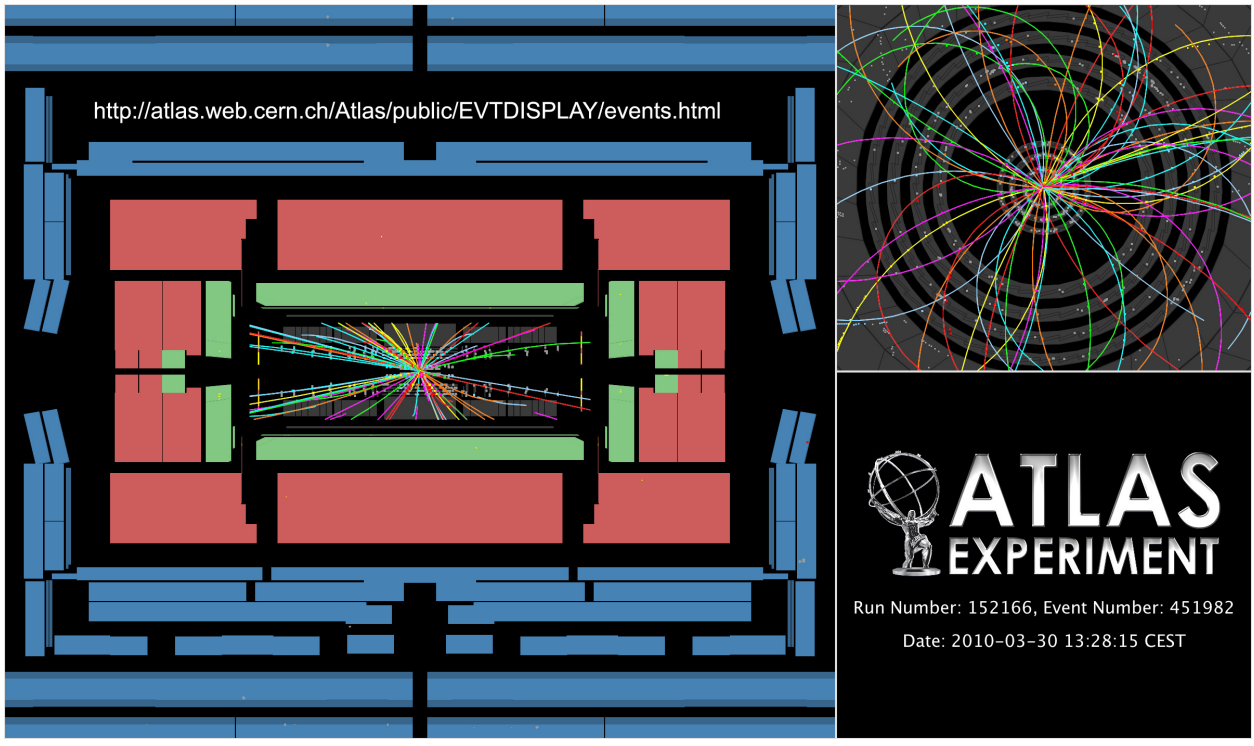

Figure 5.21: One of the first collision events recorded by ATLAS at $\sqrt{s} = 7$ TeV where all inner detectors were fully operational (30$^{\text{th}}$ March, 2010), from Reference [76].

5.3.1 Data Sample and Event Selection

The analysis is based on a sample of proton-proton collisions at $\sqrt{s} = 7$ TeV collected between March and June 2010 and reconstructed with a consistent reconstruction software setup. The

data sample corresponds to an integrated luminosity of about 15 nb^{-1}. The jet trigger `L1_J5` as introduced in Section 3.2.5.1 was used to select the events. At the analysis level, at least one jet with $p_{\text{T}}^{jet} > 20$ GeV per event is required. The jet energy is calibrated to the hadronic jet energy scale using the procedure detailed in Section 4.4.4.

The data is compared to QCD Monte Carlo simulations generated by the Pythia event generator [9] as detailed in Appendix A.3. The QCD samples are also referred to as "Dijet" samples in the following. Both the data and the Monte Carlo simulations were reconstructed with the same version of the ATLAS reconstruction software, using improved alignment constants and a more precise cluster error description in the inner detectors. In particular, the cluster errors used for the early commissioning of the inner detectors at $\sqrt{s} = 900$ GeV were based on very broad errors, reflecting a uniform distribution corresponding to the size of the cluster considered, while the new error description makes use of a more complete parameterisation of the errors as a function of the track azimuthal incidence angle and of the cluster size. The simulated geometry corresponds to a perfectly aligned detector.

Only data collected during stable beam periods in which the silicon systems were operated at full depletion voltage are used. Each event is required to have a reconstructed primary vertex with at least ten tracks, while events with one or more additional reconstructed primary vertices with more than four tracks are removed from the sample to reduce the influence of pile-up. A data sample of 2.5 million events was obtained.

5.3.2 Properties of the Primary Event Vertex

The properties of the primary event vertex are presented in this section. The number of primary vertices is shown in Figure 5.22 (left). The data (solid black dots) is compared to the Monte Carlo simulation (plain histograms), which is normalised to the data. A fairly good agreement between the data and the Monte Carlo simulation can be observed. The position of the primary vertex along the beam axis is shown in the same figure (right), which shows significant discrepancies between the data and the simulation. The longitudinal position of the interaction point can influence some properties of the tracks, for example the number of hits on the tracks in the pixel or SCT detectors. A weighting technique is therefore deployed, which reweighs the z-position of the primary vertex in the Monte Carlo simulation to the corresponding distribution measured in the data. This technique will be used throughout the thesis.

The primary event vertex is identified by choosing the reconstructed vertex with the highest $\sum_{i=1}^{n_{\text{tracks}}} p_{\text{T},i}^2$. The square root of this distribution for the primary event vertex, $\sqrt{\sum p_{\text{T}}^2}$, is presented in Figure 5.23 (left). The number of tracks associated to the primary vertex is shown in Figure 5.23 (right). A significant disagreement is visible between the data and the

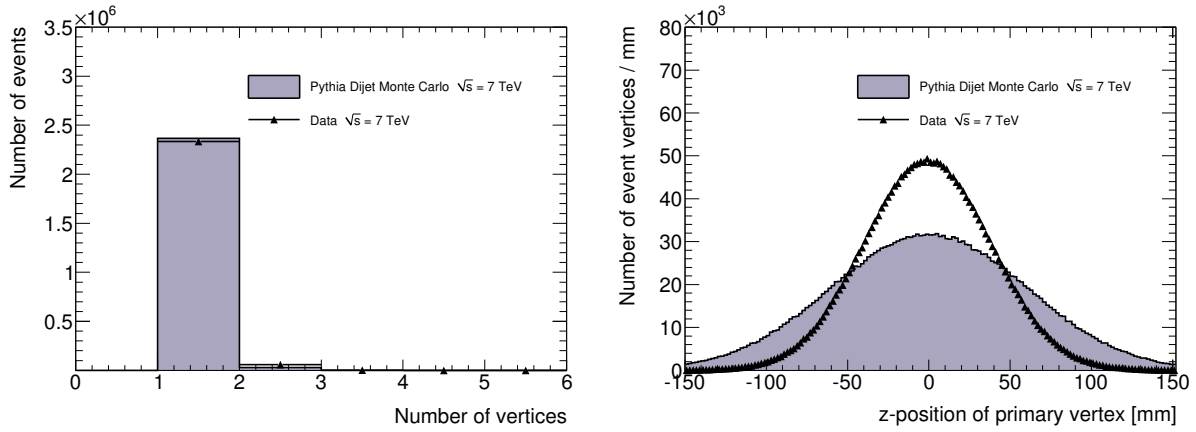

Figure 5.22: Number of reconstructed vertices (left) and the z-position of the primary event vertex (right) at $\sqrt{s} = 7$ TeV. The data (solid black dots) is compared to the Monte Carlo simulation (plain histograms), which is normalised to the data.

simulations. This disagreement points to an incorrect description of the number of primary particles in the simulation, especially at low p_{T}. This was also reported elsewhere [77].

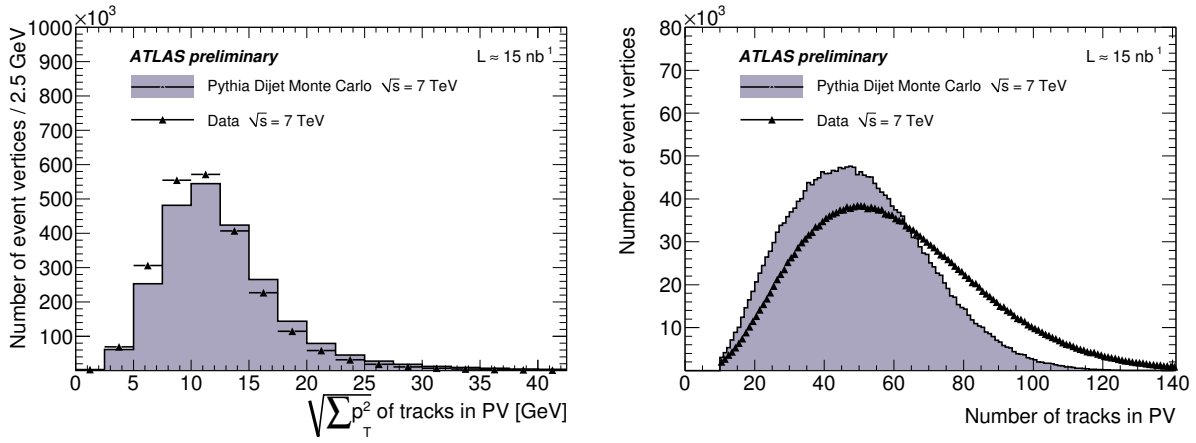

Figure 5.23: Distribution of the $\sqrt{\sum p_{\mathrm{T}}^2}$ from all tracks associated to the primary event vertex (left) and number of associated tracks (right). The data (solid black dots) is compared to the Monte Carlo simulation (plain histograms), which is normalised to the data.

5.3.3 Track Selection and Track Properties

The tracks reconstructed in the ATLAS inner detectors are the main ingredient for b-tagging. In the following, only tracks reconstructed by the inside-out approach of the NEWT track reconstruction are used. They are not required to have hits in the TRT.

5.3.3.1 Baseline track selection

The track selection for b-tagging [58] is designed to select well-measured tracks and reject fake tracks and tracks from long-lived particles (K^0_S, Λ or other hyperon decays) and material interactions (photon conversions or hadronic interactions). At least seven precision hits (pixel or micro-strip hits) are required in the silicon detectors. In addition, at least two hits in the pixel detector are required, of which at least one must be in the innermost layer. A successful extension of the track into the TRT detector is not explicitly required, but is fulfilled by most tracks within its acceptance. The transverse and longitudinal impact parameters computed with respect to the primary vertex must fulfil $|d_0| < 1$ mm and $|z_0 \sin\theta| < 1.5$ mm respectively, θ being the track polar angle. Only tracks with $p_{\mathrm{T}} > 1$ GeV are considered. The total number of tracks after these cuts is about 23 million. The following results use this selection, unless mentioned otherwise when it was mandatory to relax some of the criteria to study a particular effect.

5.3.3.2 Overall hit patterns

The patterns of hits on the tracks were studied using the data and are compared to Monte Carlo simulations. The distribution of the total number of pixel hits on the tracks is shown in Figure 5.24 (upper left) along with the distribution of the number of hits in the first pixel layer (upper right). The measurement in the first pixel layer dominates the resolution of the impact parameter of the track and is therefore essential for b-tagging. Figure 5.24 also shows the distribution of the number of hits in the SCT (lower left) and TRT (lower right) detectors on the tracks. The Monte Carlo simulations in all four hit distributions are normalised to the data, which they describe very well. The small discrepancies in the number of SCT hits on the tracks are due to different module configurations in the endcaps between the data and the simulations. The distribution of the TRT hits on the tracks shows a good agreement between the data and the Monte Carlo simulations. The discrepancies which were observed earlier in this distribution, caused by an inaccurate modelling of the drifttime in the TRT simulation, are resolved.

5.3.3.3 Track parameter distributions

Figure 5.25 shows the distributions of the basic track parameters η (upper left), ϕ (upper right) and the transverse momentum p_{T} (lower plot) in collisions at $\sqrt{s} = 7$ TeV. The overall agreement between the data and the Monte Carlo simulation is very good, but a slight excess of tracks in the data can be observed at low transverse momenta compared to the Monte Carlo predictions. The two dips in the ϕ distribution are due to disabled modules in the pixel b-layer.

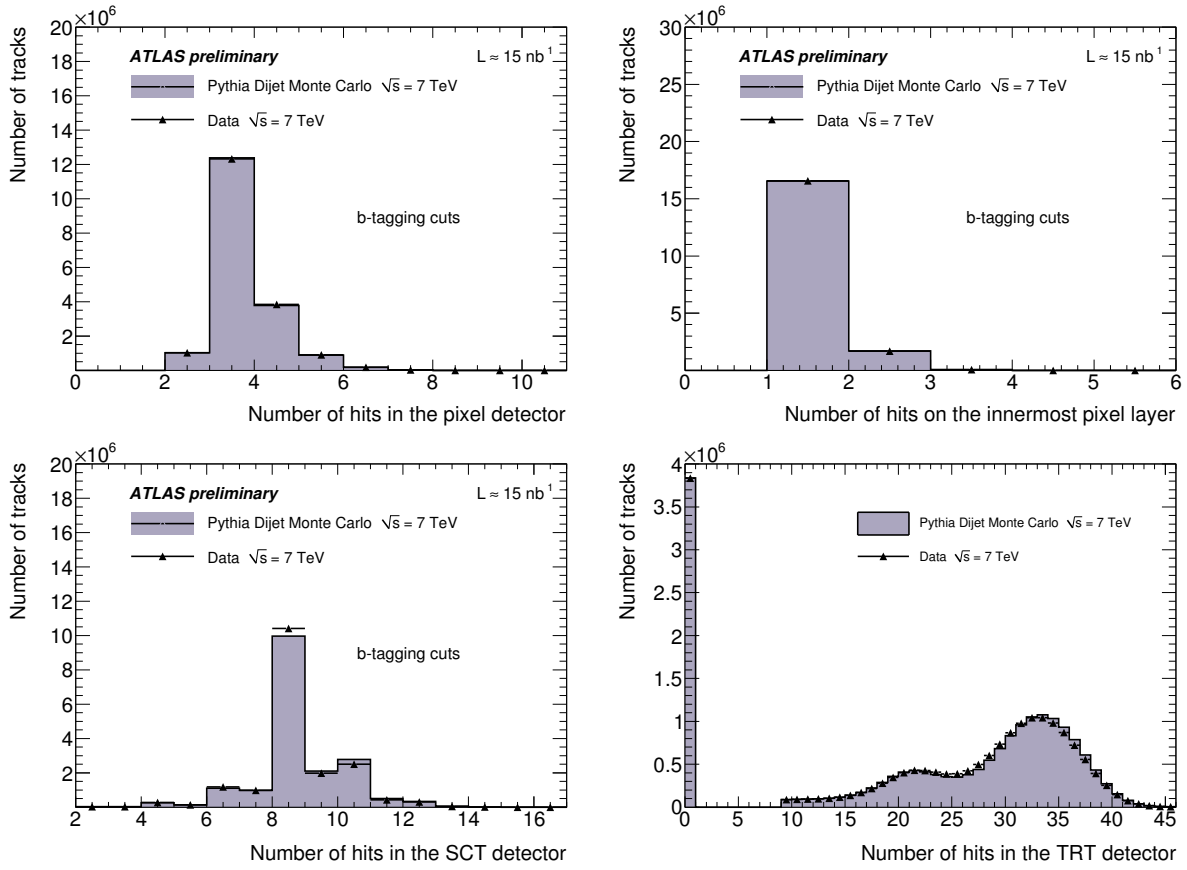

Figure 5.24: Distribution of the number of hits on the tracks in the pixel detector (upper left), the innermost pixel layer (upper right), the SCT (lower left) and the TRT detector (lower right), for tracks fulfilling the b-tagging quality cuts. The data (solid black dots) is compared to the Monte Carlo simulation (plain histogram), which is normalised to the data.

5.3.4 Transverse Impact Parameter Resolution

5.3.4.1 Transverse impact parameter distributions

The transverse impact parameter of a track, d_0, which is the distance of closest approach in the transverse plane from the track to the primary event vertex, is a key-ingredient for discriminating tracks originating from displaced vertices from tracks originating from the primary event vertex.

The distribution of the transverse impact parameter d_0 of tracks fulfilling the b-tagging quality cuts is shown in Figure 5.26 (left) along with its pull d_0/σ_{d_0} (right). The distance d_0 is measured with respect to the primary event vertex in an unbiased way: if the track under consideration was used for the reconstruction of the primary event vertex, it is removed from the primary vertex which is subsequently refitted, and the d_0 is computed with respect to this new vertex. The simulated distribution of d_0 is slightly narrower compared to the data, but overall the agreement is good. It should be noted that the d_0

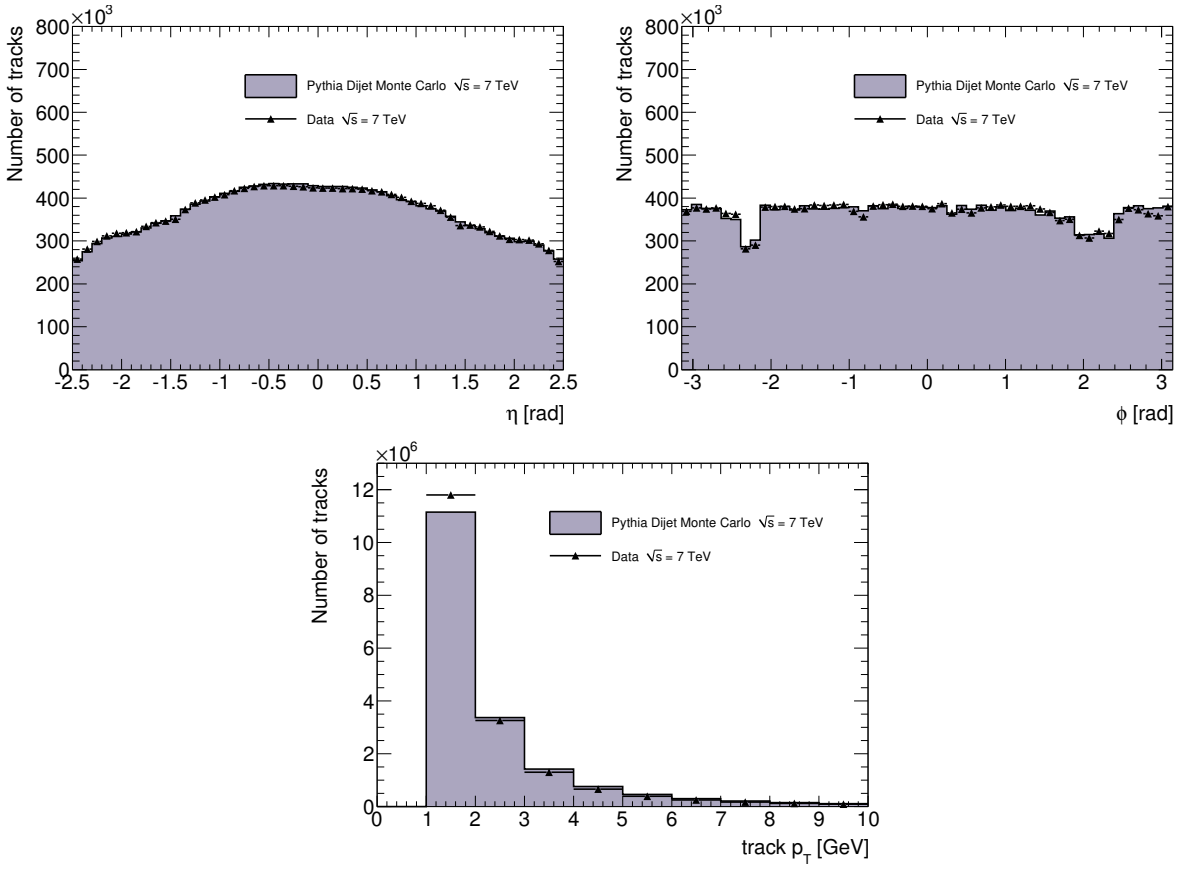

Figure 5.25: Track parameters in collisions at $\sqrt{s} = 7$ TeV: η (upper left), ϕ (upper right) and the transverse momentum p_{T} (lower plot). The two dips in the ϕ distribution are due to disabled b-layer modules. The data (solid black dots) is compared to the Monte Carlo simulation (plain histogram), which is normalised to the data.

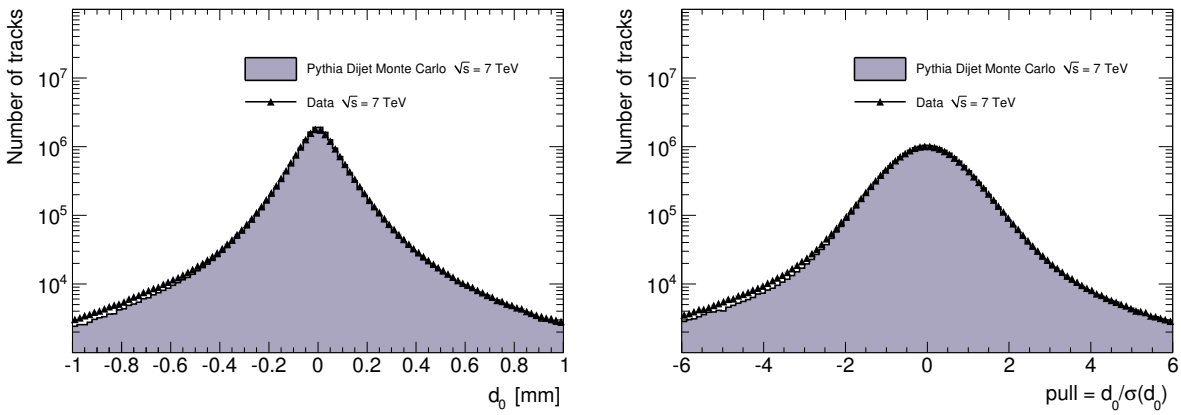

Figure 5.26: Distributions of the transverse impact parameter d_0 (left) and its pull d_0/σ_{d_0} (right) for tracks passing the b-tagging quality cuts. Data points are the solid black dots and the Monte Carlo simulation the plain histogram. The Monte Carlo is normalised to the data.

distribution shown in Figure 5.26 (and on subsequent figures as well) consists of the purely track-based d_0^{track} resolution convoluted with the resolution of the primary vertex position: $\sigma^2(d_0) = \sigma^2(d_0^{\text{track}}) + \sigma^2(\text{PV})$, where $\sigma(\text{PV})$ is the projection of the primary vertex error along the axis of closest approach of the track to the primary vertex in the transverse plane. In addition, a small fraction of tracks may not originate from the primary interaction vertex.

5.3.4.2 Transverse impact parameter resolution as a function of p_{T} and θ

The knowledge of the impact parameter resolution is crucial for the correct understanding of the b-tagging algorithms and their performance. For the study of the transverse impact parameter resolution as a function of p_{T} and θ, slightly different selection criteria are used than detailed earlier: the cuts on the impact parameters $|d_0|$ and $|z_0 \sin\theta|$ have been removed; all other cuts remain the same. The selected tracks have been divided into 15 p_{T} bins between 1 and 30 GeV and 16 θ bins. Twelve of these bins are in the barrel region ($0.19\ \pi < \theta < 0.81\ \pi$ which corresponds to $|\eta| < 1.2$). As explained in Section 5.3.4.1, the transverse impact parameter is expressed in the transverse plane at the point of closest approach to the primary event vertex. To extract the resolution, the distribution of the transverse impact parameter has been fitted within 2σ of its mean with a Gaussian function in each bin of θ and p_{T}. The width of this Gaussian $\sigma(d_0) = \sigma(d_0^{\text{track}}) \oplus \sigma(\text{PV})$ is understood as the impact parameter resolution convoluted with the uncertainty of the reconstructed primary vertex. A width of 2σ was chosen for the fit to extract the core resolution of the impact parameter and to avoid the contribution from secondary particles which populate its tails.

Figure 5.27 (left) shows a two-dimensional map of the d_0 resolution measured in the data, where the p_{T} of the tracks are shown along the x-axis and their θ along the y-axis. The value of the d_0 resolution follows the colour coding on the right of the figure. As expected, the resolution of the transverse impact parameter d_0 has a strong correlation with both p_{T} and θ. Figure 5.27 (right) shows the ratio of the two-dimensional d_0 resolution between the data and the Monte Carlo simulations. The agreement for small values of p_{T} is very good. For intermediate values, the discrepancies amount to around 6% and for large values (p_{T}>10 GeV) they are up to 15%. The differences at higher p_{T} are due to the combined effect of residual misalignments in the detector and of differences in the primary vertex resolution between the data and the Monte Carlo simulations.

To study the dependence of the transverse impact parameter resolution on p_{T} and θ in more detail, projections of the two-dimensional distributions of the resolutions onto single θ or p_{T} bins were analysed. Figure 5.28 (left) shows the d_0 resolution versus p_{T} for one central θ bin ($0.5\ \pi < \theta < 0.55\ \pi$). As expected, the resolution improves with increasing p_{T}. These results are in good agreement with the measurement of the transverse impact parameter resolution using collision-like tracks from cosmic ray data as presented in Section 5.1.4. For the present analysis, the statistic is sufficient to populate p_{T} bins up to 30 GeV. For fixed θ,

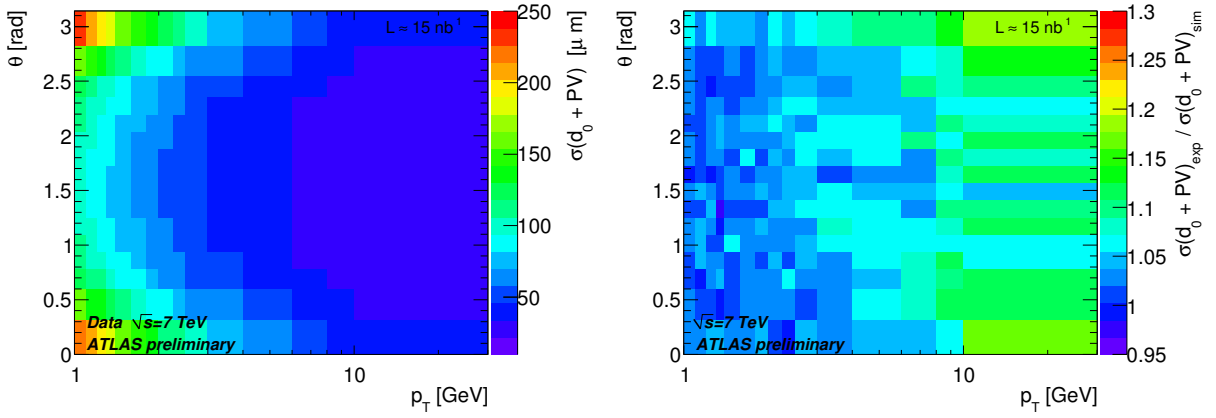

Figure 5.27: Two-dimensional map of the d_0 resolution measured in the data (left) and its ratio to the resolution in the Monte Carlo simulations (right), where the p_{T} of the tracks are shown along the x-axis and their θ along the y-axis. $\theta = \frac{\pi}{2}$ refers to the centre of the detector. The value of the d_0 resolution respectively its ratio follow the colour coding on the right of the figure.

the impact parameter resolution can be parameterised by the *EGN*-model [78]:

$$\sigma(d_0)_{\text{fixed }\theta} = \sqrt{E^2 + \frac{G^2}{p_{\mathrm{T}}} + \frac{N^2}{p_{\mathrm{T}}^2}}\,. \tag{5.5}$$

This model adds a linear term in $1/p_{\mathrm{T}}$ compared to the simpler $A \oplus B$ model used in the earlier preliminary study documented in Reference [79], where only two components, a constant term representing the intrinsic track resolution and a term in $1/p_{\mathrm{T}}^2$ modelling the multiple scattering contribution, are present. While the latter model is not compatible with the data up to high transverse momenta, the *EGN*-model describes the data well over the entire p_{T} range, as can be seen in Figure 5.28 (left). The interpretation of the fit parameters, however, is no longer straightforward, as this model does not allow a direct evaluation of the multiple scattering contribution to the impact parameter resolution. The fit is useful nevertheless, since it reduces the statistical uncertainty connected with the extraction of the resolution for a fixed transverse momentum p_{T}, which is presented in Table 5.3 for three values of p_{T} in two θ bins.

Figure 5.28 (right) shows the impact parameter resolution versus θ for one p_{T} bin (1 GeV$<$ $p_{\mathrm{T}} < 1.1$ GeV). $\theta = \frac{\pi}{2}$ refers to the centre of the detector. The dependence of the d_0 resolution on the traversed detector material and the length of the extrapolation path between the silicon layers (i.e. θ) is clearly visible. Using Equation (5.5), the parameterisation for the transverse impact parameter resolution can be expressed as

$$\sigma(d_0)_{\text{fixed }p_{\mathrm{T}}} = \sqrt{a_{p_{\mathrm{T}}}^2 + \frac{c_{p_{\mathrm{T}}}^2}{\sin\theta}} \quad \text{with} \quad a_{p_{\mathrm{T}}} = \sqrt{E^2 + \frac{G^2}{p_{\mathrm{T}}}} \quad \text{and} \quad c_{p_{\mathrm{T}}} = \frac{b}{p_{\mathrm{T}}}\,. \tag{5.6}$$

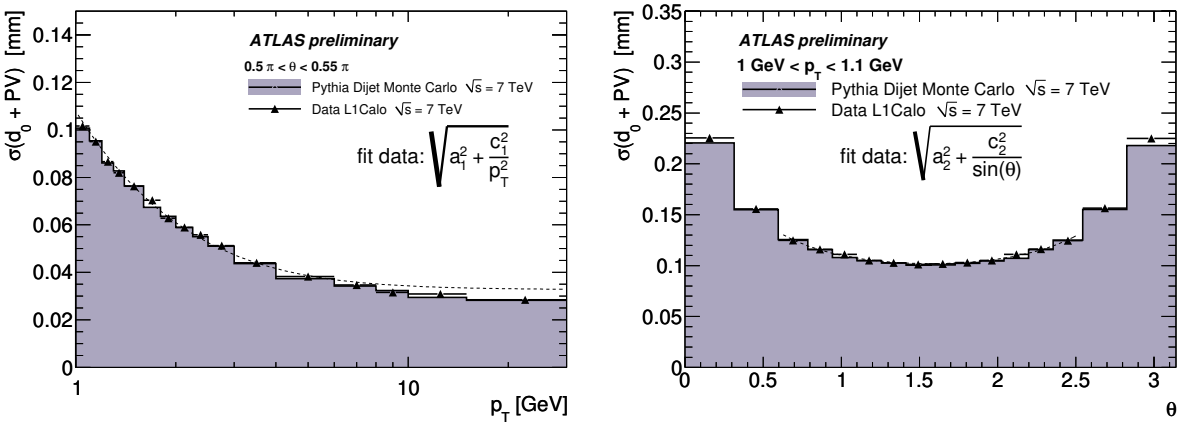

Figure 5.28: Transverse impact parameter resolution versus p_{T} for $0.5\ \pi < \theta < 0.55\ \pi$ (left), where the data is fitted by $\sqrt{E^2 + \frac{G^2}{p_{\mathrm{T}}} + \frac{N^2}{p_{\mathrm{T}}^2}}$ and transverse impact parameter resolution versus θ for 1 GeV$< p_{\mathrm{T}} <$ 1.1 GeV (right), where $\theta = \frac{\pi}{2}$ refers to the centre of the detector and the data is fitted by $\sqrt{a_{p_{\mathrm{T}}}^2 + \frac{c_{p_{\mathrm{T}}}^2}{\sin\theta}}$ in the barrel.

This parameterisation is only valid in a cylindrical geometry. The fit to the data is therefore restricted to the central part of the detector within $0.19\ \pi < \theta < 0.81\ \pi$.

This study shows that the overall agreement of the transverse impact parameter resolution between the data and the Monte Carlo simulations is very good for small values of p_{T}; discrepancies up to 15% can be observed for larger values (p_{T}>10 GeV). The differences at higher p_{T} are due to the combined effect of residual misalignments in the detector and of differences in the primary vertex resolution between the data and the Monte Carlo simulations.

5.3.5 Deconvoluted Transverse Impact Parameter Resolution

Since the impact parameters are expressed with respect to the primary vertex, the resolution of the primary vertex reconstruction is added to the intrinsic resolution of the track. Moreover, even the unbiased primary vertex resolution depends on the p_{T} and θ of the single track, due to possible correlations of this track with the remaining tracks present in the same event. This potentially distorts the distribution of the impact parameter resolution as a function of p_{T} and θ. An unfolding of the transverse impact parameter resolution from the primary vertex resolution has been carried out [74], which will be presented in this section. A detailed description of the unfolding procedure is given in Reference [74].

5.3.5.1 Unfolded impact parameter resolution in data

The deconvolution procedure [74] was applied to the data in order to derive the unfolded transverse impact parameter resolution as a function of p_{T} and θ. A two dimensional map of the deconvoluted resolution in the data is shown in Figure 5.29 (left) along with its ratio

to the predictions from the Monte Carlo simulations (right). For small p_{T}, the unfolded d_0 resolution in the data is of the order of 5% larger than the predictions from the simulation, but the difference amounts to up to 20% for medium $p_{\mathrm{T}} < 10$ GeV. In the highest p_{T} bin 10 GeV $< \mathrm{p_T} <$ 30 GeV, the difference amounts to up to 30%. The p_{T} dependence of the disagreement points towards remaining misalignments in the inner detectors. These discrepancies are slightly higher than the ones for the measured resolutions presented in the section before. This is due to the fact that the uncertainty of the primary vertex reconstruction is slightly different in the data compared to the Monte Carlo simulations: a smaller size of the beam spot observed in the data reduces the uncertainty of the primary vertex reconstruction.

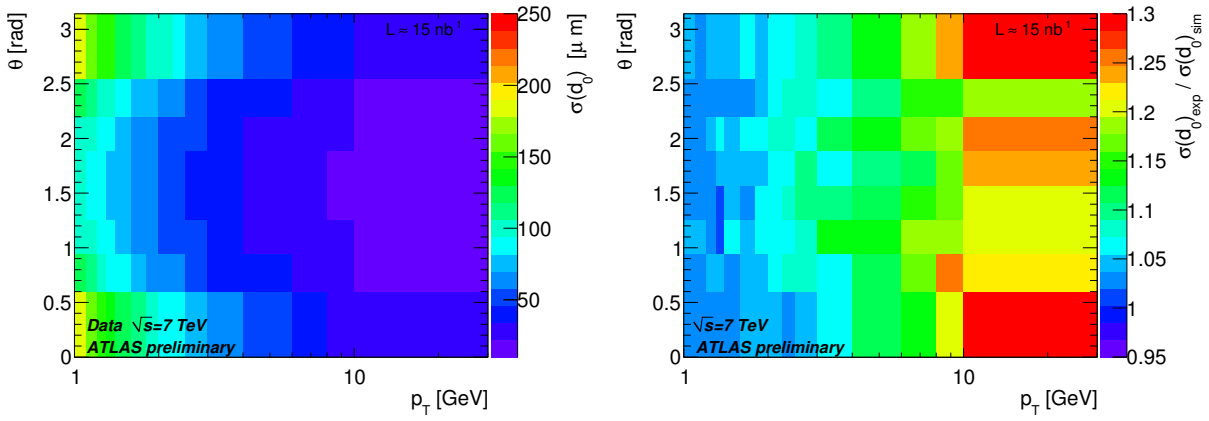

Figure 5.29: Two-dimensional map of the deconvoluted d_0 resolution measured in the data (left) and the ratio of the deconvoluted d_0 resolution between the data and the Monte Carlo simulation (right). The p_{T} of the tracks are shown along the x-axis and their θ along the y-axis. $\theta = \frac{\pi}{2}$ refers to the centre of the detector. From Reference [74].

The unfolded resolutions have been studied in more detail in each θ and p_{T} slice. Figure 5.30 shows the comparison of the unfolded resolutions to the predictions from the Monte Carlo simulations as a function of p_{T} for tracks in the interval of $0.4\ \pi < \theta < 0.5\ \pi$ (left), and as a function of θ for tracks in the range 8 GeV $< \mathrm{p_T} <$ 10 GeV (right). At low transverse momenta, where the multiple scattering and ionisation losses are dominant, the simulation describes the impact parameter resolution very precisely, while significant deviations are seen at higher values of p_{T}, reaching up to 20% at $p_{\mathrm{T}} \approx 20$ GeV. This varies depending on the θ interval considered. This points to the presence of residual misalignments in the detector.

The interpolation of the deconvoluted impact parameter resolutions with the function from Equation (5.5) allows the extraction of the resolutions in some θ bins for finite p_{T} values with increased statistical accuracy. Table 5.3 lists the resolutions of the convoluted and the deconvoluted transverse impact parameters for p_{T}-values of 1 GeV, 5 GeV and 15 GeV in one central θ bin in the barrel and one in the endcaps ($0.4\ \pi < \theta < 0.5\ \pi$ and $0.9\ \pi < \theta < \pi$, respectively). Since the θ intervals chosen for this study are quite large, some residual dependence on the difference in the rapidity distribution of tracks between the data

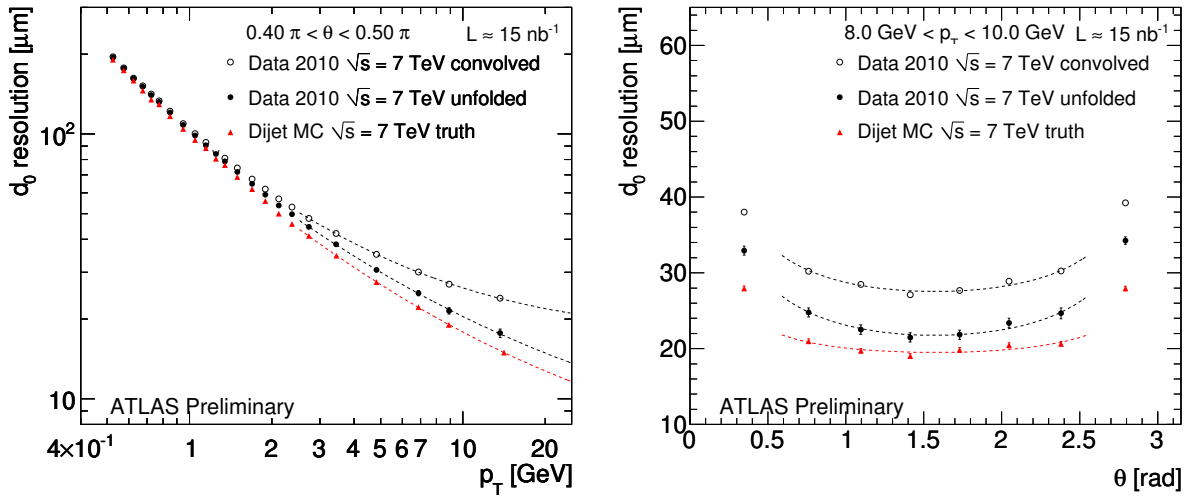

Figure 5.30: Unfolded transverse impact parameter resolution measured in the data (full circles) as a function of p_{T} for values of $0.4\ \pi < \theta < 0.5\ \pi$ (left) and as a function of θ for values of $8\ \mathrm{GeV} < \mathrm{p_T} < 10\ \mathrm{GeV}$ (right). The data is compared to the expectations from the Monte Carlo simulations (triangles). The resolution before unfolding is shown for reference (open circles). From Reference [74].

and the simulation remain: this adds a systematic uncertainty to the quoted numbers which is roughly estimated to be within 1% [74].

		$\sigma(d_0)$ [μm]		
		data		*simulation*
	p_{T}	convoluted	unfolded	MC prediction
$0.4\ \pi < \theta < 0.5\ \pi$	1 GeV	104.0 ± 0.2	102.5 ± 0.3	98.2 ± 0.1
	5 GeV	34.2 ± 0.1	29.5 ± 0.2	27.2 ± 0.0
	15 GeV	23.9 ± 0.2	17.8 ± 0.5	15.4 ± 0.0
$0.9\ \pi < \theta <\ \pi$	1 GeV	188.7 ± 0.2	188.2 ± 0.2	179.6 ± 0.0
	5 GeV	52.2 ± 0.1	48.3 ± 0.2	41.8 ± 0.0
	15 GeV	33.6 ± 0.1	28.0 ± 0.4	20.7 ± 0.0

Table 5.3: Resolution of the transverse impact parameter for three values of the transverse momentum in 7 TeV data, compared to predictions from the Monte Carlo simulation. The errors reflect the statistical uncertainties only, except for the unfolded resolutions, which also include the effect of systematic variations of the unfolding procedure. From Reference [74].

The measured resolution of the transverse impact parameter is in good agreement with a former measurement using collision-like tracks from cosmic ray data as presented in Section 5.1.4. The unfolded d_0 resolution shows a discrepancy up to 30% compared to predictions from the Monte Carlo simulations. These discrepancies are slightly higher than

the ones for the measured resolutions presented in the section before. The reason for this is that the uncertainty of the primary vertex reconstruction is slightly different in the data compared to the Monte Carlo simulations: due to a smaller size of the beam spot in the data, the uncertainty of the primary vertex calculation is smaller. The predicted resolutions in Table 5.3 using the Monte Carlo truth record are in good agreement with the expected resolutions of the ATLAS track reconstruction [58]. The p_{T} dependence of the disagreement between the predicted and the unfolded transverse impact parameter resolution points towards remaining misalignments in the inner detectors.

Chapter 6

Performance of the Track Reconstruction with the Insertable b-Layer

The present innermost pixel layer (b-layer) is expected to suffer from irreparable failures of modules with time. This will seriously deteriorate the impact parameter resolution and therefore affect the ability to identify jets originating from b-quarks. A luminosity of at least twice as high as the design value is expected before the High Luminosity LHC will be completed in 2020. With a luminosity this high, the event pileup will increase to a level that will lead to such high occupancies in the innermost pixel layer that readout inefficiencies will occur. In order to ensure the precise reconstruction of tracks in the ATLAS inner detectors, upgrade plans foresee to insert a fourth pixel layer between a new beam pipe and the present pixel b-layer, the so-called "insertable b-layer".

This chapter compares the expected track reconstruction performance in the presence of high luminosity pileup of the present ATLAS detector layout with the detector including the insertable b-layer. The study constitutes a part of the technical design report for the insertable b-layer upgrade project [80].

6.1 The Insertable b-Layer (IBL)

The Insertable b-Layer (IBL) is planned to be inserted as a fourth pixel layer between a new beam pipe and the present pixel b-layer. Figure 6.1 [80] shows the new beam pipe, the IBL with its modules, staves and support tube and the pixel b-layer as implemented in the ATLAS geometry model. The IBL is planned to be installed during the LHC shutdown in 2016.

The IBL will consist of 224 modules on 14 staves at a radius of 25.7 mm and over a range of $|z| < 332$ mm. A very low material budget of 1.5% of X_0 is foreseen, approximately half of the present b-layer. The IBL will consist of $6 \cdot 10^6$ pixels with a size of 50×250 μm^2 in $\phi - z$. Compared to the present innermost pixel layer at $R = 50.5$ mm and with a pixel size of

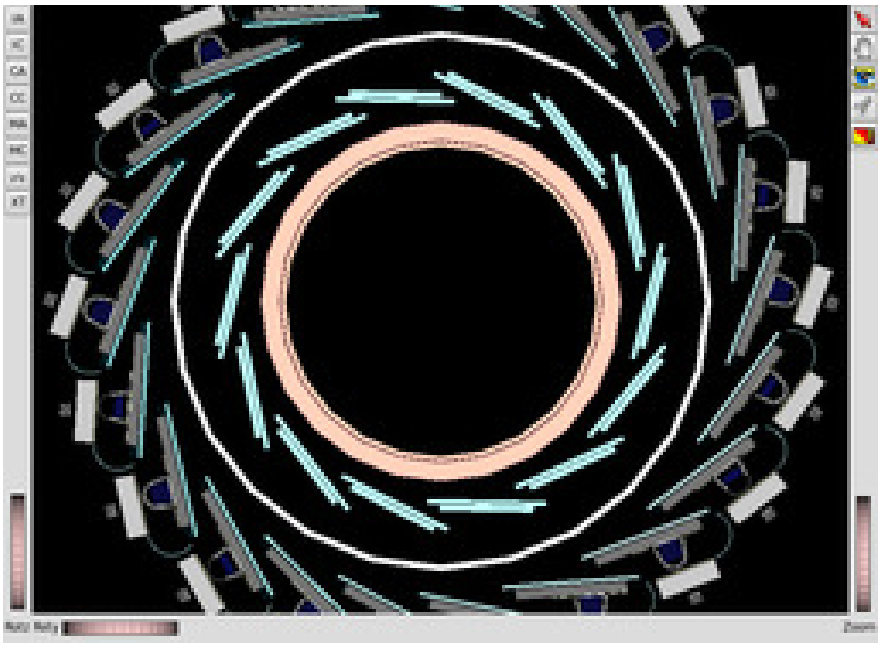

Figure 6.1: XY view showing the new (smaller) beam pipe, the IBL with modules, staves and support tube and the pixel *b*-layer as implemented in the ATLAS geometry model. From Reference [80].

50×400 μm^2 in $R - \phi$, this will result in a much improved impact parameter resolution and reduced occupancy.

6.2 Adapting the ATLAS Track Reconstruction to the IBL

This study uses the inside-out component of the primary track reconstruction package New Tracking as introduced in Section 4.2, which aims to reconstruct the tracks originating from the primary interaction(s) starting the pattern recognition in the silicon detectors. Because of the modular design of NEWT, the IBL was included into the pattern recognition simply as a fourth pixel layer at smaller radius. The Monte Carlo simulation used in this study assumes a centre-of-mass energy of 14 TeV for the event generation. More details are given in Appendix A.4.

6.3 General Track Properties

Figure 6.2 shows the number of hits on the tracks in the innermost pixel layer (upper left), in the pixel detector (upper right), the SCT (lower left) and the TRT detector (lower right) in $t\bar{t}$ events without pileup. The results for events with and without IBL are compared for tracks that pass the *b*-tagging track selection, which requires at least one associated cluster on the track in the innermost layer (pixel or IBL, respectively) and $p_{\mathrm{T}} > 1$ GeV.

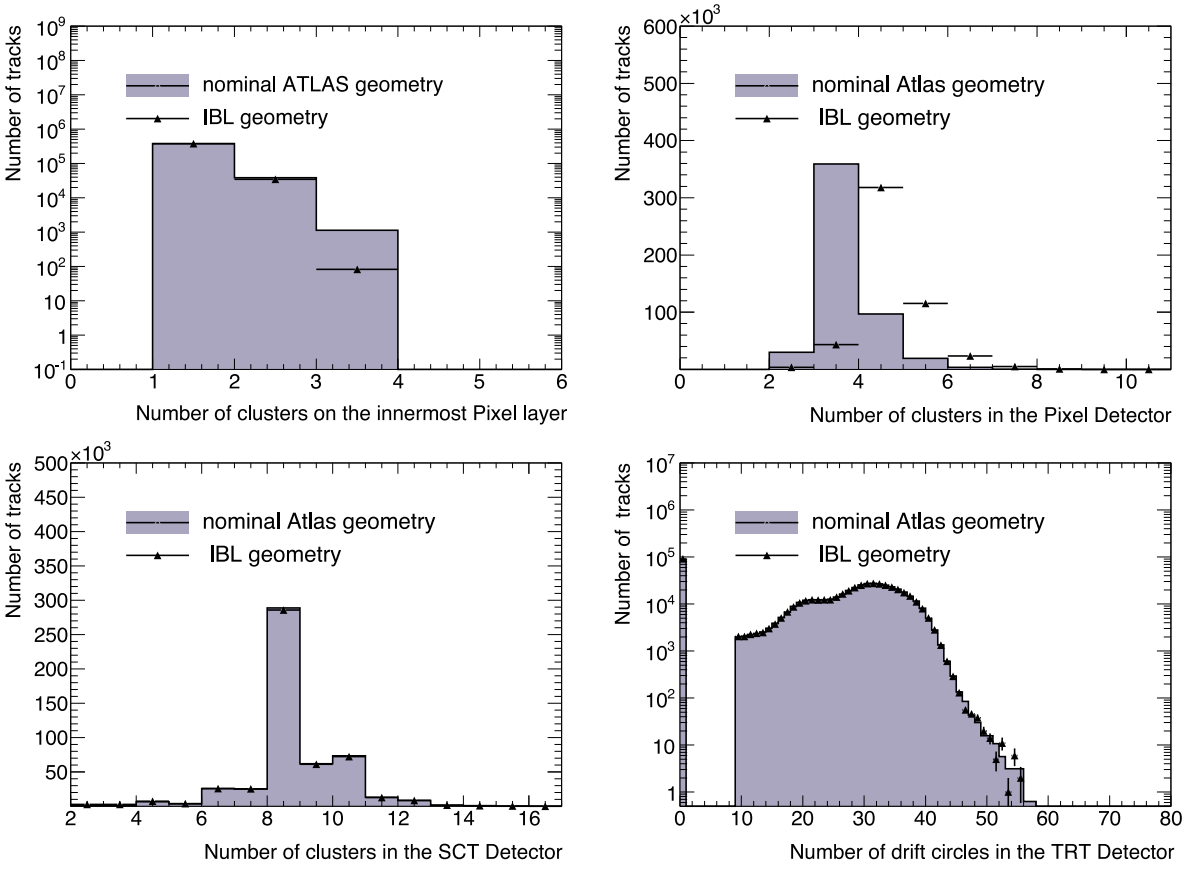

Figure 6.2: Number of hits on the tracks in the innermost pixel layer (upper left), in the pixel detector (upper right), the SCT (lower left) and the TRT detector (lower right) in $t\bar{t}$ events without pileup.

The total number of pixel (plus IBL) clusters increases by one with the IBL while the number of clusters in the innermost layer remains basically unchanged. The reduction in the number of tracks with three associated clusters in the innermost layer with IBL reflects the missing z overlap of the modules in a stave, leading only to occasional splitting of clusters across two adjacent modules in z in the very forward region. The number of associated SCT clusters and TRT drift circles is unchanged, as expected.

6.4 Impact Parameter Resolutions

The impact parameter resolutions of the transverse parameter d_0 and the longitudinal parameter z_0 are two crucial parameters affecting the b-tagging performance. Figure 6.3 shows the measured d_0 and $z \sin\theta$ impact parameter distributions with respect to the Monte Carlo truth for tracks in $t\bar{t}$ events without pileup. Compared are tracks that pass the track quality selection for the b-tagging, requiring at least one associated cluster in the innermost layer and $p_{\mathrm{T}} > 1$ GeV. A clear improvement is seen in both distributions by the addition of the IBL.

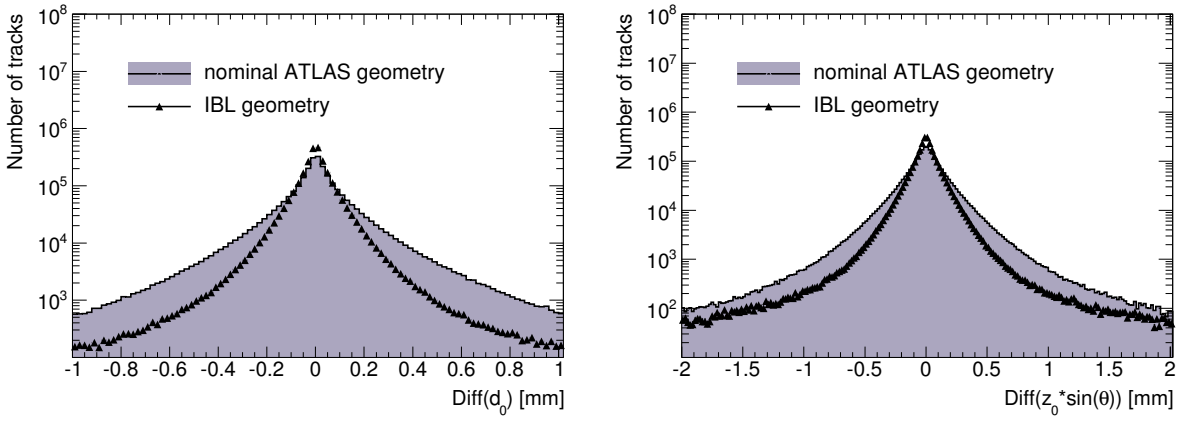

Figure 6.3: Impact parameter distributions of reconstructed tracks with and without IBL for $t\bar{t}$ events without pileup; transverse impact parameter distribution d_0 (left) and longitudinal impact parameter distribution $z_0 \sin\theta$ (right) with respect to the true d_0 respectively $z_0 \sin\theta$.

The transverse and longitudinal impact parameter resolutions have been studied in 8 p_{T} bins between 0.5 and 100 GeV and 12 $|\eta|$ bins. To extract the resolutions, the distributions of the impact parameters have been fitted in each bin with a Gaussian function within 2σ of their mean. The width of this Gaussian estimates the impact parameter resolution. A width of 2σ was chosen for the fits to extract the core resolution of the impact parameters and to avoid the contribution from secondary particles which populate the tails. Figure 6.4 illustrates the transverse impact parameter resolution (left) and the longitudinal impact parameter resolution (right) versus the pseudorapidity $|\eta|$ for tracks in $t\bar{t}$ events with 2 GeV $< p_{\mathrm{T}} <$ 4 GeV. The shape of the distributions is induced by the η dependence of the multiple scattering effects in the material of the innermost layers and the beam pipe, as well as by the effect of the

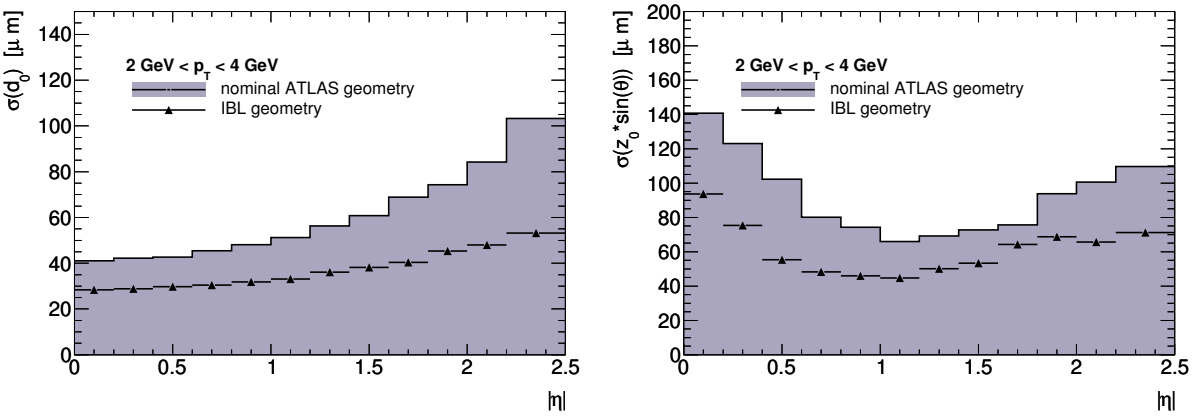

Figure 6.4: Impact parameter resolution as a function of $|\eta|$ for tracks in $t\bar{t}$ events without pileup. Results with and without IBL are compared: transverse impact parameter distribution d_0 (left) and longitudinal impact parameter distribution $z_0 \sin\theta$ (right) with respect to the true primary vertex position of the event. Results from tracks between 2 and 4 GeV are shown.

increasing z cluster size as a function of η. A significant improvement in the resolutions up to a factor of 1.8 can be observed, depending on the position in the detector.

Figure 6.5 shows the p_{T} dependence of the d_0 and $z_0 \sin\theta$ impact parameter resolutions. For the slice between 0.2 and 0.4 in $|\eta|$, the IBL leads to an improvement in in the intrinsic resolution up to a factor 1.8. The improvement in the $z_0 \sin\theta$ resolution illustrates the change in the z pitch between the IBL and the current pixel detectors.

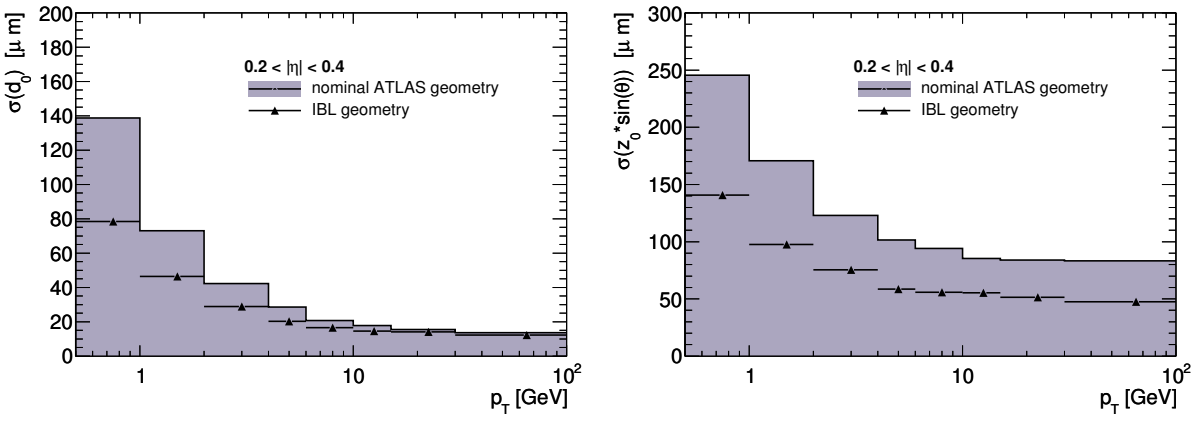

Figure 6.5: Impact parameter resolution as a function of p_{T} for tracks in $t\bar{t}$ events without pileup. Compared are the results with and without IBL: transverse impact parameter distribution d_0 (left) and longitudinal impact parameter distribution $z_0 \sin\theta$ (right) with respect to the reconstructed primary vertex of the event. Results for tracks with $0.2 < |\eta| < 0.4$ are shown.

6.5 Stability of the Track Reconstruction with IBL against Pileup

The track reconstruction of events with high luminosity pileup suffers from the increased combinatorial background at all levels, from seeding to track finding and selection of good tracks, up to the reconstruction in the TRT at high occupancy. At the same time, the number of shared clusters increases as hits from neighbouring tracks merge into single larger clusters. In addition, the track reconstruction needs to be robust against possible detector defects that may develop in time. An optimal working point for the track reconstruction needs to be found that limits the rate of fake tracks from pileup while preserving the tracking performance for b-tagging and high-p_{T} jets.

For the present detector, tighter track selection cuts in the reconstruction requiring nine instead of seven silicon (pixel and SCT) clusters and removing tracks with a hole in the pixel detector reduce the rate of additional fake tracks in events with high luminosity pileup with only modest loss in track reconstruction efficiency. This can be seen in Figure 6.6 in $t\bar{t}$ events. The track reconstruction efficiency is shown on the left and the fraction of reconstructed

tracks to the number of generated tracks on the right. The nominal track selection is shown in dashed blue and the track selection optimised for high luminosity in solid blue. For a small rate of failed modules, the tracking efficiency can be mostly recovered, provided that inactive modules are known to the reconstruction.

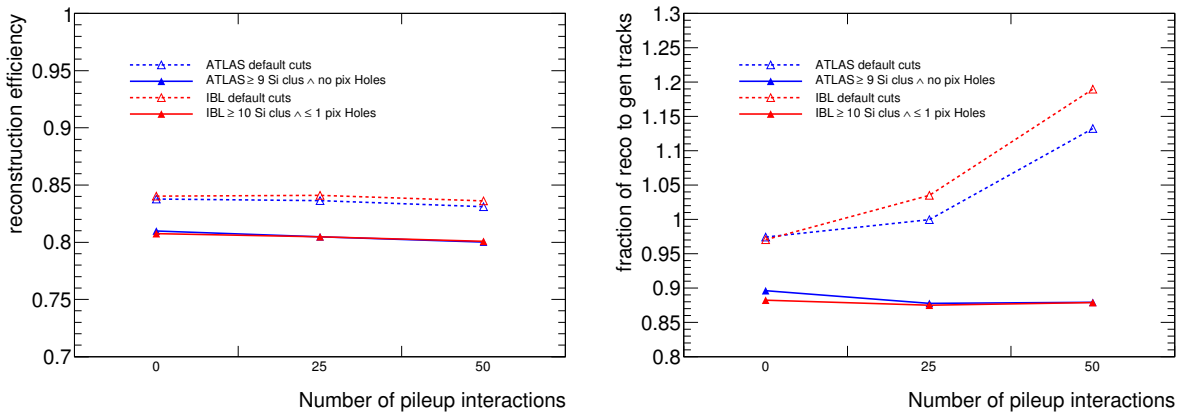

Figure 6.6: Efficiency for reconstructing primary tracks ($p_{\mathrm{T}} > 1$ GeV) with and without the IBL in $t\bar{t}$ events (left) and the ratio of reconstructed tracks to generated primary particles as a function of the average number pileup events (right). Shown are the results for the nominal track selection (dashed) and for the track selection optimised for high luminosity (solid).

In the case of the IBL, using the same cut of seven silicon clusters for events with pileup leads to a higher rate of the reconstructed tracks compared to the present detector. The extra track candidates are fakes due to an increased combinatorial background from the enlarged number of measurement layers and the presence of pileup. A more appropriate tighter track selection can be used for the IBL to remove the surplus in the rate of track candidates in events with high luminosity pileup. In addition, one can take advantage of the additional layer to introduce robustness in the reconstruction against readout or module inefficiencies in the *b*-layer at high luminosity. The tighter track selection for the detector with the IBL requires ten silicon (IBL, pixel and SCT) clusters on the track, while allowing for up to one pixel hole. In addition, for both geometries with and without IBL, the p_{T} cut is raised from 500 MeV to 900 MeV to reduce the combinatorial background from soft tracks from pileup interactions. In both cases, the tighter track selection results in very similar track reconstruction efficiencies and low rates of additional tracks, almost independently of the level of pileup.

The extra tracks accepted without the tighter track selection lead to a larger rate of tracks with significant offsets and thus can affect the primary vertex reconstruction and *b*-tagging. Figure 6.7 shows the number of *b*-tagging quality tracks per event as a function of the average number of pileup events for different track selections and detector layouts (upper left), the number of jets per event with $p_{\mathrm{T}}^{jet} > 15$ GeV that have at least one *b*-tagging quality track and are therefore considered by the *b*-tagging algorithms (upper right) and the

number of *b*-tagging quality tracks in jets from Monte Carlo truth per event as a function of the average number of pileup interactions (lower plot). The last plot indicates that additional tracks stemming from pileup interactions are reconstructed within the truth jet from the hard physics interaction and effect the *b*-tagging performance. This effect cannot be entirely suppressed by the tighter track selection. All three plots show that the dependence on pileup can be reduced by using the tighter track selection cuts.

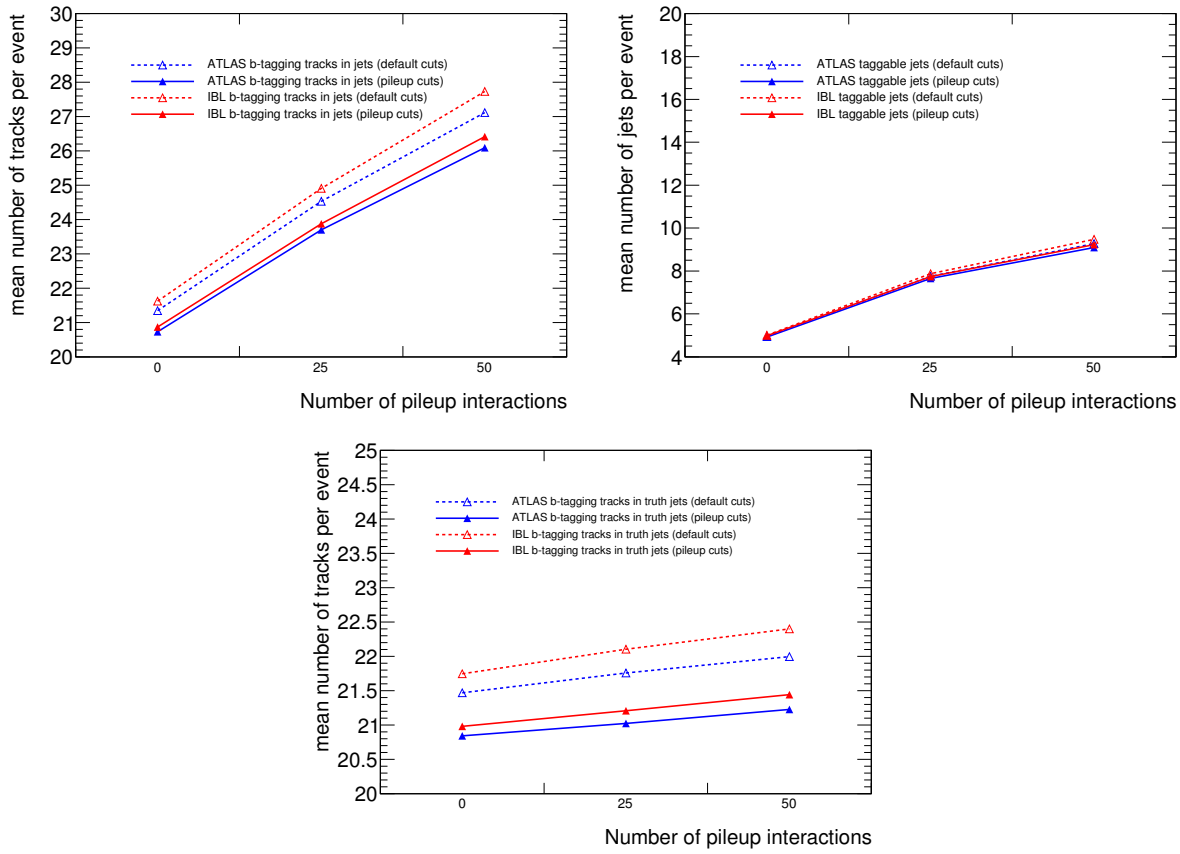

Figure 6.7: Number of *b*-tagging quality tracks per event as a function of the average number of pileup events for different track selections and detector layouts (upper left), number of jets per event with $p_{\mathrm{T}} > 15$ GeV that have at least one *b*-tagging quality track and are therefore considered by the *b* tagging algorithm (upper right) and number of *b*-tagging quality tracks in jets from Monte Carlo truth per event as a function of the average number of pileup interactions (lower plot). All three plots compare the nominal ATLAS geometry with the IBL geometry for $t\bar{t}$ Monte Carlo samples and different track selections.

6.6 Effects of Detector Defects and Readout Problems

Hard failures in the *b*-layer and in the other layers will appear with time. For this study, the current failed modules were taken into account for the simulation. Inefficiencies induced by high occupancies will affect the *b*-layer more than other layers because of its closer proximity to the interaction point, and would thereby limit the *b*-tagging. Known dead modules in

other layers can be handled in the reconstruction within limits, but if dead modules line up in too many layers this may lead to tracking inefficiencies even at low luminosity, since the number of layers available to constrain the tracking is reduced. This will also cause more fakes.

Three different failure scenarios were studied for events with Phase I pileup using dedicated $t\bar{t}$ Monte Carlo samples in order to demonstrate how the performance is recovered with the IBL:

- Loss of 10% of the clusters in the *b*-layer e.g. due to readout inefficiencies at high luminosity (also known as "double-column problem").
- A catastrophic failure of the full *b*-layer as a worse case scenario.
- Disabling 10% of the readout drivers (RODs) in the SCT in order to emulate the effects of dead modules.

The first scenario leads to holes in the track reconstruction with IBL, as the efficiency of the detector is degraded. In the two other scenarios the dead modules are known and the reconstruction can attempt to allow for the failures by adapting the cuts as discussed in Section 5.2.1.

Figure 6.8 shows the efficiency to reconstruct *b*-tagging quality tracks as a function of the average number of pileup events for all three scenarios: the loss of 10% of the clusters in the *b*-layer (upper left), the catastrophic failure of the full *b*-layer (upper right) and disabling 10% of the readout drivers in the SCT (lower plot). Compared are the results for the detector with and without the IBL using the high luminosity track selection. With the nominal ATLAS layout, the loss in *b*-tagging quality tracks is directly proportional to the loss in η coverage in the *b*-layer due to failures, even though the tracks may still be found. This is due to the requirement of at least one *b*-layer hit in the track selection. With IBL, most of the inefficiency is recovered, even in case of the second scenario assuming a complete failure of the *b*-layer. For the third scenario which assumes failures of SCT readout drivers, the efficiency with IBL is significantly better than without, but the performance cannot be recovered completely as too many clusters are lost on the tracks in the affected $\eta - \phi$ regions. For such a scenario a dedicated retuning of the track reconstruction and *b*-tagging software would be needed to further improve the results with IBL.

Overall, this study shows that the addition of the IBL to the ATLAS detector layout will make the track reconstruction software much more reliable and robust against irreparable or temporary failures of modules in both the pixel and the SCT detectors. The track reconstruction efficiencies of high-quality tracks used for *b*-tagging can be almost fully recovered in all three considered failure scenarios.

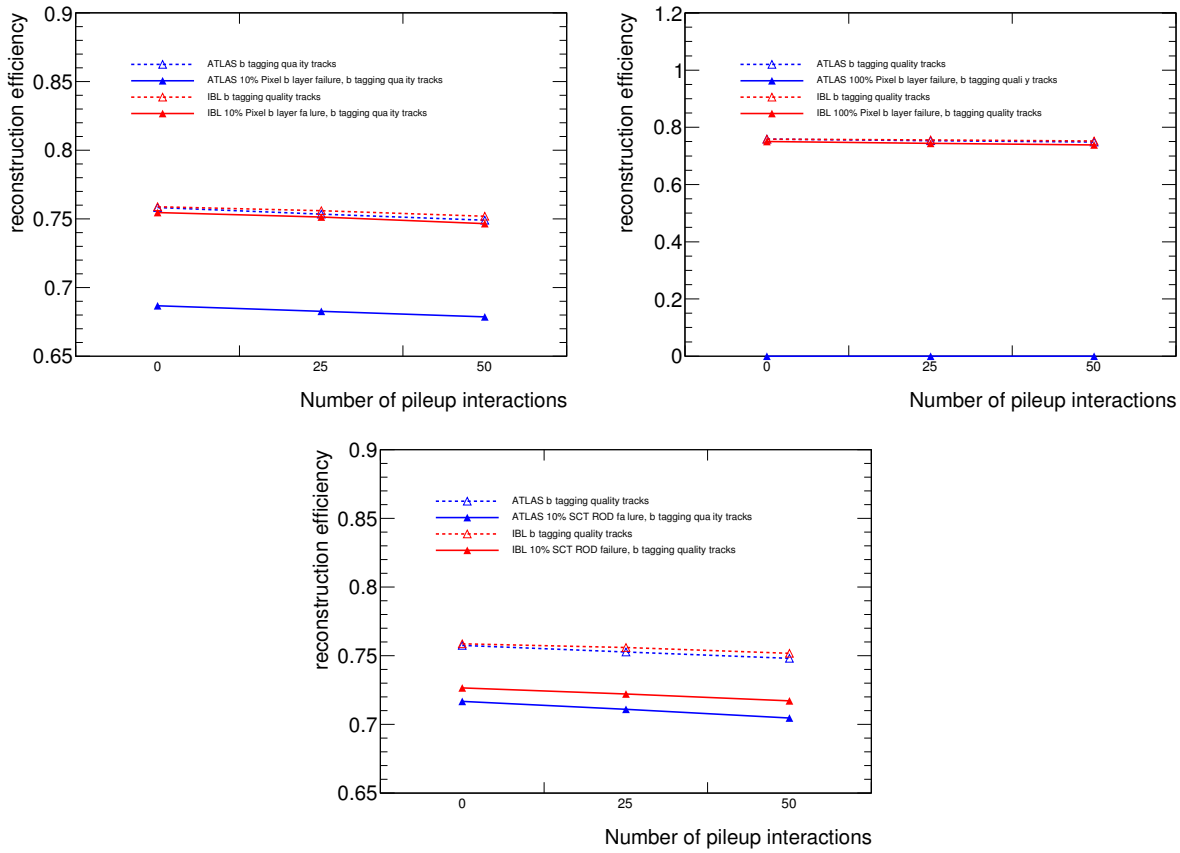

Figure 6.8: Efficiency for *b*-tagging quality tracks with detector defects (solid lines) and without (dashed). Shown are the results for the three failure scenarios as a function of the average number of pileup events, for a detector with and without IBL: loss of 10% of the clusters in the *b*-layer (upper left), catastrophic failure of the full *b*-layer (upper right) and disabling 10% of the readout drivers in the SCT (lower plot).

Chapter 7

Performance of Robust b-Tagging Algorithms in Early Data

The identification of jets originating from b-quarks (b-tagging) is an important part of the LHC physics program. Two algorithms are of special importance for early data analyses, the jet probability tagging algorithm JetProb and the secondary vertex tagging algorithm SV0. The first section of this chapter presents a study of the JetProb algorithm using p_{T}- and η-dependent track resolution functions in proton-proton collisions at $\sqrt{s} = 7$ TeV. The second section describes a data-driven measurement of the b-tagging efficiency of the SV0 tagging algorithm relying on muons in jets. The analysis was carried out to estimate a subset of the systematic uncertainties and to cross check the preliminary result documented in Reference [81]. The b-tagging efficiency measurement was conducted in the context of the first b-tagging calibration studies in 2010, and was used among others by the first measurement of the top quark-pair production cross section with the ATLAS detector [82].

7.1 The JetProb Algorithm with p_{T}- and η-dependent Resolution Functions

7.1.1 Event and Object Selection

This study uses the same event selection as detailed in Section 5.3. Jets are required to be well measured and to have a transverse momentum above 20 GeV. Only tracks associated to these jets and fulfilling the b-tagging track selection requirements detailed in Section 5.3.3.1 are considered in the following. A dataset corresponding to an integrated luminosity of 15 nb^{-1} was analysed. To account for differences between the data and the Monte Carlo simulation, the distributions of the primary vertex z position and the transverse jet momentum p_{T}^{jet} were reweighted in the simulation to the corresponding distributions in the data.

7.1.2 The Track Resolution Function $\mathcal{R}$

The basic functionality of the jet probability tagging algorithm JetProb is outlined in Section 4.6.4.1. The JetProb algorithm compares all selected tracks in the jet with a positive transverse impact parameter significance $S_{d_0} = \text{sign}(d_0) \cdot \frac{|d_0|}{\sigma_{d0}}$ to a track resolution function $\mathcal{R}$ in order to calculate the probability of the track to come from the primary vertex. The resolution function $\mathcal{R}$ [63, 64] is obtained in a data-driven way by selecting tracks in jets with negative S_{d0}, and by symmetrising this distribution around $S_{d0} = 0$. As illustrated in Figure 4.2, the negative side of the S_{d0} distribution is dominated by light-quark jets, whereas the positive side by the contributions from bottom- and charm-quark jets. The comparison of a track with the experimental resolution function therefore gives the probability of this track to originate from the primary vertex. The default track resolution function [64] using tracks in jets with negative S_{d0} is presented in Figure 7.1. The shape of the resolution function has been fitted with a functional form corresponding to the sum of two Gaussian cores and two exponentials to describe the tails. Their individual contributions are shown in different colours in Figure 7.1.

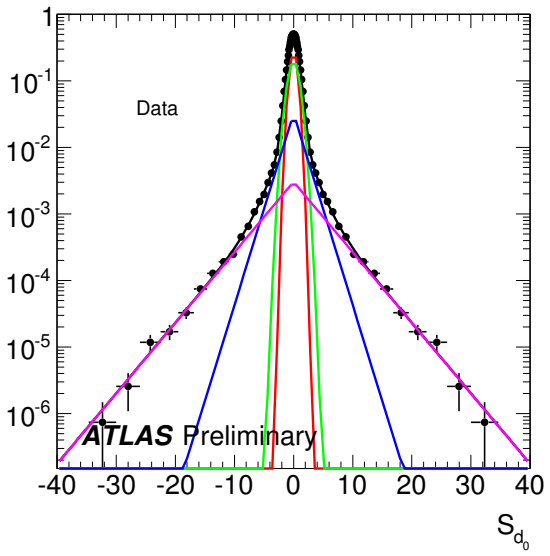

Figure 7.1: The default resolution function for the jet probability tagging algorithm using tracks in jets with negative S_{d0}, symmetrised around $S_{d0} = 0$. From Reference [64].

7.1.3 Motivation for p_{T}- and η-dependent Track Resolution Functions

The transverse impact parameter resolution of tracks strongly depends on their transverse momentum p_{T} and the amount of material they traverse, which can be parameterised either by the polar angle θ or the pseudorapidity $\eta = -\ln\tan\left(\frac{\theta}{2}\right)$ (see Section 5.3.4.2). Figure 7.2 shows the impact of different track momenta and pseudorapidities on the resolution functions of tracks in four different p_{T} and η bins in Pythia QCD Monte Carlo samples as introduced

in Appendix A.3: 1 GeV $< p_{\mathrm{T}} <$ 3 GeV (top) and 6 GeV $< p_{\mathrm{T}} < \infty$ GeV (bottom), $0.4 < \eta < 0.8$ (left) and $1.8 < \eta < 2.5$ (right). The resolution functions are normalised such that the integral of the positive side of the S_{d0} distribution is equal to unity. The shape of the resolution functions are quite different between the track categories as can be seen in Figure 7.2, especially for different p_{T} bins. This can have an impact on the performance of the JetProb algorithm as a whole. The shape of the resolution functions have been fitted with a functional form corresponding to either the sum of five Gaussians or to the sum of four Gaussians and an exponential to describe the tails.

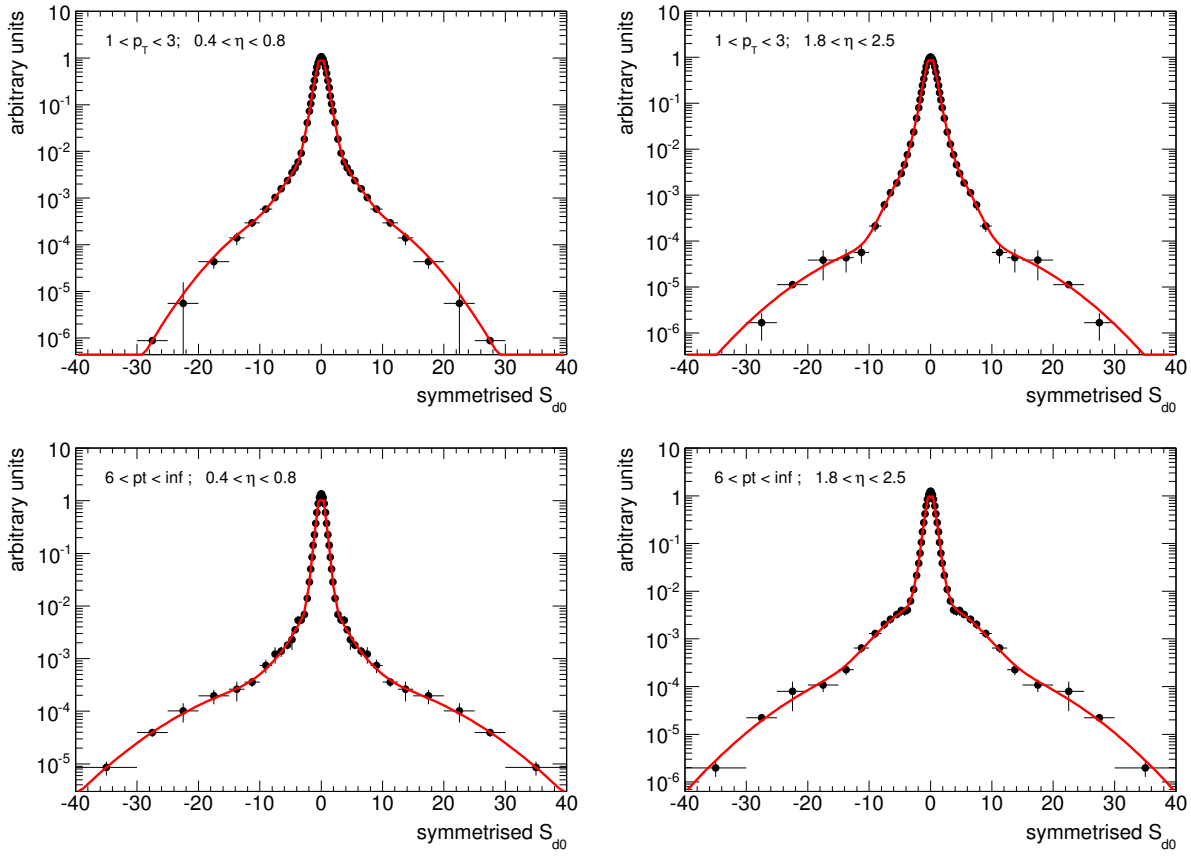

Figure 7.2: S_{d0} distribution of tracks in jets with negative significance, symmetrised around $S_{d0} = 0$, in Pythia QCD Monte Carlo samples in four different p_{T} and η bins: 1 GeV $< p_{\mathrm{T}} <$ 3 GeV (top) and 6 GeV $< p_{\mathrm{T}} < \infty$ GeV (bottom), $0.4 < \eta < 0.8$ (left) and $1.8 < \eta < 2.5$ (right).

A second effect which influences the resolution of the transverse impact parameter significantly is the presence of shared hits on the tracks. These tracks share either at least one pixel cluster with another track, or two SCT clusters. Figure 7.3 shows the transverse impact parameter distribution [74] of good tracks (solid black dots) and of tracks which share hits (red open squares). The distribution for tracks with shared hits is normalised to the same area as the distribution for tracks without shared hits. The presence of shared hits worsens the impact parameter resolution significantly. This could potentially influence the S_{d0} distribution of the tracks as well, if the transverse impact parameter error for tracks with shared hits is not estimated correctly.

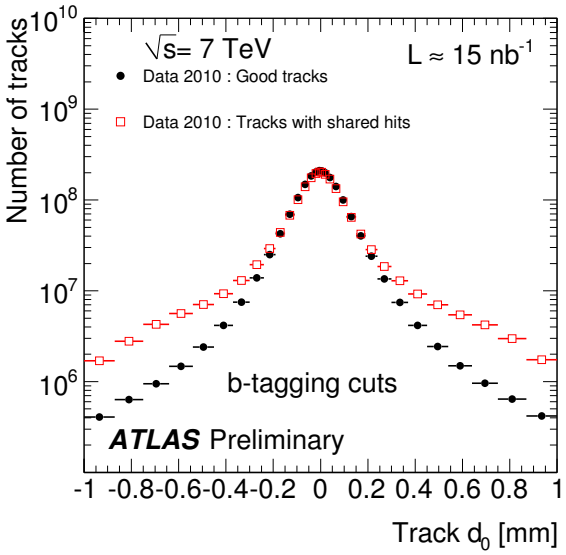

Figure 7.3: Transverse impact parameter of good tracks (solid black dots) and of tracks which share hits (red open squares), from Reference [74]. The distribution for tracks with shared hits is normalised to the same area as the distribution for tracks without shared hits.

Different resolution functions are therefore constructed for good tracks and tracks which share hits. In the following, the performance of the JetProb algorithm will be studied in three p_{T} and twelve η bins for good tracks and one p_{T} and six η bins for tracks with shared hits; the exact binning is given in Table 7.1.

good tracks:	
p_{T}-bins [GeV]	1, 3, 6, ∞.
η-bins [Rad]	-2.5, -1.8, -1.5, -0.8, -0.4, 0.0, 0.4, 0.8, 1.5, 1.8, 2.5.
tracks with shared hits:	
p_{T}-bins [GeV]	1, ∞.
η-bins [Rad]	-2.5, -1.8, -1.2, 0.0, 1.2, 1.8, 2.5.

Table 7.1: Binning of the p_{T}- and η-dependent track resolution functions for good tracks and tracks with shared hits.

7.1.4 Performance in Monte Carlo Simulations

The configuration of the JetProb algorithm with p_{T}- and η-dependent resolution functions was validated using the Pythia QCD Monte Carlo samples. A measure of the performance of a *b*-tagging algorithm is the rejection of light jets as a function of the *b*-tagging efficiency.

The b-tagging efficiency is defined as the fraction of taggable jets labelled as b-jet which are tagged by the algorithm. A jet is considered taggable if it fulfils $p_{\mathrm{T}}^{jet} > 20$ GeV and $|\eta^{jet}| < 2.5$. The light jet rejection is the inverse of the mistag rate, which is defined as the fraction of taggable jets labelled as light which were tagged as a b-jet by the algorithm.

Figure 7.4 shows the light-jet rejection versus the b-tagging efficiency for the default JetProb algorithm in black and the modified JetProb algorithm using p_{T}- and η-dependent resolution functions in red (left) and the ratio between the modified and the default JetProb algorithm (right). The modified JetProb algorithm shows a slightly better rejection for lower b-tagging efficiencies (up to 15%). The performance for b-tagging efficiencies greater than 50% is almost identical.

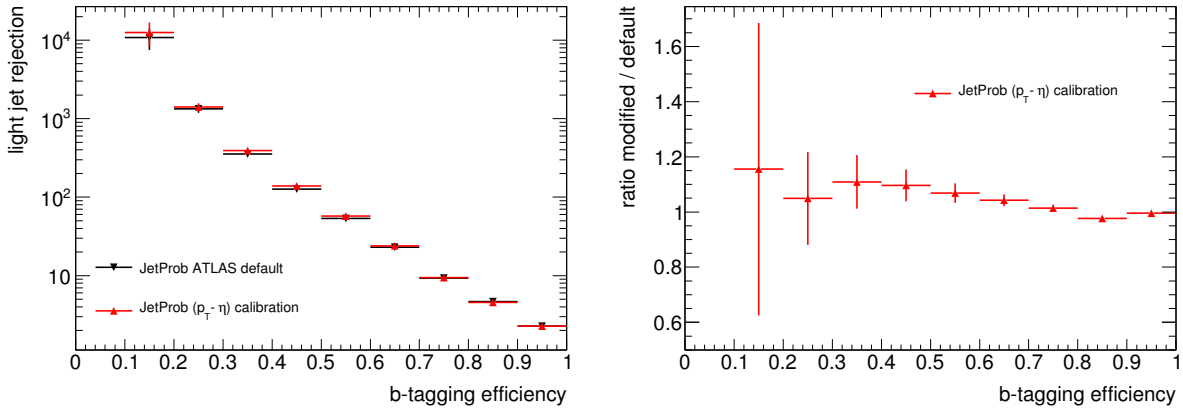

Figure 7.4: Light jet rejection versus b-tagging efficiency of the default JetProb algorithm in black and the modified JetProb algorithm using p_{T}- and η-dependent resolution functions in red (left) and the ratio between the modified and the default JetProb rejection (right). The overall performance is almost identical.

Figure 7.5 shows the b-tagging efficiency versus η (top left) and p_{T}^{jet} (top right) as well as the mistag rate versus η (bottom left) and p_{T}^{jet} (bottom right) for the operating point $-\log_{10}(\text{jet probability}) > 1.6$. The distribution of the jet probability is presented in Figure 7.7 for data and Monte Carlo simulation. Using the negative logarithm of the jet probability zooms into the region which is highly populated by b-jets. The default JetProb configuration in Figure 7.5 is shown in black and the modified JetProb algorithm using p_{T}- and η-dependent resolution functions in red. Both algorithms show identical b-tagging efficiencies, but the mistag rate in the endcaps at $|\eta| > 1.5$ is slightly improved using the p_{T}- and η-dependent resolution functions.

This study shows that the mistag rate of the JetProb algorithm can be reduced from 8% to 7% in the endcap region using p_{T}- and η-dependent track resolution functions. The underlying reason for this is that tracks in the endcaps traverse more material and are subject to more multiple scattering, and therefore show a worse impact parameter resolution. Both JetProb configurations show identical mistag rates in the centre of the detector. Since jets are predominantly produced centrally (as can be seen in Reference [83]), the overall mistag rate is

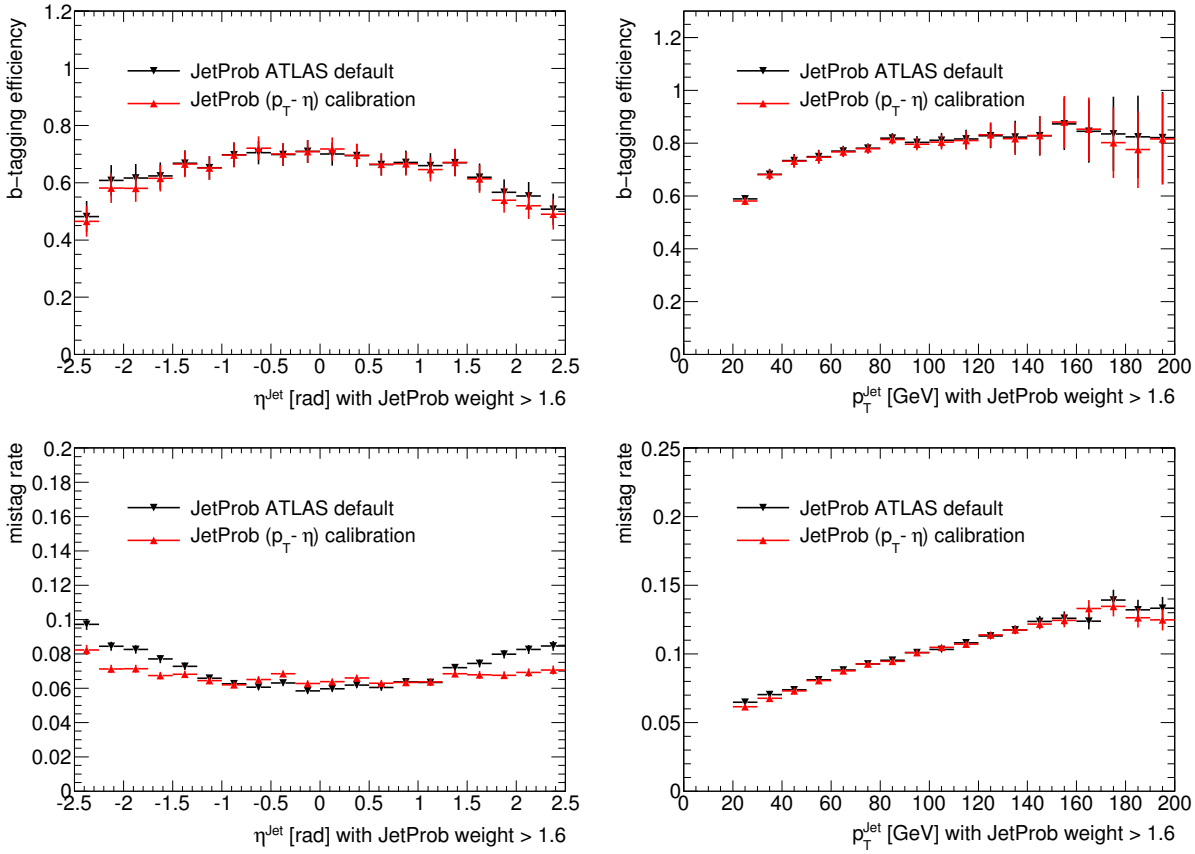

Figure 7.5: top: b-tagging efficiency versus η (left) and p_{T} (right) for the default and the p_{T}- and η-calibrated JetProb tagging algorithm for jets with $-\log_{10}(\text{jet probability}) > 1.6$. bottom: mistag rate versus η (left) and p_{T} (right) for the default and the p_{T}- and η-calibrated JetProb tagging algorithm for jets with $-\log_{10}(\text{jet probability}) > 1.6$.

almost identical for both algorithms. This study therefore confirms the validity of the default JetProb configuration in ATLAS. Despite the differences in the transverse impact parameter resolution and its significance in different p_{T} and η bins, the overall b-tagging performance of the JetProb algorithm is only changed marginally when using p_{T}- and η-dependent track resolution functions.

7.1.5 Performance in Data

The track probability of the p_{T}- and η-calibrated JetProb algorithm in the data compared to the Pythia QCD Monte Carlo samples is shown in Figure 7.6. The simulation has been normalised to the same number of tracks as in the data. Different sets of resolution functions have been obtained for the data and the Monte Carlo samples individually as outlined in Section 7.1.2. A slight overshoot of tracks with very small probability of originating from the primary vertex can be observed in the Monte Carlo simulations compared to the data. This could point to a slightly different heavy-flavour composition or rate of light-quark jets with γ-conversions, hadronic interactions, K_S or a different rate of secondaries in general in the

simulation compared to the data. The shape of the distributions is overall in good agreement between the data and the Monte Carlo simulations.

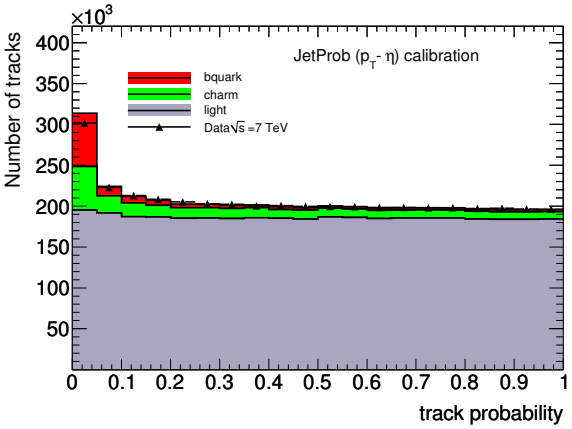

Figure 7.6: Track probability of the p_{T}- and η-calibrated JetProb tagging algorithm in data compared to Pythia Monte Carlo samples.

Figure 7.7 shows the combined jet weight (left) and its negative logarithm (right). The negative logarithm of the jet probability zooms into the region which is highly populated by *b*-jets and is most commonly used to apply the *b*-tagging requirement of the JetProb algorithm in physics analyses. The Monte Carlo simulation has been normalised to the number of jets in the data in both plots. A slight overshoot of jets with small probability of originating from the primary vertex can be observed in the Monte Carlo simulations compared to the data. This overshoot has the same origin than the one observed in the track probability distribution. The shape of the distributions is overall in good agreement between the data and the Monte Carlo simulations.

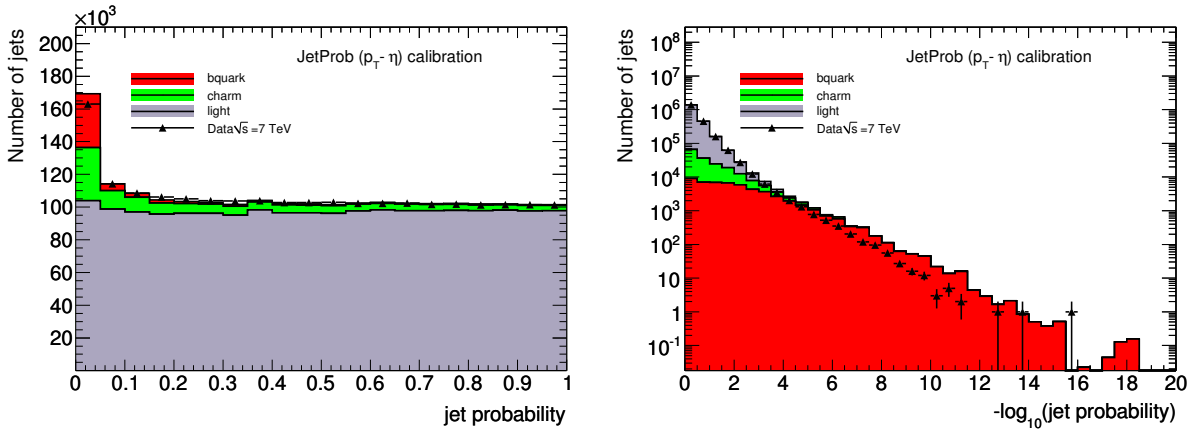

Figure 7.7: Jet probability of the p_{T}- and η-calibrated JetProb tagging algorithm in data compared to Monte Carlo simulation.

7.2 Efficiency Measurement of the SV0 Tagging Algorithm

The efficiency of a b-tagging algorithm can be measured in the data using a sample of jets containing a muon [84, 81]. The relative momentum with respect to the jet axis of a muon associated to a jet, p_{T}^{rel}, has a different shape for b-, c and light-quark jets. Fitting this distribution with templates for all three quark-flavour jets individually provides an estimate of the flavour composition of the sample. The fits are carried out before and after applying the b-tagging requirement using the SV0 tagging algorithm. The b-tagging efficiency is estimated by the the ratio of the b-jet content before and after applying the b-tagging requirement.

7.2.1 Data Samples and Object Selection

7.2.1.1 Data sample

The data sample for this analysis was collected between March and August 2010 using the jet-muon trigger with the lowest threshold (see Section 3.2.5.1). The data sample corresponds to an integrated luminosity of 2.9 pb^{-1}. Only events are considered where the inner detectors, the calorimeters and the muon system were fully operational and which have a reconstructed primary vertex with at least ten tracks associated to it.

The sample of jets with muons for the efficiency measurement is enriched in heavy-flavour content by requiring that at least one jet in each event has a reconstructed SV0 vertex with $L/\sigma(L) > 1$. This reduces the dependence of the p_{T}^{rel} fits on the templates for light-jets. To avoid a bias in the measurement due to this requirement, the loosely b-tagged jet, if it contains a muon, is not included into the efficiency measurement.

7.2.1.2 Monte Carlo simulations

The simulated samples used for this measurement are the Pythia QCD Monte Carlo samples as detailed in Appendix A.3. Special muon-filtered samples (referred to as JXμ) are used for the b- and c-jet templates, which require a muon at generator level with $p_{\mathrm{T}}^{\mu} > 3$ GeV. Due to the limited statistics available in these samples, the different JX samples were not added according to their production cross sections. To account for differences between the data and the simulation, the distribution of the primary vertex z position and the p_{T}^{jet}-spectrum were reweighted in the simulation.

7.2.1.3 Object selection

The first step of the object selection rejects badly or misreconstructed jets using the loose jet cleaning cuts [85]. The remaining jets are required to fulfil the following selection criteria:

- 25 GeV $< p_{\mathrm{T}}^{jet}(EM + JES) <$ 85 GeV
- $|\eta^{jet}| < 2.5$

A jet is considered tagged if the decay length significance of the SV0 tagging algorithm $L/\sigma(L) > 5.72$. This cut corresponds to a 50% b-tagging efficiency according to Monte Carlo estimates.

Only jets with associated muons are selected for the analysis. The associated muon has to pass the following requirements. They insure that the muon is well reconstructed and reject a certain amount of background from punch-through or decays-in-flight from pions or kaons.

- At least seven hits in the silicon detectors (including both pixel and SCT detectors).
- $|\eta^{\mu}| < 2.5$
- Only consider tracks within $\Delta R < 0.4$ of the jet from the inside-out sequence of New Tracking in the inner detectors and the STACO sequence in the muon system.
- The transverse momentum of the muon, p_T^{μ}, is greater than 4 GeV.
- At least two hits in the pixel detector.
- At least four hits in the SCT detector.
- No explicit cut on the number of TRT hits on the tracks is applied. However, most tracks within its acceptance $|\eta| < 2$ do have a successful extension into the TRT and the corresponding improved momentum resolution.
- The track is well reconstructed in the inner detectors, i.e. the χ^2 of the track fit divided by the number of degrees of freedom for the fit is smaller than three.
- The transverse impact parameter $|d_0|$ measured with respect to the primary vertex is smaller than 2 mm.
- The longitudinal impact parameter measured with respect to the primary vertex multiplied by $\sin\theta$, $|z_0 \sin\theta|$, is smaller than 2 mm.

7.2.2 Measurement of the *b*-Tagging Efficiency

The b-tagging efficiency is defined as the fraction of real b-jets which are tagged by the tagging algorithm. In order to measure this efficiency in the data, the b-jet content before and after

applying the *b*-tagging requirement needs to be known. The *b*-jet content in a sample of muons in jets can be estimated using the relative momentum of the muon with respect to the jet axis, p_{T}^{rel}. Muons from *b*-hadron decays have a different p_{T}^{rel} spectrum than muons in *c*- and light-jets. Separate p_{T}^{rel} templates for all three quark flavours can be fitted to the p_{T}^{rel} distribution in the data in order to obtain the fraction of *b*-jets before and after applying the SV0 *b*-tagging requirement. The efficiency of the SV0 algorithm ϵ_b^{data} can be calculated using [81]

$$\epsilon_b^{data} = \frac{f_b^{tag} \cdot N^{tag}}{f_b \cdot N}, \tag{7.1}$$

where f_b and f_b^{tag} are the fractions of *b*-jets before and after applying the SV0 tagging requirement, and N respectively N^{tag} the number of jets in the two samples. A data-to-simulation scale factor is defined as

$$\kappa_{\epsilon_b}^{data/sim} = \frac{\epsilon_b^{data}}{\epsilon_b^{sim}}. \tag{7.2}$$

This scale factor is a measure for the agreement between the data and the Monte Carlo simulation, and can be used to correct the simulation in physics analyses to account for possible discrepancies. The scale factor $\kappa_{\epsilon_b}^{data/sim}$ calculated for *b*-jets from semi-leptonic decays is assumed to be valid for all types of *b*-jets, especially also *b*-jets originating from hadronic decays.

7.2.3 The p_{T}^{rel} Method and Construction of Templates

The p_{T}^{rel} is calculated from the muon momentum $\vec{p}^{\,\mu}$ and the jet momentum $\vec{p}^{\,jet}$. The vector $\vec{p}^{\,jet} + \vec{p}^{\,\mu}$ estimates the *b*-quark direction, and the component of the muon momentum $\vec{p}^{\,\mu}$ perpendicular to this direction is:

$$p_{\mathrm{T}}^{rel} = \frac{|\vec{p}^{\,\mu} \times (\vec{p}^{\,jet} + \vec{p}^{\,\mu})|}{|\vec{p}^{\,jet} + \vec{p}^{\,\mu}|}. \tag{7.3}$$

Templates are constructed separately for *b*-, *c*- and light-quark jets and are fitted to the corresponding inclusive distribution in the data using a binned maximum likelihood technique where each bin is treated as an independent Poisson variable. Statistical fluctuations of the p_{T}^{rel} templates are not considered during the fit, a systematic uncertainty is determined separately.

The p_{T}^{rel} templates for *b*- and *c*-jets are derived using muons associated to true *b*- and *c*-jets from the Pythia QCD JXμ samples. Due to the limited statistics of the simulated samples, they are not added together according to their production cross sections. This introduces a bias which will be discussed in Section 7.2.6. Three different definitions of the light-jet

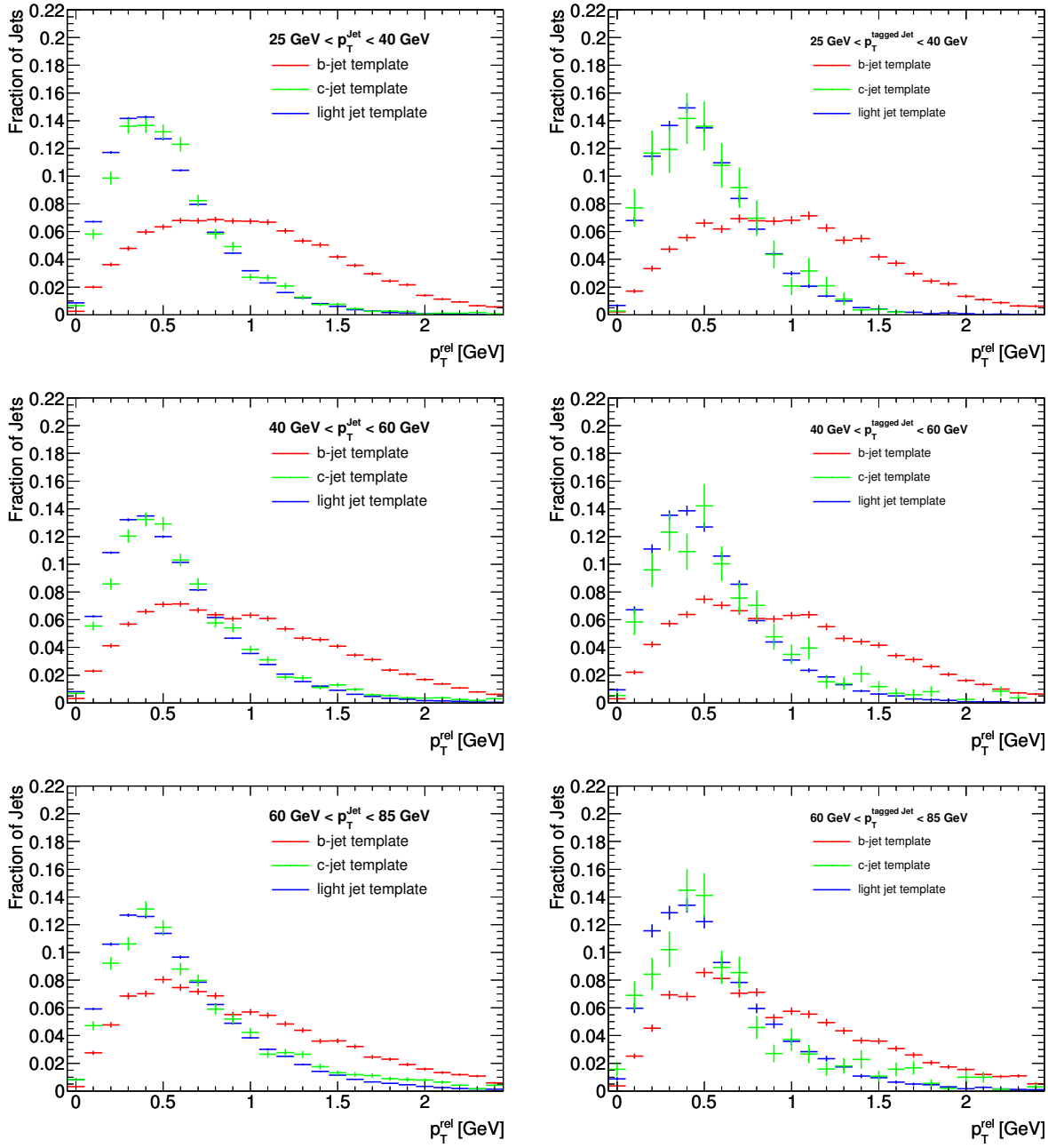

Figure 7.8: p_{T}^{rel} templates for jets before applying the SV0 b-tagging requirement (left) and after (right) for the three analysis bins: 25 GeV$< p_{\mathrm{T}}^{jet} <$ 40 GeV (top row), 40 GeV$< p_{\mathrm{T}}^{jet} <$ 60 GeV (middle row) and 60 GeV$< p_{\mathrm{T}}^{jet} <$ 85 GeV (bottom row).

template are used for this measurement. The fist set of templates is derived from the data using all tracks in jets passing the track requirements in the inner detectors as discussed in the section before. The two other definitions rely on the Pythia QCD JX samples: reconstructed muons in true light jets and, using the same technique as in the data, all tracks in jets. The raw measurement of the SV0 *b*-tagging efficiency in the next section as well as the systematic uncertainties discussed in Section 7.2.5 are estimated using the data-driven light-jet template. The three different light-jet templates from the data and the Monte Carlo simulations are used to estimate the systematic uncertainties associated to the choice of light-jet template and to correct the final efficiency measurement.

The p_{T}^{rel} measurement is carried out in three bins of p_{T}^{jet}: $25-40$ GeV, $40-60$ GeV and $60-85$ GeV. Figure 7.8 shows the p_{T}^{rel} templates in all three analysis bins (top, middle and bottom) before and after applying the SV0 *b*-tagging requirement. Only the data-driven light-jet template using tracks in jets is shown.

7.2.4 *b*-Tagging Efficiency Measurement in Data

Figure 7.9 presents the fitted p_{T}^{rel} distributions in the data before (left) and after (right) applying the SV0 *b*-tagging requirement in all three analysis bins. Due to the similar shape of the *c*- and light-jet templates, the p_{T}^{rel} fits are not very reliable to measure their fractions correctly. This is evident in the fitted distributions after applying the *b*-tagging requirement in the second and third analysis bin. A difference in the shape can be observed between the data and the fitted templates, for example in the first and second bin before and the second bin after applying the *b*-tagging requirement. Effects which influence the shape of the templates are considered in Section 7.2.5 as systematic uncertainties. Figure 7.10 shows the uncorrected efficiency measurement of the SV0 tagging algorithm for the working point $L/\sigma(L) > 5.72$ in the data and the Pythia Monte Carlo simulation (left) as well as the uncorrected efficiency scale factor (right). The raw efficiencies are in good agreement with the ones documented in Reference [84].

7.2.5 Study of Systematic Uncertainties

In the following, the systematic uncertainties which were considered for the SV0 *b*-tagging efficiency measurement [81] are presented. The systematic uncertainties connected to the modelling of *b*-decays and the fragmentation process in the Monte Carlo simulations are discussed in detail. All other sources of systematic uncertainties are summarised; a more complete evaluation is documented in Reference [81] or Reference [84].

The systematic uncertainties which are considered either have a direct impact on the shape of the templates or on the sample composition of the jets. A new series of templates is built for

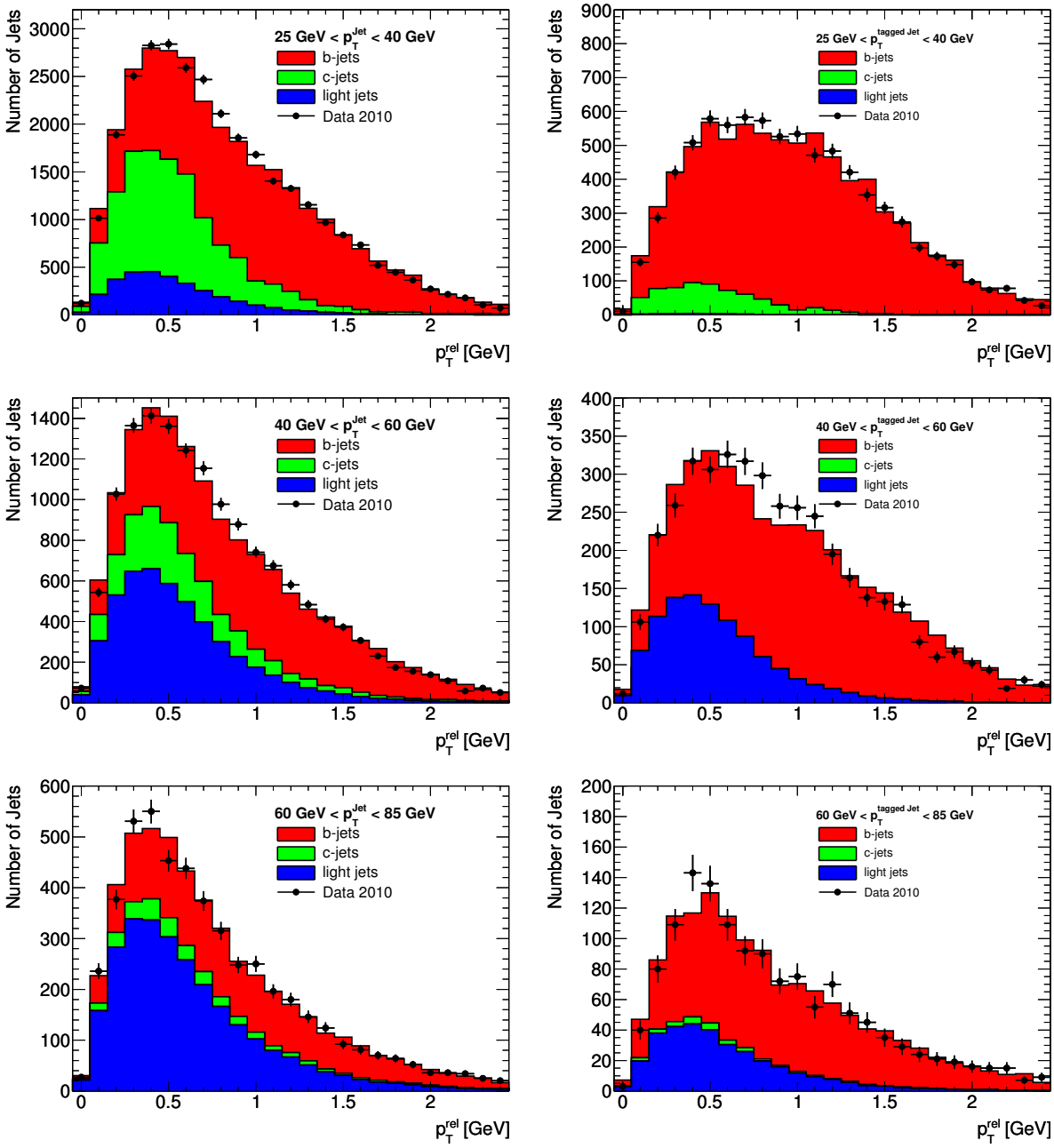

Figure 7.9: Fitted p_{T}^{rel} distributions in the data before (left) and after (right) applying the SV0 b-tagging requirement in the three analysis bins: 25 GeV$< p_{\mathrm{T}}^{jet} <$ 40 GeV (top row), 40 GeV$< p_{\mathrm{T}}^{jet} <$ 60 GeV (middle row) and 60 GeV$< p_{\mathrm{T}}^{jet} <$ 85 GeV (bottom row).

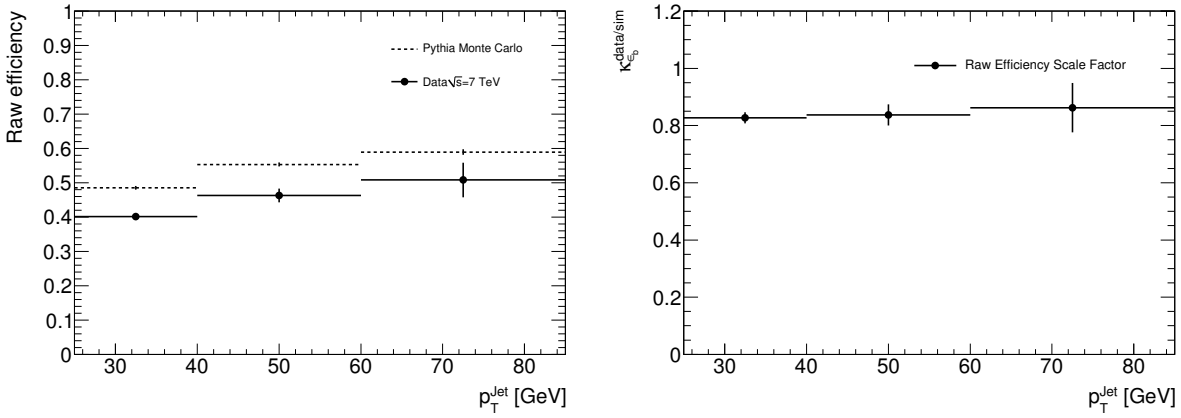

Figure 7.10: Uncorrected *b*-tagging efficiency measurement of the SV0 algorithm in the data and the Pythia Monte Carlo simulation (left) and the resulting uncorrected efficiency scale factor (right).

each effect and the *b*-tagging efficiency is re-evaluated. Some of the studied effects introduce a bias to the measurement which needs to be corrected for. The correction procedure is outlined in Section 7.2.6. A summary of the uncertainties [81] is given in Table 7.2. The total uncertainties vary between 12% in the first bin and 10% in the other analysis bins.

Relative Uncertainty [%]	p_T^{jet} [GeV]		
	$25-40$	$40-60$	$60-85$
Modelling of *b*-decays	1.3	0.2	0.5
Fragmentation	0.1	0.1	0.1
Modelling of the *b*-hadron direction	6	6	6
Non-*b*-jet templates	6	6	6
Jet p_{T} spectrum	6	3	3
Scale factor for inclusive *b*-jets	5	4	0.7
p_{T}^{rel} template statistics	2	2	2
Misidentified muons in *b*-jets	0.7	0.7	0.7
Jet energy scale	0.2	0.2	0.2
Modelling of *b*-production	0.2	0.2	0.2
Total	12	10	10

Table 7.2: The systematic uncertainties of the efficiency scale factors, from Reference [81]. The largest ones arise from the modelling of the *b*-hadron direction, the non-*b*-jet templates and the jet p_{T} spectrum in simulation.

7.2.5.1 Semi-leptonic b-decay modelling

The p_{T}^{rel} spectrum of b-jets consists of two components: direct $\bar{b} \to \mu^+ X$ decays and cascade $\bar{b} \to \bar{c}/c \to \mu^{-/+} X$ decays. Figure 7.11 (left) shows the muon momentum spectrum p^* in the b-hadron rest frame of muons from the two decay components individually. The p_{T}^{rel} measurement is not very sensitive to the distribution of the cascade decays due to its similarity to the c- and light-jet templates. An incorrect modelling of the direct b-decay component, however, could influence the measurement significantly. Figure 7.11 (right) shows the direct component of $\bar{b} \to e^+ X$ decays measured by the BaBar collaboration [86] and the corresponding distribution from the Pythia QCD samples. Differences in the shape between the two distributions could arise from the different meson- and baryon-fractions observed by the BaBar experiment and predicted for the LHC. The two $\bar{b} \to e^+ X$ distributions measured by the BaBar collaboration and obtained from the Pythia QCD samples were used to construct a weighting function which is applied to the direct $\bar{b} \to \mu^+ X$ component in the b-jet templates. Figure 7.12 shows the b-jet templates after the reweighting (top three rows) and the resulting change to the efficiency scale factor (bottom).

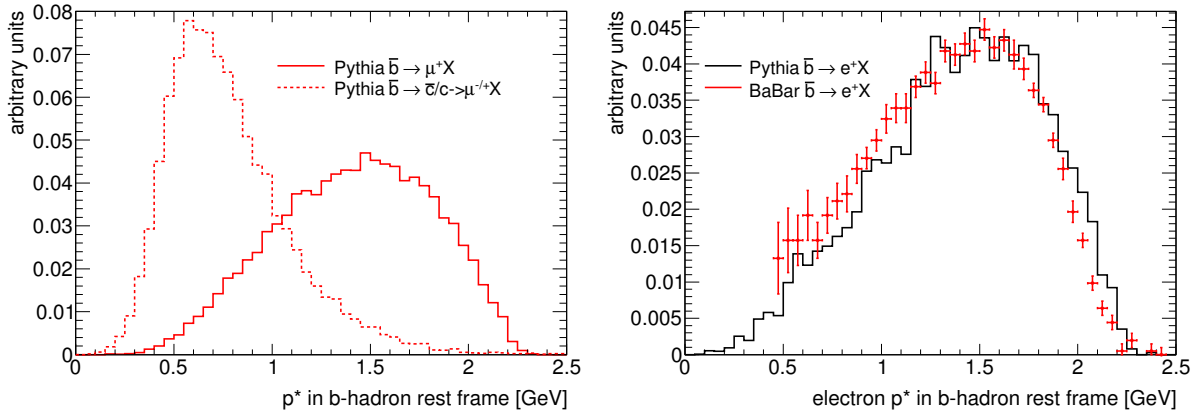

Figure 7.11: Muon momentum spectrum p^* in the b-hadron rest frame of muons from direct $\bar{b} \to \mu^+ X$ decays and from cascade $\bar{b} \to \bar{c}/c \to \mu^{-/+} X$ decays in the Pythia QCD JXμ samples (left) and comparison of the measured $\bar{b} \to e^+ X$ spectrum by the BaBar [86] collaboration with the prediction from Pythia QCD Monte Carlo (right).

Uncertainties in the ratio between the direct and the cascade decays also affect the p_{T}^{rel} measurement. The branching ratios of the two semi-leptonic b-decay components are $BR(\bar{b} \to l^+ X) = (10.69 \pm 0.22)\%$ and $BR(\bar{b} \to \bar{c}/c \to l^{-/+} X) = (9.62 \pm 0.53)\%$, respectively [4], giving the ratio $\frac{BR(\bar{b} \to l^+ X)}{BR(\bar{b} \to \bar{c}/c \to l^{-/+} X)} = 1.11 \pm 0.07$, where l denotes either a muon or an electron. To evaluate the systematic uncertainty due to this effect, the ratio has been varied within the quoted uncertainty and the b-jet templates have been reweighted accordingly. The resulting changes to the b-jet templates are shown in Figure 7.13 (top three rows) along with the influence on the scale factor (bottom).

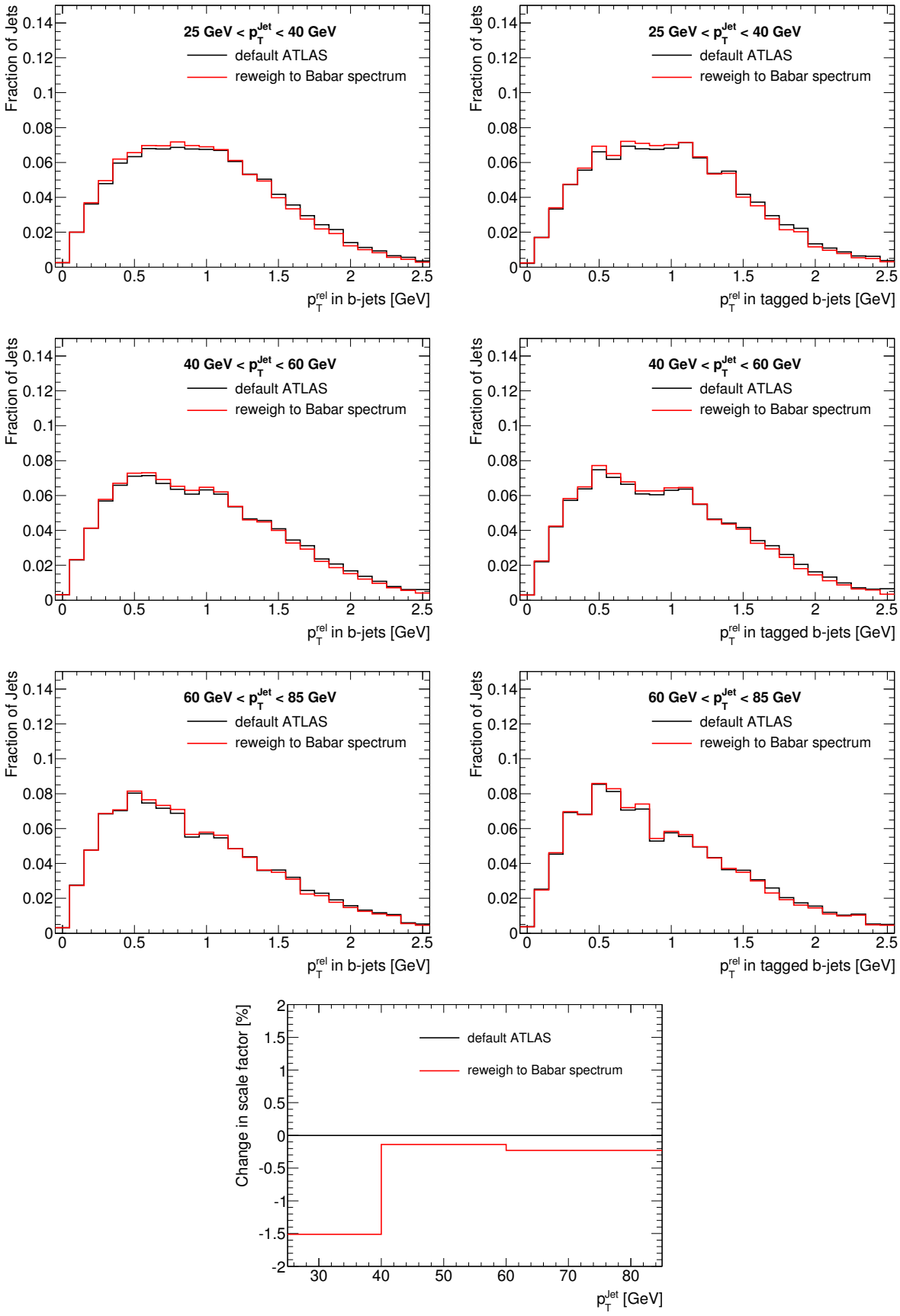

Figure 7.12: b-templates after reweighting the direct b-decay component in the b-jet templates (top three rows). The weighting function was constructed using the $\bar{b} \to e^+X$ measurement by the BaBar collaboration [86] and the corresponding distribution from the Pythia QCD samples. The resulting change to the efficiency scale factor is shown in the bottom plot.

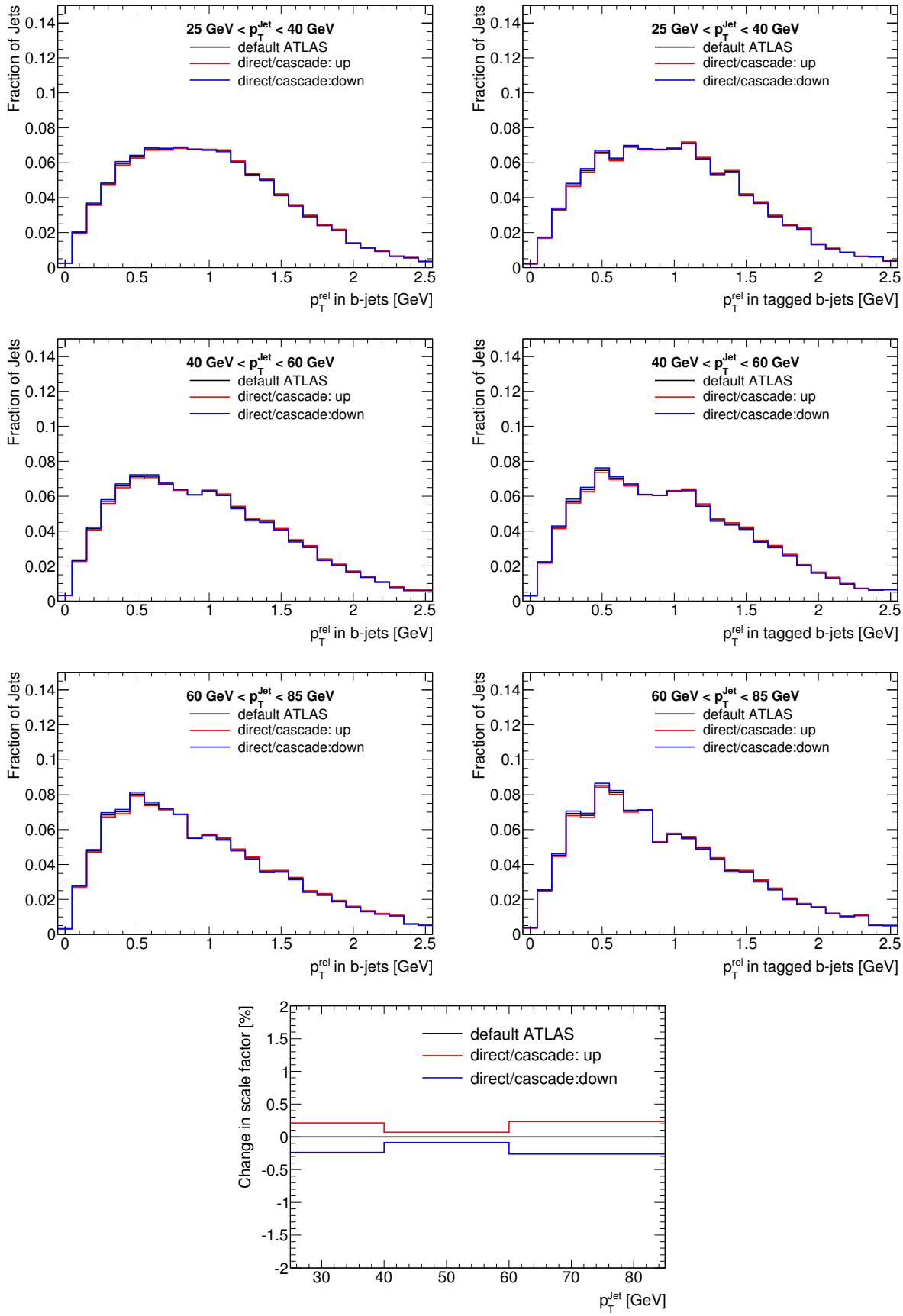

Figure 7.13: b-templates after varying the ratio of the direct $\bar{b} \to \mu^+ X$ to the cascade $\bar{b} \to \bar{c}/c \to \mu^{-/+} X$ component within its measured uncertainty (top three rows) and the resulting change to the efficiency scale factor (bottom).

The systematic uncertainties estimated by reweighting the direct b-decay component in the b-jet templates according to the measurement of the $\bar{b} \to e^+X$ decays by the BaBar experiment and by varying the ratio between the direct and the cascade decays amount to 1.3% in the first bin, 0.2% in the second bin and 0.5% in the last bin. The overall effect on the b-tagging efficiency measurement is rather small. This is due to the fact that even though the measurements of the b-fractions are influenced before and after applying the b-tagging requirement, some of these effects cancel when taking the ratio to calculate the b-tagging efficiency.

7.2.5.2 Fragmentation

The impact of an incorrect modelling of the fragmentation on the efficiency measurement was investigated by varying the fraction x_b of the b-quark energy carried onto the b-hadron up respectively down by 5%. The resulting change to the b-templates is shown in Figure 7.14 (top three rows) as well as the resulting change to the efficiency scale factor (bottom). The uncertainty was estimated to be 0.1%.

7.2.5.3 Other sources of systematic uncertainties

The other sources of systematic uncertainties which were considered in Reference [81] are summarised in the following.

Modelling of the *b*-hadron direction

The direction of the b-hadron is approximated by the direction of the jet and the muon, and is a key component of the p_{T}^{rel} calculation. A comparison between an independent jet axis formed by all tracks in the jet and the calorimeter jet direction revealed small differences in the jet direction resolution between the data and the Monte Carlo simulation [81]. To improve the data to Monte Carlo agreement, the calorimeter-based jet axis in the simulation was smeared using a Gaussian with width of 0.015 radians, and the b- and c-jet templates were rederived. The smearing introduces a bias in the p_{T}^{rel} measurement, which is corrected using the procedure discussed in Section 7.2.6. The change to the b-tagging efficiency results in a systematic uncertainty of 6%.

Non-*b*-jet templates

The combination of three different light-jet template definitions [81] as introduced earlier are used for this measurement: tracks in jets from data, reconstructed muons in true light-jets and tracks in jets from the Pythia JX samples. The final result uses the average efficiency

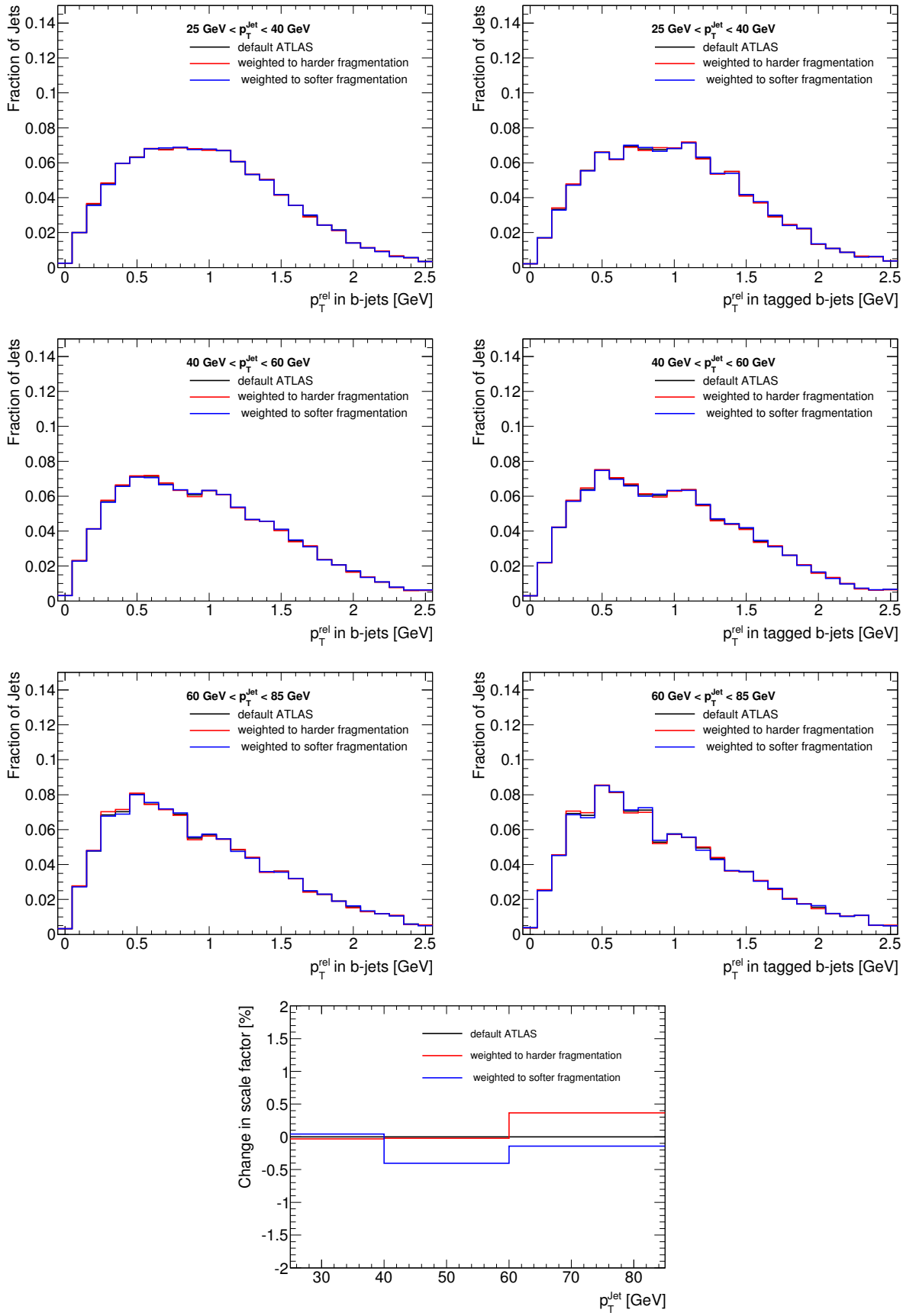

Figure 7.14: Change to b-templates due to the variation of the fraction x_b of the b-quark energy carried onto the b-hadron by 5% (top three rows) and the resulting change to the efficiency scale factor (bottom).

from all three measurements, and the full spread of the efficiencies as systematic uncertainty, as will be discussed in Section 7.2.6. The resulting uncertainties are 6% in all three analysis bins.

Jet p_{T} spectrum

Due to statistical limitations in the simulated JX and JXμ samples used in this analysis, the samples were added together not using the production cross-section weights [81] for the construction of b- and c-jet templates. The reconstructed p_{T}^{jet} spectrum in the simulation was reweighted according to the one measured in data. This introduces a small bias to the underlying truth p_{T} spectrum due to the different resolutions of jets with small respectively large transverse momenta. The correction procedure of the b-tagging efficiency is discussed in Section 7.2.6. This results in systematic uncertainties of 6% in the first analysis bin and 3% in all other bins.

Scale factor for inclusive jets

To investigate the validity of the assumption that the b-tagging efficiency scale factor of jets from semi-leptonic b-decays is equivalent to the efficiency scale factor of b-jets from hadronic decays, the number of displaced tracks in jets were compared both in the data and the Monte Carlo samples [81]. The ratio of the normalised track multiplicities of jets with and without a muon in the simulation was reweighted to match the measured distributions in the data. The changes in the Monte Carlo efficiencies are taken as systematic uncertainties, which vary between 5% in the first bin, 4% in the second bin and 0.7% in the last bin.

p_{T}^{rel} template statistics

To account for the limited statistics in the three flavour templates, 10 000 pseudo-experiments were carried out [81] where each template was varied independently within its statistical errors. The standard deviation of 2% of the resulting b-tagging efficiency measurements was taken as the systematic uncertainty.

Misidentified muons in b-jets

The effect of misidentified muons in the b-jet templates was estimated [81] using the truth information in the Pythia QCD JX samples. The fraction of reconstructed muons not matching a truth track from a real muon was increased by a factor of three and the b-templates rederived. This results in a change of b-tagging efficiency of 0.7%, which is taken as the systematic uncertainty.

Jet energy scale

To estimate the systematic uncertainty associated with an inaccurate description of the jet energy scale in the Monte Carlo simulation compared to the data, the transverse momentum p_{T}^{jet} of each jet was varied within its uncertainty [81] and the p_{T}^{rel} templates for b- and c-quarks rederived. This results in a systematic uncertainty of the p_{T}^{rel} method of 0.2%. This uncertainty does not account for differences in the energy scale of jets from semi-leptonic b-decays.

Modelling of b-production

Three main mechanisms exist for the production of b-jets: flavour creation, flavour excitation and gluon splitting (see Section 2.4.1). The b-tagging efficiency for b-jets from gluon splitting is assumed to be different due to the presence of possibly two b-hadrons in the jet. The systematic uncertainty is estimated by varying the fraction of double-b-jets to single-b-jets in the simulation by a factor of two respectively zero [81], and to rederive the b-templates. The change to the b-tagging efficiency results in a systematic uncertainty of 0.2%.

7.2.6 Corrections Applied to the Efficiency Measurement

The final b-tagging efficiency measurement using p_{T}^{rel} is corrected for three effects [81]:

- Shape of the light-flavour template: The average of the lowest and highest efficiency obtained by using the three different definitions of the light-jet template is used for the final result, with a systematic uncertainty covering its spread.
- Jet p_{T} bias: A correction is applied due to the missing cross section weighting in the simulation. The p_{T}^{rel} fits were carried out using the correct cross section weights, and the baseline efficiency measurement is corrected to these efficiencies. The full change to efficiency between the two measurements is taken as the systematic uncertainty.
- b-hadron direction modelling: The efficiency measurement is corrected for half of the difference in efficiency between the unsmeared and the smeared scenarios. The full difference due to this effect is taken as the systematic uncertainty.

7.2.7 Final b-Tagging Efficiencies

Figure 7.15 shows the final b-tagging efficiencies [81] (left) which have been corrected as described in Section 7.2.6 as well as the resulting efficiency scale factors [81] (right). The measured scale factors and their statistical errors are shown in black and statistical plus systematic uncertainties as a yellow band. The individual values are listed in Table 7.3. The

measured b-tagging efficiency of the SV0 algorithm is consistent with predictions from the Pythia Monte Carlo samples.

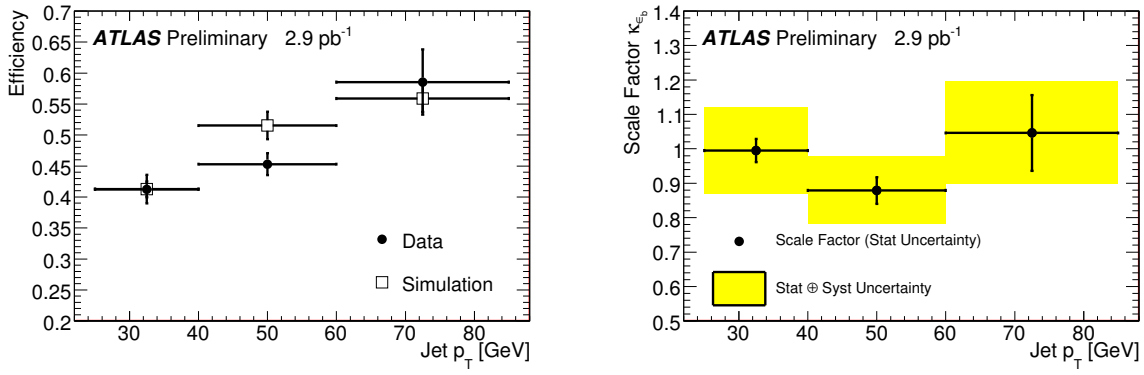

Figure 7.15: Efficiency of the SV0 tagging algorithm in data and Pythia Monte Carlo (left) and the efficiency scale factor (right), from Reference [81].

$\kappa_{\epsilon_b}^{data/sim}$	p_{T}^{jet} [GeV]		
	25-40	40-60	60-85
	$1.00 \pm 0.03 \pm 0.12$	$0.88 \pm 0.04 \pm 0.09$	$1.05 \pm 0.11 \pm 0.10$

Table 7.3: Measured b-tagging scale factors $\kappa_{\epsilon_b}^{data/sim}$, from Reference [81].

This measurement constituted the first data-driven b-tagging efficiency measurement in ATLAS and relied on a very robust method. The measured b-tagging efficiency was used among others for the first ATLAS measurements of the top quark-pair production cross section [82] and the inclusive and dijet cross section of b-jets [26]. More sophisticated measurements of the b-tagging efficiency relying on top-antitop events [58] or the System 8 method [58] will be used in the future, which can measure the efficiency up to much higher jet transverse momenta p_{T}^{jet}. First preliminary results of a measurement using top-antitop events are available [87].

Chapter 8

Measurement of the b-Jet Production Cross Section

This chapter presents the measurement of the b-jet differential cross section in proton-proton collisions at $\sqrt{s} = 7$ TeV by employing soft muons associated to a jet to estimate the fraction of b-jets. The measurement tests the extension of Quantum Chromodynamics calculations to the new energy regime at the LHC, and is of special interest in the light of the initial disagreement at the Tevatron between the data and the Monte Carlo predictions. The measurement uses 4.6 pb^{-1} of data recorded by the ATLAS detector in 2010 and collected with a jet-muon trigger. The production cross section is computed as a function of the transverse momentum of the b-jet and compared to NLO QCD calculations. The fraction of jets originating from b-quarks is determined by fitting the distribution of the muon momentum perpendicular to the b-jet axis, p_{T}^{rel}. The measurement is documented as an ATLAS internal report [88] and as a conference note [89].

8.1 Outline of the Analysis

The analysis begins with a standard set of selection cuts at the trigger and the offline level. These selection cuts are optimised to isolate a sample of muon + jet events, a substantial fraction of which will be b-jets. The fraction of b-jets in the selected data sample is measured by the p_{T}^{rel} method, which can also be used to measure the b-tagging efficiency (see Section 7.2). The distribution of the muon momentum perpendicular to the b-jet axis, p_{T}^{rel}, has different shapes for light-, c- and b-quark jets. Fitting templates for the three different quark-flavour jets independently to the p_{T}^{rel} distribution from data gives an estimate of the fraction of b-jets. The p_{T}^{rel} method is very robust at low jet transverse momenta, but becomes less discriminating at high momenta. For small angles, the uncertainty in p_{T}^{rel} grows linearly with the transverse momentum of the muon due to the jet angular resolution. The observed p_{T}^{rel} distributions, broadened by smearing, ultimately become largely insensitive to the underlying p_{T}^{rel} distribution because of the growth of its uncertainty. The measurement of the b-jet cross

section is therefore carried out within a rapidity region of $|y| < 2.1$ and in four bins of p_{T}^{b-jet} between 30 GeV and 140 GeV, where p_T^{b-jet} denotes the b-jet momentum after correcting for the energy of the muon and the neutrino from the semi-leptonic b-decay. The acceptance is defined by the requirement of at least one jet satisfying these rapidity and momentum cuts. The analysis objects used are jets from the anti-$\mathrm{k_T}$ jet finding algorithm [60] with a resolution parameter of 0.4 and muons using the combined information of inner detectors and muon chambers.

The differential b-jet cross section can be calculated as follows:

$$\frac{d\sigma(pp \to bX, b-jet)}{dp_T^{b-jet}} = \frac{F_b(p_T^{b-jet})N^{jets}}{B\mathcal{L}_{int}\epsilon^{\mu,jet}(p_T^{\mu}, p_T^{b-jet})} \frac{1}{\Delta p_T^{b-jet}}, \tag{8.1}$$

where p_T^{b-jet} denotes the fully corrected b-jet momentum, $F_b(p_T^{b-jet})$ the fraction of jets containing muons from b-quark decays (as measured by p_{T}^{rel}) , N^{jets} the number of selected jets containing a muon, B the branching fraction of $\bar{b} \to \mu X$ to inclusive b-decays and $\mathcal{L}_{int}$ the integrated luminosity. $\epsilon^{\mu,jet}(p_T^{\mu}, p_T^{b-jet})$ is the efficiency for detecting and selecting an event (within the acceptance); it is a product of efficiencies for trigger, jet and muon reconstruction and selection cuts. Δp_T^{b-jet} is the bin width in the considered p_T^{b-jet} bin.

8.2 Data Sample and Event Selection

8.2.1 Data Sample and Luminosity Measurement

This analysis relies on a sample of proton-proton collisions at $\sqrt{s} = 7$ TeV collected between March and November 2010. A run selection based on a good run list is applied, which requires stable beam conditions and fully operational inner detector, muon and calorimeter systems. The effective integrated luminosity of the data sample is $\mathcal{L} = 4615\ \mathrm{nb}^{-1}$ using a jet-muon trigger, corresponding to the full 2010 dataset. This luminosity estimate has an uncertainty of 3.4% [90].

8.2.2 Event Selection

Muon + jet events are selected using the jet-muon trigger as introduced in Section 3.2.5.1. The trigger requires at the second trigger level a reconstructed jet with $p_{\mathrm{T}} > 5$ GeV matched to a reconstructed muon with $p_{\mathrm{T}} > 4$ GeV. In addition to the trigger, a well reconstructed primary vertex with at least ten tracks is required. Table 8.1 gives an overview of the number of events before and after each selection cut.

	Number of events
after trigger	$2.04503 \cdot 10^8$
after good run list	$3.7142 \cdot 10^6$
after PV event selection	$3.70838 \cdot 10^6$

Table 8.1: Number of selected events for the cross section measurement.

8.2.3 Simulated Samples

The simulated samples used in this measurement are outlined in Appendix A.3. Two main simulated samples are used with different selection cuts in the event generation. The J0-J6 QCD samples, referred to as the JX QCD samples, are samples generated in bins with non-overlapping parton transverse momenta $\hat{p_{\mathrm{T}}}$. The J0-J4 muon-filtered QCD samples, referred to as the JXμ QCD samples, in addition to non-overlapping parton transverse momenta $\hat{p_{\mathrm{T}}}$ are required to have a muon with $p_{\mathrm{T}} > 3$ GeV at generator level. These JXμ samples thus contain muons from b- and c-decays, but do not fully simulate muons from in-flight decays, since pions and kaons are treated as stable particles on generator level.

The simulated JX and JXμ samples are constructed such that each of the J0-J6 (J0-J4) samples cover a different jet p_{T} range. They are added according to their cross-sections (listed in Table A.1) to form an inclusive set. Events in the J0 sample, corresponding to the lowest jet p_{T} range, have the largest cross section and therefore get the largest weight. The number of events in the J0 sample is small compared to the cross-section this sample represents. Due to the soft jet p_{T} spectrum in the J0 sample, only a few events pass the event selection. These few jets get a large weight and tend to cause substantial statistical fluctuations in distributions such as p_{T}^{rel}. To circumvent this problem, the lowest of the JX and JXμ samples, J0 and J0μ, are omitted. This will be discussed in more detail in Section 8.7.2.

Table 8.2 lists the different data and simulated samples and their usage in this analysis. The JXμ samples are used to measure reconstruction and selection efficiencies, calculate unfolding corrections, construct templates for b- and c-jets needed for the p_{T}^{rel} measurement and to carry out a closure test of the p_{T}^{rel} method. The QCD JX samples are used to calculate the fraction of b-jets in an inclusive jet sample and to estimate the influence of decay-in flight and punch-through muons on the analysis.

The simulation generally models the data well, but there are a few exceptions. The interaction region is considerably wider in the simulation than in the data. To partly correct for this, the distribution of the primary vertex z position is reweighted in the simulation to the one observed in the data. Furthermore, the beamspot position in the transverse plane is not the same in the data and the simulation, something which is not accounted for in the

Sample	trigger	Usage
Data 2010	μ-jet	measurement of b-fraction
Data 2010	jet	track template
JXμ	μ-jet	b/c templates, p_{T}^{rel} closure test, selection efficiencies, MC spectrum for unfolding
JXμ	-	reconstruction efficiencies, truth spectrum for unfolding
JX	μ-jet	true b-fractions
JX	jet	muon light template

Table 8.2: Data and simulated samples and their usage.

analysis. Since the p_{T} spectrum of jets is harder in the data than in the simulation, this distribution is reweighted in the simulation in order to agree with the data.

8.3 Object Reconstruction and Selection

This analysis relies on a sample of muons in jets. The jets are reconstructed using the anti-k_{T} jet finding algorithm [60] and are calibrated at the hadronic scale which is referred to as $EM + JES$. Only muons reconstructed by the combined algorithm STACO [62] are considered for the analysis.

8.3.1 Jet Preselection

The first step in the jet preselection rejects badly or misreconstructed jets using the recommended loose jet cleaning cuts [85], while the next step preselects the jets for the analysis using the following criteria:

- 20 GeV $< p_{\mathrm{T}}^{jet}(EM + JES) <$ 180 GeV
- $|y^{jet}| < 2.1$

The restriction on the rapidity $|y^{jet}| < 2.1$ originates from the requirement that the complete jet is contained within the acceptance of the inner detectors, which end at $|\eta| < 2.5$.

8.3.2 Muon-in-Jet Selection

Only jets with associated muons are selected for the analysis. The associated muon has to pass the following basic requirements. They will be referred to as reconstruction cuts later on.

- At least seven hits in the silicon detectors (including both SCT and pixel detectors).
- $|\eta^{\mu}| < 2.5$
- Only consider tracks within $\Delta R < 0.4$ of the jet from the inside-out sequence of New Tracking in the inner detectors and the STACO sequence in the muon system.

Additional quality cuts are imposed on the muon track, to insure that it is well reconstructed and to reject a certain amount a background from misreconstructed tracks and decays-in-flight (referred to as selection cuts):

- The transverse momentum of the muon p_{T}^{μ} is greater than 4 GeV.
- At least two hits in the pixel detector.
- At least one hit in the innermost pixel layer.
- At least four hits in the SCT detector.
- No explicit cut on the number of TRT hits on track is applied. However, most tracks do have a successful extension into the TRT and the corresponding improved momentum resolution.
- The track is well reconstructed in the inner detector, i.e. the χ^2 of the track fit divided by the number of degrees of freedom for the fit is smaller than three.
- The transverse impact parameter $|d_0|$ measured with respect to the primary vertex is smaller than 2 mm.
- The longitudinal impact parameter measured with respect to the primary vertex multiplied by $\sin\theta$, $|z_0 \sin\theta|$, is smaller than 2 mm.

If more than one muon in a jet passes these selection cuts, the muon with the highest transverse momentum is used for the analysis.

8.3.3 Validation of Semi-Leptonic b-Jet Correction

The momentum of a jet which contains a b-hadron decaying into a muon can be corrected for the undetected energy in the calorimeters of the muon and its neutrino (called μJES, see Section 4.6.7). The resolution in p_{T}^{b-jet} and the migration of truth jets into different reconstructed p_{T}^{b-jet} bins are inputs into the bin selection procedure and to the unfolding

procedure. The binning does not depend strongly on the resolution, but the unfolding does. The semi-leptonic correction factors [67] were obtained in 2008 using different Monte Carlo simulations. Additional cross checks to validate the correction with the present simulation samples were therefore performed.

A closure test was carried out on the Pythia $JX\mu$ QCD Monte Carlo samples. A 2-dimensional scatter plot of the corrected jet momentum versus true jet momentum is shown in Figure 8.1 (left). To validate the correction factor, the jet response $p_{\mathrm{T}}^{reco}/p_{\mathrm{T}}^{truth}$, where p_{T}^{reco} denotes either the calorimeter momentum p_{T}^{jet} or the fully corrected b-jet momentum p_{T}^{b-jet}, was studied. The result is shown in the same figure on the right. At very low p_{T}^{b-jet}, an over-correction of $\sim 12\%$ can be observed, which is caused by an overestimation of the hadronic response in the calorimeters. This will be corrected by the unfolding procedure, which is outlined in Section 8.6. Overall, a significant improvement in the correct estimate of the b-jet momentum can be reached by using the semi-leptonic correction.

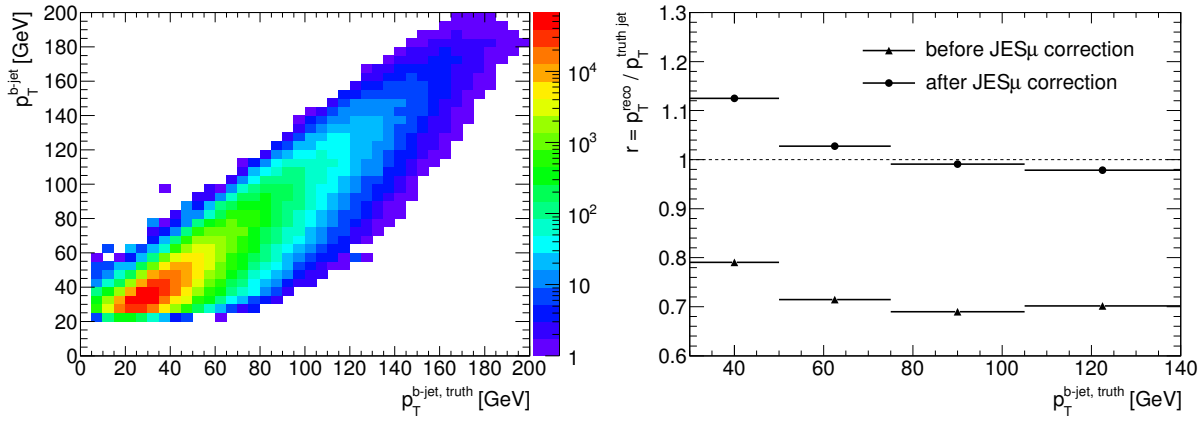

Figure 8.1: Validation of $JES\mu$ correction. 2-dimensional scatter plot of corrected jet momentum versus true jet momentum (left) and the jet response $p_{\mathrm{T}}^{reco}/p_{\mathrm{T}}^{truth}$ before and after applying the μJES correction (right).

Figure 8.2 (left) shows the bin migration of true jets in the corrected b-jet momentum bins, normalised to the number of jets in each truth jet bin. Between 60% and 80% of truth jets are reconstructed in the correct p_{T}^{b-jet} bin. Figure 8.2 (right) shows the same plot, but this time normalised to the number of jets per p_{T}^{b-jet} bin. A non-negligible number of jets (40-44%) migrate from lower truth jet p_{T}^{b-jet} bins to higher bins due to the falling p_{T} spectrum. The unfolding procedure will correct for this effect. The effect of using or not using the semi-leptonic correction factor on the unfolding was studied in detail. The dependence of the unfolding factor on the p_{T}^{b-jet} bin is much smaller if the semi-leptonic correction is used since it improves the jet momentum resolution.

To evaluate the uncertainty of the semi-leptonic correction, the sum of the transverse momenta of all tracks in muon-jets $\Sigma p_{\mathrm{T}}^{\text{tracks in jets}}$ is compared to the transverse momentum of

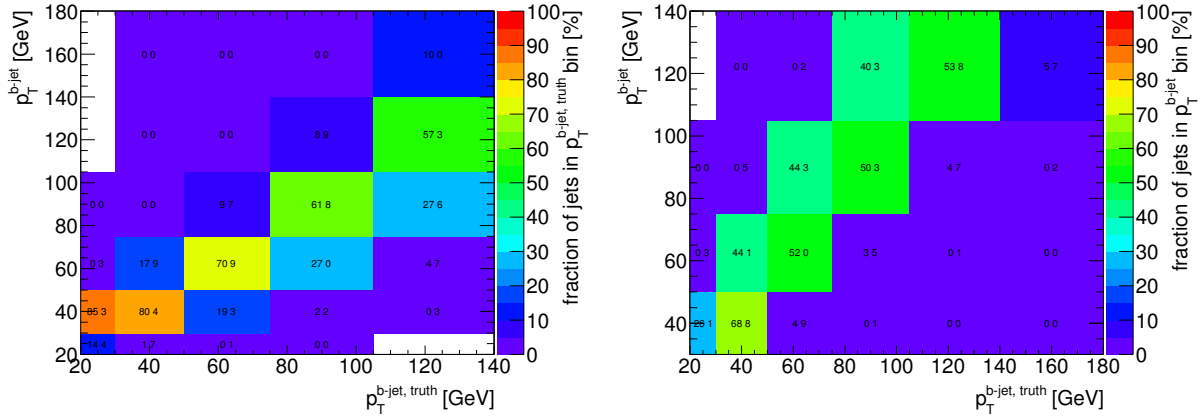

Figure 8.2: Bin migration due to jet energy resolution for corrected b-jets. left: Migration of truth jets normalised from bottom to top in different corrected b-jet bins. right: Fractional contribution of truth jets normalised from left to right in each corrected b-jet bin.

the jet p_{T}^{reco}, following the study in Reference [91]:

$$r^{tracks} = \frac{\Sigma p_{\mathrm{T}}^{\text{tracks in jets}}}{p_{\mathrm{T}}^{reco}} \tag{8.2}$$

p_{T}^{reco} can denote the calorimeter jet momentum p_{T}^{jet}, the jet momentum corrected for the muonic momentum $p_{\mathrm{T}}^{jet} + p_{\mathrm{T}}^{\mu}$ or the fully corrected b-jet transverse momentum p_{T}^{b-jet}. The comparison of this distribution for $p_{\mathrm{T}}^{reco} = p_{\mathrm{T}}^{b-jet}$ between the data and the Pythia JXμ samples in the four analysis bins is presented in Figure 8.3 (upper two rows). Deviations between the data and the Monte Carlo simulations can be used to estimate an uncertainty of the correction. The comparison of the fitted mean values $\sigma(r^{tracks})$ between the data and the Pythia Monte Carlo samples is shown in Figure 8.3 (lower plot). The deviation of $\sigma(r_{Data}^{tracks})/\sigma(r_{MC}^{tracks})$ from unity gives the uncertainty of the semi-leptonic b-jet calibration. The double fraction is shown for the three steps of the correction procedure: only using the calorimeter jet momentum (green), correcting the jet momentum for the muonic momentum only (red) and correcting for the momentum from both the muon and the neutrino (black).

The good agreement between the data and the Pythia Monte Carlo simulation leads to a conservative estimate of the semi-leptonic b-jet uncertainty of 2.5% in all p_{T}^{b-jet} bins. This uncertainty is added in quadrature to the generic jet energy scale uncertainty.

8.3.4 Final Jet Correction and Selection for the Analysis

After applying the semi-leptonic b-jet correction, the final sample of jets for the analysis is selected:

- 25 GeV $< p_{\mathrm{T}}^{b-jet} <$ 180 GeV

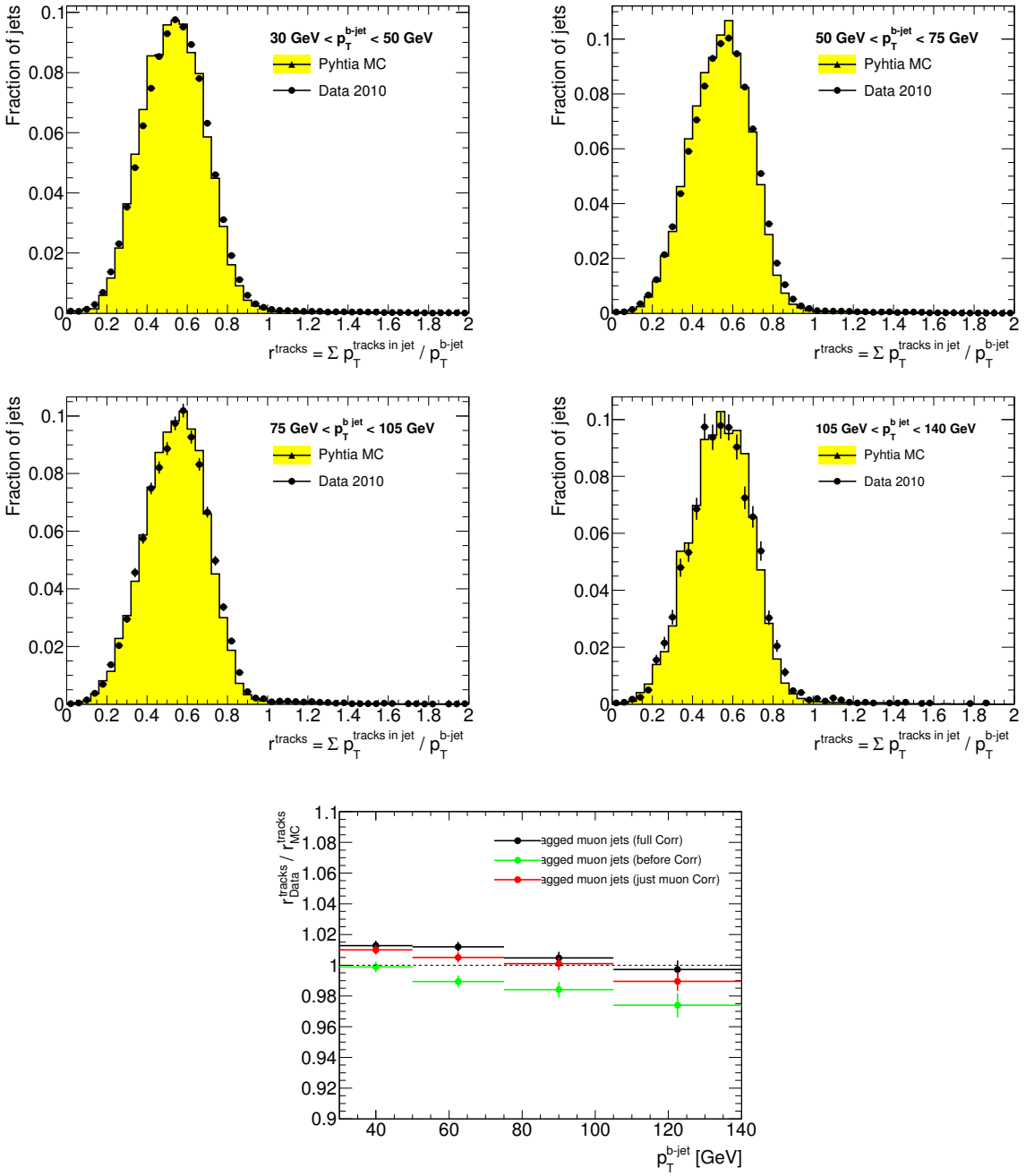

Figure 8.3: Track response $r^{tracks} = \frac{\Sigma p_{\mathrm{T}}^{\text{tracks in jets}}}{p_{\mathrm{T}}^{b-jet}}$ compared between the data and the Pythia JXμ samples (upper two rows) and double fraction of fitted mean value (lower plot) for tagged muon jets. The deviation of the double fraction from 1 gives the uncertainty of the semi-leptonic *b*-jet calibration. The double fraction is shown for three steps of the correction procedure: before, just correcting for the muonic momentum and the full correction.

Table 8.3 shows the number of jets before and after each set of cuts. Due to the change in the transverse momentum of the jet when applying the semi-leptonic correction, some jets migrate from lower $p_{\mathrm{T}}^{\mathrm{jet}}$-bins into higher p_{T}^{b-jet}-bins. This explains why there are more jets after the final jet correction and selection than before.

Number of Jets	p_{T}^{b-jet} [GeV]			
	30-50	50-75	75-105	105-140
after jet cleaning	$2.20282 \cdot 10^6$	636178	187631	59044
after jet preselection	$2.04892 \cdot 10^6$	589062	173926	54939
after muon-in-jet selection	713298	163308	40641	11327
after final jet correction and selection	$1.12919 \cdot 10^6$	387319	92755	24036

Table 8.3: Number of selected jets after all selection cuts.

8.4 Kinematic Ranges for the Analysis

The measurement of the b-jet differential cross section is carried out in bins of p_{T}^{b-jet} over rapidity range y. The y range of this analysis is limited to the region $|y^{jet}| < 2.1$. The p_{T}^{b-jet} binning has been optimised between bin width and resulting migration of jets in neighbouring bins. Four analysis bins are used: 30-50 GeV, 50-75 GeV, 75-105 GeV and 105-140 GeV.

8.5 Efficiencies

The efficiencies for the event and object reconstruction and selection can be divided into four main components:

$$\epsilon^{\mu,jet}(p_{\mathrm{T}}^{\mu}, p_{\mathrm{T}}^{b-jet}) = \epsilon_{trigger} \cdot \epsilon_{reconstruction} \cdot \epsilon_{selection} \cdot C_{acceptance} \tag{8.3}$$

Care has been taken to minimise the correlation between the components by dividing them into independent steps. All efficiencies are listed in Table 8.4.

8.5.1 Jet-Muon Trigger Efficiency

The jet-muon trigger efficiency is obtained from data in three steps [88], using fully corrected jets with associated muons for the calculation. The first step consists of measuring the

efficiency of the single jet trigger with respect to the fully efficient minimum bias trigger. In the second step, the efficiency of the jet-muon trigger with respect to the single jet trigger is measured. In the third step, the two efficiencies are combined to get the overall efficiency of the trigger.

8.5.2 Reconstruction Efficiencies

The reconstruction efficiency can be split into two components, the jet reconstruction and the muon reconstruction efficiency:

$$\epsilon_{reconstruction} = \epsilon_{jet-rec} \cdot \epsilon_{muon-rec} \tag{8.4}$$

8.5.2.1 Jet reconstruction efficiency

The jet reconstruction efficiency is calculated according to the following equation:

$$\epsilon_{jet-rec} = \frac{\#\text{ reco jets matched to truth with } dR < 0.4 \;\&\; |y^{reco\ jet}| < 2.1}{\#\text{ true b} - \text{jets where } \bar{b} \to \mu X \;\&\; |y^{true\ b-jet}| < 2.1} \tag{8.5}$$

The Pythia JXμ samples were used without a trigger requirement in the event selection but keeping the cut on the number of tracks associated to the primary vertex. Figure 8.4 (left) shows the efficiency to reconstruct a jet within $|y^{jet}| < 2.1$ versus the true transverse momentum of the b-jet $p_{\mathrm{T}}^{true\ b-jet}$. The efficiency is flat over the shown $p_{\mathrm{T}}^{true\ b-jet}$ region and is above 96%.

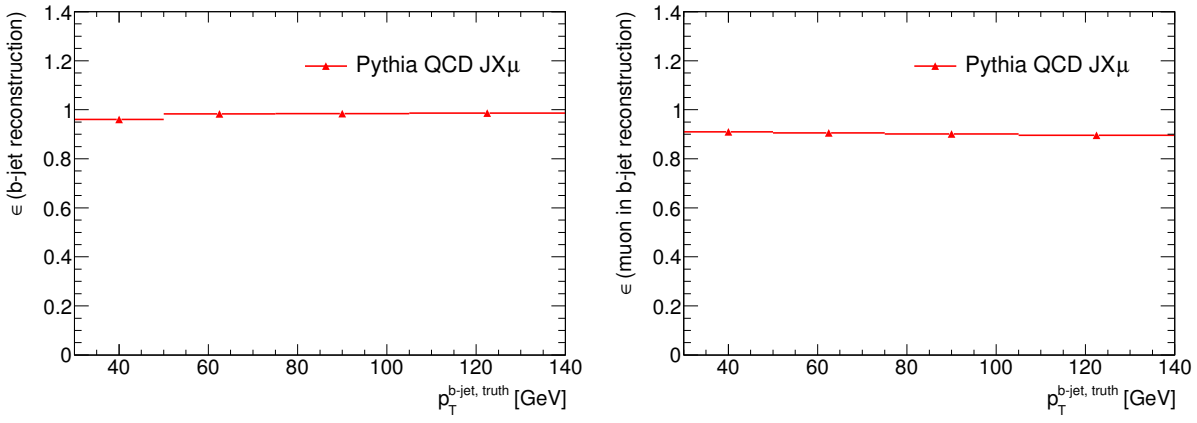

Figure 8.4: Jet and muon reconstruction efficiencies versus true b-jet transverse momentum $p_{\mathrm{T}}^{b-jet,truth}$ (left respectively right), calculated using the truth record in the Pythia QCD JXμ samples.

8.5.2.2 Muon reconstruction efficiency

The muon reconstruction efficiency is calculated as follows:

$$\epsilon_{muon-rec} = \frac{\text{\# reco muons matched to truth jet}}{\text{\# true reconstructable muons within dR} < 0.3 \text{ of } \bar{b} \to \mu X - \text{jets}} \tag{8.6}$$

A true muon is reconstructable if it fulfils $|\eta^{true\ \mu}| < 2.5$ and $p_{\mathrm{T}}^{true\ \mu} > 4$ GeV. A muon is called reconstructed if it fulfils the reconstruction cuts defined in Section 8.3.2, if more than 70% of the weighted hit content of the inner detector track originates from a single generated particle and if the reconstructed track is within $dR < 0.4$ of the truth jet.

The Pythia JXμ samples were used without a trigger requirement in the event selection but with the cut on the number of tracks associated to the primary vertex. The Monte Carlo reconstruction efficiency was corrected for differences between the data and the Monte Carlo simulation with muon-by-muon scale factors [92]. The resulting muon reconstruction efficiency versus the true transverse momentum of the b-jet $p_{\mathrm{T}}^{true\ b-jet}$ is shown in Figure 8.4 (right). The efficiency is flat over the shown $p_{\mathrm{T}}^{true\ b-jet}$ region and is above 89%.

8.5.3 Selection Efficiencies

The overall efficiency to select b-jets from $\bar{b} \to \mu X$ decays can be divided into three components:

$$\epsilon_{selection} = \epsilon_{PV\ event-sel} \cdot \epsilon_{finaljet-sel} \cdot \epsilon_{muon-sel}. \tag{8.7}$$

The efficiencies are obtained using the Pythia JXμ samples. To exclude correlations, the selection criteria used in this step are distinct from the reconstruction cuts used in the previous section.

8.5.3.1 Primary vertex event selection efficiency

The primary vertex event selection efficiency is calculated by

$$\epsilon_{PV\ event-sel} = \frac{\text{\# true } \bar{\mathrm{b}} \to \mu\mathrm{X} - \text{jets after PV event selection}}{\text{\# true } \bar{\mathrm{b}} \to \mu\mathrm{X} - \text{jets before PV event selection}} \tag{8.8}$$

The primary vertex event selection requires a reconstructed primary vertex with at least ten associated tracks. The efficiency for this selection is above 99% and is shown in Figure 8.5 (upper left) versus the true transverse momentum of the b-jet $p_{\mathrm{T}}^{true\ b-jet}$.

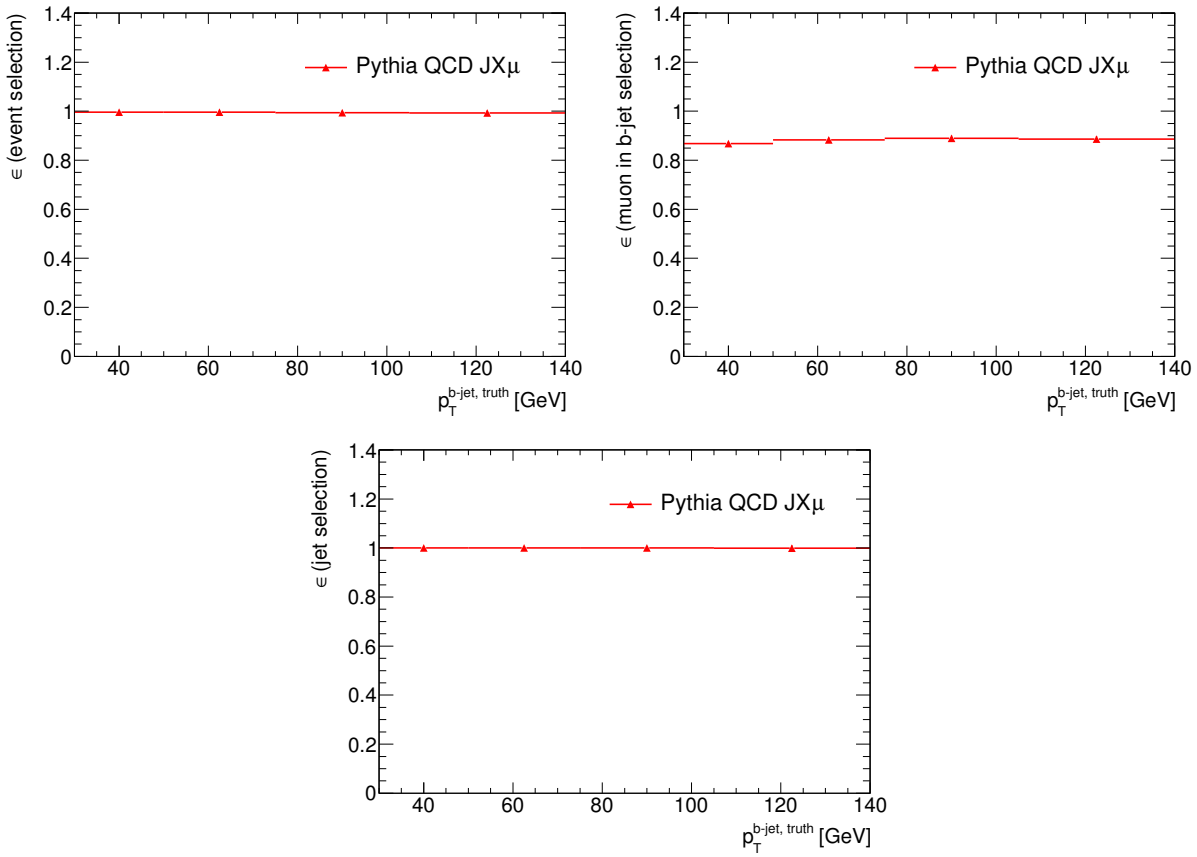

Figure 8.5: Primary vertex selection efficiency (upper left), muon selection efficiency (upper right) and final jet selection efficiency (lower plot) on Pythia QCD JXμ samples versus true b-jet momentum $p_{\mathrm{T}}^{b-jet,truth}$.

8.5.3.2 Muon selection efficiency

The muon selection efficiency is calculated by

$$\epsilon_{jet-sel} = \frac{\#\text{ true } \bar{\mathrm{b}} \to \mu\mathrm{X} - \text{jets after muon selection}}{\#\text{ true } \bar{\mathrm{b}} \to \mu\mathrm{X} - \text{jets before muon selection}} \tag{8.9}$$

The muon selection cuts are distinct from the reconstruction cuts used to calculate the reconstruction efficiency in the section before, and are listed in Section 8.3.2. The muon selection efficiency is above 86% and is shown in Figure 8.5 (upper right) versus the true transverse momentum of the b-jet $p_{\mathrm{T}}^{true\ b-jet}$.

8.5.3.3 Jet selection efficiency

The jet selection efficiency is calculated by

$$\epsilon_{jet-sel} = \frac{\#\text{ true } \bar{\text{b}} \rightarrow \mu\text{X} - \text{jets after final jet selection}}{\#\text{ true } \bar{\text{b}} \rightarrow \mu\text{X} - \text{jets before final jet selection}} \tag{8.10}$$

The final jet selection selects the jets after the semi-leptonic correction for the missing muon and neutrino energy has been applied. The efficiency for this selection is 100% and is shown in Figure 8.5 (lower plot) versus the true transverse momentum of the b-jet $p_{\mathrm{T}}^{true\ b-jet}$.

8.5.4 Acceptance Correction

For the efficiency calculations discussed so far, the fraction of muons from $\bar{b} \rightarrow \mu X$ decays which have a transverse momentum of $p_{\mathrm{T}}^{\mu} < 4$ GeV and thus will typically not reach the muon system have not been taken into account. Figure 8.6 shows the acceptance, which is defined as

$$C_{Acceptance} = \frac{\#\text{ true muons in jets from } \bar{\text{b}} \rightarrow \mu\text{X} - \text{decays with } \mathrm{p_T}(\mu) > 4\text{ GeV}}{\text{all true muons in jets from } \bar{\text{b}} \rightarrow \mu\text{X} - \text{decays}} \tag{8.11}$$

The acceptance is above 91%.

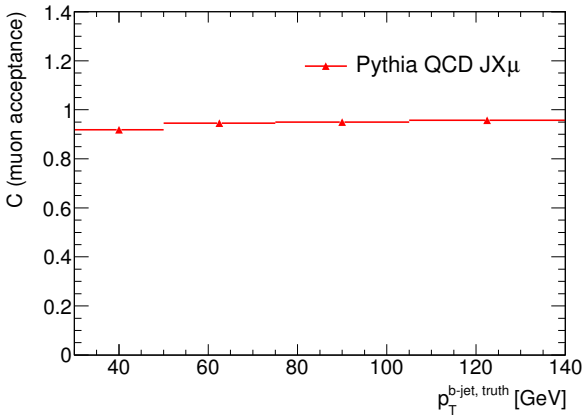

Figure 8.6: Muon acceptance correction for muons outside the muon system acceptance.

8.5.5 Backgrounds to the Analysis

The main source of background for this measurement are misidentified or fake muons associated to a jet. They originate from decays in flight or hadrons reaching the muon system and thus being reconstructed as muons ("punch-through"). These sources of muons in jets should have a significant different p_{T}^{rel} shape than muons from real b-decays. To account for this,

data-driven light-jet templates are used for the p_{T}^{rel} measurement. An additional systematic uncertainty is assigned to the p_{T}^{rel} fit to account for misidentified muons in real b-jets, which do not originate from $\bar{b} \to \mu X$ decays. This is discussed in Section 8.7.5.7.

8.5.6 Summary of Efficiencies

Table 8.4 lists the individual values for each efficiency in bins of the true or reconstructed transverse momentum of the b-jet. The overall efficiency $\epsilon^{\mu,jet}(p_T^{\mu}, p_T^{b-jet})$ varies between 24.4% in the first and 47.5% in the last analysis bin and is dominated by the trigger efficiency.

Efficiencies [%]	p_{T}^{b-jet} [GeV]			
	30-50	50-75	75-105	105-140
Trigger efficiency	35.2 (1.3)	52.4 (2.5)	58.3 (5.4)	63.9 (13.5)
PV event selection efficiency	99.6 (0.8)	99.6 (0.8)	99.3 (0.8)	99.3 (1.1)
Jet reconstruction efficiency	96.0 (0.4)	98.3 (0.6)	98.4 (0.7)	98.6 (0.9)
Jet selection efficiency	100.0 (0.9)	100.0 (0.9)	100.0 (0.9)	100.0 (1.2)
Muon reconstruction efficiency	91.0 (0.4)	90.6 (0.6)	90.2 (0.6)	89.6 (0.8)
Muon selection efficiency	86.7 (0.8)	88.3 (1.0)	88.9 (1.1)	88.6 (1.2)
Muon acceptance	91.9 (0.7)	94.6 (0.8)	95.0 (0.8)	95.7 (1.0)
Overall efficiency	24.4 (1.0)	38.8 (2.0)	43.4 (4.1)	47.5 (10.1)

Table 8.4: Reconstruction and selection efficiencies. Numbers in parentheses correspond to statistical errors.

8.6 Unfolding

The unfolding procedure corrects the reconstructed and fully corrected number of jets per analysis bin back to the true number of jets in each bin. It therefore corrects for the migration of jets between bins as well as any remaining inefficiencies or detector effects not been considered. The unfolding factor is calculated using the Pythia QCD JXμ samples. In order to calculate the unfolding factors, the true simulated number of b-jets from $\bar{b} \to \mu X$ decays, $T_i^{N^{jets}}$, is divided by the efficiency-corrected number of reconstructed jets with associated muon fulfilling the selection criteria for the analysis $R_i^{N^{jets}}$. The reconstructed Monte Carlo spectrum is corrected for reconstruction and selection efficiencies (trigger, jet and muon reconstruction and selection, muon acceptance) as well as the true fraction of b-jets in the sample. The trigger efficiency is taken from the Pythia JXμ samples. The correction factor

C_i is then calculated using

$$C_i = \frac{T_i^{N^{jets}}}{R_i^{N^{jets}}}. \tag{8.12}$$

The correction factors in each bin are listed in Table 8.5 and presented in Figure 8.7 (left). The systematic uncertainties (shown in yellow) were estimated by varying the jet energies within their uncertainties.

C_i	p_{T}^{b-jet} [GeV]			
	30-50	50-75	75-105	105-140
	$1.11 \pm 0.02\ ^{+0.01}_{-0.01}$	$0.78 \pm 0.02\ ^{+0.14}_{-0.11}$	$0.83 \pm 0.02\ ^{+0.16}_{-0.13}$	$0.90 \pm 0.03\ ^{+0.18}_{-0.14}$

Table 8.5: Correction factors for unfolding. The first error corresponds to the statistical error, the second one to a systematic error due to the combined jet and semi-leptonic b-jet energy scale uncertainty.

The unfolded number of jets in the data, $U_i^{N^{jets}}$, is obtained by multiplying the measured number of jets in data $D_i^{N^{jets}}$ by the correction factor

$$U_i^{N^{jets}} = C_i \cdot D_i^{N^{jets}}. \tag{8.13}$$

Both the data spectrum, $D_i^{N^{jets}}$, and the unfolded spectrum, $U_i^{N^{jets}}$, are shown in Figure 8.7 (right).

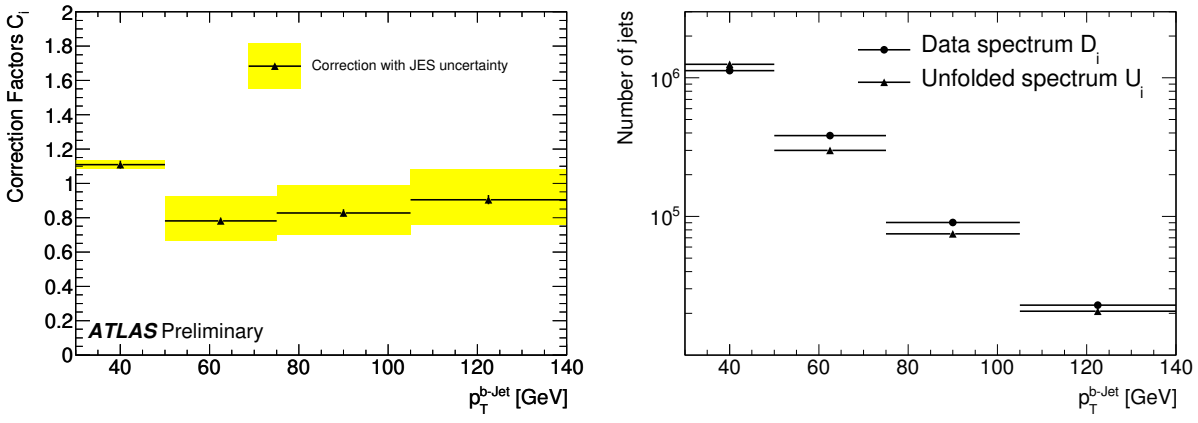

Figure 8.7: Unfolding correction factors (left) and the number of jets in the data before and after unfolding (right). The systematic uncertainties of the unfolding factors (in yellow) were estimated by varying the jet energies within their uncertainties.

The influence of bin-to-bin migrations due to the jet energy resolution was studied separately. The correction factor due to this effect, obtained by comparing the number of

true and reconstructed jets in each analysis bin, is shown in Figure 8.8 (left). The resulting unfolding factors are shown in in the same figure (right). Apart from the first bin, the unfolding factors are now very close to unity. This shows that the bin migrations have a large influence on the shape and magnitude of the unfolding correction factors.

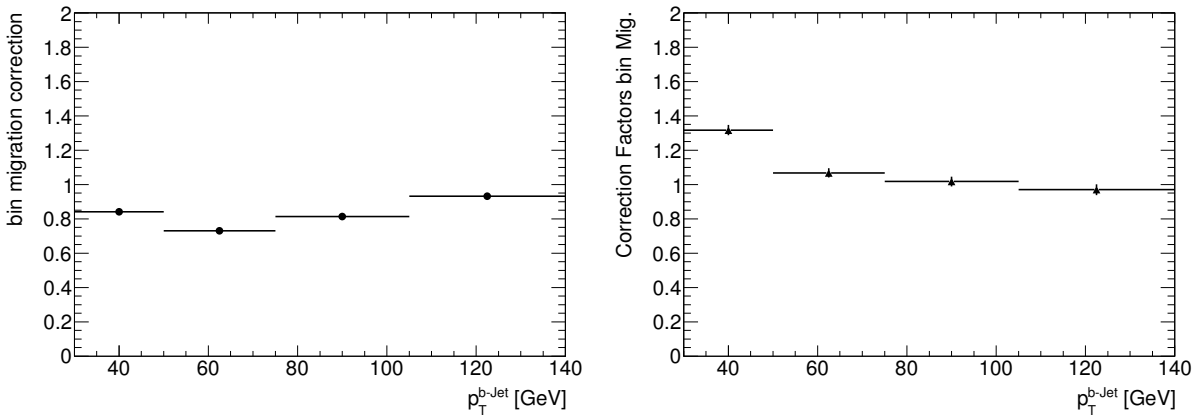

Figure 8.8: Correction factor due to bin migration (left) and the resulting unfolding factors after applying the bin migration correction (right).

8.7 *b*-Fraction Measurement using Muons in Jets

8.7.1 Definition of p_{T}^{rel}

The p_{T}^{rel} is calculated from the muon momentum $\vec{p}^{\,\mu}$ and the b-jet momentum $\vec{p}^{\,b-jet}$. The vector $\vec{p}^{\,b-jet}$ estimates the b-quark direction, from this the component of the muon momentum $\vec{p}^{\,\mu}$ perpendicular to this direction is taken:

$$p_{\mathrm{T}}^{rel} = \frac{\left|\vec{p}^{\,\mu} \times \vec{p}^{\,b-jet}\right|}{\left|\vec{p}^{\,b-jet}\right|} \tag{8.14}$$

Templates for the transverse momentum of muons in jets relative to the jet axis, p_{T}^{rel}, are constructed for b-, c- and light-quark jets separately. These templates are fit to the data to obtain the fraction of b-jets in the data sample. The fits are performed using a binned maximum likelihood method where each bin i is treated as an independent Poisson variable,

$$\begin{aligned} T(i) &= F_b \cdot T_b(i) + F_c \cdot T_c(i) + F_{light} \cdot T_{light}(i) \\ \mathcal{F}_{likelihood} &= -\Sigma_{i=0}^{N_{bins}-1}[D(i) \cdot \log T(i) - T(i)]. \end{aligned} \tag{8.15}$$

F_f denotes the fraction of jets with flavour f ($f = b,\ c$ or $light$), $T_f(i)$ bin i in the p_{T}^{rel} template of flavour f and $D(i)$ the measured number of jets in the data in bin i of the p_{T}^{rel} distribution. Equation (8.15) is minimised by fitting all three flavour fractions F_f independently. The likelihood function $\mathcal{F}_{likelihood}$ does not include a term for statistical fluctuations in the p_{T}^{rel} templates. A systematic uncertainty is assigned to account for the finite template statistics. Table 8.2 gives an overview of the data and simulated samples used for the p_{T}^{rel} measurement.

8.7.2 p_{T}^{rel} Templates for *b*-, *c*- and Light-Quark Jets

8.7.2.1 *b*- and *c*-jet templates

The p_{T}^{rel} templates for b- and c-jets are computed using the JXμ QCD samples. The b-jet template consists of the direct decay component $\bar{b} \rightarrow \mu^{+} X$ and the cascade component $\bar{b} \rightarrow \bar{c}/c \rightarrow \mu^{-/+} X$. Section 8.7.5.2 studies in more detail the influence of the b-decay modelling on the p_{T}^{rel} measurement. Figure 8.9 shows the shape of the b-templates (top two rows) and the c-templates (bottom two rows) for each of the JXμ subsamples for all four analysis bins. Adding these templates according to their respective cross sections will result in noisy templates due to the large influence of the J0 sample. The shape of the templates is different for the individual JXμ samples. This change is large enough to influence the p_{T}^{rel} fit. Therefore cross section weighted templates excluding the J0 sample will be used in the analysis.

8.7.2.2 Light-jet templates

The determination of the light-jet template is more complicated. The statistics of muons in true light-quark jets from the Pythia QCD Monte Carlo samples is not sufficient for a reliable fit. Additionally, the simulation does not fully model sources of muons in light-jets such as decays-in-flight and hadrons which reach the muon system ("punch-through" particles). Several definitions of the light-jet template are discussed in the following, one definition using the truth record and three possible data-driven light-jet template definitions. All four definitions are compared in Figure 8.10, obtained from the QCD JX samples.

Muons in light-jets: Reconstructed muons in real light-jets, which are selected using the truth record in the JX samples. The templates are shown in black in Figure 8.10.

Muons in anti-tagged jets: Reconstructed muons in jets which are identified by the b-tagging software as having a very low probability of originating from a b-quark (*anti-tagging*). The baseline tagging combination of the impact parameter algorithm IP3D and the secondary vertex algorithm SV1 is used for the anti-tagging. During the event selection, only events where all jets have a combined weight less then -0.81 are selected. Templates constructed

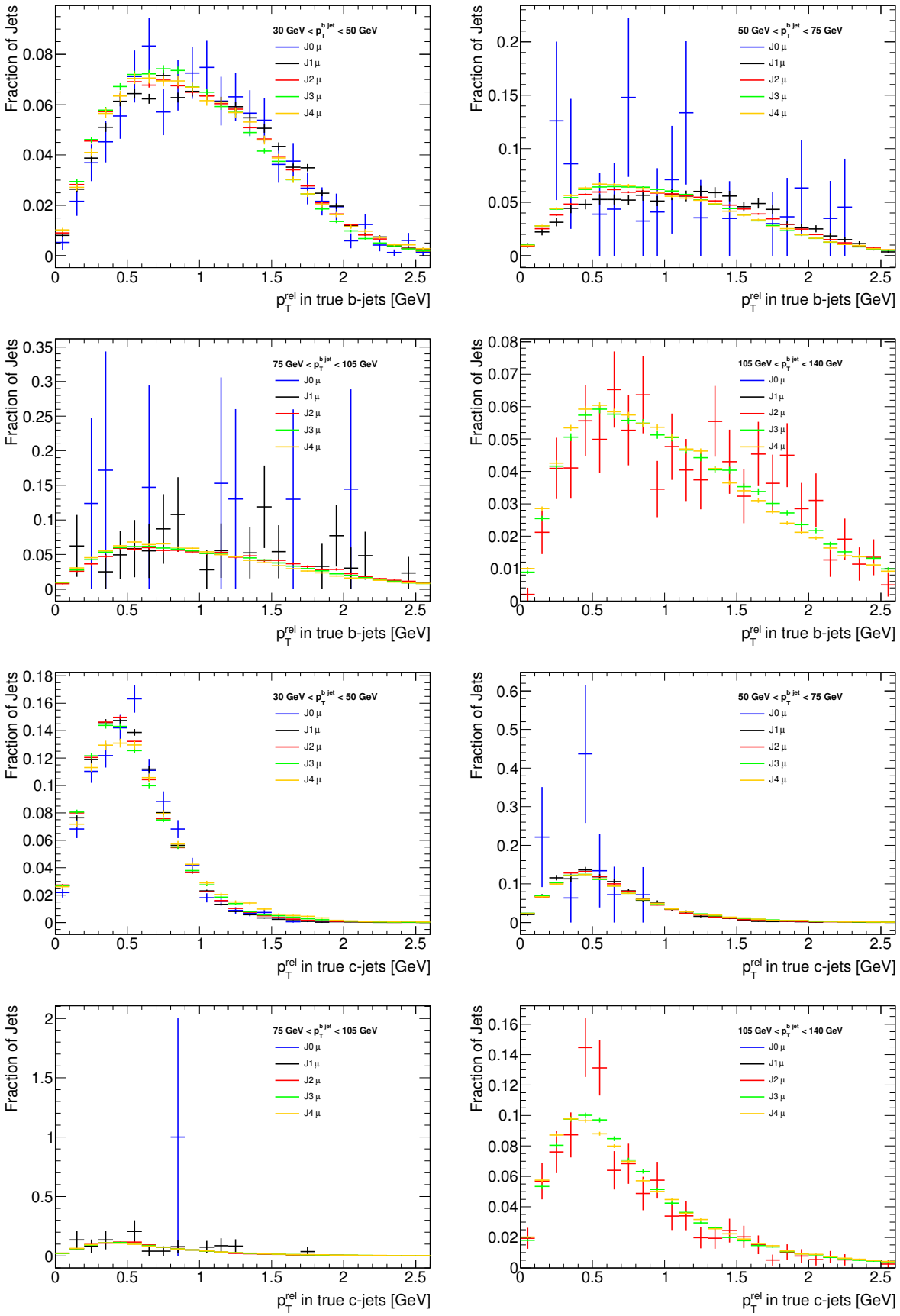

Figure 8.9: *b*-templates (upper two rows) and *c*-templates (lower two rows) from each JXμ sample. The *b*-jet template consists of the direct decay component $\bar{b} \to \mu^+ X$ and the cascade component $\bar{b} \to \bar{c}/c \to \mu^{-/+} X$.

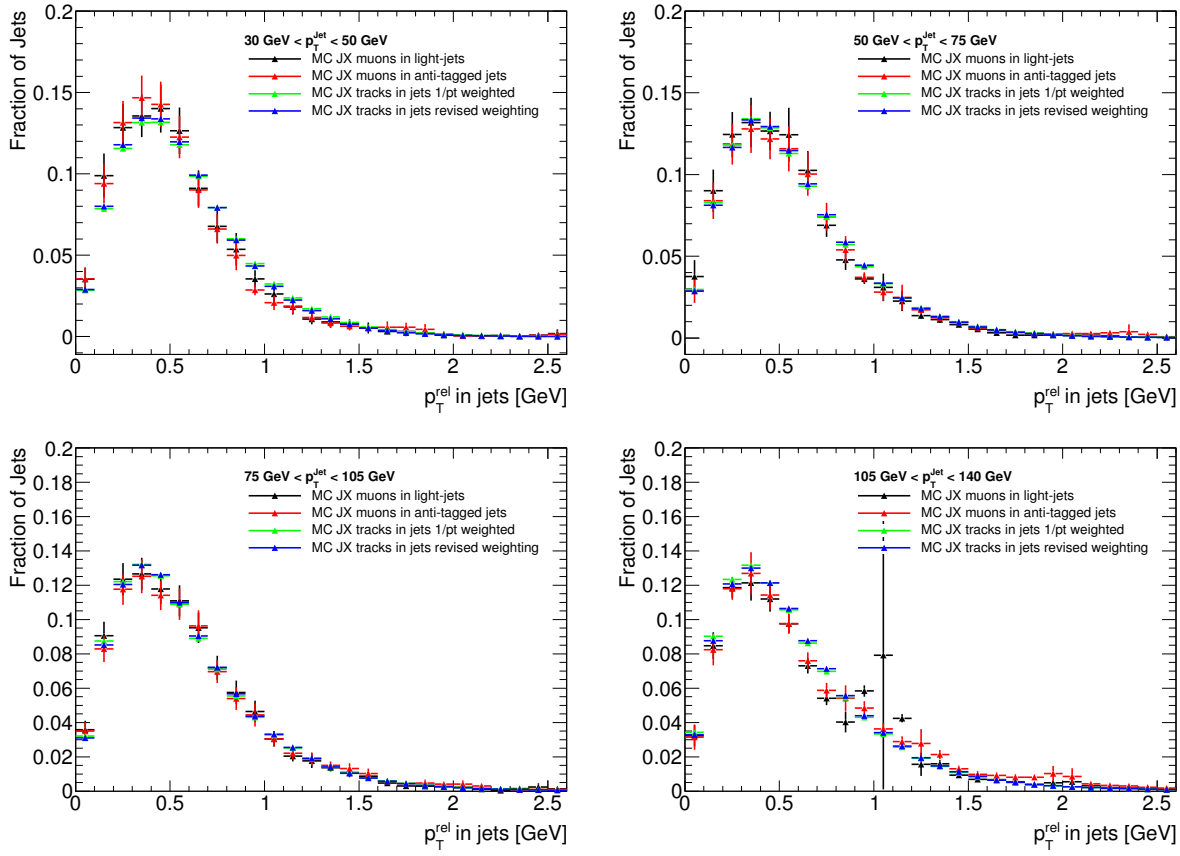

Figure 8.10: Different definitions of light-templates on Pythia QCD JX samples.

by this method contain a non-negligible contamination of b-jets (between 3 and 5%), which needs to be corrected for during the fit. The templates are shown in red in Figure 8.10.

Reweighted tracks in jets: Studies on Monte Carlo show that the dominant source of muons in light-jets are decays-in-flight from pions or kaons [88]. The probability for such a decay-in-flight is anti-proportional to the transverse momentum of the particle. One possibility for constructing the light-jet template is therefore to use tracks in jets, and to weigh them according to this probability with $1/p_{\mathrm{T}}$. The resulting templates are shown in green in Figure 8.10. This is a very coarse description of the probability for a decay in flight. A more refined weighting function was derived using the QCD JX samples [88] and is shown in blue. When making templates based on tracks in jets, a correction is applied to the jet as if the track was a muon. The track momentum is subtracted from the jet momentum and replaced by the average energy loss of a muon in the calorimeter (≈ 3 GeV). All kinematic cuts normally placed on the muon-jet are then applied to the corrected jet. The semi-leptonic correction is applied to this manipulated jet in the same way it is done for real b-jets containing a muon. The p_{T}^{rel} variable is subsequently calculated in the same way as for b- and c-jets. To reduce the influence of tracks from b-decays, the anti-tagging procedure as described for the anti-tagged light-jet template is used for the construction of the track-based ones as well.

Figure 8.10 shows that the track-based templates give a very good description of the real p_{T}^{rel} shape in light-jets at high jet p_{T}, but some small deviations at low jet p_{T}. Since these templates do not suffer from b-jet contamination, the track-templates using the refined weighting function are used for the baseline measurement and to derive the systematic uncertainties. The measurement is corrected for the bias introduced by this choice of light-jet template as discussed in Section 8.7.6.1. A systematic uncertainty to account for this effect is estimated in Section 8.7.5.1.

Figure 8.11 shows the templates for b-, c- and light-quark jets. The b- and c-templates from Pythia Monte Carlo simulations are shown as well as the default data-driven light-jet template of tracks in jets using the refined weighting function. The b- and c-templates are constructed by adding the different JXμ samples weighted according to their respective production cross sections.

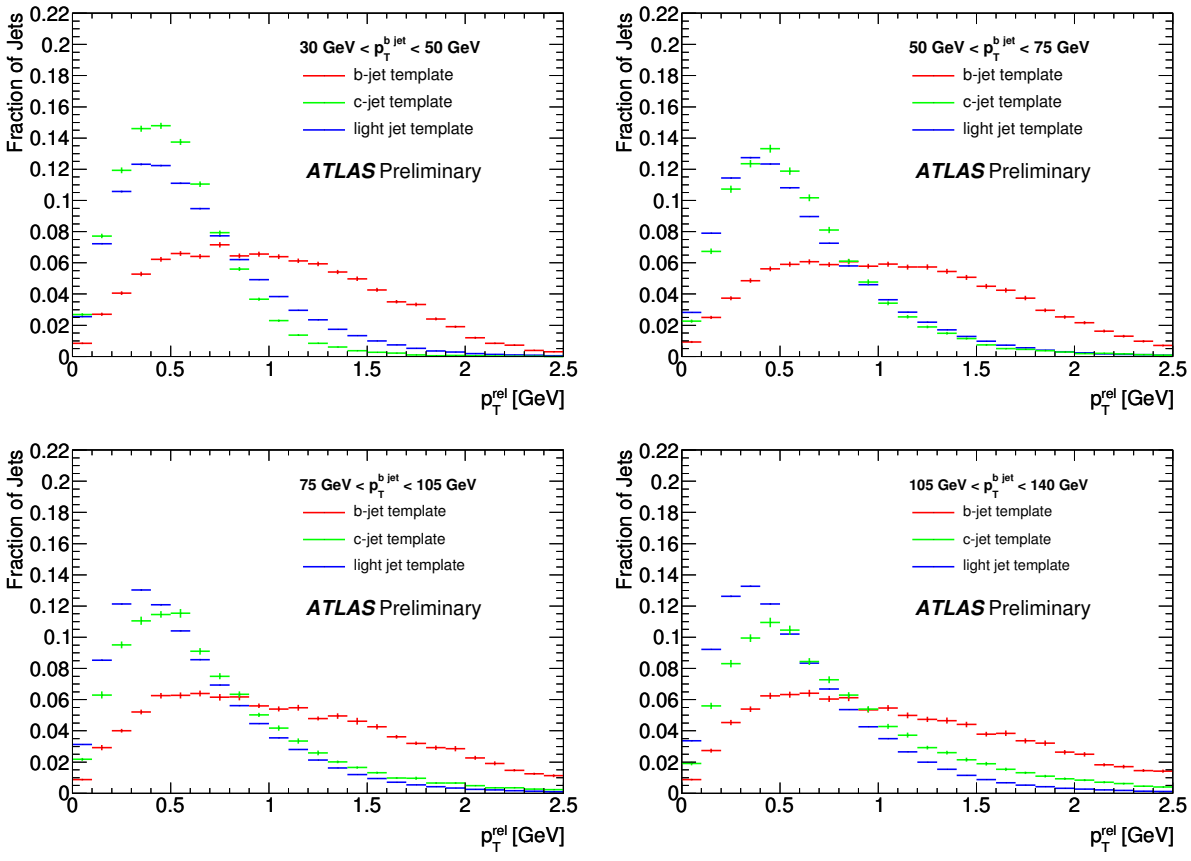

Figure 8.11: Templates for the p_{T}^{rel} fits. The b- and c-templates from the Pythia JXμ samples are weighted according to their production cross sections, the light-jet template is the default template of weighted tracks in jets from data.

8.7.3 Closure-Test using Monte Carlo Simulations

A closure test was carried out on the simulated JXμ samples to validate the p_{T}^{rel} method. Figure 8.12 shows the fits of the p_{T}^{rel} templates to the inclusive p_{T}^{rel} distributions in the JXμ samples. The fits in each of the four analysis bins are shown as well as the resulting b-fractions. The true b-fractions in the simulation are measured within 1 and 4% using the p_{T}^{rel} method.

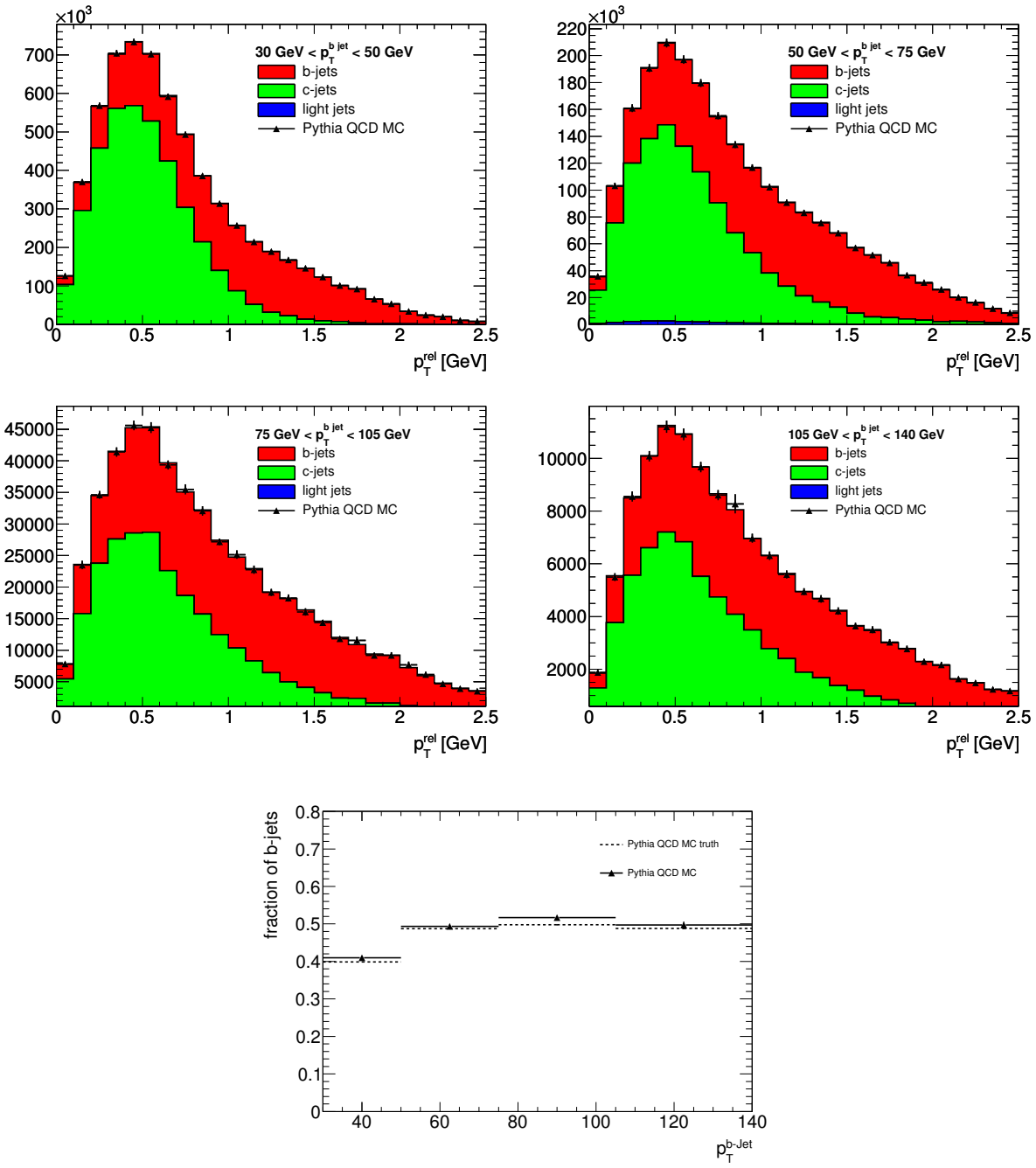

Figure 8.12: p_{T}^{rel} fits using the Pythia QCD JXμ samples. The fits in all considered p_{T}^{b-jet}-bins are shown (upper two rows) along with the b-fractions (lower plot).

8.7.4 b-Fraction Measurement in the Data

Figure 8.13 presents the raw b-fraction measurement in the data using the p_{T}^{rel} method. The p_{T}^{rel} fits in the four analysis bins are shown in the upper two rows and the measured b-fractions in the lower plot. The measurement is compared to the true b-fractions predicted by the Pythia QCD JX samples. The systematic uncertainties associated with the p_{T}^{rel} method are discussed in the next section, and the procedure to correct for biases in the measurement in Section 8.7.6. The final b-fractions are presented in Section 8.7.7.

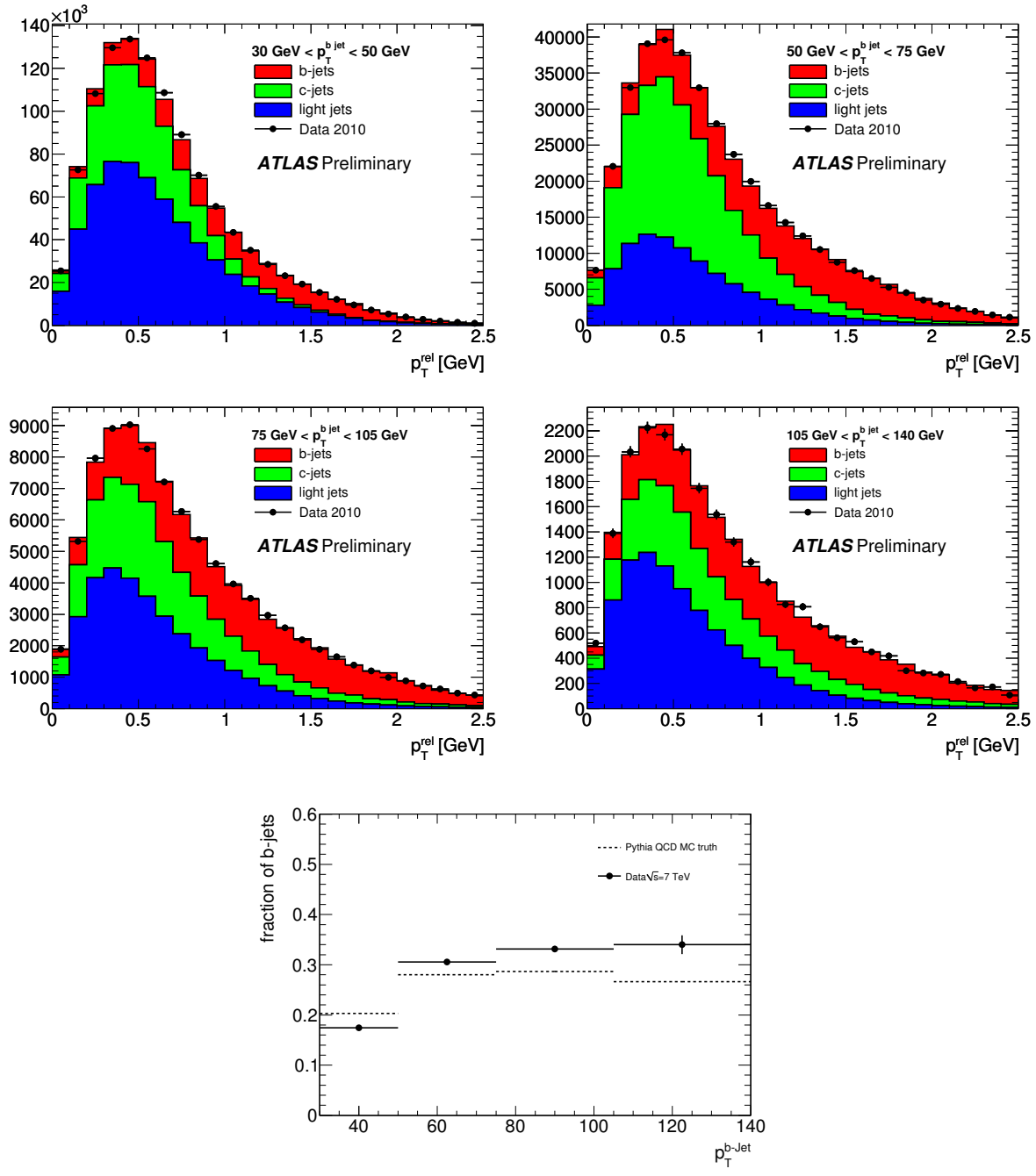

Figure 8.13: p_{T}^{rel} fits to the data in the four analysis bins (upper two rows) and resulting b-fractions (lower plot).

8.7.5 Study of Systematic Uncertainties

Systematic effects that contribute to the uncertainty of the b-jet fraction measurement were studied. A new series of templates was constructed for each effect and the b-jet fraction re-evaluated. The deviation of these b-jet fraction measurements from the baseline measurement is taken as the uncertainty. Most uncertainties were considered as discussed in Section 7.2.5 and in Reference [81]. The construction of the altered templates and the corresponding uncertainties on the p_{T}^{rel} method are discussed here. A summary of the uncertainties can be found in Table 8.6.

8.7.5.1 Definition of light-jet template

As discussed previously in Section 8.7.2.2, the definition of the light-jet templates poses some difficulties. In addition to the default p_{T}^{rel} light-jet templates from weighted tracks in jets, templates from muons in anti-tagged jets are also valid. They are used to derive the systematic uncertainty and to correct the baseline measurement. Figure 8.14 shows the light-jet templates from the two definitions (top two rows) and the resulting change to the b-fractions (lower plots). When using the anti-tagged template, the fitted b-fraction is corrected for the b-contamination in the template. For this, estimates from Pythia QCD Monte Carlo samples are used. The variation of the b-contamination by $\pm$ 50% is shown as well in Figure 8.14. It is clearly visible that the p_{T}^{rel} fits are very sensitive to the shape of the light template. Even moderate variations in the light-template shape result in significant changes in the measured b-fractions. Since both methods of defining the light-jet template are valid, the true value of the measured b-fraction is assumed to lie between the measured values. The measured b-fraction is therefore corrected for this effect as detailed in Section 8.7.6.1. After correction, the relative systematic uncertainty varies between ± 2 and ± 18%.

8.7.5.2 Semi-leptonic b-decay modelling

The shape of the muon momentum spectrum in the b-hadron rest frame, denoted as p^*, directly affects the shape of the p_{T}^{rel} distribution for b-jets. Therefore uncertainties in the modelling of the p^* spectrum need to be taken into account. The p^* spectrum has two components, one from direct $\bar{b} \to \mu^+ X$ decays and one from cascade $\bar{b} \to \bar{c}/c \to \mu^{-/+} X$ decays, as shown in Figure 8.15.

The p^* spectrum of the direct and the cascade b-decay component is compared between the Pythia and the Evtgen generator in Figure 8.16 (top). A sample of fully simulated and reconstructed events from the Evtgen generator is compared to the Pythia JX samples. Unfortunately, both samples suffer from limited statistics. Within the current statistics, no

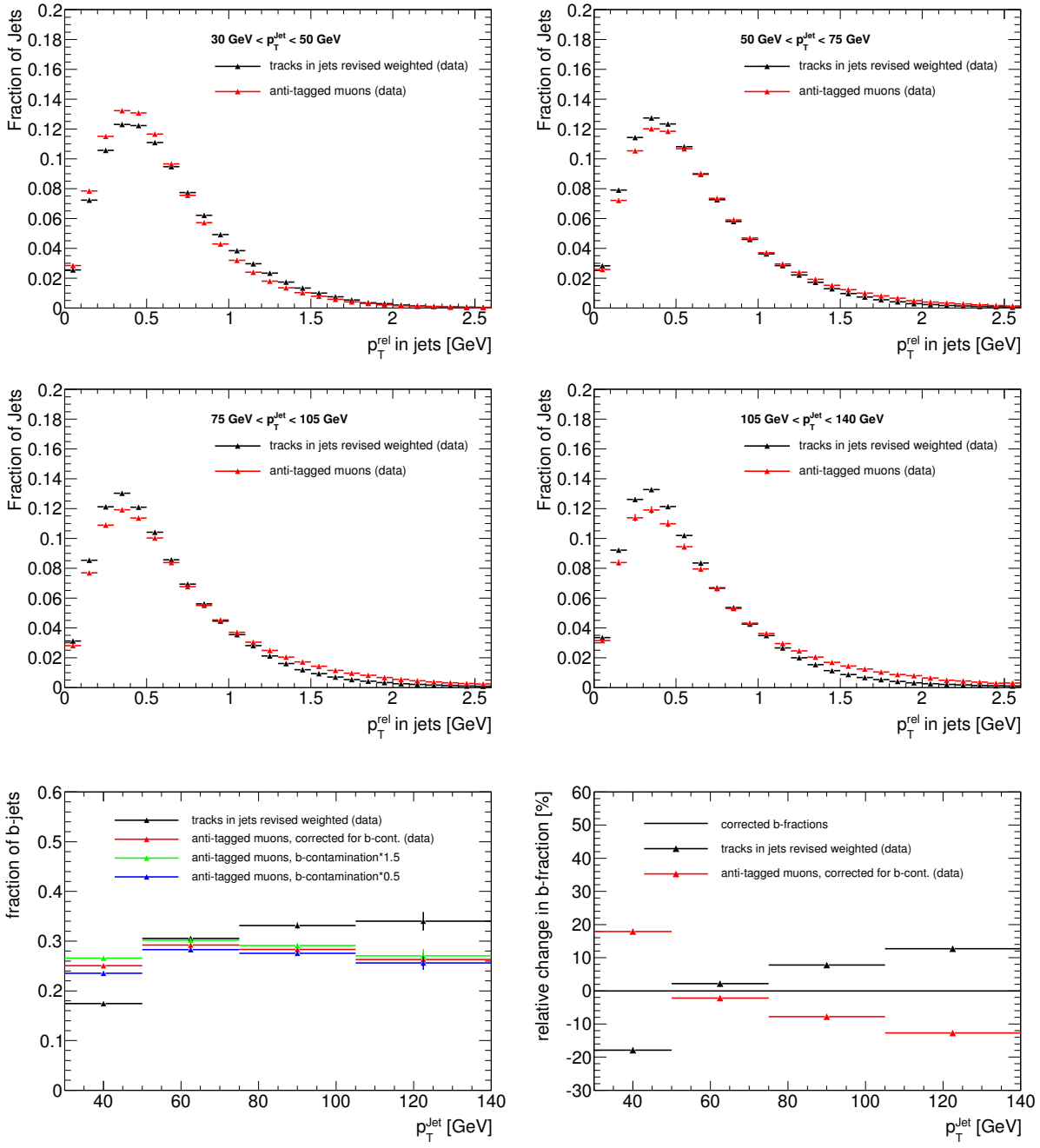

Figure 8.14: Change to light-jet templates due to template definition (top two rows) and resulting change to *b*-fraction measurement (bottom plots). The *b*-fraction measurement using the anti-tagged templates are corrected for the *b*-contamination of the templates. The variation of the *b*-contamination by $\pm$ 50% is shown as well.

large deviations between Pythia and Evtgen can be observed. This confirms the use of the Pythia JXμ samples as default samples for *b*- and *c*-template production.

To investigate the effect of variations of the p^* spectrum, the direct p^* spectrum of $\bar{b} \to l^+ X$ decays in Pythia, where l denotes either a muon or an electron, is compared to the corresponding spectra measured by the DELPHI [93] and the BaBar [86] collaborations (Figure 8.16 bottom). A weighting function was derived and subsequently applied to the

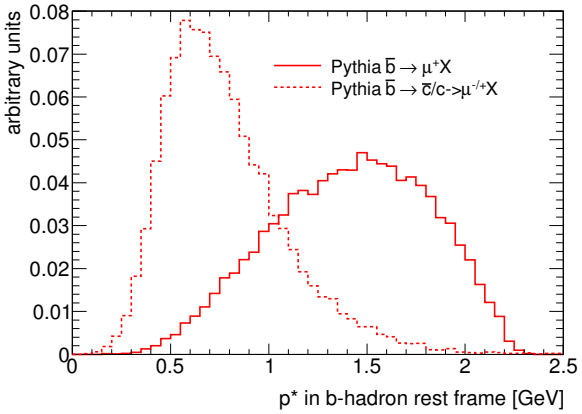

Figure 8.15: p^* of the direct $\bar{b} \to \mu^+ X$ decay component (solid line) and the cascade $\bar{b} \to \bar{c}/c \to \mu^{-/+} X$ decay component (dashed line).

Pythia p^* spectrum of muons from direct $\bar{b} \to \mu^+ X$ decays in the b-jet templates. The resulting changes of the b-jet templates are shown in Figure 8.17 (upper plots). The fits were repeated

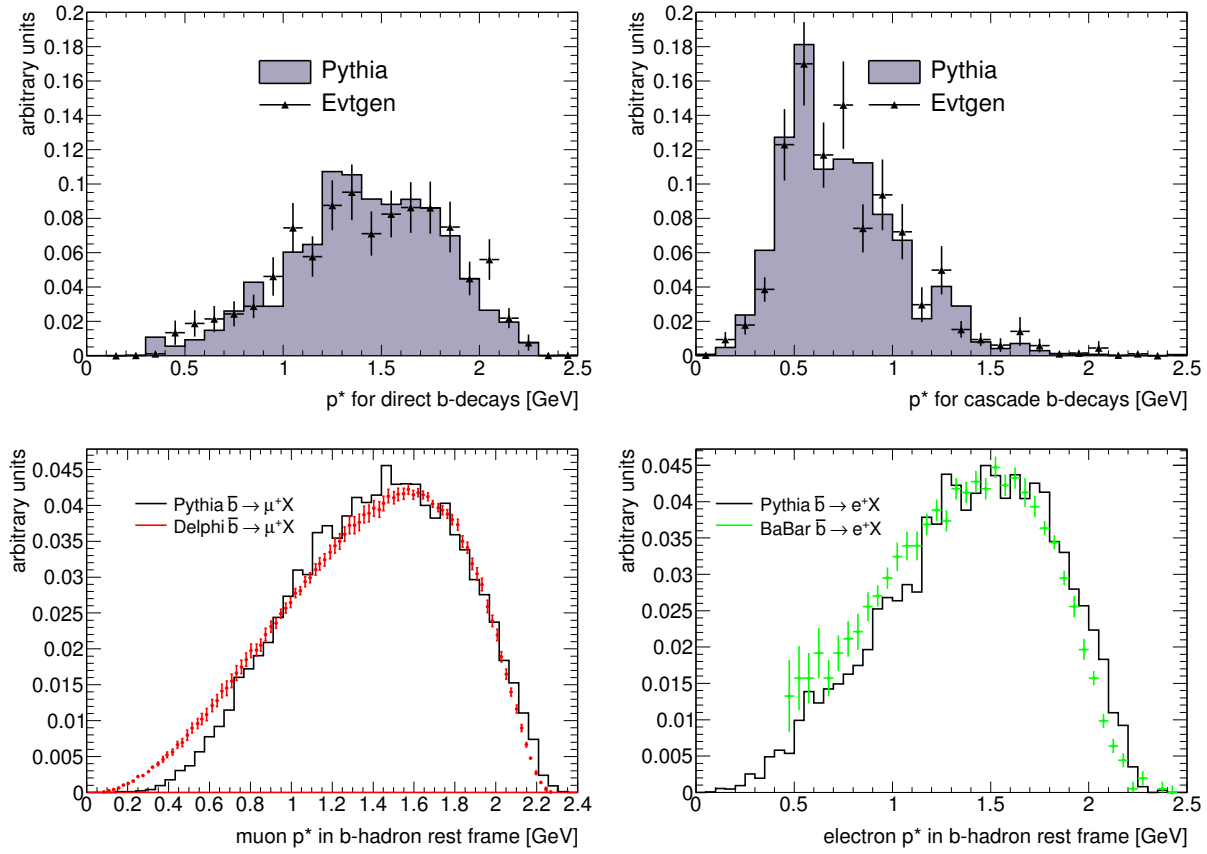

Figure 8.16: top: Comparison of p^* for the direct $\bar{b} \to \mu^+ X$ (left) and the cascade $\bar{b} \to \bar{c}/c \to \mu^{-/+} X$ (right) b-decay component between Pythia and Evtgen.
bottom: Comparison of the measured $\bar{b} \to \mu^+ X$ spectrum by the DELPHI collaboration [93] (left) and the measured $\bar{b} \to e^+ X$ spectrum by the BaBar collaboration [86] (right) with the corresponding predictions from the Pythia QCD JXμ samples (right).

with the modified p_{T}^{rel} templates, and the change to the b-fractions is shown in Figure 8.17 (lower plots). A significant change is observed when the direct $\bar{b} \to \mu^+ X$ decays from the Pythia QCD JXμ samples are reweighted to the measured distributions. This effect needs to be corrected for. The procedure used is discussed in Section 8.7.6.2. After correction, the systematic uncertainties are estimated to lie between 2 and 8%.

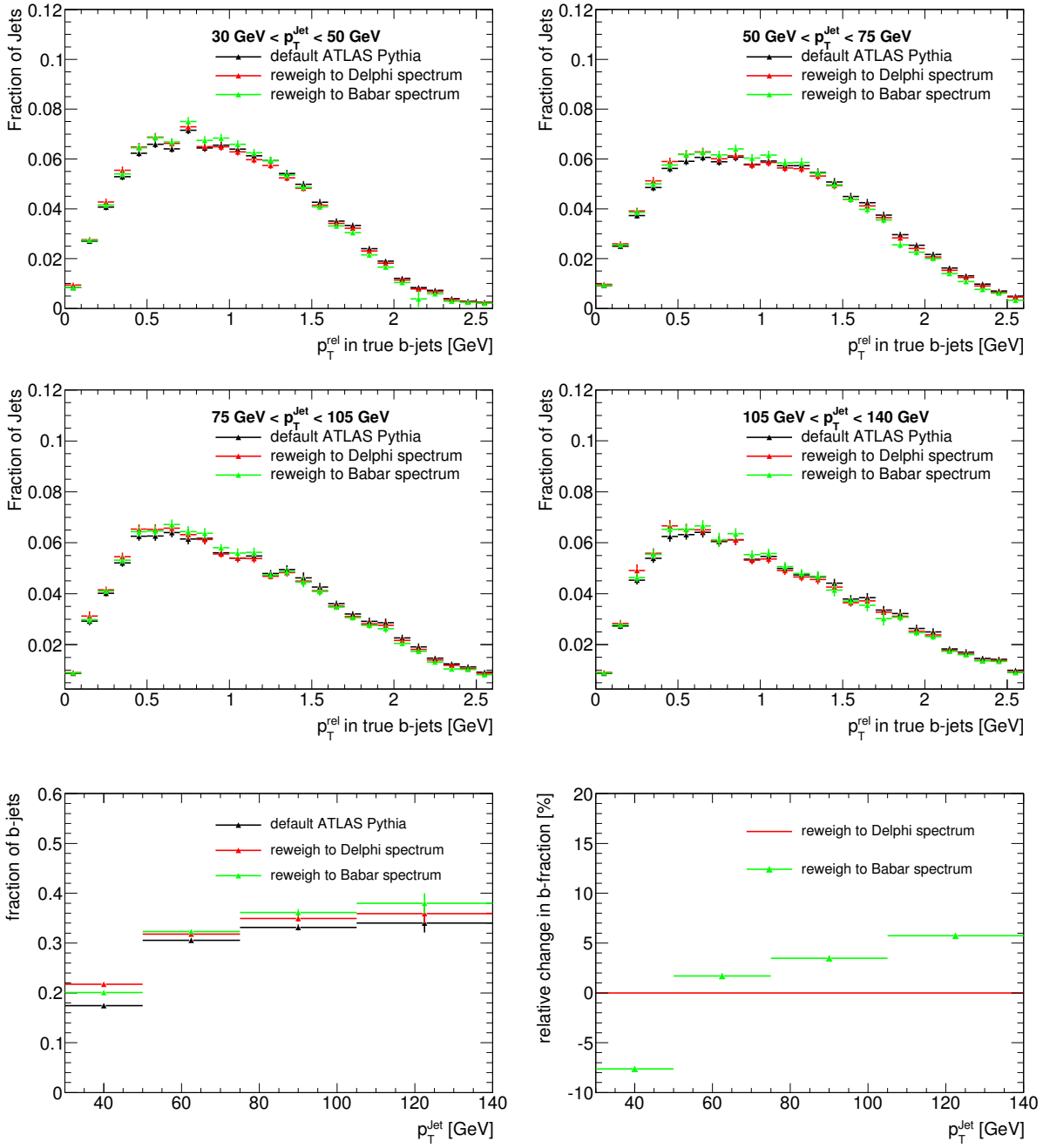

Figure 8.17: Reweighting of the muon p^* from the direct b-decay component in the b-jet templates from the Pythia JXμ samples to match the measurements by the DELPHI and the BaBar experiments (top two rows) and resulting change to the measured b-fractions (lower plots).

The branching ratios of the direct and the cascade b-decays are $BR(\bar{b} \to l^+ X) = (10.69 \pm 0.22)\%$ and $BR(\bar{b} \to \bar{c}/c \to l^{-/+} X) = (9.62 \pm 0.53)\%$, respectively [4], giving the ratio $\frac{BR(\bar{b} \to l^+ X)}{BR(\bar{b} \to \bar{c}/c \to l^{-/+} X)} = 1.11 \pm 0.065$; l denotes either a muon or an electron. This ratio was varied within the quoted uncertainty and the b-jet templates were reweighted accordingly. The resulting changes to the b-jet templates are shown in Figure 8.18 (upper two rows). The p_{T}^{rel} fits were repeated with the modied p_{T}^{rel} templates, and the change to the b-fractions is shown in Figure 8.18 (lower plots). The estimated systematic uncertainty varies between +2.7 and -2.4%.

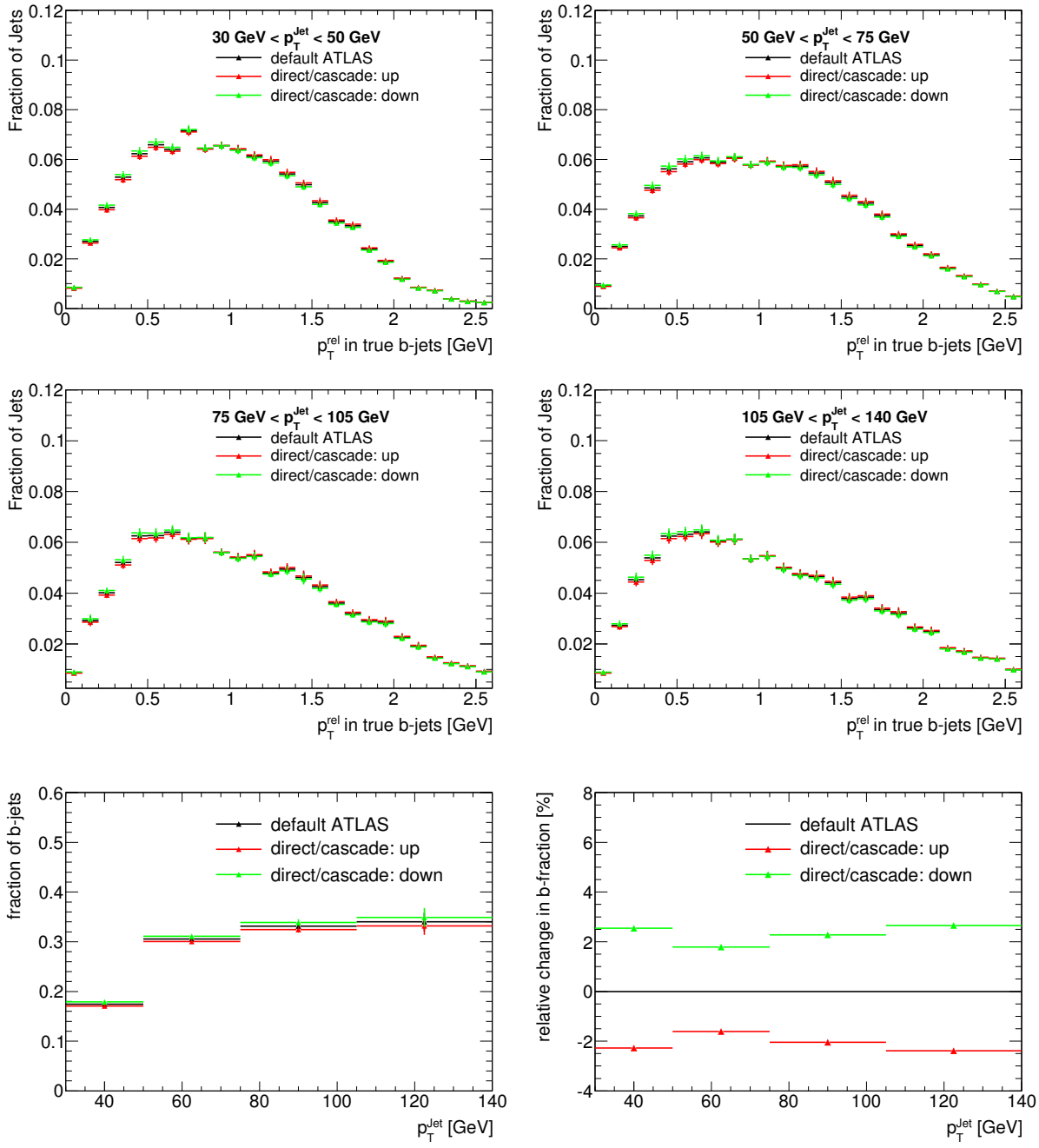

Figure 8.18: Change to b-templates after varying the ratio of the direct b-decay component $\bar{b} \to \mu^+ X$ to the cascade component $\bar{b} \to \bar{c}/c \to \mu^{-/+} X$ within its measured uncertainty (top two rows) and the resulting change to the b-fraction measurement (lower plots).

8.7.5.3 p_{T}^{rel} Template statistics

To evaluate the influence of the finite template statistics on the p_{T}^{rel} fits, 10 000 pseudo-experiments were performed. In these pseudo-experiments, each bin of the *b*-, *c*- and light-jet templates was varied within its statistical error. The distribution of the resulting *b*-fractions can be seen in Figure 8.19 for each bin. In the first bin, two local maxima are visible in the fitted *b*-fractions. The RMS of these distributions are taken as systematic uncertainties and vary between 1.3 and 9.1%.

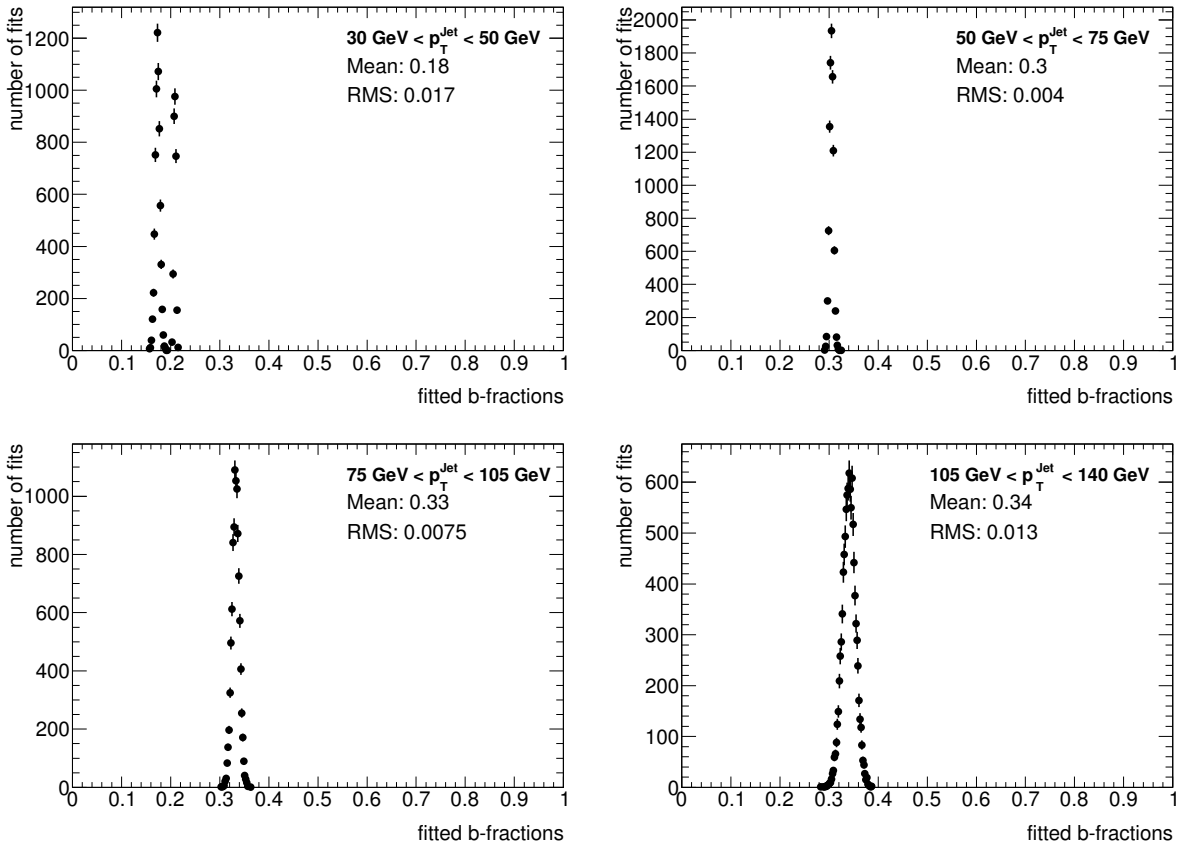

Figure 8.19: Variations in the measured *b*-fractions due to statistical fluctuations in the p_{T}^{rel} templates.

8.7.5.4 *b*-Fragmentation modelling

An incorrect modelling of the fraction X_b of the *b*-quark energy that the *b*-hadron carries away after the fragmentation of the quark can affect the momentum spectrum of the muons from *b*-decays and thus the p_{T}^{rel} distribution. To investigate the impact of fragmentation on the measurement of the *b*-fractions, the p_{T}^{rel} templates were re-derived while X_b was varied by $\pm 5\%$. The resulting *b*-templates are shown in Figure 8.20 (upper plots). The p_{T}^{rel} fits were re-evaluated using these altered p_{T}^{rel} templates. The resulting *b*-fractions shown in Figure 8.20 (lower plots) result in an uncertainty between +11 and -6.3%.

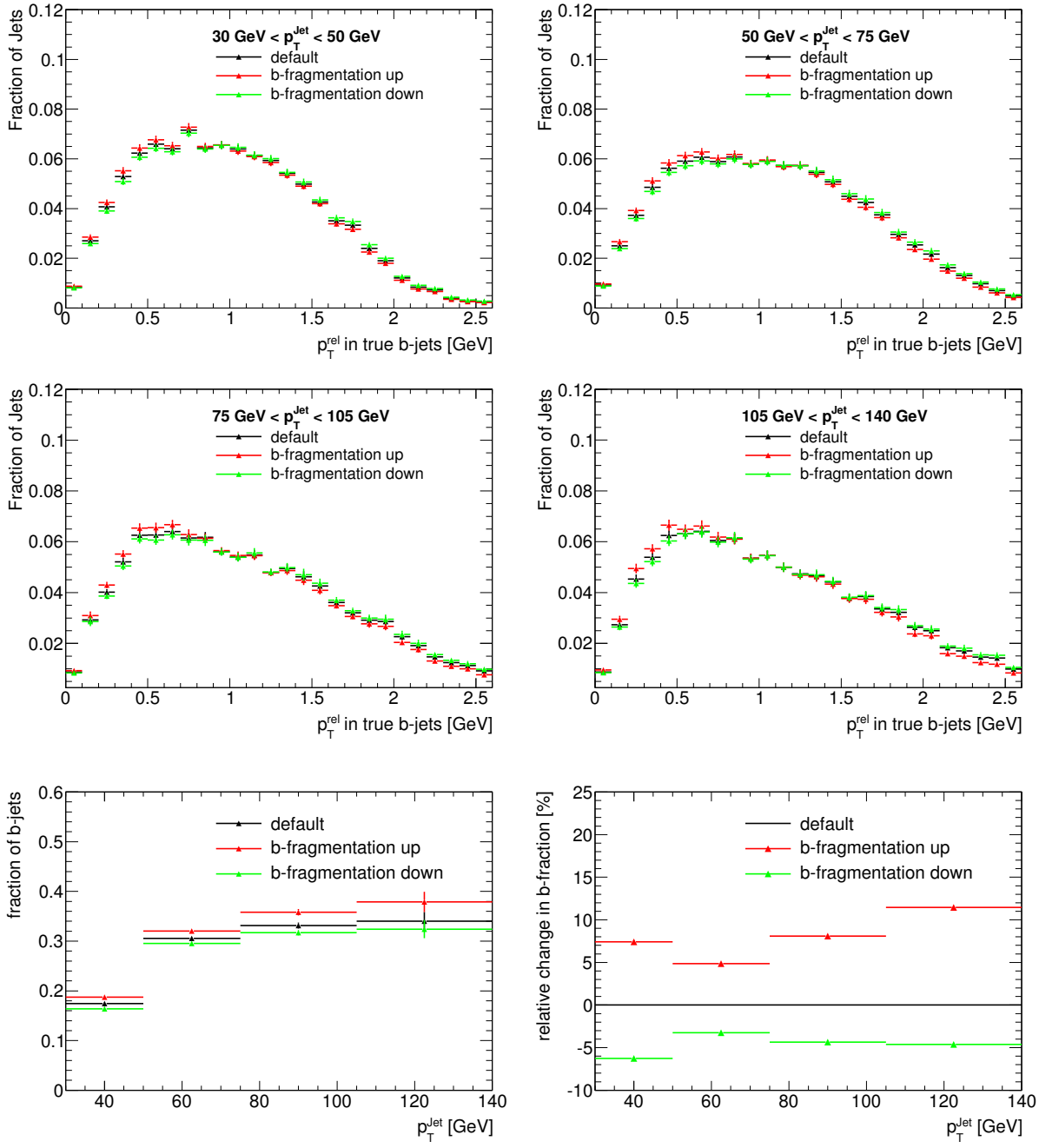

Figure 8.20: Change to the b-jet templates when varying the fraction X_b of the b-quark energy that the b-hadron carries after the fragmentation process by $\pm 5\%$ (upper two rows) and resulting change to the b-fraction measurements (lower plots).

8.7.5.5 Combined jet and semi-leptonic b-jet energy scale uncertainty

To evaluate the influence of the combined jet and semi-leptonic b-jet energy scale uncertainty on the p_{T}^{rel} measurement, the momentum of each jet was varied up respectively down within its uncertainty [94]. For this variation, a dedicated tool [95] was used, plus an additional 2.5% uncertainty for the semi-leptonic b-jet energy scale (see Section 8.3.3).

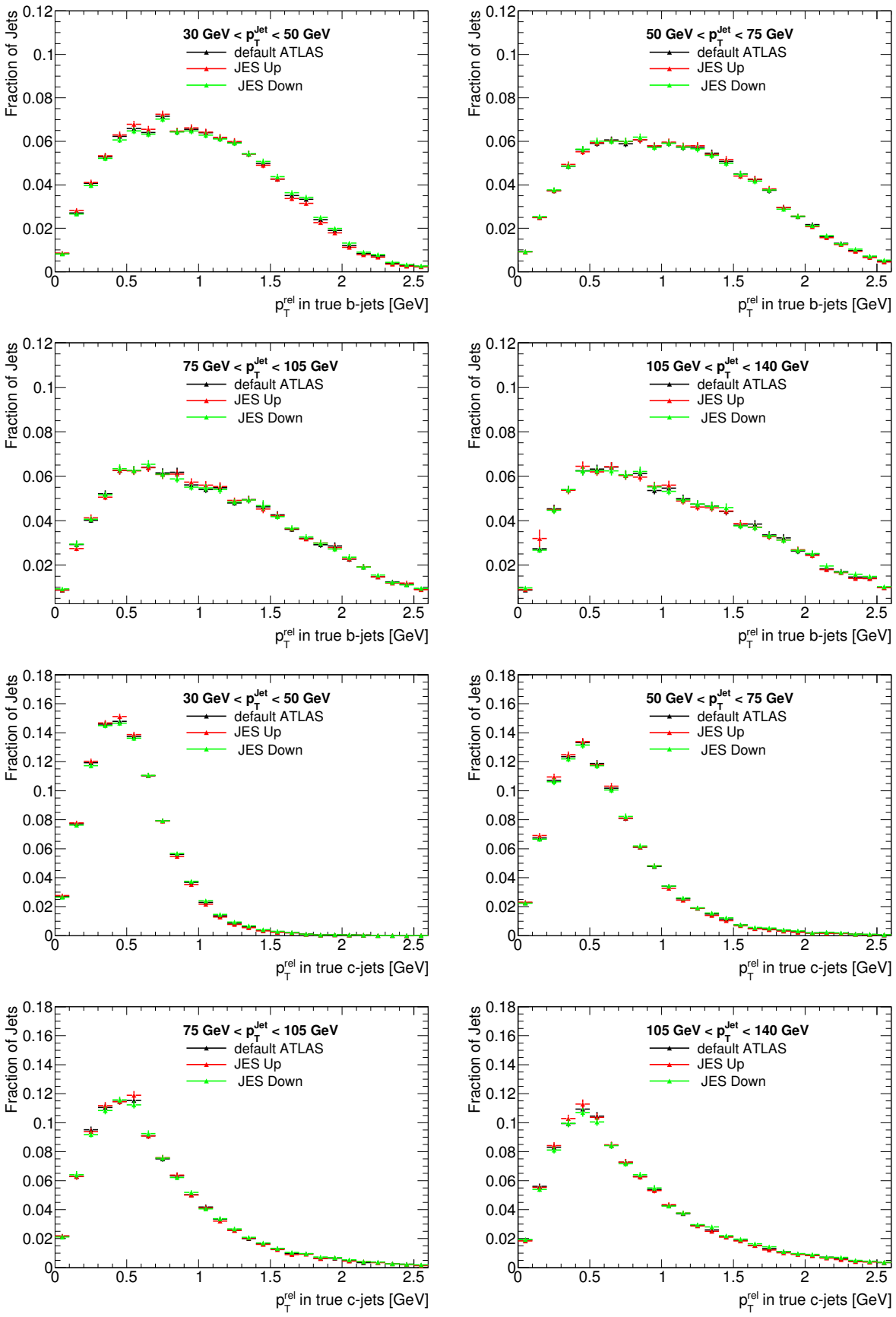

Figure 8.21: Change to the *b*-templates (upper two rows) and the *c*-templates (lower two rows) when varying the jet momentum within its uncertainty.

Figure 8.21 shows the change of the b- and c-templates by varying the jet momentum within its uncertainty. The resulting change to the b-fractions is shown in Figure 8.22. The associated uncertainty varies between +6 and -5.8%.

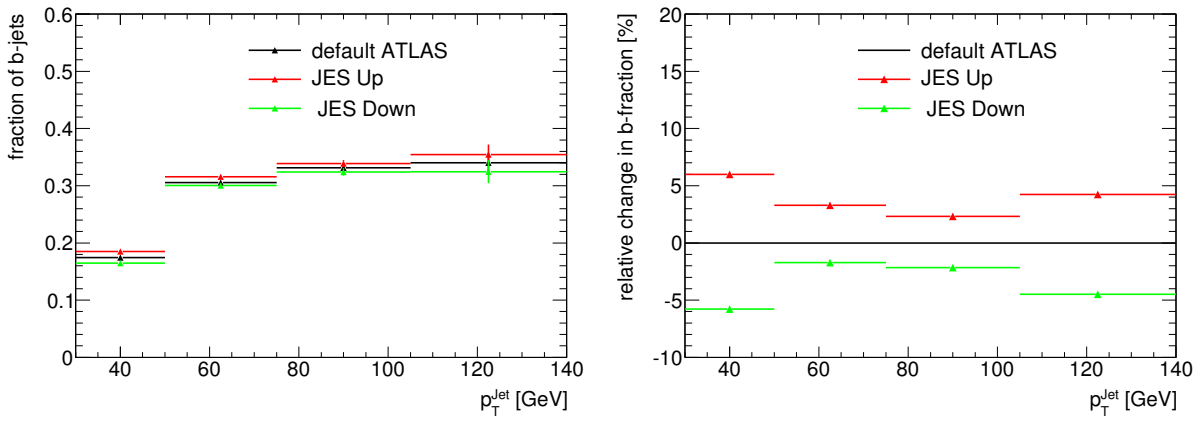

Figure 8.22: Change to b-fraction measurement due to the jet energy scale uncertainty.

8.7.5.6 Modelling of b- and c-quark production mechanism

There are three main production mechanisms for b-quarks: flavour creation, flavour excitation and gluon splitting (see also Section 2.4.1). In the case of gluon splitting, the angle between the two b-quarks can be small enough such that both quarks are within a single jet. Such a b-jet which originates from two b-quarks has a larger probability of containing a muon with high transverse momentum. A difference in the ratio of double-b to single-b jets in data and simulation would therefore bias the p_{T}^{rel} measurement. A systematic uncertainty associated to the b-quark production is estimated by varying the ratio of double-b jets to single-b jets in the simulation and reweighting the b-jet templates accordingly. When building the p_{T}^{rel} templates, jets originating from two b-quarks within $\Delta R < 0.4$ of a reconstructed jet were either given a weight of 0.5 or a weight of two (effectively dividing in half or doubling the double-b contribution). Figure 8.23 shows the change to the b-jet templates (upper plots) and to the measured b-fractions (lower plots) due to this effect. The uncertainty on the b-fraction measurement varies between +3.4 and -5.5%.

Like b-quarks, c-quarks can also be produced through gluon splitting. Again, the angle between the two c-quarks can be small enough such that both quarks are within the same jet. To study the systematic change associated with the c-production mechanism, the same technique was used to construct the p_{T}^{rel} templates as for the estimation of the uncertainty due to gluon splitting into two b-quarks, but by varying the fractions of single-c to double-c jets. Figure 8.24 shows the changes to the c-jet templates (upper plots) and to the measured b-fractions (lower plots). The systematic uncertainties vary between +5 and -6.6% and are assumed to be uncorrelated to the uncertainties due to gluon splitting into two b-quarks.

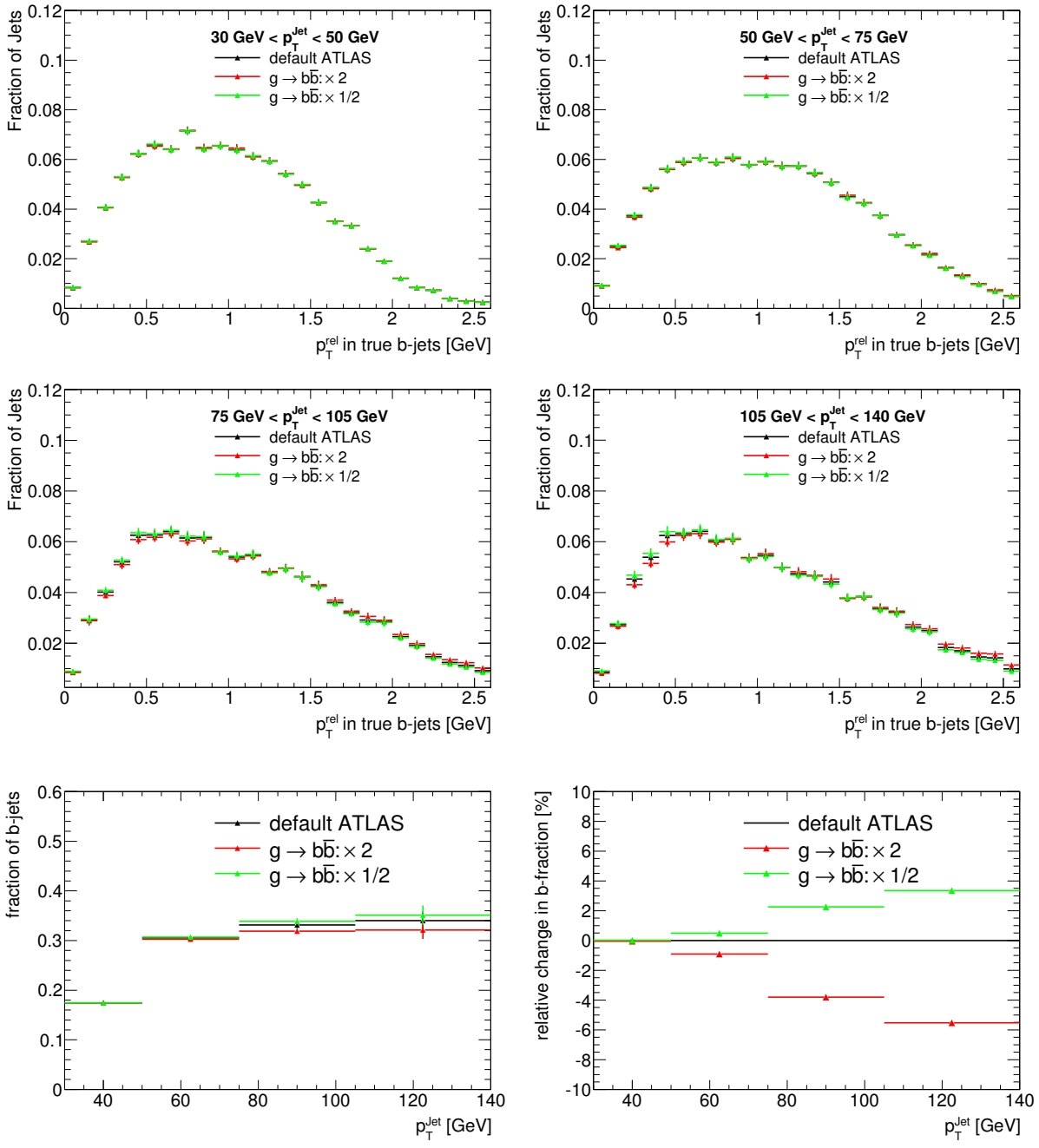

Figure 8.23: Change to the *b*-jet templates after varying the fraction of *b*-jets from gluon splitting by a factor of 0.5 and 2 (upper two rows) and the resulting change to the *b*-fraction measurements (lower plots).

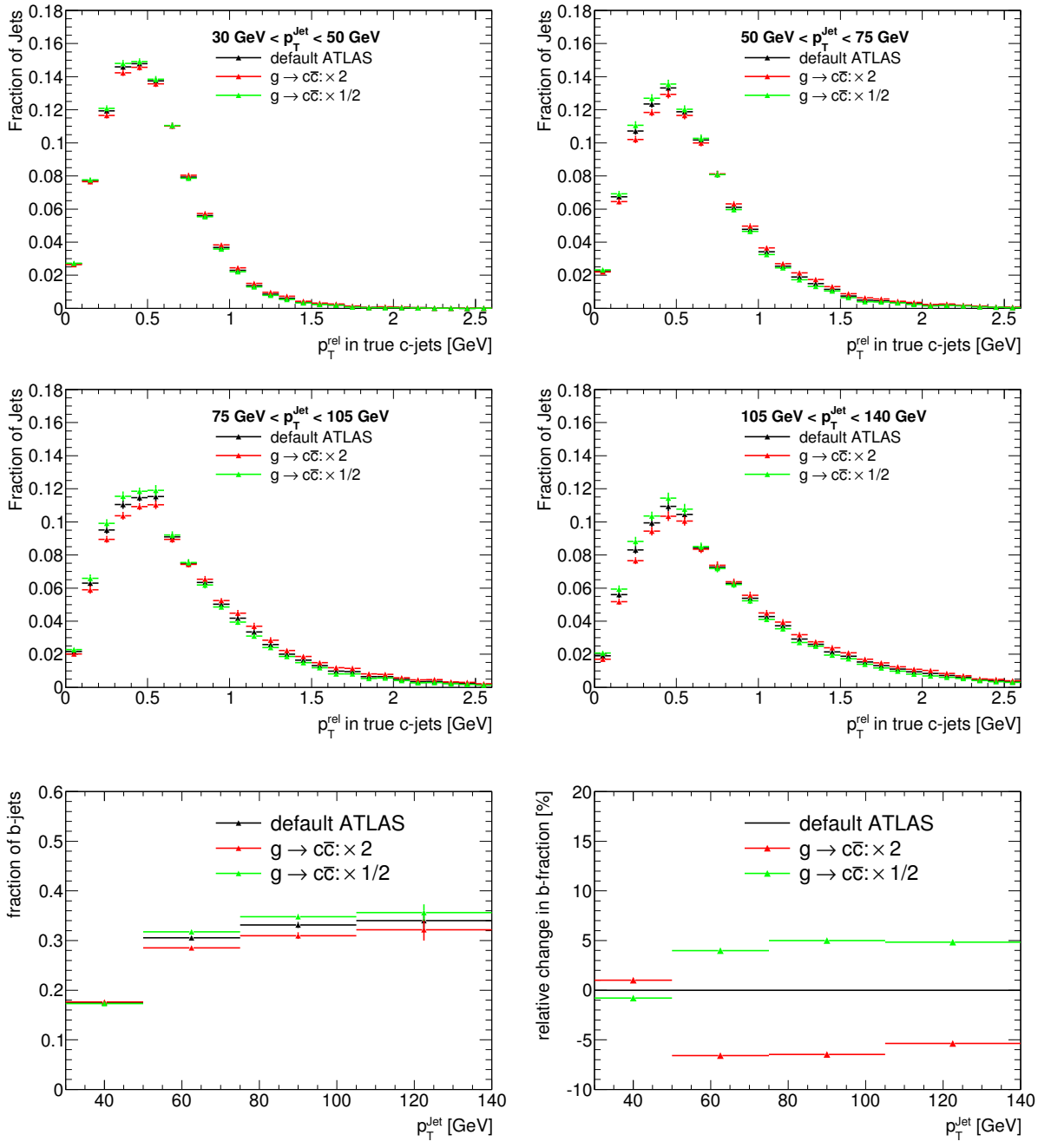

Figure 8.24: Change to the *c*-jet templates after varying the fraction of *c*-jets from gluon splitting by a factor of 0.5 and 2 (upper two rows) and the resulting change to the *b*-fraction measurements (lower plots).

8.7.5.7 Misidentified muons in b-jets

A fraction of particles from decays-in-flight or punch through within real b-jets can reach the muon system and thus be misidentified as muons from $\bar{b} \to \mu X$ decays. Figure 8.25 shows the rate of these misidentified muons, which varies between 3.5% and 5.5%.

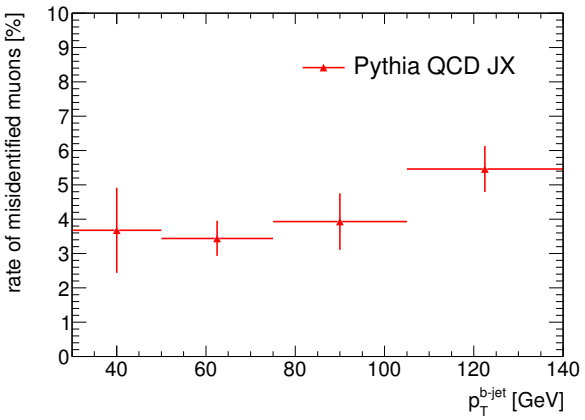

Figure 8.25: Rate of misidentified muons within real b-jets, which come from decays-in-flight or punch-through and can reach the muon system.

A systematic uncertainty for the p_{T}^{rel} measurement is estimated by varying the contribution of muons in b-jets which do not come from real $\bar{b} \to \mu X$ decays. The JX samples were used because the muon-filtered JXμ samples would introduce a bias due to the muon filter at the generator level. The resulting templates are shown in Figure 8.26. As they are very noisy, 10 000 pseudo-experiments were used to estimate the b-fractions. The mean b-fractions from these pseudo-experiments are compared in the lower plots. The resulting uncertainty varies between +3.4 and -0.2%.

8.7.5.8 Jet direction resolution

The jet direction is a variable directly entering the p_{T}^{rel} calculation. A poor jet direction resolution makes the p_{T}^{rel} distributions for b-, c- and light-quark jets look more similar. Any difference in the jet direction resolution between the data and the simulation would therefore bias the result. A dedicated study was carried out [88] to estimate any possible contributions to the jet-direction resolution in addition to that described by the simulation. As a result, the calorimeter-based jet axis in the simulation was smeared with a Gaussian of width 0.006 in η and 0.004 in ϕ to cover these discrepancies. The smearing was applied to the jets at $EM + JES$-calibration scale, and the jet energy corrections for the muon and missing neutrino energies recalculated. The b- and c-templates were rederived using the smeared jet axis. Figure 8.27 shows the changes to the b-jet templates (upper two rows) and the c-jet templates (lower two rows). The resulting change to the b-fraction measurements are

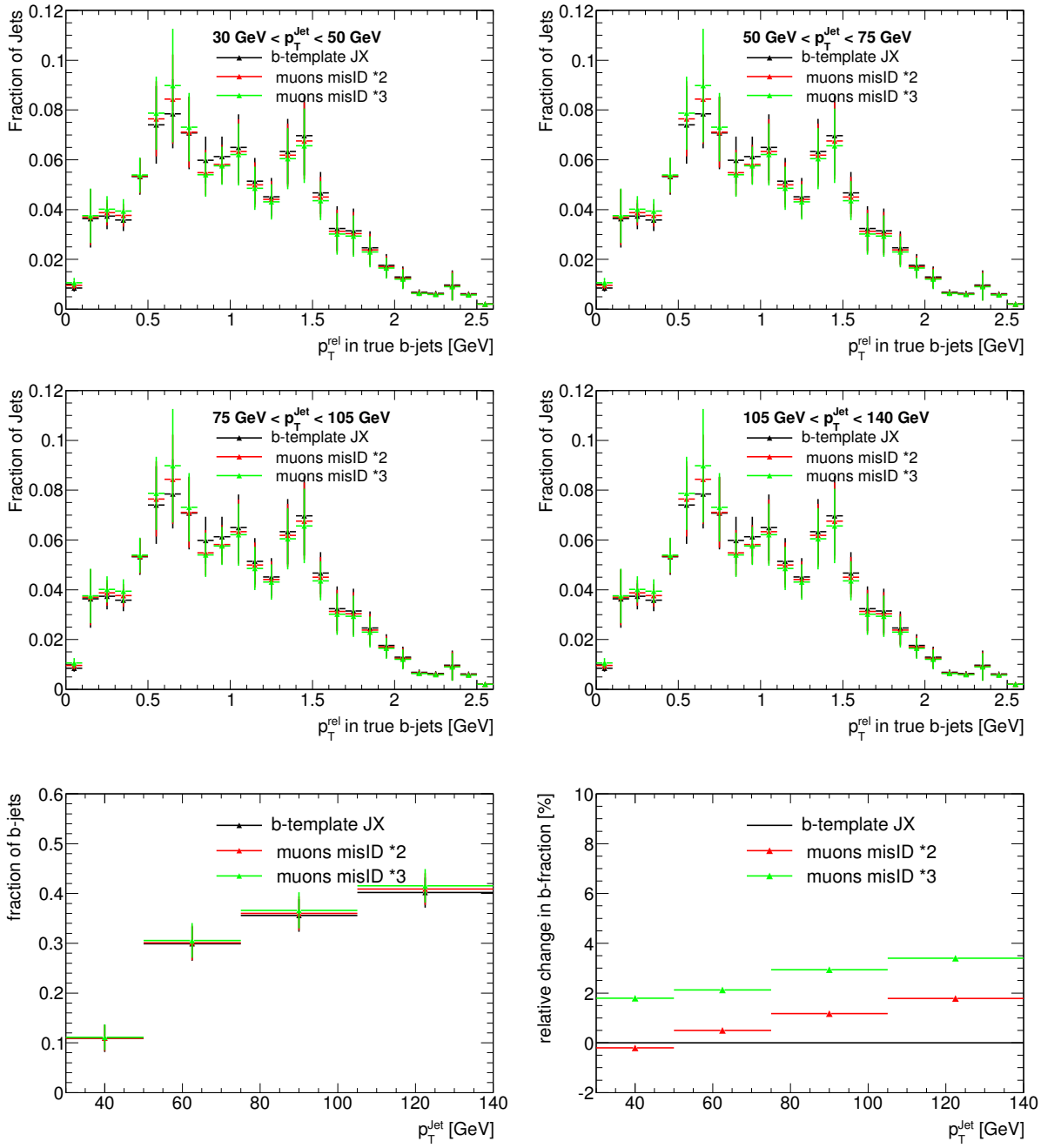

Figure 8.26: Change to the *b*-jet templates from the JX samples when increasing the rate of misidentified muons by a factor of two or three (upper two rows) and resulting change to the *b*-fraction measurement (lower plots). To be less sensitive to the limited statistics of the *b*-templates from the JX samples, the mean *b*-fractions from 10 000 pseudo-experiments are compared.

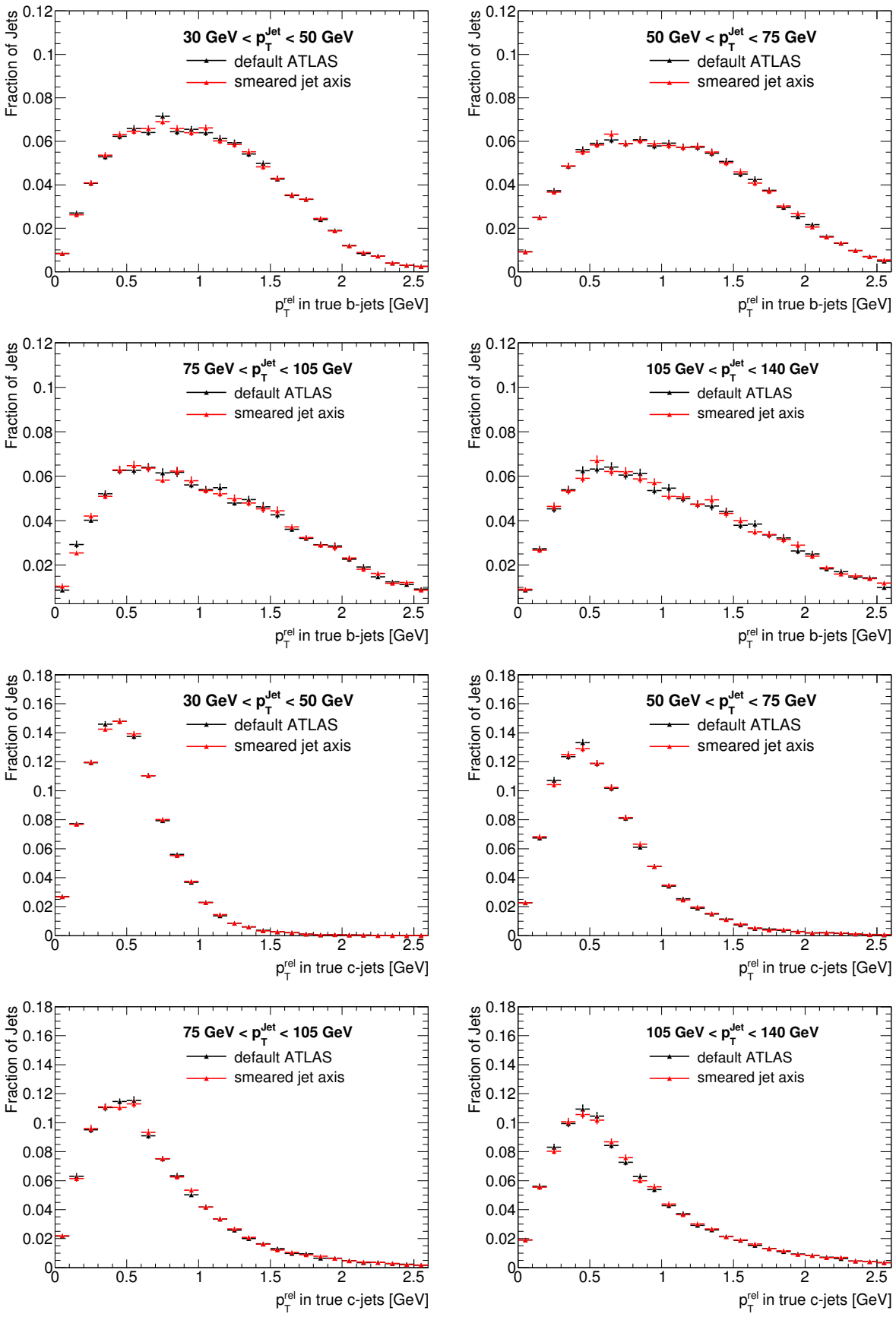

Figure 8.27: Change to the *b*-jet templates (upper two rows) and in the *c*-jet templates (lower two rows) for the jet direction smearing.

presented in Figure 8.28. The estimated systematic uncertainty varies between +0.7 and -1.7%.

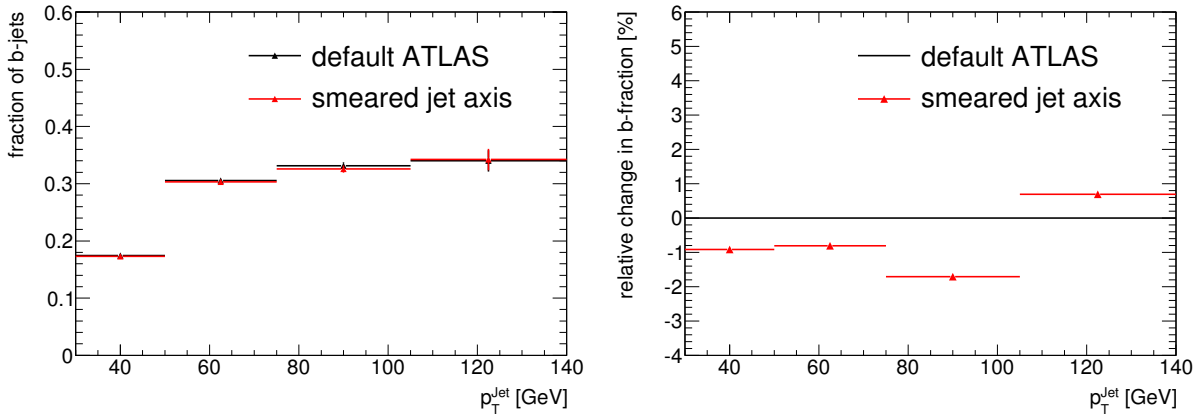

Figure 8.28: Change to the b-fraction measurement for the jet direction smearing.

8.7.5.9 b-hadron fractions

The influence of the b-hadron composition on the shape of the b-templates was studied by varying their individual contributions. Figure 8.29 (left) shows the spectrum of the momentum p^* of muons from $B^{+/-}$-, B_0-, B_S- and Λ_B-hadron decays in their respective rest frames. To study their influence on the shape of the b-templates and the p_{T}^{rel} fits, their individual contributions to the templates were changed by reweighting their fractions, see Figure 8.29 (right). Changing their respective contributions by a few percent results in less than 0.3% change to the measured b-fractions. This effect is therefore negligible.

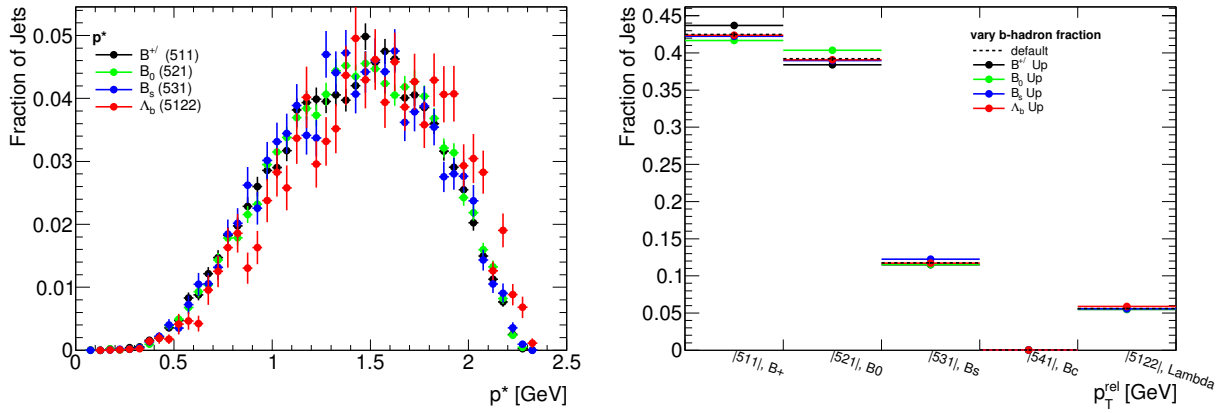

Figure 8.29: Shape of the p^* distribution separate for muons from $B^{+/-}$-, B_0-, B_S- and Λ_B-hadron decays (left) and their relative contributions to the b-jet templates (right).

8.7.5.10 Muon direction resolution

Although the muon direction also directly enters the p_{T}^{rel} calculation, the muon angular resolution is very good compared to that of the jet. Therefore the uncertainty associated with this is negligible.

8.7.5.11 Muon Momentum Scale

The muon momentum also enters the p_{T}^{rel} calculation, so that any difference between the muon momentum scale in the data and the simulation would lead to a bias in the p_{T}^{rel} measurement. The reconstruction of the J/ψ resonance in ATLAS from muon track daughters [96] shows that the reconstructed mass is 3 096 $\pm$ 3 MeV, to be compared with the mass of 3 096.916 $\pm$ 0.011 MeV by the Particle Data Group [4]. This measurement shows an excellent agreement and excludes larger differences in the muon momentum scales of more than a few per mille. Therefore the uncertainty is negligible.

8.7.5.12 Summary of systematic uncertainties

Table 8.6 summarises the systematic uncertainties which were evaluated for the b-fraction measurement using the p_{T}^{rel} method. The measurement is dominated by the uncertainty on the light-jet template definition.

8.7.6 Correction Procedure of *b*-Fractions

Two of the studies to estimate the systematic uncertainties revealed that the default measurement introduces a bias: the study concerning the definition of the light-jet template and the study concerning the semi-leptonic b-decay modelling in Pythia using measurements by the DELPHI and the BaBar collaborations. The correction procedure applied to obtain the final b-fractions is discussed here. The correction factors are listed in Table 8.7.

8.7.6.1 Correction due to light-jet template definition

To correct for the bias introduced by the choice of light-jet template, the true value of the b-fractions is calculated from the average value of the b-fraction measurements using the two different definitions. The spread of the two measurements is taken as uncertainty. A

Relative Uncertainties [%]	p_{T}^{b-jet} [GeV]			
	30-50	50-75	75-105	105-140
Definition of light-jet template				
Use two valid definitions for the light-jet template on data.	± 18.0	± 2.2	± 7.5	± 13.0
Semi-leptonic b-decay modelling				
Reweigh the direct b-decay component in Pythia to the measured spectra by the DELPHI and the BaBar experiments.	± 8.2	± 1.7	± 3.4	± 5.4
Vary the relative contribution of the direct and the cascade decays within their measured uncertainty.	$^{+2.5}_{-2.3}$	$^{+1.8}_{-1.6}$	$^{+2.3}_{-2.0}$	$^{+2.7}_{-2.4}$
p_{T}^{rel} *Template statistics*				
Use pseudo-experiments and vary all three templates within their statistical errors.	± 9.1	± 1.3	± 2.3	± 3.9
b-Fragmentation				
Vary the the fraction of the b-quark energy carried onto the b-hadron by $\pm 5\%$.	$^{+7.4}_{-6.3}$	$^{+4.9}_{-3.2}$	$^{+8.1}_{-4.3}$	$^{+11.0}_{-4.6}$
b-Jet energy scale				
Vary the jet energy within its uncertainty.	$^{+6.0}_{-5.8}$	$^{+3.3}_{-1.7}$	$^{+2.3}_{-2.1}$	$^{+4.2}_{-4.5}$
Modelling of b- and c-quark production mechanism				
Vary the contribution of b-jets from gluon splitting.	$^{+0.0}_{-0.1}$	$^{+0.5}_{-0.9}$	$^{+2.3}_{-3.8}$	$^{+3.4}_{-5.5}$
Vary the contribution of c-jets from gluon splitting.	$^{+1.0}_{-0.8}$	$^{+4.0}_{-6.6}$	$^{+5.0}_{-6.5}$	$^{+4.8}_{-5.4}$
Misidentified muons in b-jets				
Vary the contribution of muons in b-jets which do not come from real $\bar{b} \to \mu X$ decays.	$^{+1.8}_{-0.2}$	$^{+2.1}_{-0.0}$	$^{+2.9}_{-0.0}$	$^{+3.4}_{-0.0}$
Jet direction				
Smear the jet axis for the b- and c-jet templates.	± 0.9	± 0.8	± 1.7	± 0.7
Total systematic uncertainty	$^{+24.0}_{-23.6}$	$^{+8.3}_{-8.4}$	$^{+13.8}_{-12.6}$	$^{+20.1}_{-17.9}$

Table 8.6: The relative systematic uncertainties of the measured b-fractions.

correction factor C_b^{light} is calculated as follows:

$$\begin{aligned} C_b^{light} &= \frac{F_b + F_b^{anti-tagged}}{2F_b} \\ rel\ uncertainty^{light} &= \pm \frac{|F_b - F_b^{anti-tagged}|}{2C_b^{light} F_b}. \end{aligned} \tag{8.16}$$

F_b and $F_b^{anti-tagged}$ denote the b-fraction measured with the track respectively the anti-tagged light-jet template.

8.7.6.2 Correction due to semi-leptonic b-decay modelling in Pythia

A full correction to the measured p^* spectrum by the DELPHI collaboration is applied for the bias introduced by the semi-leptonic b-decay modelling in Pythia, as this p^* distribution is the most up-to-date measurement of the lepton momentum in the b-hadron rest frame. The variations between the b-fraction measurements using templates reweighted to the spectra by the DELPHI and the BaBar collaborations are taken as the uncertainty. The correction factor $C_b^{b-decay}$ is calculated as follows:

$$\begin{aligned} C_b^{b-decay} &= \frac{F_b^{DELPHI}}{F_b} \\ rel\ uncertainty^{b-decay} &= \pm \frac{|F_b^{DELPHI} - F_b^{BaBar}|}{C_b^{b-decay} F_b}. \end{aligned} \tag{8.17}$$

In this definition, F_b^{DELPHI} and F_b^{BaBar} denote the measured b-fractions using b-jet templates reweighted to the spectra by the DELPHI and the BaBar collaborations. F_b denotes the default b-fraction measurement using the b-jet templates from the Pythia QCD JXμ samples.

The sources of the two systematic biases are treated as being independent, and the two correction factors are therefore combined by multiplying them. The systematic errors for the light-jet template and the semi-leptonic b-decay modelling in Table 8.6 were calculated as discussed in this section.

Correction factors C_b	p_{T}^{b-jet} [GeV]			
	30-50	50-75	75-105	105-140
Definition of light-jet template	1.22	0.98	0.93	0.88
Semi-leptonic b-decay modelling	1.24	1.04	1.05	1.06
total	1.51	1.02	0.98	0.94

Table 8.7: Correction factors for the b-fraction measurement.

8.7.7 Final b-Fractions

The final measured b-fractions are shown in Figure 8.30, which were corrected using the procedure detailed in the section before. The statistical errors are shown in black and the statistical plus systematic errors as a yellow band. The measured b-fractions are compared to

predictions from the Pythia JX QCD Monte Carlo samples (dashed line). The values of the measured and predicted *b*-fractions are detailed in Table 8.8. The predictions from Pythia are systematically lower but consistent with the measured *b*-fractions in the data within their systematic uncertainties. The underestimation of the *b*-fractions by Pythia is due to the fact that the generator only calculates the leading-order matrix elements, and that the subsequent parton shower underestimates the higher-order contributions.

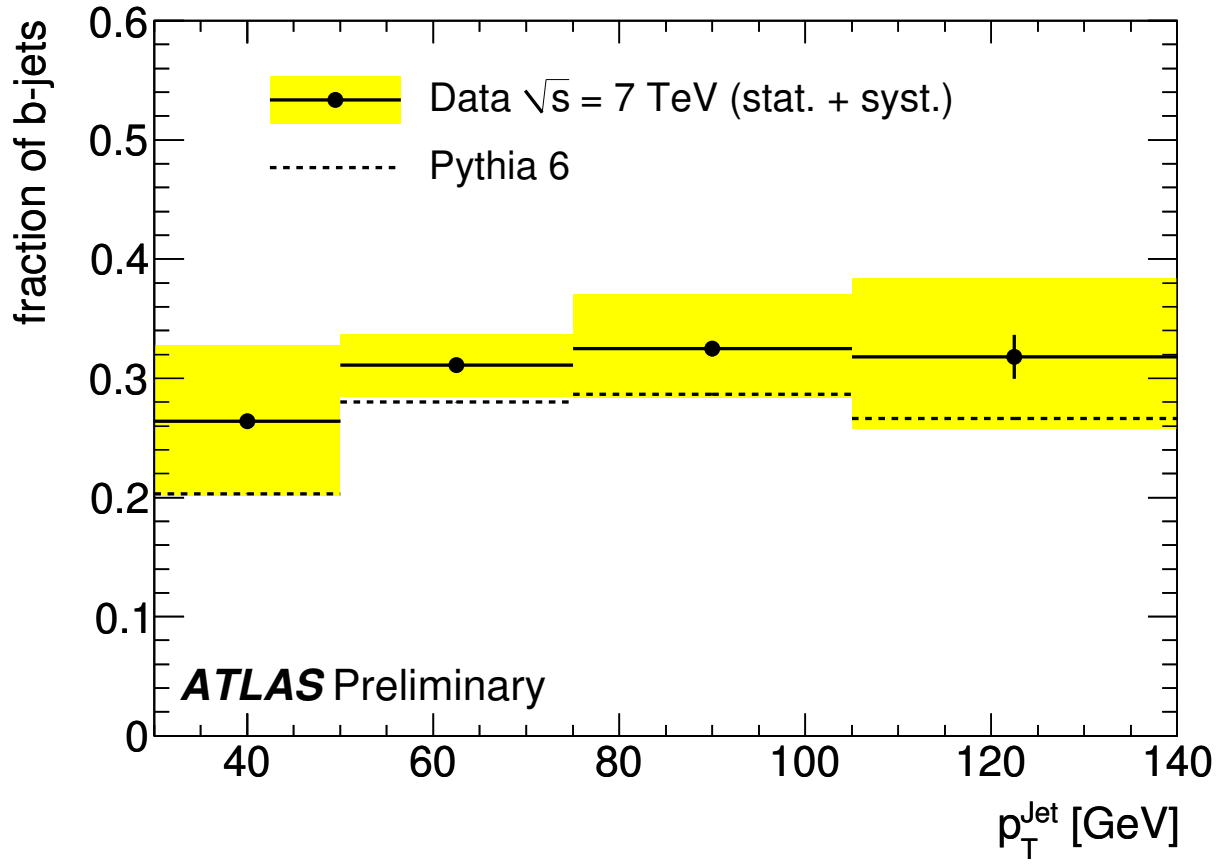

Figure 8.30: Measured *b*-fractions in the data using the p_{T}^{rel} method. Statistical errors are shown in black, statistical plus systematic errors as a yellow band. The predictions from the Pythia QCD Monte Carlo samples are given for reference.

b-fractions [%]	p_{T}^{b-jet} [GeV]			
	30-50	50-75	75-105	105-140
ATLAS *prelim*	$26.4 \pm 0.2\ ^{+6.3}_{-6.2}$	$31.1 \pm 0.2 \pm 2.6$	$32.5 \pm 0.6\ ^{+4.5}_{-4.1}$	$31.8 \pm 1.9\ ^{+6.4}_{-5.7}$
Pythia QCD	20.3	28.1	29.1	27.3

Table 8.8: Preliminary *b*-fraction measurement by ATLAS and predictions from Pythia JX samples.

8.7.8 Cross Check: Flavour Composition of the Muon Significance

The significance $S_{d0} = \text{sign}(d_0) \cdot \frac{|d_0|}{\sigma_{d0}}$, signed with respect to the jet axis, is sensitive to the lifetime of the particle. Particles with a long lifetime (like b-hadrons) have a positive S_{d0}, whereas short-lived particles are distributed around $S_{d0} = 0$ according to the detector resolution. This distribution is independent of the p_{T}^{rel} distribution and can therefore be used as a control plot for the measured b-fractions. Figure 8.31 shows the muon significance in the data and its flavour composition. The templates for b- and c-jets are taken from the Pythia JXμ samples, the templates for light-jets use the significance of muons in anti-tagged jets from the data. The relative fractions of the flavours are taken from the p_{T}^{rel} fits. The distinction between light- and c-jets is not very powerful in the p_{T}^{rel} fits. It is therefore the positive side of the significance in Figure 8.31 which can be used as a cross check for the correct estimation of the b-fractions in the sample. There is reasonable agreement between the data and the flavour templates.

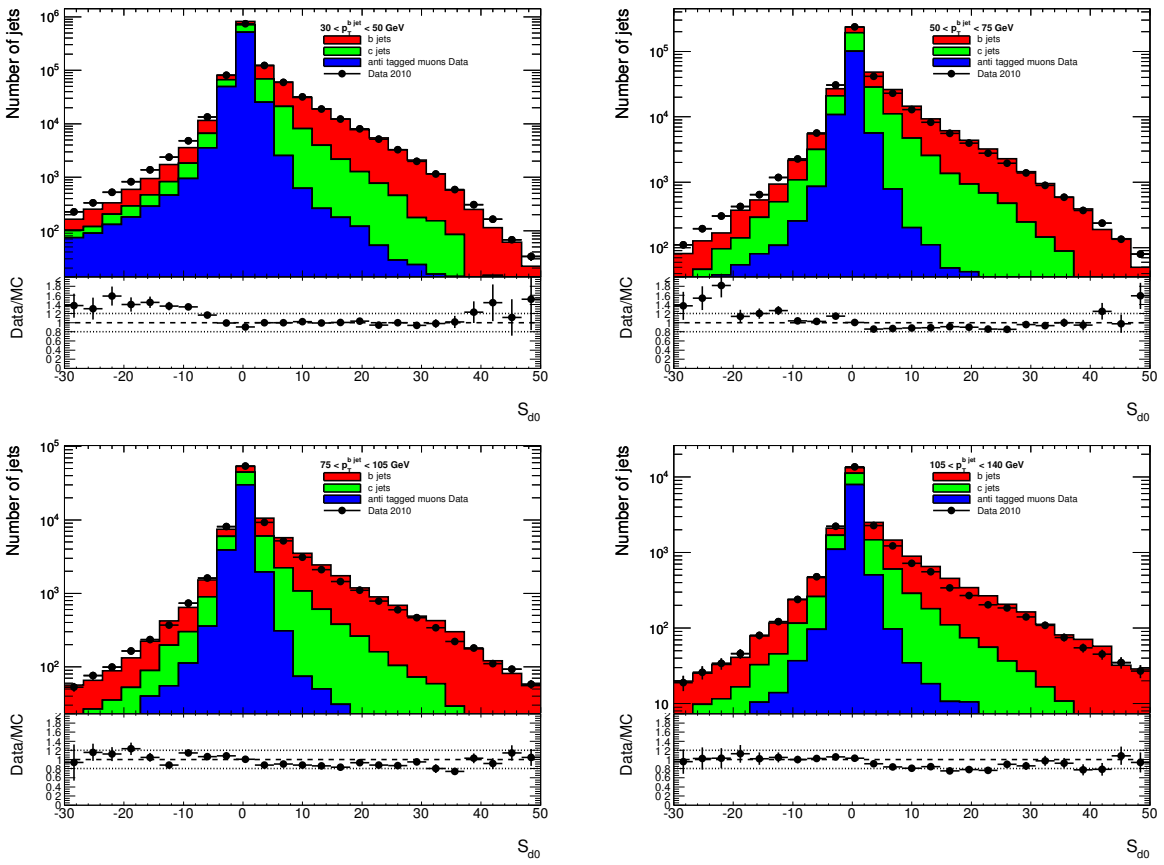

Figure 8.31: Flavour composition of the muon significance S_{d0}. The flavour fractions are taken from the p_{T}^{rel} fits. The templates for b- and c-jets are from the Pythia JXμ samples and the light-jet templates use muons in anti-tagged jets.

8.8 b-Jet Differential Cross Section Measurement

8.8.1 Measured b-Jet Differential Cross Section

The b-jet differential cross section $d\sigma(pp \to bX, b-jet, |y^{b-jet}| < 2.1)/dp_{\mathrm{T}}^{b-jet}$, calculated following Equation (8.1), is shown in Figure 8.32. The calculation uses the fraction of jets from b-quark decays $F_b(p_T^{b-jet})$ as measured by the p_{T}^{rel} method in Section 8.7, the unfolded number of selected jets containing a muon N^{jets} as presented in Section 8.6, the branching fraction of $\bar{b} \to \mu X$ to inclusive b-decays B as listed in Table 2.3 and the integrated luminosity of $\mathcal{L}_{int} = 4.6 \pm 0.2\ \mathrm{pb}^{-1}$ as stated in Section 8.2.1. The efficiency for object reconstruction and selection $\epsilon^{\mu,jet}(p_T^{\mu}, p_T^{b-jet})$ is listed in Table 8.4. The measured b-jet differential cross section values and their statistical uncertainties are shown in black in Figure 8.32 and statistical plus systematic uncertainties as a yellow band. The sources of systematic uncertainties and their relative contributions are listed in Table 8.9. They are dominated by the uncertainties of the b-fraction measurement and the unfolding procedure. Table 8.10 lists the measured values of the b-jet differential cross section.

The measured b-jet differential cross section is compared to next-to-leading order (NLO) Powheg calculations using Pythia 6 to generate the parton shower (see Appendix A.5 for more information). Two different sets of parton density functions were used for the event generation, MSTW 2008 NLO [97] (blue) and CTEQ6.6 [98] (red). The systematic uncertainties of the calculations were estimated by varying the factorisation and renormalisation scales independently by a factor of two for the Powheg predictions relying on the MSTW 2008 parton density function set. The variations are shown in dashed blue in Figure 8.32. Both calculations reproduce the measurement rather well. The predictions using CTEQ6.6 give a very good agreement with the measured cross section. The central values using MSTW 2008

Systematic uncertainties [%]	p_{T}^{b-jet} [GeV]			
	30-50	50-75	75-105	105-140
b-fractions	$^{+24.0}_{-23.6}$	$^{+8.3}_{-8.4}$	$^{+13.8}_{-12.6}$	$^{+20.1}_{-17.9}$
Unfolding	$^{+0.9}_{-0.8}$	$^{+18.3}_{-14.4}$	$^{+19.3}_{-15.4}$	$^{+19.9}_{-15.7}$
Luminosity			$\pm$ 3.4	
Branching ratio			$^{+2.6}_{-2.9}$	
Total systematic error	$^{+24.3}_{-23.8}$	$^{+20.4}_{-17.0}$	$^{+24.0}_{-20.2}$	$^{+28.5}_{-24.0}$

Table 8.9: Overview of the systematic uncertainties for the b-jet differential cross section measurement.

NLO predict a p_{T}^{b-jet} dependence slightly harder than the measurement, but differences are within the systematic uncertainties.

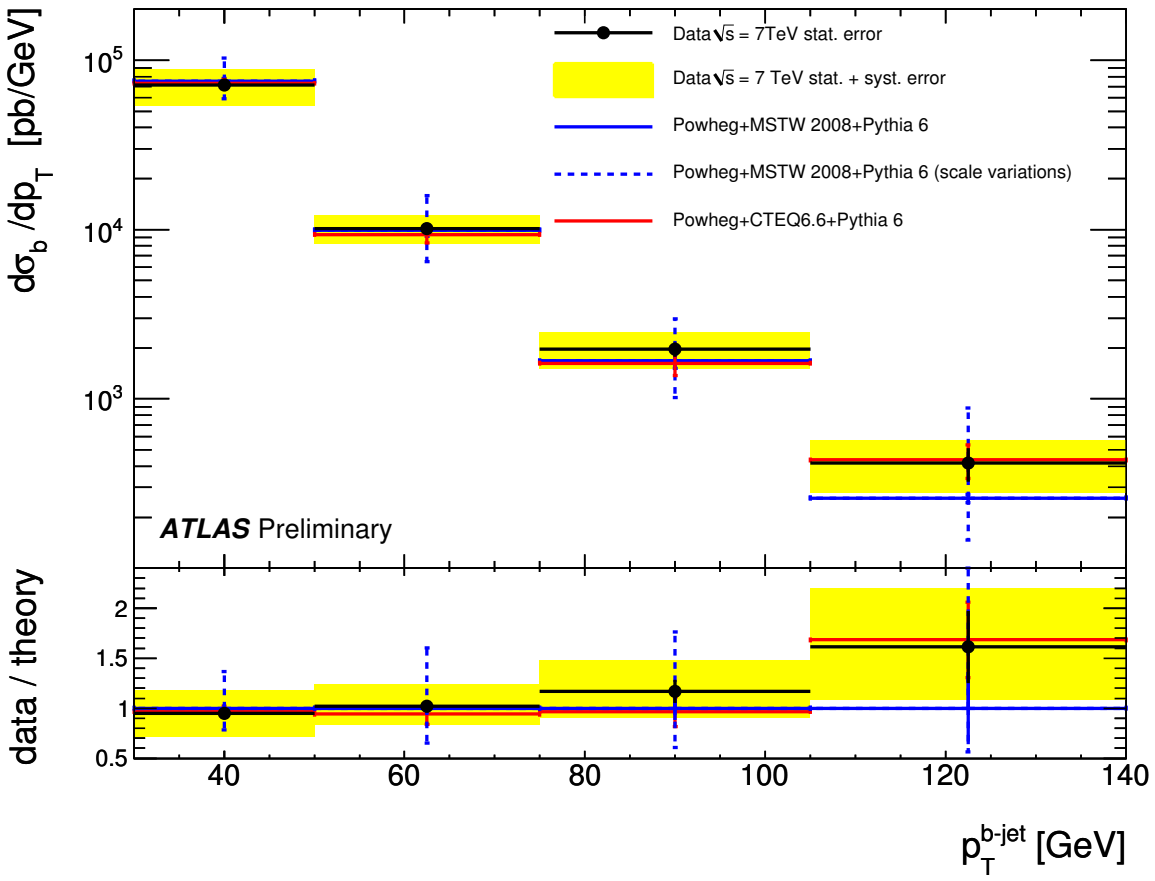

Figure 8.32: Measured *b*-jet differential cross section $d\sigma(pp \to bX, b-jet, |y^{b-jet}| < 2.1)/dp_{\mathrm{T}}^{b-jet}$. The measured cross section values and their statistical uncertainties are shown in black and statistical plus systematic uncertainties as a yellow band. The data is compared to NLO predictions using Powheg and Pythia 6. Two different sets of parton density functions were used for the event generation, MSTW 2008 (blue) and CTEQ6.6 (red). The factorisation and renormalisation scales of the Powheg prediction using MSTW 2008 were varied independently by a factor of two to obtain a systematic uncertainty (dashed blue). The ratio of the data to the Powheg prediction using MSTW 2008 is shown at the bottom of the figure, along with the ratio between the two predictions using different parton density function sets.

σ_b	p_{T}^{b-jet} [GeV]			
[10^4 pb/GeV]	30-50	50-75	75-105	105-140
ATLAS *prelim*	$7.1 \pm 0.3 \pm 1.7$	$1.0 \pm 0.1 \pm 0.2$	$0.20 \pm 0.02\,^{+0.05}_{-0.04}$	$0.042 \pm 0.009\,^{+0.012}_{-0.010}$

Table 8.10: Preliminary measurement by ATLAS of the *b*-jet differential cross section.

8.8.2 Comparison with Different b-Jet Cross Section Measurement

The inclusive differential cross section of b-jets produced in proton-proton collisions at $\sqrt{s} = 7$ TeV has been measured by the ATLAS experiment [26], with a dataset corresponding to an integrated luminosity of 3.1 pb^{-1}. The analysis relies on the presence of a displaced vertex from the decay of long-lived hadrons to select a jet sample enriched in b-jets. The invariant mass of the charged particles forming the vertex is used to estimate the fraction of jets from b-quark production.

Figure 8.33 shows the comparison of the two measurements. The data points with yellow systematic uncertainties denote the b-jet cross section measurement using the p_{T}^{rel} of muons in jets, and the data triangles with orange systematic uncertainties the b-jet cross section measurement using a reconstructed secondary vertex (SV). The two measurements are

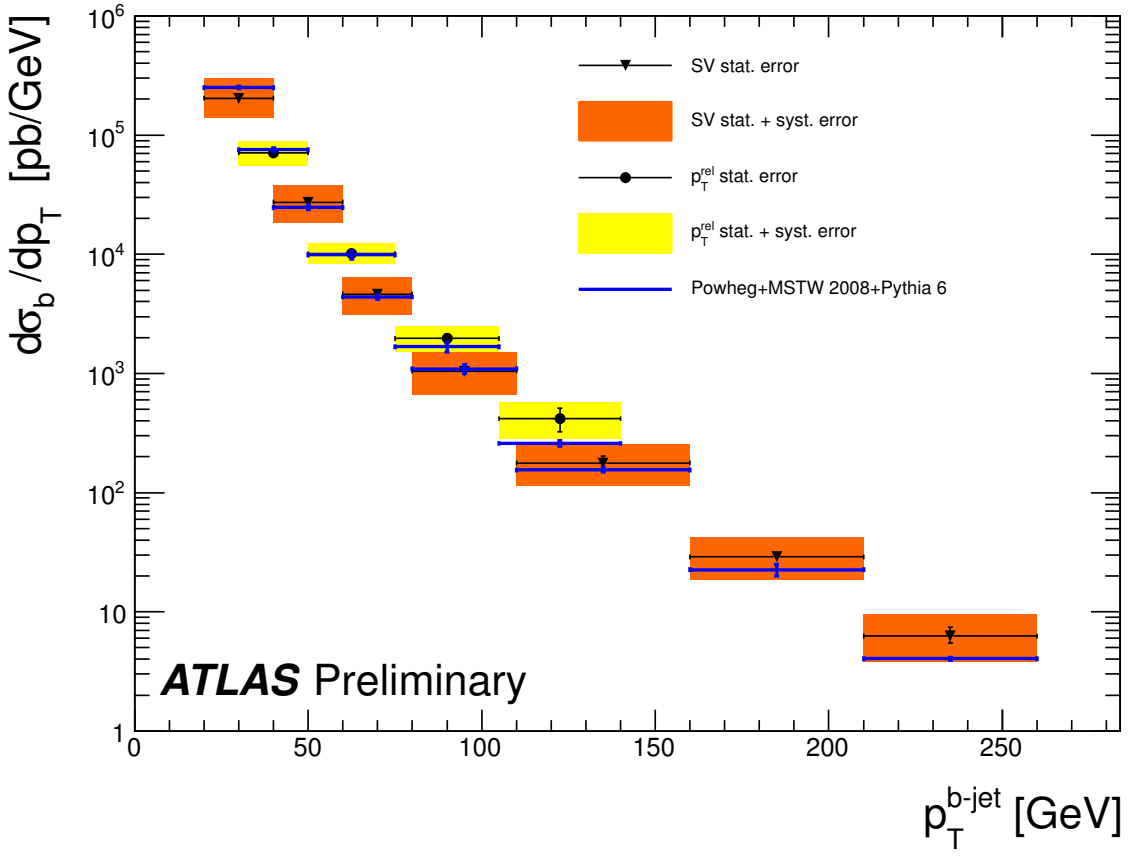

Figure 8.33: Comparison between two measurements of the b-jet differential cross section $d\sigma(pp \to bX, b-jet, |y^{b-jet}| < 2.1)/dp_{\mathrm{T}}^{b-jet}$ with the ATLAS detector, using the p_{T}^{rel} of muons in jets (yellow) and reconstructed secondary vertices SV [26] (orange). Neither statistical correlations nor correlations between the systematic uncertainties of the two measurements such as the luminosity or the jet energy scale uncertainty were taken into account. The measurements are compared to NLO predictions using Powheg, Pythia 6 and the parton density functions MSTW 2008. Only the central values of the theoretical predictions are shown.

consistent with each other, however neither statistical correlations nor correlations between the systematic uncertainties of the two measurements such as the luminosity or the jet energy scale uncertainty were taken into account. The data measurements are compared to NLO predictions using Powheg, the shower Monte Carlo generator Pythia 6 and the parton density functions MSTW 2008. Only the central values of the theoretical predictions are shown. Both measurements agree well with each other, and are consistent with the NLO predictions.

Chapter 9

Summary and Conclusions

The ATLAS detector at the Large Hadron Collider in Geneva, Switzerland, has been successfully commissioned during the last years. The LHC opened up a new energy frontier by colliding two proton beams with unprecedented centre-of-mass energy of 7 TeV. First physics measurements testing the Standard Model of elementary particle physics were successfully carried out. During my three years as a PhD student at CERN between 2008 and 2011, I had the opportunity to work on many aspects of commissioning the ATLAS track reconstruction and b-tagging software and to carry out one of the first measurements of the b-jet production cross section with the ATLAS detector at $\sqrt{s} = 7$ TeV.

The commissioning of the ATLAS track reconstruction software consisted of several steps. The first stage of the commissioning relied on trajectories from cosmic ray particles traversing the ATLAS detector. After adapting the standard track reconstruction software to these specific trajectories, the reconstruction efficiency for cosmic-ray particles within the acceptance of the inner detectors is above 99.7%. A comparison of basic track reconstruction parameters shows good agreement between the data and the Monte Carlo simulations. The next stage of the commissioning used the first collision events at a centre-of-mass energy of 900 GeV and 7 TeV recorded by the ATLAS detector. Detailed comparisons of the data with the Monte Carlo simulations were carried out, showing very good agreement down to the number of hits on the tracks in each subdetector. An incorrect modelling of the number of TRT hits on the tracks in the Monte Carlo simulation was identified and could be solved. The transverse impact parameter resolution and its dependence on the transverse momentum and the traversed material in the inner detectors was studied in great detail in collisions at $\sqrt{s} = 7$ TeV. In the central barrel, the transverse momentum resolution is 23.9 ± 0.2 μm for tracks with a transverse momentum of 15 GeV. This resolution still contains the uncertainty from the primary vertex reconstruction. Data and Monte Carlo simulation are in very good agreement at low transverse momenta, but the agreement worsens at larger momenta $p_{\mathrm{T}} > 10$ GeV due to remaining misalignments in the inner detectors. The data shows a 15% worse resolution in this region than predicted from Monte Carlo simulations. Additional studies need to be carried out to study the transverse impact parameter resolution

with an improved detector alignment. If the differences between the data and the Monte Carlo simulations persist, a strategy needs to be developed to smear the transverse impact parameter resolution in the simulation to agree with the data.

The expected track reconstruction performance at high luminosity was studied in the context of the insertable b-layer (IBL) technical design report. Detailed comparisons of the track reconstruction performance in simulated data samples between the present ATLAS detector layout and an upgraded detector including the IBL within the volume of the innermost pixel layer were carried out. The IBL leads to an improvement in the resolution of the transverse impact parameter d_0 and the longitudinal impact parameter $z_0 \sin\theta$ by up to a factor of 1.8. In addition, the track reconstruction efficiency can be mostly recovered even in case of severe detector failures of the innermost pixel layers or several layers of the SCT detector. The ATLAS Collaboration took this study into consideration when planning the IBL upgrade for the next LHC shutdown in 2016.

The precision track reconstruction plays an important role in the identification of b-jets. The influence of the transverse impact parameter resolution on the performance of the jet probability tagging algorithm JetProb was studied. A modified algorithm using p_{T}- and η-dependent track resolution functions was analysed, which results in an improved mistag rate in the detector endcaps at constant b-tagging efficiency. The jet probability algorithm was validated using 15 nb^{-1} of data at $\sqrt{s} = 7$ TeV and shows good agreement between the data and the Monte Carlo simulations. Despite the differences in the transverse impact parameter resolution and its significance of tracks in different p_{T} and η bins, the overall b-tagging performance of the JetProb algorithm is only changed marginally when using p_{T}- and η-dependent track resolution functions. This study therefore confirms the validity of the default JetProb configuration in ATLAS. The performance of the second early data b-tagging algorithm, the secondary vertex tagging algorithm SV0, was studied with a data sample which corresponds to an integrated luminosity of 3 pb^{-1} at $\sqrt{s} = 7$ TeV. The relative momentum of muons associated to jets with respect to the jet axis was used for a data-driven measurement of the b-tagging efficiency in three bins of p_{T}^{jet} between 25 GeV and 85 GeV. The total systematic uncertainties of this measurement vary between 12% in the first analysis bin and 10% in the other two bins. The measured b-tagging efficiencies are consistent with the predictions from Monte Carlo simulations. This measurement relied on a very robust method to estimate the b-tagging efficiency, which is limited to $p_{\mathrm{T}}^{jet} < 85$ GeV. First preliminary results measuring the b-tagging efficiency in top-antitop events are available, which can measure the efficiency up to much higher jet transverse momenta. The robust b-tagging algorithms like the jet probability tagging algorithm or the secondary vertex tagging algorithm SV0 will soon be superseded by the more powerful combination of the impact parameter tagging algorithm IP3D and the secondary vertex tagging algorithm SV1.

In addition to commissioning the tracking and b-tagging algorithms, the measurement of the inclusive b-jet differential cross section $d\sigma(pp \to bX, b-jet, |y^{b-jet}| < 2.1)/dp_{\mathrm{T}}^{b-jet}$ using

muons in jets was presented. The measurement was carried out in four analysis bins with b-jets fulfilling 30 GeV$< p_{\mathrm{T}}^{b-jet} <$ 140 GeV and $|y^{b-jet}| < 2.1$, and using the 2010 dataset which corresponds to an effective integrated luminosity of $\mathcal{L}_{int} = 4.6 \pm 0.2$ pb^{-1}. The fraction of b-jets in the data sample was estimated using the semi-leptonic decay of b-hadrons into muons. The uncertainties of the measurement vary between 4 and 21% (statistical) and 20 and 28% (systematic). The systematic uncertainties are dominated by the uncertainties of the b-fraction measurement and the unfolding procedure. The measured cross section is reproduced well by next-to-leading order QCD calculations and is in very good agreement with another ATLAS measurement, which relies on the invariant mass of the charged particles forming a secondary vertex to estimate the fraction of b-jets. The comparison of the b-jet cross section between the data and the theoretical predictions shows that the Quantum Chromodynamics calculations have been successfully extended to the new energy regime at the LHC. The initial disagreements at the Tevatron between the data and the Monte Carlo predictions were not repeated at the LHC. Stringent tests of the underlying strong interaction dynamics of QCD such as this measurement give valuable input to many other measurements or searches in the top-quark, Higgs-boson or Super Symmetry sector, since many of these searches rely on the correct description of background processes containing b-quarks. The precision of the presented b-jet cross section measurement could be improved by either reducing the dominant sources of uncertainty in the b-fraction measurement or by improving the b-jet energy resolution and scale uncertainty, which dominate the uncertainty of the unfolding procedure. The extension of the presented measurement to higher transverse momenta is not possible, since the b-fraction measurement looses its discriminating power between b-jets and c-/light-jets for b-jet transverse momenta larger than 140 GeV. Other methods relying for example on the invariant mass of the charged particles forming a secondary vertex to estimate the fraction of b-jets are able to extend the b-jet cross section measurement to much higher b-jet transverse momenta.

Appendix A

Monte Carlo Datasets

A.1 Events from Cosmic Ray Showers

The simulation of cosmic-ray events [99] uses a specialised single particle generator to produce cosmic ray events. Single muons are generated at the earth's surface in a square region (typically 600 m by 600 m) above the ATLAS detector and with the standard cosmic-ray spectrum [100]. The upper and lower energy cutoffs of the spectrum are configurable. Only those muons pointing to a sphere of configurable size (typically 20 m) centred at the geometric origin of the ATLAS detector are propagated through the bedrock and the ATLAS cavern during the simulation. After that, a second filter level is applied to the generated events. This filter requires at least one simulated hit inside a certain configurable ATLAS detector volume. The digitisation of cosmic-ray events uses a number of (mostly timing) changes compared to collisions.

The cosmic-ray simulation has some known limitations:

- The timing of the events (trigger and readout from the detector) is not fully simulated. This is especially affecting the muon detector.
- The three trigger levels are not simulated at all.
- The μ^+/μ^- ratio in simulation is set to 1.5, which is not the same as in data [101]. The simulation flux calculation is done according to Reference [102].

30 000 Monte Carlo cosmic ray events passing the pixel detector with improved truth information in the inner detectors were privately produced and used for the validation study on Monte Carlo simulations. For the comparison between the data from run 121330 and the simulation, the official DPD from the tracking performance group was used.

A.2 Minimum Bias Collision Events

The simulation of minimum bias proton-proton collision events [103] at a centre-of-mass energy of 900 GeV uses the Pythia 6.4.21 generator [9] with a specific set of optimised parameters and the the MRST LO* parton distribution functions [104]. The simulated events consist of a cross-section weighted mixture of non-diffractive, single-diffractive and double-diffractive inelastic processes. The detector response is generated by the Geant4 [50] simulation of the ATLAS detector, which is subsequently reconstructed and analysed using the same software release as the data. The simulated geometry corresponds to a perfectly aligned detector, and the majority of the disabled pixel modules and front-end chips seen in the data were masked in the simulation as well.

A.3 QCD Collision Events

The simulated QCD samples from pp collisions at $\sqrt{s} = 7$ TeV used in this thesis are generated with Pythia 6.4.21 [9] using the MRST LO* parton distribution functions [104]. They are also referred to as "Dijet" samples. To simulate the detector response, the generated events are processed through a Geant4 [50] simulation of the ATLAS detector, and then reconstructed and analysed as the data. The simulated geometry corresponds to a perfectly aligned detector and the majority of the disabled pixel modules and front-end chips seen in the data were masked in the simulation.

Two main simulated samples are used with different selection cuts in the event generation. They are listed in Table A.1. The J0-J6 QCD samples, referred to as the JX QCD samples, are samples generated in bins with non-overlapping parton transverse momenta $\hat{p_{\mathrm{T}}}$. The J0-J4 muon-filtered QCD samples, referred to as the JXμ QCD samples, in addition to non-overlapping parton transverse momenta $\hat{p_{\mathrm{T}}}$ require to have a muon with $p_{\mathrm{T}} > 3$ GeV at generator level. These JXμ samples thus contain muons from b- and c-decays, but do not fully simulate muons from in-flight decays, since pions and kaons are treated as stable particles on generator level. The simulated JX and JXμ samples are constructed such that each of the J0-J6 (J0μ-J4μ) samples cover a different jet p_{T} range. They are added together with event weights according to their cross-sections to form an inclusive set.

The tracking and b-tagging studies presented in Chapter 5 and Chapter 7 use the QCD Monte Carlo DPDs produced by the flavour tagging group which are consistent with the May reprocessing campaign. The measurement of the b-jet cross section in Chapter 8 uses QCD Monte Carlo DPDs from the Autumn reprocessing campaign in 2010. A special DPD version was used, containing truth jets which include muons and neutrinos during the clustering process.

Sample	σ (nb)	Comment
J0 QCD	$9.86 \cdot 10^6$	$8 < \hat{p_{\mathrm{T}}} < 17$ GeV
J1 QCD	$6.78 \cdot 10^5$	$17 < \hat{p_{\mathrm{T}}} < 35$ GeV
J2 QCD	$4.10 \cdot 10^4$	$35 < \hat{p_{\mathrm{T}}} < 70$ GeV
J3 QCD	$2.20 \cdot 10^3$	$70 < \hat{p_{\mathrm{T}}} < 140$ GeV
J4 QCD	$8.77 \cdot 10^1$	$140 < \hat{p_{\mathrm{T}}} < 280$ GeV
J5 QCD	$2.35 \cdot 10^0$	$280 < \hat{p_{\mathrm{T}}} < 560$ GeV
J6 QCD	$3.36 \cdot 10^{-2}$	$560 < \hat{p_{\mathrm{T}}} < 1120$ GeV
J0 muon-filtered QCD	$9.86 \cdot 10^6$	$8 < \hat{p_{\mathrm{T}}} < 17$ GeV, $p_{\mathrm{T}}^{\mu} > 3$ GeV at generator level
J1 muon-filtered QCD	$6.78 \cdot 10^5$	$17 < \hat{p_{\mathrm{T}}} < 35$ GeV, $p_{\mathrm{T}}^{\mu} > 3$ GeV at generator level
J2 muon-filtered QCD	$4.10 \cdot 10^4$	$35 < \hat{p_{\mathrm{T}}} < 70$ GeV, $p_{\mathrm{T}}^{\mu} > 3$ GeV at generator level
J3 muon-filtered QCD	$2.19 \cdot 10^3$	$70 < \hat{p_{\mathrm{T}}} < 140$ GeV, $p_{\mathrm{T}}^{\mu} > 3$ GeV at generator level
J4 muon-filtered QCD	$8.70 \cdot 10^1$	$140 < \hat{p_{\mathrm{T}}} < 280$ GeV, $p_{\mathrm{T}}^{\mu} > 3$ GeV at generator level

Table A.1: Simulated QCD Monte Carlo samples.

A.4 Top-Antitop Events for the IBL Upgrade Study

Top-Antitop events for the IBL upgrade study are generated using the next-to-leading order (NLO) generator MC@NLO [14] at a centre-of-mass energy of 14 TeV, relying on the CTEQ6 parton density function set. The Herwig [11] parton shower program is used for the hadronisation, relying on Jimmy [12] for the underlying event model. Two different geometries are used during the generation of the detector response with Geant4: the nominal ATLAS detector layout and a modified layout including the IBL as fourth pixel layer between the beam pipe and the pixel b-layer. For the reconstruction, slightly different reconstruction versions are used which include modifications and algorithm tunings depending on the detector layout. Some of the events are overlayed before the generation of the detector response with minimum bias events generated by the Pythia program as detailed in Section A.2, but at $\sqrt{s} = 14$ TeV. The number of overlayed events is varied depending on the luminosity scenario the sample represents.

A.5 Bottom-Quark Events

The next-to-leading order (NLO) generation of bottom-quark events at $\sqrt{s} = 7$ TeV for the calculations of the differential b-jet cross section [88] is carried out using the Powheg program [105, 106] to generate $b\bar{b}$ events. A weighting technique is used to ensure a full coverage of the p_{T} and y spectrum. A kinematic cut is placed on the events of $p_{\mathrm{T}} > 1\,\mathrm{GeV}$ to cut off divergences. Two different parton density functions were used for the event generation,

MSTW 2008 NLO [97] and CTEQ6.6 [98]. The hard processes were showered with Pythia 6.4 [9] using the tuned set of parameters AMBT1 [107] and analysed using Rivet [108]. To estimate systematic errors in the calculation, the factorisation and renormalisation scales of the Powheg prediction using the MSTW 2008 parton density function were varied independently by a factor of two.

Acknowledgements

I am very grateful for the continuous professional advice and guidance from my supervisors. You made my time as a PhD student at CERN very interesting and successful.

I would like to thank the Bundesministerium für Bildung und Forschung (BMBF) and CERN for giving me the opportunity to spend the time of my PhD at CERN within the German Doctoral Student Programme (Wolfgang-Gentner-Stipendien). It was very interesting and exciting to be at CERN during the start-up of the LHC, and to see the ATLAS experiment record the first collisions and carry out the first measurements.

Special thanks go to my team of proof-readers. Your feedback and suggestions helped me a lot! I would also like to say thank you to everyone in ATLAS I worked with as well as all my friends at CERN who cycled, ran, swam, raced, hiked and ate with me.

Last but not least I would like to thank my family!

Curriculum Vitae

Dipl.-Phys. Johanna E. Fleckner

* 11 January 1983 in Gießen (Germany)
German

Email: Johanna.Fleckner@cern.ch

Education	
since August 2011	Analyst at Blue Yonder GmbH & Co KG, Karlsruhe
2008 to 2011	German Doctoral Student Programme at CERN (Wolfgang-Gentner-Stipendien)
2008 to 2011	Postgraduate student Johannes-Gutenberg-University of Mainz
2002 to 2007	Physics undergraduate Johannes-Gutenberg-University of Mainz
3 December 2007	Diploma degree in experimental elementary particle physics secondary subjects: computer science and instrumentation for particle physics experiments
1993 to 2002	Marienschule Limburg (High School and College)
7 June 2002	Abitur (final high school examination) focus: mathematics, physics and English

Bibliography

[1] J. W. von Goethe, *Faust. Eine Tragödie.*

[2] D. J. Griffiths, *Introduction to elementary particles.* WILEY-VCH, 2004.

[3] D. H. Perkins, *Introduction to High Energy Physics.* Cambridge University Press, 2000.

[4] K. Nakamura et al., *Review of particle physics*, J. Phys. G **37** (2010) 075021.

[5] R. Ellis, W. J. Stirling, and B. R. Webber, *QCD and Collider Physics.* Cambridge University Press, 2003.

[6] J. M. Campbell, J. W. Huston, and W. J. Stirling, *Hard interactions for quarks and gluons: a primer for LHC physics*, Rep. Prog. Phys. **70** (2007).

[7] J. Huston et al., *New Generation of Parton Distributions with Uncertainties from Global QCD Analysis*, JHEP **0207** (2002) 012, `arXiv:0201195v3 [hep-ph]`.

[8] A. Buckley et al., *General-purpose event generators for LHC physics*, `arXiv:1101.2599 [hep-ph]`. Submitted to Physics Reports.

[9] T. Sjostrand et al., *PYTHIA 6.4 Physics and Manual*, JHEP **05** (2006) 026.

[10] E. Ben-Haim, *La Fonction de fragmentation du quark b, du LEP au TeVatron.* PhD thesis, Paris 6, Paris, 2004. Presented on 21 Dec 2004.

[11] G. Corcella et al., *HERWIG 6.5*, JHEP **0101** (2001) 010, `arXiv:0011363;0210213 [hep-ph]`.

[12] J. Butterworth, J. R. Forshaw, and M. Seymour, *Multiparton interactions in photoproduction at HERA*, Z. Phys. C **72** (1996).

[13] http://www.slac.stanford.edu/ ∼lange/EvtGen.

[14] S. Frixione and B. Webber, *Matching NLO QCD computations and parton shower simulations*, JHEP **0206** (2002) 029, `arXiv:0204244 [hep-ph]`.

[15] S. Frixione et al., *Matching NLO QCD computations with parton shower simulations: the POWHEG method*, JHEP **11** (2007) 070.

[16] R. K. Ellis, S. Dawson, and P. Nason, *The total cross section for the production of heavy quarks in hadronic collisions*, Nucl. Phys. B **303** (1988).

[17] S. Frixione and M. L. Mangano, *Heavy-quark jets in hadronic collisions*, Nucl. Phys. B **483** (1997).

[18] M. Mangano, *The saga of bottom production in $p\bar{p}$ collisions*, `arXiv:0411020v1 [hep-ph]`.

[19] The CDF Collaboration, F. Abe et al., *Measurement of the B Meson Differential Cross*

Section, $d\sigma/dp_t$, in $p\bar{p}$ Collisions at $\sqrt{s} = 1.8$ TeV, Phys. Rev. Lett. **75** (1995) 1451.

[20] The DØ Collaboration, B. Abbott et al., *Cross Section for b-Jet Production in $\bar{p}p$ Collisions at $\sqrt{s}$ = 1.8 TeV*, Phys. Rev. Lett. **85** (2000) 5068.

[21] The CDF Collaboration, A. Abulencia et al., *Measurement of the B+ production cross section in $p\bar{p}$ collisions at $\sqrt{s} = 1960$ GeV*, Phys. Rev. D **75** (2007) 012010.

[22] The LHCb Collaboration, *Measurements of B^0 mesons production cross-section in pp collisions at $\sqrt{s}$ = 7 TeV using $B^0 \to D^{*-}\mu^+\nu_\mu X$ decays*, LHCb-CONF-2010-012 (2010).

[23] The LHCb Collaboration, R. Aaij et al., *Measurement of $\sigma(pp \to b\bar{b}X)$ at $\sqrt{s} = 7$ TeV in the forward region*, Physics Letters B **694** (2010) 209.

[24] The CMS Collaboration, V. Khachatryan et al., *Inclusive b-hadron production cross section with muons in pp collisions at $\sqrt{s}$ = 7 TeV*, JHEP **03** (2011) 090.

[25] The CMS Collaboration, V. Khachatryan et al., *Measurement of the B^+ Production Cross Section in pp Collisions at $\sqrt{s}$ = 7 TeV*, Phys. Rev. Lett. **106** (2011) 112001.

[26] The ATLAS Collaboration, *Measurement of the inclusive and dijet cross section of b-jets in pp collisions at $\sqrt{s} = 7$ TeV with the ATLAS detector*, ATLAS-CONF-2011-056 (2011).

[27] The CMS Collaboration, *Inclusive b-jet production in pp collisions at sqrt(s)=7 TeV*, CMS-PAS-BPH-10-009 (2010).

[28] L. Evans and P. Bryant, *LHC Machine*, JINST **3** (2008) S08001.

[29] http://atlas.ch/.

[30] The ALICE Collaboration, K. Aamodt et al., *The ALICE Experiment at the CERN Large Hadron Collider*, JINST **3** (2008) S08002.

[31] The ATLAS Collaboration, G. Aad et al., *The ATLAS Experiment at the CERN Large Hadron Collider*, JINST **3** (2008) S08003.

[32] The CMS Collaboration, S. Chatrchyan et al., *The CMS Experiment at the CERN Large Hadron Collider*, JINST **3** (2008) S08004.

[33] The LHCb Collaboration, A. Alves Jr et al., *The LHCb Experiment at the CERN Large Hadron Collider*, JINST **3** (2008) S08005.

[34] http://lhc-injection-test.web.cern.ch/lhc-injection-test/.

[35] O. Aberle et al., *The LHC Injection Tests*, LHC-Performance-Note-001 (2008).

[36] M. Bajko et al., *Report of the Task Force on the Incident of 19th September 2008 at the LHC*, LHC-PROJECT-Report-1168 (2009).

[37] C. Grupen and B. Shwartz, *Particle Detectors; Second Edition.* Cambridge University Press, 2008.

[38] The ATLAS Collaboration, G. Aad et al., *ATLAS level-1 trigger: Technical Design Report.* Technical Design Report ATLAS. CERN, Geneva, 1998.

[39] S. Fratina et al., *The TRT Fast-OR Trigger*, ATL-INDET-PUB-2009-002 (2009).

[40] J. Baines et al., *Measurement of Level 2 Event Trigger Efficiencies for the 2008 Cosmic Data Taking*, ATL-INDET-INT-2010-005. (2010).

[41] The ATLAS Collaboration, *Performance of the Minimum Bias Trigger in pp Collisions at* $\sqrt{s} = 900\ GeV$, ATLAS-CONF-2010-025 (2010).

[42] The ATLAS Collaboration, *Performance of the ATLAS Jet Trigger in the Early* $\sqrt{s}$*=7 TeV Data*, ATLAS-CONF-2010-094 (2010).

[43] A. Coccaro, *Tracking and b-tagging in the ATLAS trigger system.* PhD thesis, Universita' di Genova, Genoa, 2010. Presented on 26 Mar 2010.

[44] The ATLAS Collaboration, G. Aad et al., *ATLAS computing: Technical Design Report.* Technical Design Report ATLAS. CERN, Geneva, 2005.

[45] S. Klous, *Event streaming in the online system*, Real Time Conference 2010, 17th IEEE-NPSS (2010).

[46] P. Onyisi, *Operation of the ATLAS detector with first collisions at 7 TeV at the LHC*, PoS ICHEP (2010) 495.

[47] M. Baak et al., *Data Quality Status Flags and Good Run Lists for Physics Analysis in ATLAS*, ATL-COM-GEN-2009-015 (2009).

[48] https://twiki.cern.ch/twiki/bin/view/Atlas/AthenaFramework.

[49] The ATLAS Collaboration, G. Aad et al., *The ATLAS Simulation Infrastructure.*, Eur. Phys. J. C **70** (2010) 823.

[50] S. Agostinelli et al., *GEANT4: A simulation toolkit*, Nucl. Instrum. Meth. A **506** (2003) 250.

[51] P. F. Akesson et al., *ATLAS Tracking Event Data Model*, ATL-SOFT-PUB-2006-004 (2006).

[52] T. Cornelissen et al., *Concepts, Design and Implementation of the ATLAS New Tracking (NEWT)*, ATL-SOFT-PUB-2007-007 (2007).

[53] F. Akesson et al., *ATLAS Inner Detector Event Data Model*, ATL-SOFT-PUB-2007-006 (2007).

[54] R. Frühwirth and others, *Application of Kalman Filtering to Track and Vertex Fitting*, Nucl. Inst. Meth. A **262** (1987).

[55] The ATLAS Collaboration, *Performance of the ATLAS Silicon Pattern Recognition Algorithm in Data and Simulation at* $\sqrt{s} = 7\ TeV$, ATLAS-CONF-2010-072 (2010).

[56] H. Zhu, *Photon conversion reconstruction and its application to the Higgs search in the ATLAS experiment at the Large Hadron Collider.* PhD thesis, University of Sheffield, Sheffield, 2009.

[57] R. Duda and P. Hart, *Use of the Hough Transformation to Detect Lines and Curves in Pictures*, ACM, Vol. 15 (1972) .

[58] The ATLAS Collaboration, G. Aad et al., *Expected Performance of the ATLAS Experiment - Detector, Trigger and Physics*, `arXiv:0901.0512 [hep-ph]`.

[59] The ATLAS Collaboration, *Performance of primary vertex reconstruction in*

proton-proton collisions at $\sqrt{s}$ =7 TeV in the ATLAS experiment, ATLAS-CONF-2010-069 (2010).

[60] M. Cacciari, G. P. Salam, and G. Soyez, *The anti-k_t jet clustering algorithm*, JHEP **04** (2008) 063.

[61] The ATLAS Collaboration, *Jet energy scale and its systematic uncertainty in proton-proton collisions at sqrt(s)=7 TeV in ATLAS 2010 data*, ATLAS-CONF-2011-032 (2011).

[62] S. Hassani et al., *A muon identification and combined reconstruction procedure for the ATLAS detector at the LHC using the (MUONBOY, STACO, MuTag) reconstruction packages*, Nucl. Instrum. Methods A **572** (2007) 77.

[63] The ATLAS Collaboration, *First look at the JetProb b-tagging algorithm in the 900 GeV collision data with the ATLAS detector*, ATLAS-CONF-2010-010 (2010).

[64] The ATLAS Collaboration, *Performance of Impact Parameter-Based b-tagging Algorithms with the ATLAS Detector using Proton-Proton Collisions at s = 7 TeV*, ATLAS-CONF-2010-091 (2010).

[65] The ATLAS Collaboration, *Performance of the ATLAS Secondary Vertex b-tagging Algorithm in 7 TeV Collision Data*, ATLAS-CONF-2010-042 (2010).

[66] The ATLAS Collaboration, *Performance of the ATLAS Secondary Vertex b-tagging Algorithm in 900 GeV Collision Data*, ATLAS-CONF-2010-004 (2010).

[67] D. Lòpez Mateos, E. Hughes, and A. Schwartzman, *Jet Energy Correction to Semileptonic b-jets from Missing Neutrino Energy*, ATL-COM-PHYS-2008-086 (2008).

[68] T. G. Cornelissen, *Track Fitting in the ATLAS Experiment*. PhD thesis, Univ. Amsterdam, Amsterdam, 2006.

[69] T. Cornelissen et al., *Performance of the ATLAS Inner Detector Track Reconstruction of Cosmic Ray Data*, ATL-INDET-INT-2010-020 (2010).

[70] A. Salzburger, *The ATLAS Track Extrapolation Package*, ATL-SOFT-PUB-2007-005 (2007).

[71] The ATLAS Collaboration, G. Aad et al., *The ATLAS Inner Detector commissioning and calibration*, Eur. Phys. J. C **70** (2010).

[72] http://atlas.web.cern.ch/Atlas/public/EVTDISPLAY/events2009.html.

[73] https://twiki.cern.ch/twiki/bin/view/AtlasPublic/InnerDetPublicResults.

[74] The ATLAS Collaboration, *Tracking Studies for b-tagging with 7 TeV Collision Data with the ATLAS Detector*, ATLAS-CONF-2010-070 (2010).

[75] J. Fleckner, *Performance of Track and Vertex Reconstruction and b-Tagging Studies with ATLAS in pp Collisions at $\sqrt{s}$ = 7 TeV*, PoS ICHEP (2010) 011.

[76] http://atlas.web.cern.ch/Atlas/public/EVTDISPLAY/events.html.

[77] The ATLAS Collaboration, *Charged particle multiplicities in pp interactions for track pT > 100 MeV at $\sqrt{s}$ = 0.9 and 7 TeV measured with the ATLAS detector at the LHC*, ATLAS-CONF-2010-046 (2010).

[78] A. Salzburger, *A Parametrization for Fast Simulation of Muon Tracks in the ATLAS Inner Detector and Muon System*. PhD thesis, Leopold-Franzens-Univ. Innsbruck, Innsbruck, 2003.

[79] The ATLAS Collaboration, *Tracking studies for b-tagging with 7 TeV collision data with the ATLAS detector*, ATLAS-CONF-2010-040 (2010).

[80] The ATLAS Collaboration, G. Aad et al., *ATLAS Insertable B-Layer Technical Design Report*. Technical Design Report ATLAS. Geneva, 2010.

[81] The ATLAS Collaboration, *Calibrating the b-Tag and Mistag Efficiencies of the SV0 b-Tagging Algorithm in 3 pb^{-1} of Data with the ATLAS Detector*, ATLAS-CONF-2010-099 (2010).

[82] The ATLAS Collaboration, G. Aad et al., *Measurement of the top quark-pair production cross section with ATLAS in pp collisions at* $\sqrt{s} = 7$ TeV, `arXiv:1012.1792v2 [hep-ph]`. Submitted to Eur. Phys. J. C.

[83] The ATLAS Collaboration, G. Aad et al., *Measurement of inclusive jet and dijet cross sections in proton-proton collisions at 7 TeV centre-of-mass energy with the ATLAS detector*, Eur. Phys. J. C **71** (2011).

[84] S. Aoun et al., *Calibrating the Efficiency of the SV0 Algorithm Using the pTrel Method in 3 pb^{-1} of Data*, ATL-COM-PHYS-2010-758 (2010).

[85] https://twiki.cern.ch/twiki/bin/view/AtlasProtected/HowToCleanJets.

[86] The BaBar Collaboration, B. Aubert et al., *Measurement of the electron energy spectrum and its moments in inclusive* $B \to Xe\nu$ *decays*, Phys. Rev. D **69** (2004).

[87] The ATLAS Collaboration, *Calibrating the b-Tag Efficiency and Mistag Rate in 35 pb^{-1} of Data with the ATLAS Detector*, ATLAS-CONF-2011-089 (2011).

[88] S. Aoun et al., *A Measurement of the b-jet production cross section with 2010 ATLAS data using muons in jets*, ATL-COM-PHYS-2011-221 (2011).

[89] The ATLAS Collaboration, *Measurement of the b-jet production cross section using muons in jets with ATLAS in pp Collisions at* $\sqrt{s} = 7$ *TeV*, ATLAS-CONF-2011-057 (2011).

[90] The ATLAS Collaboration, *Updated Luminosity Determination in pp Collisions at root(s)=7 TeV using the ATLAS Detector*, ATLAS-CONF-2011-011 (2011).

[91] The ATLAS Collaboration, *Determination of the Atlas jet energy measurement uncertainties using tracks in proton proton collisions at* $\sqrt{s} = 7$ *TeV*, ATLAS-COM-CONF-2011-045 (2011).

[92] https://twiki.cern.ch/twiki/bin/view/AtlasProtected/MCPAnalysisGuidelinesRel15.

[93] The DELPHI Collaboration, J. Abdallah et al., *Determination of heavy quark non-perturbative parameters from spectral moments in semileptonic B decays*, Eur. Phys. J. C **45** (2006).

[94] The ATLAS Collaboration, *Final jet energy scale and its systematic uncertainty for jets produced in proton-proton collisions at sqrts = 7 TeV and measured with the ATLAS detector for the 2010 dataset*, ATLAS-COM-CONF-2011-053 (2011).

[95] https://twiki.cern.ch/twiki/bin/view/AtlasProtected/JESUncertaintyProvider.

[96] The ATLAS Collaboration, *A first measurement of the differential cross section for the $J/\psi \to \mu^+\mu^-$ resonance and the non-prompt to prompt J/ψ cross section ratio with pp collisions at $\sqrt{s}$ = 7 TeV in ATLAS*, ATLAS-CONF-2010-062 (2010) .

[97] A. Martin et al., *Parton distributions for the LHC*, `arXiv:0901.0002 [hep-ph]`.

[98] P. Nadolsky et al., *Implications of CTEQ global analysis for collider observables*, `arXiv:0802.0007 [hep-ph]`.

[99] K. Assamagan et al., *The ATLAS Monte Carlo Project*, ATL-COM-SOFT-2008-024 (2008). To be submitted to JINST.

[100] C. Amsler et al., *Review of Particle Physics*, Physics Letters B **667** (2008).

[101] P. Achard et al., *Measurement of the atmospheric muon spectrum from 20 to 3000 GeV*, Physics Letters B **598** (2004).

[102] A. Dar, *Atmospheric Neutrinos, Astrophysical Neutrons, and Proton-Decay Experiments*, Phys. Rev. Lett. **51** (1983).

[103] The ATLAS Collaboration, *Charged particle multiplicities in pp interactions at $\sqrt{s} = 7$ TeV measured with the ATLAS detector at the LHC*, ATLAS-CONF-2010-024 (2010).

[104] A. Sherstnev et al., *Parton Distributions for LO Generators*, Eur. Phys. J. C **55** (2008).

[105] S. Frixione, P. Nason, and G. Ridolfi, *The POWHEG-hvq manual version 1.0*, `arXiv:0707.3081 [hep-ph]`.

[106] S. Alioli et al., *A general framework for implementing NLO calculations in shower Monte Carlo programs: the POWHEG BOX*, JHEP **06** (2010) 043.

[107] The ATLAS Collaboration, *Charged particle multiplicities in pp interactions at $\sqrt{s}$ = 0.9 and 7 TeV in a diffractive limited phase space measured with the ATLAS detector at the LHC and a new Pythia 6 tune*, ATLAS-CONF-2010-031 (2010).

[108] A. Buckley et al., *Rivet user manual*, `arXiv:1003.0694v4 [hep-ph]`.

List of Figures

List of Tables